

Correlating Raman scattering signatures with microstructural properties of tribological surfaces

Dissertation

submitted in partial fulfillment of
the requirements for the degree of

Dr. rer. nat.

to the Faculty of Physics
TU Dortmund University, Germany

by

Henning Moldenhauer

Dortmund, May 2021

Date of the oral examination: 13 July 2021

Examination board:

Dr. Jörg Debus

Prof. Dr. Heinz Hövel

Prof. Dr. Gudrun Hiller

Prof. Dr. Zhe Wang

Table of Contents

1	Introduction	1
2	Theoretical Background	5
2.1	Raman Scattering	5
2.1.1	Vibrations in a Crystal	8
2.1.2	Stretching Modes and Group Theory	10
2.1.3	The Intensity of a Raman Line	12
2.1.4	Line Shapes of Raman Signals	12
2.1.5	The Frequency Position of a Raman Line	16
2.1.6	Penetration Depth of Light in Matter	16
2.1.7	Resonant Raman Scattering	18
2.2	Tribology	19
2.2.1	Materials and their Mechanical Properties	20
2.2.2	Materials and their Surface Properties	23
2.2.3	Flash Temperatures in Mechanical Contacts	24
2.3	Fundamental Properties of Selected Materials	27
2.3.1	Iron Oxides	28
2.3.2	Carbon and Related Structures	30
2.3.3	Molybdenum Disulfide	34
2.3.4	Tungsten Carbides and Oxides	36
3	Experimental Methods and Data Analysis	37
3.1	Raman Spectroscopy	37
3.1.1	Basic Raman Spectroscopy Instrumentation	37
3.1.2	Confocal Raman Spectroscopy	39
3.2	Sample Preparation and Further Characterization	41
3.2.1	Sample Preparation by Physical Vapor Deposition	41
3.2.2	Characterization of Mechanical Properties	42
3.2.3	Characterization of Topography	44
3.2.4	Characterization of Sample Structure and Composition	45
3.3	Data Processing – The Spectrum Analysis Package	46
3.3.1	Spike Removal	47
3.3.2	Raman Scattering Mappings	50
3.3.3	Principal Component Analysis	50
4	Definition of Tribological Material	53
4.1	Magnetite and Hematite Formation	54
4.2	Oxygen Incorporation in Tungsten Carbide	59
4.3	Tribofilm Formation of Sputtered MoS _x Thin Films	61

5	Microstructural Properties and Interatomic Interactions	71
5.1	Effects of the Deposition Parameters on the Properties of Amorphous Carbon Films	71
5.2	Structural, Mechanical and Tribological Properties of As-Deposited MoS _x Films	84
5.3	Raman Characterization of Thermally Annealed MoS _x Films	91
6	Optical Characterization of Tribological Amorphous Carbon at Steel Surfaces	101
7	Summary and Outlook	119
A	Supporting Methods	123
A.1	Fabry-Perot Interferometry	123
A.2	Focus Stacking	124
A.3	Knife-Edge Method	124
A.4	Spectrometer Resolution and Line Width	126
B	Spectrum Analysis	127
B.1	How to Generate Mappings	127
B.2	How to Interpret Mappings	129
B.3	Exemplary Principal Component Analysis	130
C	Character Tables	133
D	Amorphous Carbon Layers – Supplementary	135
	List of Acronyms	137
	List of Symbols	139
	List of Constants	143
	List of Figures	146
	List of Tables	147
	List of Publications	149
	Bibliography	151
	Acknowledgments	175

Chapter 1

Introduction

The overall field of friction and wear – tribology – has a huge impact on all scales of daily life [Czi15b; Men20]. Tribological systems range from atomic scales in the nanometer domain through microsystems up to macroscopical devices that are hundreds of meters in size. Tribological processes influence energy consumption and economic costs of such devices. A recent study of Holmberg and Erdemir showed, that 20% of the world’s total energy consumption is due to tribological losses and an additional 3% due to remanufacturing of worn parts [Hol17]. By advancing surfaces, materials and lubrication technologies, the energy losses could be reduced by 40% within the next 15 years, leading to a reduction of approximately 9% of the total energy consumption. This reduction in energy consumption would reduce the global CO₂ emissions by $3140 \text{ MtCO}_2 = 3.14 \text{ PgCO}_2$, which is equivalent to 0.86 PgC, or in other words, it would decrease the yearly human made carbon flux into the atmosphere by 10% [Cia13]. Summing up, advances in tribology directly promise progress in climate protection.

Even today, many fundamental processes of tribology are not yet fully understood [Wan13; Urb10], so that there is still a lot of progress to be expected in tribology. In particular, the energy dissipation in a tribological contact [Par14] and the processes at the micro- and nanoscale are currently of interest [Nia16]. For the dissipation of energy, different processes are involved. Some of the important processes are the relaxation of electron-hole pairs (fluorescence), the rupture of chemical bonds (triboluminescence) or the excitation of collective vibrations in crystalline materials (phonons). Ultimately, most of these processes manifest themselves as heat [Par14]. For each of the underlying processes, the symmetry properties of the contacting surfaces are of great importance and significantly influence the relaxation process. It is well known, that at contacting surfaces layers of tribological material (tribofilms) form without any human intervention [Sta14c]. In metallic contacts, these tribolayers or tribofilms consist of particles in the micro- and nanoscale [Czi15e], which – as stated before – tremendously impact the tribological processes [Hof16]. The layers define the short- and long-term behavior of the contacting surfaces [Urb10].

In order to determine the symmetry properties of the contacting surfaces and gain insight into the underlying processes Raman scattering is utilized. Raman scattering is the vibrational response of a molecule placed in an electrical field. A recorded Raman spectrum supplies a physico-chemical fingerprint for each material, which allows one to gain insight into the interatomic interactions (see Chapter 2). Raman spectroscopy is a powerful optical scattering technique that is used for a wide range of applications [Die18a; Gou07; Web00]. Among others, Raman scattering can be and has been used for material identification, discovery of novel effects and insights into elementary mechanisms. The main advantages of Raman spectroscopy are its applicability to solids, liquids and solutions and its ease of use.

Often no or only little sample preparation is needed for Raman spectroscopy. Combining the scattering technique with microscopy makes micro-Raman spectroscopy a method that delivers molecular information at the micrometer scale [Van13a], allowing surfaces to be mapped. By analyzing spatially resolved Raman scattering mappings – commonly called Raman scattering images – with chemometrical methods like Principal Component Analysis (**PCA**), the distribution of different chemical species may be visualized [Lew01]. This visualization provides a high information density in an easily accessible manner. These features of Raman spectroscopy, as well as the availability of high-quality and inexpensive equipment, have contributed to the widespread use of this technique.

The goal of this thesis is an advancement of the knowledge on the fundamental tribological processes in the contact of relative moving surfaces using Raman spectroscopy. Therefore, this thesis is structured as follows:

Chapter 2 presents the theoretical principles of the Raman effect, lattice vibrations in a crystal, as well as crystallographic space groups and their relation to Raman activity. Additionally discussed are the experimentally relevant properties of the Raman signals, like intensity, shape and position. Also the penetration depth of an electromagnetic wave into matter is presented. Next to the basics of Raman scattering, an introduction to tribology is given. Here, the phenomena of wear and friction are defined. Subsequent to these definitions, the mechanical and surface properties are briefly discussed. The section on tribology ends with the presentation of a method to estimate flash temperatures occurring in tribological contacts. Chapter 2 closes with a presentation of the most important properties of the mainly investigated materials throughout this thesis. Here, typical products of metal corrosion (iron oxides), surface protection coatings (amorphous carbon and tungsten carbide) and solid lubricants (molybdenum disulfide) are introduced.

Chapter 3 introduces the experimental and analytical methods. Here, a basic Raman setup and a confocal Raman setup are presented. This is followed by a discussion on sample preparation and its mechanical, topographical, structural and compositional characterization. The chapter ends with a description of the analysis procedure, including the presentation of methods of spike removal, Raman mapping and dimensionality reduction of experimental data. The presented methods are combined to the self-developed software package **spectrum analysis**.

Chapter 4 gives a first Raman spectroscopic view on wear. Here, several indicators for tribofilms in different tribological systems are presented. For uncoated steel-steel contacts, a spatial distribution of multiple iron oxide configurations is detected, while for tungsten-carbide coated contacts an oxygen incorporation is observed. Additionally, for dry-lubricant MoS_x coatings, third-body particles with a different chemical behavior than the original coating are detected. All of the detected indicators might be used to monitor the degree of wear of the respective surfaces and may allow for prediction of their tribological behavior.

Chapter 5 utilizes Raman spectroscopy and X-ray methods to gain insights into the microstructural properties and interatomic interactions of protective and lubricating coatings. Here, the interaction effects of the deposition parameters on the structural and mechanical properties of amorphous carbon and MoS_x films are investigated, as well as structural and tribological changes of post-growth annealed MoS_x films. For amorphous carbon films, a correlation of deposition parameters and sp^3 formation is determined. The sp^3 content might be roughly estimated using multi-wavelength Raman spectroscopy. For MoS_x coatings, influences of the deposition parameters on bond lengths and inter-layer spacing, as

well as a spectral estimation for the films' frictional behavior are shown. Here, Raman scattering is used to estimate the shear resistance of a coating or to detect stacking faults in the deposited films.

Chapter 6 investigates the formation and properties of tribofilms from lubricated and non-lubricated steel-steel interaction with spatially resolved Raman spectroscopy. Here, a layered tribofilm with nano-sized hematite, magnetite and amorphous carbon particles is revealed. Oxygen is shown to play a key role in the tribological process. Additionally, Raman spectroscopy is combined with chemometrical methods, which allows one to correlate spectral information with surface properties. These correlations may be used to advance the understanding of the spatial formation of tribofilms.

In Chapter 7 the results from the previous chapters are summarized and an outlook on improvements to the measurement technique is given. In the appendix brief introductions to supporting methods, like Fabry-Perot interferometry, focus stacking and the knife-edge method, as well as an introduction to the `spectrum analysis` package are given.

Chapter 2

Theoretical Background

In this chapter an introduction to Raman spectroscopy¹ and tribology is given. The chapter closes with a section on fundamental properties of selected materials that are investigated throughout this work.

An introduction to Raman scattering is found in the book by Vandenabeele [Van13c], which the following section is based on. Furthermore, the review by Gouadec gives an overview on Raman scattering and its extension to the nanoscopic scale [Gou07]. A theoretical in-depth discussion of the phenomenon is given by Cardona et. al [Car83b; Pag91]. Vast information on Raman and Brillouin Scattering is reported in the dedicated *Light Scattering in Solids* series. An overview of the different volumes and the topics of the chapters is given in references [Car91; Car00]. The following section presents the Raman effect, it's dispersion relation in a crystal and alterations to the optical response, like shape and frequency. Additionally, the wavelength-dependent penetration depth is presented.

For an introduction to the various fields of tribology, the handbook by Czichos is recommended [Czi15c]. In the present section, the very basic concepts of friction and wear, as well as the mechanical and surface properties of materials are presented. The section ends with a model to estimate the flash temperatures in a contact.

2.1 Raman Scattering

Placing a molecule into an electrical field E induces an electrical dipole moment p , which can be described as

$$p = \alpha \cdot E + \frac{1}{2} \beta_{\text{hyp}} \cdot E^2 + \frac{1}{6} \gamma_{\text{hyp}} \cdot E^3 + \dots \quad (2.1)$$

Here, α is the polarizability tensor, β_{hyp} the hyperpolarizability tensor and γ_{hyp} the 2nd hyperpolarizability tensor. Typically α is in the range of $10^{-40} \text{ C m}^2/\text{V}$. Each higher order tensor decreases by a factor of about 10^{-10} m/V , which allows one to neglect their influence in the following and reduce equation (2.1) to

$$p = \alpha \cdot E. \quad (2.2)$$

The electrical field is caused by a beam of light, which is described as

$$E = E_0 \cdot \cos(2\pi \cdot \nu_0 t). \quad (2.3)$$

¹Raman spectroscopy is named after the Indian physicist Chandrasekhara Venkata Raman (*1888; †1970) who discovered this type of scattering with his assistant Kariamanikkam Srinivasa Krishnan as optical analogue to the Compton Effect [Ram28a; Ram28b].

Here, E_0 is the amplitude of the electrical field, ν_0 the frequency of the incident radiation and t the moment of investigation. In order to calculate the dipole moment p , the polarizability tensor is expressed as a Taylor series with the normal coordinate Q of the molecule of interest, as the polarizability strongly depends on the possible vibrations of the molecule (see also Section 2.1.1).

$$\alpha = \alpha_0 + \sum_j \left(\frac{\partial \alpha}{\partial Q_j} \right)_0 \cdot Q_j + \sum_{j,k} \left(\frac{\partial^2 \alpha}{\partial Q_j \partial Q_k} \right)_0 \cdot Q_j \cdot Q_k + \dots \quad (2.4)$$

Here, Q_j and Q_k are the j^{th} and k^{th} normal vibrations of the molecule, with vibrational frequencies ν_j and ν_k . Only the first approximation is used in the following², meaning that the different normal vibrations are independent from each other and no cross relations are taken into account. Therefore, taking one specific normal vibration Q_N it can be described by

$$\alpha_N = \alpha_0 + \alpha'_N \cdot Q_N \quad \text{with } \alpha'_N = \left(\frac{\partial \alpha}{\partial Q_N} \right)_0. \quad (2.5)$$

In the first approximation the normal coordinate behaves like a harmonic oscillator and therefore varies over time like

$$Q_N = Q_{N,0} \cdot \cos(2\pi \cdot \nu_N t + \phi_N), \quad (2.6)$$

with the amplitude of the normal vibration $Q_{N,0}$, the frequency of the normal vibration ν_N and a phase angle ϕ_N . By substituting equations (2.3), (2.5) and (2.6) in the simplified definition of the dipole moment using equation (2.2) and applying a cosine product-to-sum identity the frequency dependence of the dipole moment for a selected normal vibration can be written as

$$p_N = \alpha_0 E_0 \cos(2\pi \cdot \nu_0 t) + \frac{1}{2} \alpha'_N E_0 Q_{N,0} \cos(2\pi \cdot (\nu_0 \pm \nu_N) t \pm \phi_N). \quad (2.7)$$

From this equation it becomes clear that the induced dipole moment can be split into three components with different frequency dependencies

$$p_N = p(\nu_0) + p(\nu_0 + \nu_N) + p(\nu_0 - \nu_N). \quad (2.8)$$

The first term is only dependent on the frequency of the incident radiation ν_0 . This describes an oscillation of the induced dipole with the same frequency as the stimulating light field. This behavior is an elastic scattering behavior, which is called Rayleigh scattering³. The second and third term in equation (2.8) correspond to inelastic scattering processes. Here the frequency of the incident field is shifted by the frequency of the normal vibration of the material of interest. The energy is either increased ($\nu_0 + \nu_N$) or reduced ($\nu_0 - \nu_N$) compared to the incident frequency. This form of scattering is called Raman scattering, whereas the increase is called anti-Stokes scattering and the reduction is called Stokes scattering⁴.

²This approximation is often referenced as Placzek's theory. George Placzek (*1905; †1955) argued that the amplitude of the normal vibrations is small and therefore only the linear term in equation (2.4) is used [Pla34] (see §16 on pages 275 - 278).

³The scattering is named after Lord Rayleigh (John William Strutt, *1842; †1919) who used this type of scattering to explain the color of the sky and to determine the size of a molecule [Str71].

⁴The scattering is named after the Irish physicist George Gabriel Stokes (*1819; †1903), who coined the term fluorescence [Sto52].

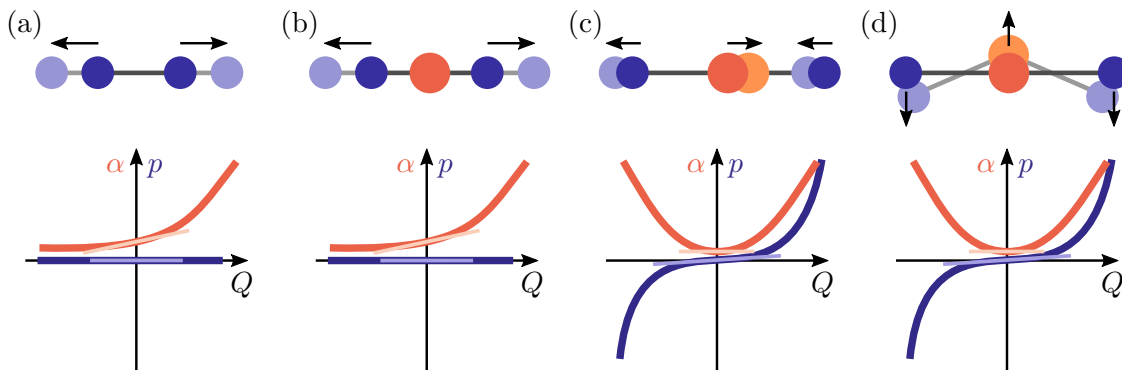


Figure 2.1 Schemes of the normal modes of (a) a diatomic molecule and (b-d) a triatomic molecule. The polarizability α (orange) and the dipole moment p (blue) are indicated, with their gradients at $Q = 0$. For non-vanishing gradients of the polarizability (dipole moment) the corresponding mode is Raman (infrared) active. Adapted from [Die18b].

Furthermore, equation (2.7) indicates that only for $\alpha'_N \neq 0$ Raman scattering is excited. This leads to the selection rule of Raman scattering:

$$\alpha'_N = \left(\frac{\partial \alpha}{\partial Q_N} \right)_0 \neq 0. \quad (2.9)$$

It means that, for each normal vibration Q_N , Raman scattering only appears, where the polarizability α is changed. This selection rule is visualized in Figure 2.1. Here, the vibration modes of a diatomic molecule and a triatomic molecule are presented. As shown before, a vibration mode is Raman active for a non-vanishing derivative of the polarizability. For a non-vanishing derivative of the dipole moment the vibration mode is infrared active. Both scattering phenomena are complementary to each other. In Figure 2.1 (a) the solely possible symmetric vibration of a homo-diatomic molecule is presented [Die18b]. The molecule has no permanent dipole p , which is also true for small perturbations from its equilibrium, and is therefore not infrared active. In contrast, the polarizability changes with the distance between the two atoms. For a vanishing distance, the electron density can be described by an electron density of a single atom, while for an infinite distance the electron density can be described by the electron densities of two individual atoms with half mass. The polarizability of the latter case is larger than the polarizability of the first case, leading to a monotonous polarizability, with a non-vanishing derivative at the equilibrium position. Therefore, the vibration mode is Raman active.

The vibration modes of a linear triatomic molecule are shown in Figures 2.1 (b-d). In a first approximation for the symmetric stretching mode (see Figure 2.1 (b)), the dipole moment remains constant along the normal coordinate, but the opposite signs of the individual bonds lead to infrared inactivity. The molecule is Raman active, which is explained by the previously used arguments for the Raman activity of the diatomic molecule. For anti-symmetric stretching (see Figure 2.1 (c)) and bending vibrations (see Figure 2.1 (d)) the dipole moment changes its sign, when passing through the equilibrium position. Therefore, the derivative of the dipole moment is non-zero, leading to infrared activity of both modes. Contrasting, the changes of the polarizability are symmetric to sign inversion, leading to a vanishing derivative. Therefore, both modes are Raman inactive.

2.1.1 Vibrations in a Crystal

The general mechanism of Raman scattering is explained in the previous section. Here, the polarizability tensor plays a key role and is used to define a selection rule for the occurrence of Raman scattering. The polarizability tensor is strongly dependent on the normal vibrations of the scattering system. As crystal-like systems are of major interest in this thesis, this section presents a classical model describing vibrations in crystals. It is based on reference [Gro12b].

In the suggested model, each atom η of unit cell N with mass m_η shall experience small displacements $u_{N\eta j}$ along direction j from its equilibrium position. As the atom is placed in a lattice and coupled to other atoms ζ in unit cell M , the coupling constants $C_{N\eta j}^{M\zeta k}$ and the corresponding displacements $u_{M\zeta k}$ along directions k of these atoms influence the motion of the displaced atom η and force it back into its equilibrium state.

$$m_\eta \frac{\partial^2 u_{N\eta j}}{\partial t^2} + \sum_{M\zeta k} C_{N\eta j}^{M\zeta k} u_{M\zeta k} = 0 \quad (2.10)$$

The number of differential equations in the system presented in equation (2.10) is proportional to Avogadro's constant N_A for a realistic crystal, but fortunately the periodicity of the crystal lattice allows one to make the following ansatz

$$u_{N\eta j} = \frac{1}{\sqrt{m_\eta}} A_{\eta j}(\mathbf{q}) e^{i(\mathbf{q}\mathbf{R}_\eta - \omega t)}. \quad (2.11)$$

Here, \mathbf{q} is the wave vector and $A(\mathbf{q})$ the amplitude of the displacement u . This plane wave is only defined at the lattice sites \mathbf{R}_η and oscillates with frequency ω . Using this ansatz in equation (2.10) gives

$$-\omega^2 A_{\eta j}(\mathbf{q}) + \sum_{\zeta k} D_{\eta j}^{\zeta k}(\mathbf{q}) A_{\zeta k}(\mathbf{q}) = 0 \quad \text{with} \quad D_{\eta j}^{\zeta k}(\mathbf{q}) = \sum_M \frac{1}{\sqrt{m_\eta m_\zeta}} C_{N\eta j}^{M\zeta k} e^{i\mathbf{q}(\mathbf{R}_\eta - \mathbf{R}_\zeta)}. \quad (2.12)$$

The parameters $D_{\eta j}^{\zeta k}(\mathbf{q})$ construct the dynamical matrix (for further reading see references [Kee96] and [Sol07]), which is a linear homogeneous system of equations. This formalism reduces the number of equations to be solved from being proportional to N_A to only three equations for each atom in the base of the unit cell, for each wave vector \mathbf{q} . So for a mono-atomic base systems of three equations, and for a di-atomic base systems of six equations have to be solved. The linear homogeneous system of equations is solvable for

$$\det\{D_{\eta j}^{\zeta k}(\mathbf{q}) - \omega^2 \mathbf{1}\} = 0. \quad (2.13)$$

This equation gives n solutions $\omega(\mathbf{q})$ for each atom in the unit cell, where n is the dimension of the vector space \mathbb{R}^n . The relation $\omega(\mathbf{q})$ is called the dispersion of the wave vector, while each of the different $\omega(\mathbf{q})$ is called a branch of the dispersion.

As an example a di-atomic linear chain with a lattice constant a and coupling constant C is analyzed in the following. Using

$$D_{\eta j}^{\zeta k}(q) = \begin{pmatrix} \frac{2C}{m_1} & -\frac{C}{\sqrt{m_1 m_2}}(1 + e^{-iqa}) \\ -\frac{C}{\sqrt{m_1 m_2}}(1 + e^{iqa}) & \frac{2C}{m_2} \end{pmatrix} \quad (2.14)$$

in equation (2.13) and solving the equation gives

$$\omega^2 = \frac{C}{m_{\text{red}}} \pm \sqrt{\frac{C^2}{m_{\text{red}}^2} + \frac{4C^2}{m_1 m_2} \sin^2\left(\frac{qa}{2}\right)} \quad \text{with} \quad \frac{1}{m_{\text{red}}} = \frac{1}{m_1} + \frac{1}{m_2}, \quad (2.15)$$

where m_{red} is the reduced mass of the unit cell. This is the dispersion relation between ω and q , which is restricted by the periodicity of the crystal to possible values of q in the range of $-\pi/a \leq q \leq \pi/a$. The enclosed region of these values is called the first Brillouin zone⁵ of the crystal.

Figure 2.2 shows the positive half of the first Brillouin zone of the di-atomic chain. The two solutions ω_+ and ω_- of equation (2.15) build the two plotted branches of the dispersion relation. They are called the optical (ω_+) and the acoustic (ω_-) branch. The names of the dispersion branches are based on the phase relation of the atoms, whereas at the zone boarder the atoms of the acoustic branch oscillate in phase with the same amplitude, the atoms of the optical branch oscillate with opposing phase with an amplitude anti-proportional to their weight ratio. Whether the atoms oscillate parallel or perpendicular to the direction of propagation of the wave, the modes are called longitudinal (parallel) or transversal (perpendicular). Often these modes are abbreviated by TA (transversal acoustic), LA (longitudinal acoustic), TO (transversal optical) and LO (longitudinal optical). Additionally, acoustic (ZA) and optical (ZO) out-of-plane modes are observable in several crystal structures [Nik17]. One lattice vibration is commonly called phonon or vibration mode.

In the discussed model, only longitudinal modes are considered. Here, for low q the acoustic branch shows an oscillating frequency of zero, which is equal to the motion of the complete crystal, whereas the optical branch shows a non-zero oscillating frequency of $(2C/m_{\text{red}})^{0.5}$.

At the boundary $q = \pi/a$ of the Brillouin zone, the di-atomic linear chain shows a frequency gap. This gap grows with the mass ratio m_1/m_2 of the two atoms in the chain. It vanishes for $m_1 = m_2$. For the example given, non-equal oscillation frequencies are observed for both dispersion branches. For a more detailed discussion see reference [Gro12b].

In a 3-dimensional crystal with j atoms per unit cell the solution of equation (2.13) delivers three acoustic and $3j - 3$ optical branches of the dispersion relation. Depending on the atomic species and their bonds, it is possible that several branches are degenerate and less than the expected number of branches is observed.

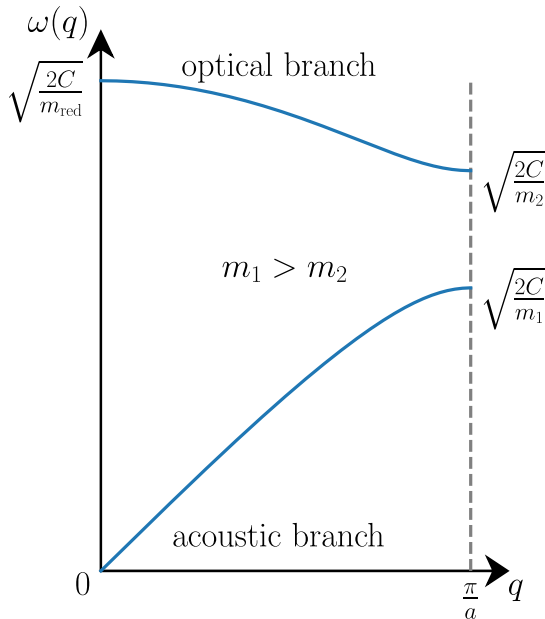


Figure 2.2 Exemplary dispersion relation of a di-atomic linear chain in the first Brillouin zone with $m_1 = 2m_2$.

⁵The concept of the Brillouin zone was developed by the french physicist Leon Brillouin (*1889; †1969).

In general, the dispersion relations are always shown along specific directions in q -space which connect points of high symmetry in the Brillouin zone, called critical points of the Brillouin zone. Here, $q = 0$ is always the center of the Brillouin zone, which is called the Γ point. The other critical points depend on the symmetry of the crystal. Details are presented in reference [Set10].

In order to conduct experiments with phonons, it is important to have a look at the relation of the wavelength of the exciting electromagnetic field and the wave vector. The two parameters are linked by the definition of the wave vector's magnitude $|\mathbf{q}| = 2\pi/\lambda$. From this relation typical excitation wavelengths in the visible spectrum ($< 10^3$ nm) show $|\mathbf{q}_0| \sim 10^5 \text{ cm}^{-1}$, whereas at the boundary of the Brillouin zone, the relation $2\pi/\lambda = \pi/a$ has to be fulfilled. This leads to $|\mathbf{q}_{\pi/a}| \sim 10^8 \text{ cm}^{-1}$ for typical lattice constants ($\sim 10^3$ pm). So the excitation of a crystal with visible light inspects only lattice vibrations at the center of the Brillouin zone, whereas extremely short wavelengths are needed to investigate phonons at the boundary of the Brillouin zone⁶.

Additionally to the prior described lattice vibrations, phonon modes might arise or vary due to higher-order terms in equation (2.4), temperature or pressure dependence, applied electrical fields or other effects (see reference [Mit69] for details).

2.1.2 Stretching Modes and Group Theory

Point groups are helpful in analyzing vibrational spectra and they deliver an idea of how many modes are to be expected during measurements⁷. Furthermore, point groups can be used to determine Raman or infrared activity. Point groups are commonly noted using the Schoenflies⁸ notation and are classified by several families [Gro12c]. The crystallographic families of the point groups are

- C_N (cyclic) with a N -fold rotation axis,
- S_{2N} (Spiegel) with a $2N$ -fold rotation-reflection axis,
- D_N (dihedral) with a N -fold rotation axis and additional N twofold axes perpendicular to that axis,
- T (tetrahedral) with the rotation axes of a tetrahedron.
- O (octahedral) with the rotation axes of an octahedron,

Here, the superscripts h (horizontal), v (vertical) and d (diagonal) add mirror planes to the selected point group. Examples are MoS_2 , which belongs to the D_{6h} point group [Zha13a], or Fe_3O_4 (magnetite), which belongs to the O_h point group [Far97], whereas $\alpha\text{-Fe}_2\text{O}_3$ (hematite) belongs to the D_{3d} point group [Far97].

Each point group allows a different set of symmetry operations and has an irreducible representation (Mulliken symbols). They can be written in a character table, as shown in Table 2.1. For character tables of materials used in this thesis see also Appendix C. Other important character tables are presented in the appendix of Cotton's book [Cot90a]. The

⁶To generate wavelengths in the range of crystal lattice constants neutron scattering can be utilized.

⁷As a rule of thumb it can be stated that the higher the symmetry of the material's point group, the lower the number of observable Raman peaks [Col11].

⁸Arthur Moritz Schoenflies (*1853; †1928) was a German mathematician who found the complete list of all 230 crystallographic space groups [Sch91].

Table 2.1 Character table of the D_{3d} point group.

D_{3d}	E	$2C_3$	$3C_2$	i	$2S_6$	$3\sigma_d$	
A_{1g}	1	1	1	1	1	1	$x^2 + y^2, z^2$
A_{2g}	1	1	-1	1	1	-1	R_z
E_g	2	-1	0	2	-1	0	(R_x, R_y) $(x^2 - y^2, xy), (xz, yz)$
A_{1u}	1	1	1	-1	-1	-1	
A_{2u}	1	1	-1	-1	-1	1	z
E_u	2	-1	0	-2	1	0	(x, y)

center columns of Table 2.1 exemplary shows the symmetry operations of the respective point group. The overall possible symmetry operations are [Mau19b]

- E, which is a rotation by 360° ,
- C_N , which is a rotation by $360^\circ/N$,
- S_N , which is a rotation by $360^\circ/N$ followed by a reflexion in a plane perpendicular to the rotation axis,
- σ , which is a reflection operation (equivalent to S_1),
- i, which is an inversion operation (equivalent to S_2).

Again, the superscripts of the reflection indicate horizontal (h), vertical (v) or diagonal (d) mirror planes. The rotation axis of highest order is called principal rotation axis. In the leftmost column of Table 2.1 the irreducible representations (Mulliken symbols) are shown. They are [Cot90b]

- A, a single degenerate representation (1 in column E), symmetric with respect to the principal rotation axis,
- B, a single degenerate representation (1 in column E), antisymmetric with respect to the principal rotation axis,
- E, a double degenerate representation (2 in column E),
- T, a triple degenerate representation (3 in column E).

The subscripts resemble symmetry (g) or antisymmetry (u) with respect to a center of inversion. The subscripted numbers denote symmetric (1) and antisymmetric (2) behavior with respect to a non-principal rotation axis. Superscripted single (') and double (") primes show symmetry and antisymmetry towards a horizontal mirror plane, perpendicular to the principal rotation axis.

The numbers given in the body of the table indicate whether the irreducible representation is symmetric (1) or antisymmetric (-1). The two columns on the right show which irreducible representations describe translational movement of the three Cartesian coordinates (x , y and z), rotations along these coordinates (R_x , R_y and R_z) and functions of the quadratic terms of the coordinates (x^2 , y^2 , z^2 , xy , xz and yz). Here, the translational

movement and the rotation correspond to infrared activity, whereas the quadratic terms indicate Raman activity [Mau19a]. For the example of hematite this results in the Raman active modes of A_{1g} and E_g (compare Section 4.1).

2.1.3 The Intensity of a Raman Line

As described before, only the linear terms of equation (2.4) are used. This follows Placzek's theory and leads to the intensity of the Stokes-Raman line for a specific transition from one vibrational fundamental to the next higher vibration as follows [Woo67]

$$I = \text{const} \cdot \frac{(\nu_0 - \nu_N)^4}{m_{\text{red}} \nu_N (1 - \exp\{-h\nu_N/k_B T\})} (\alpha'_N)^2 E_0^2. \quad (2.16)$$

Here, h is the Planck constant and k_B the Boltzmann constant. The other parameters are used as previously defined. From equation (2.16) several properties of Raman scattering can be derived:

- The Raman scattering intensity varies with ν^4 , leading to strongly amplified intensities for low excitation wavelengths λ , as the wavelength and the vibrational frequency are inversely proportional $\nu = c/\lambda$.
- The Raman scattering intensity is proportional to the square of the incident amplitude E_0 , so an increase of the incident intensity linearly amplifies the Raman signal.
- As stated before in equation (2.9), Raman scattering can only be observed for non-vanishing polarizability-gradients $\alpha'_N \neq 0$.
- The scattering intensity is proportional to m_{red}^{-1} , which leads to higher Raman intensities for lighter atoms.
- Furthermore, the scattering intensity is proportional to ν_N^{-1} , which assures that scattering frequencies close to the excitation wavelength are of greater intensity than faraway frequencies.
- The last proportionality of $(1 - \exp\{-h\nu_N/k_B T\})^{-1}$ shows that the Raman scattering intensity is proportional to temperature. This is due to the fact that at temperatures different from zero some of the scatterers might be in a higher vibrational level than in the lowest. This temperature dependence leads to an increase of the Raman scattering intensity for low temperatures. For high temperatures, the scattering intensity decreases.

For an in-depth discussion, which additionally takes different excitation and detection angles, or different polarizations into account, see references [Woo67] or [Lon02b].

2.1.4 Line Shapes of Raman Signals

Theoretically, the Raman line is of a Lorentzian-shaped profile [She84; Yog16]. In multiple experiments various influences on the Raman line profile were detected. Some influences are the sample temperature, stress, electron-phonon interaction or quantum confinement

[Yog16]. The influences on the Raman line can even be used as pressure sensor [Bop85]. Besides these and other influences, the experimentally collected Raman signal is always a convolution of the Raman line and the instrumental transfer function [She84; Yak93], leading to a further change of the line profile.

In this section the commonly used line profiles to describe Raman and spectral data are presented. The functions are taken from the `lmfit` package [New20]. The parameters to describe the functions are the area under the curve A , the frequency position of the peak ω , the variance σ and the asymmetry factor q . The parameters are subscripted, accordingly to their respective distribution: Lorentzian (**L**), Doniach-Sunjić (**DS**), Gaussian (**G**), Voigt (**V**) and Breit-Wigner-Fano (**BWF**). Additionally, the Full Width at Half Maximum (**FWHM**) Γ is given as well, which is also subscripted accordingly.

The Lorentzian Distribution (also Cauchy distribution or Breit-Wigner distribution) is the characteristic line shape of many spectroscopic lines [Dem11]. This is a consequence of the Heisenberg uncertainty principle $\tau_t \Delta E \geq \hbar$, which relates the lifetime τ_t of a state to its energy E . Here, only for infinite lifetimes the energy width is defined as single integer (namely zero), whereas for finite lifetimes the energy width of a state is always widened to an energy range, resulting in a Lorentzian shape. The derivation of the line profile is performed in the book on laser spectroscopy by Demtröder [Dem11] and not further discussed here. Exemplary Lorentzian distributions are shown in Figure 2.3. Here, the area under the curve and the peak position are kept at fixed values, while the width of the peak is varied. The peak function is defined as follows

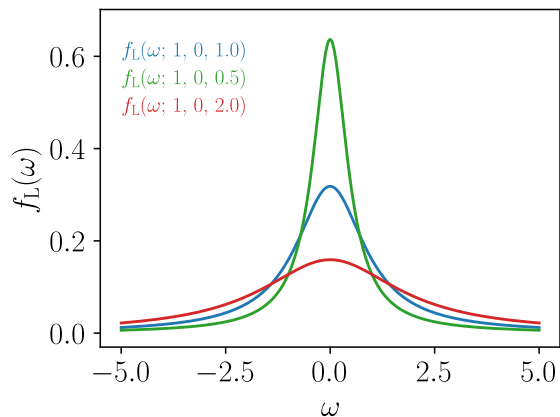


Figure 2.3 Exemplary Lorentzian distributions with varied σ_L and fixed A_L and ω_L .

The Lorentzian broadening of the spectral line is also called natural width of the line. This type of widening is a homogeneous broadening, as all scatterers share the same transition probability to turn from one state to an other state.

$$f_L(\omega; A_L, \omega_L, \sigma_L) = \frac{A_L}{\pi} \frac{\sigma_L}{(\omega - \omega_L)^2 + \sigma_L^2} \quad \text{and} \quad \Gamma_L = 2\sigma_L. \quad (2.17)$$

The Lorentzian broadening of the spectral line is also called natural width of the line. This type of widening is a homogeneous broadening, as all scatterers share the same transition probability to turn from one state to an other state.

Asymmetric Broadening of the line shape is the formation of a low or high energy asymmetry of the respective line. It is observed among others for quantum confined particles [Kum14], nanoparticles [Gou07] and crystalline imperfections, like point defects, dislocations or crystallite boundaries [Fal00]. For quantum confined particles, an exponentially damped integration of multiple Lorentzians can be utilized for peak fitting. A good explanation is presented in reference [Kum14]. For more details on asymmetric vibrational spectra of nanoparticles and disorder induced asymmetry, see the corresponding references.

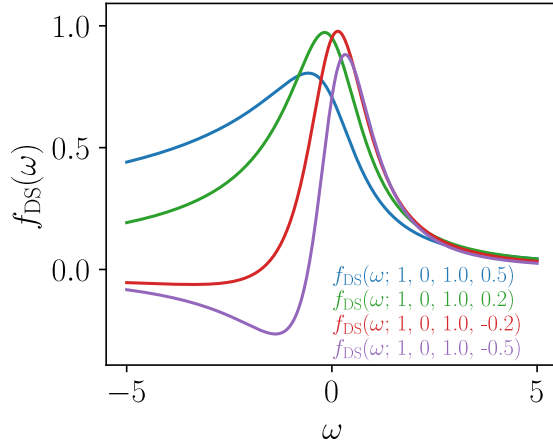


Figure 2.4 Exemplary Doniach-Sunjic distributions with varied q_{DS} and fixed A_{DS} , ω_{DS} and σ_{DS} .

$$f_{\text{DS}}(\omega; A_{\text{DS}}, \omega_{\text{DS}}, \sigma_{\text{DS}}, q_{\text{DS}}) = \frac{A_{\text{DS}} \cos \left[\pi \frac{q_{\text{DS}}}{2} + (1 - q_{\text{DS}}) \arctan \left(\frac{\omega - \omega_{\text{DS}}}{\sigma_{\text{DS}}} \right) \right]}{\sigma_{\text{DS}}^{1-q_{\text{DS}}} \left(1 + \frac{\omega - \omega_{\text{DS}}}{\sigma_{\text{DS}}} \right)^{(1-q_{\text{DS}})/2}}. \quad (2.18)$$

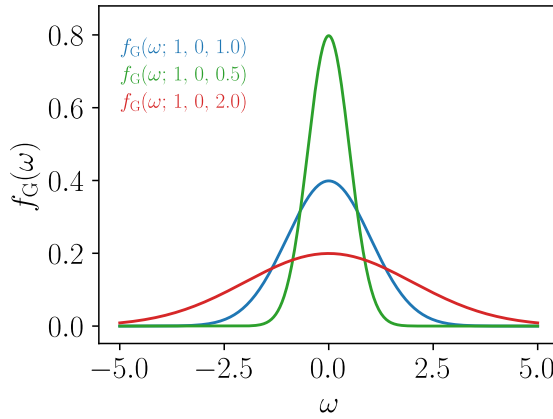


Figure 2.5 Exemplary Gaussian distributions with varied σ_{G} and fixed A_{G} and ω_{G} .

In comparison to the Lorentzian line shape, the normal distribution has an expanded width at the peak and declines faster to zero. Exemplary Gaussian distributions with varying line width are shown in Figure 2.5. The peak function is defined as follows

$$f_{\text{G}}(\omega; A_{\text{G}}, \omega_{\text{G}}, \sigma_{\text{G}}) = \frac{A_{\text{G}}}{\sigma_{\text{G}} \sqrt{2\pi}} e^{-(\omega - \omega_{\text{G}})^2 / (2\sigma_{\text{G}}^2)} \quad \text{and} \quad \Gamma_{\text{G}} = 2\sqrt{2 \ln 2} \sigma_{\text{G}}. \quad (2.19)$$

The Doniach-Sunjic Profile is an asymmetric Lorentzian profile introduced by Doniach and Sunjic [Don70]. The profile is commonly used for peak shapes measured with photoelectron- and X-ray absorption. Here, q_{DS} is the asymmetry factor of the profile. For $q_{\text{DS}} = 0$ the profile is of Lorentzian shape, whereas for $q_{\text{DS}} > 0$ an asymmetric shoulder is introduced at the low-energy flank of the profile. For $q_{\text{DS}} < 0$ the distribution shows a resonance behavior. Exemplary Doniach-Sunjic distributions are shown in Figure 2.4, with fixed area under the curve, peak position and width, while the asymmetry factor is varied. The function is defined as follows

The Gaussian Distribution (also normal distribution) is the typical line shape of liquids, solids and amorphous condensed matter [Dem11]. This results from atoms positioned at slightly different lattice positions, with slightly different local electrical fields. These fields lead to small shifts of each of the Lorentzian profiles. The superposition of these profiles leads to a Gaussian profile, instead of a Lorentzian. This type of broadening is called inhomogeneous broadening. Here, the transition probability of all scatterers of turning from one state to another is not equal. The transition probability differs for disjunct subsets of the scatterers. In

The Voigt Distribution is a convolution of the Lorentzian and the Gaussian distribution. The distribution can be used to determine the Gaussian and Lorentzian share in a collected profile. This allows for an estimation whether the natural (Lorentzian) influences or the inhomogeneous (Gaussian) influences are of dominating impact on the scatterer of interest. In order to reduce computing time the distribution can be approximated by a pseudo-Voigt profile, which is a weighted sum of a Gaussian and a Lorentzian distribution [Ida00]. Exemplary Voigt distributions are shown in Figure 2.6. Here, the area under the curve and the peak position are kept constant, while both line widths are varied. The peak function is defined as follows

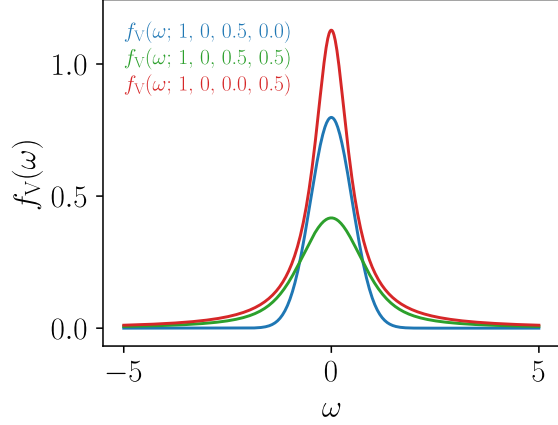


Figure 2.6 Exemplary Voigt distributions with varied σ_G and σ_L , while A_V and ω_V are fixed.

$$f_V(\omega; A_V, \omega_V, \sigma_G, \sigma_L) = \frac{A_V}{\sigma_G \sqrt{2\pi}} \operatorname{Re}(w(z)), \quad (2.20)$$

$$\text{with } w(z) = e^{-z^2} \operatorname{erfc}(-iz) \quad \text{and} \quad z = \frac{\omega - \omega_V + i\sigma_L}{\sigma_G \sqrt{2}}. \quad (2.21)$$

The full width at half maximum of the Voigt profile Γ_V is approximated as suggested by Olivero and Longbothum [Oli77].

$$\Gamma_V = 0.5346\Gamma_L + \sqrt{0.2166\Gamma_L^2 + \Gamma_G^2}. \quad (2.22)$$

The Breit-Wigner-Fano Function is an asymmetric alternative to the Gaussian profile, which is commonly used for amorphous carbon signatures [Fer00]. The line shape arises from an interaction of discrete Raman modes with a continuum of Raman active excitations [Dre82]. Here, q_{BWF} is the asymmetry factor of the profile. For the limit $q_{\text{BWF}}^{-1} \rightarrow 0$ the profile is of Lorentzian shape. For the limit $q_{\text{BWF}} \rightarrow 0$ the profile shows a flipped Lorentzian shape. Exemplary Breit-Wigner-Fano distributions are shown in Figure 2.7. Here, the asymmetry factor is varied, while the other parameters are set to constant values. It is

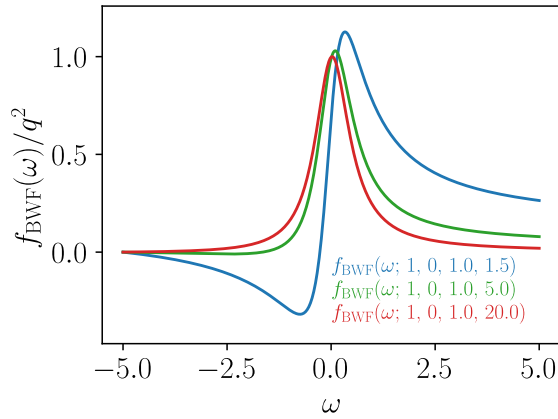


Figure 2.7 Exemplary Breit-Wigner-Fano distributions with varied asymmetry factor q_{BWF} .

$$f_{\text{BWF}}(\omega; A_{\text{BWF}}, \omega_{\text{BWF}}, \sigma_{\text{BWF}}, q_{\text{BWF}}) = A_{\text{BWF}} \frac{(q_{\text{BWF}} \sigma_{\text{BWF}}/2 + \omega - \omega_{\text{BWF}})^2}{(\sigma_{\text{BWF}}/2)^2 + (\omega - \omega_{\text{BWF}})^2}. \quad (2.23)$$

The position of the BWF function ω_{BWF} and its maximum do not correspond. The maximum can be calculated by

$$\omega_{\text{BWF, max}} = \omega_{\text{BWF}} + \frac{\sigma_{\text{BWF}}}{2q_{\text{BWF}}}. \quad (2.24)$$

2.1.5 The Frequency Position of a Raman Line

In this subsection, influences on the Raman line position are discussed. It is shown how the line position can be estimated and how the position might be shifted.

Line Positions of a Raman band are determined by their ground state and their first vibrationally excited state [Van13c]. A single position can be estimated using

$$\nu_N = \frac{1}{2\pi} \sqrt{\frac{\kappa}{m_{\text{red}}}}, \quad (2.25)$$

with κ the binding strength and m_{red} the reduced mass of the Raman transition of interest. The reduced mass is defined as

$$\frac{1}{m_{\text{red}}} = \sum_j \frac{1}{m_j}, \quad (2.26)$$

for each atom participating in the bond of interest. The Raman band position is basically determined by the two factors stated. Once these are known the band position can be calculated. As the binding strength and the reduced mass are relatively stable for a specific bond type, characteristic frequencies for each bond type can be determined [Van13c]. Herewith an indication of the spectral position of a particular Raman band is given. Whether this band is present or not is still dependent on a change in polarizability, as stated with the selection rule of Raman scattering (see equation (2.9)).

Frequency Shifts are movements of the Raman band position. As stated in equation (2.25) the band position depends on the binding strength κ and the reduced mass m_{red} . As the binding strength is strongly dependent on the inter- and intramolecular interactions [Van13c], the Raman band position can be shifted. Hydrogen bonding, substituents in functional groups as well as electron donors and acceptors can influence the position of the Raman signal in the resulting spectrum. As a result, the binding strength is also affected by the state of hybridization of the selected atom. The band position of the C–H stretching vibration for sp^3 , sp^2 and sp hybridized bonds rises with the percentage of s-character of the carbon atom. With a higher percentage of the s-character of the carbon atom, the force constant increases.

2.1.6 Penetration Depth of Light in Matter

An electromagnetic wave, such as light, might penetrate matter up to a certain depth. In order to create a basic understanding of the depth of penetration, this section derives it from a complex plane wave and the complex index of refraction. The current section is based on reference [Fox01].

Table 2.2 The extinction coefficient and the penetration depth for different materials and wavelengths taken from reference [Pol20].

Material	355 nm		532 nm		633 nm		1064 nm		References
	κ	δ_p/nm	κ	δ_p/nm	κ	δ_p/nm	κ	δ_p/nm	
amorphous carbon (a-C)	0.92	31	0.85	50	0.74	68	1.15	74	[Ara77]
a-C, 450 °C annealed	0.40	71	0.17	249	0.11	458			[Smi84]
Fe ₂ O ₃	1.12	25	0.56	76	0.07	720	0.01	8467	[Que85]
Fe ₃ O ₄	0.11	257	0.09	470	0.15	336	0.37	229	[Que85]
MoS ₂ (bulk)	2.70	10	1.20	35	0.91	55	0.04	2117	[Erm20]
Al ₂ O ₃	0.02	1413	0.02	2117	0.02	2519	0.02	4234	[Que85]
α -MoO ₃	0.31	91	0.009	4704	0.006	8395	0.003	28 223	[Laj13]
ethlyen glycol	3.2×10^{-8}	8.8×10^8	4.8×10^{-8}	5.9×10^8	5.7×10^{-8}	5×10^8	2×10^{-6}	1.4×10^7	[San14]

An electromagnetic field propagating in time t and along the z direction is described by

$$E(z, t) = E_0 e^{i(kz - \omega t)}. \quad (2.27)$$

Here, $k = 2\pi/\lambda$ is the wave vector of the propagating field and ω the frequency of the electromagnetic wave. The wave vector k can be written using the index of refraction $n = \lambda_0/\lambda$, with λ_0 being the free-space wavelength. In the following, the generalized case of both parameters, the wave vector k and the index of refraction n , being of complex value is used. This is marked by underlined characters. This leads to

$$\underline{k} = \frac{2\pi \underline{n}}{\lambda_0} \quad \text{with} \quad \underline{n} = n + i\kappa. \quad (2.28)$$

Herein, the complex index of refraction \underline{n} consists of two components, the non-complex coefficient of refraction n and the coefficient of extinction κ . Inserting the complex wave vector from equation (2.28) into the plane wave in equation (2.27) and using the definition of the complex index of refraction yields

$$E(z, t) = E_0 e^{i\left(\frac{2\pi}{\lambda_0}(n+i\kappa)z - \omega t\right)} = E_0 e^{-\frac{2\pi}{\lambda_0}\kappa z} e^{i\left(\frac{2\pi}{\lambda_0}nz - \omega t\right)} \quad (2.29)$$

$$= E_0 e^{-\frac{2\pi}{\lambda_0}\kappa z} e^{i(kz - \omega t)}. \quad (2.30)$$

Here, an exponential decay, proportional to κ , is superimposed on the previous electromagnetic field, leading to κ being an indicator for the attenuation of an electromagnetic wave propagating through a material. Furthermore, as the intensity of an electromagnetic wave is proportional to the square of the electromagnetic field, it is proportional to $\exp\left(-\frac{4\pi}{\lambda_0}\kappa z\right)$, which is used to define the attenuation coefficient $\alpha_{\text{at}} = 4\pi\kappa/\lambda_0$. Herewith, the depth of penetration can be determined. The depth of penetration δ_p is defined as depth, where the intensity is reduced by $1/e$. Solving the proportionality for this depth gives (see also reference [Hec17])

$$\delta_p = 1/\alpha_{\text{at}} = \lambda_0/4\pi\kappa. \quad (2.31)$$

This shows that the penetration depth is proportional to λ_0 , leading to low depths of penetration (more surface sensitive) for short wavelengths and to high depths of penetration

for longer wavelengths (more bulk sensitive). Furthermore, the penetration depth is anti-proportional to κ , leading to small (high) depths of penetration for high (small) values of the extinction coefficient. In general, κ is wavelength dependent.

Typical extinction coefficients of materials used in this thesis range from $\kappa_{\text{Fe}_2\text{O}_3}(633 \text{ nm}) = 0.07$ to $\kappa_{\text{MoS}_2}(355 \text{ nm}) = 2.7$ and are listed in Table 2.2. Using equation (2.31) typical penetration depths are in the range from $\delta_{\text{p, MoS}_2}(355 \text{ nm}) = 10 \text{ nm}$ to $\delta_{\text{p, Fe}_2\text{O}_3}(633 \text{ nm}) = 720 \text{ nm}$. The wavelength-dependent extinction coefficients are taken from the **refractive index database** [Pol20].

2.1.7 Resonant Raman Scattering

In Section 2.1 the classical polarizability tensor is used as introduction to Raman scattering. In order to get more fundamental molecular properties and explain phenomena like resonant Raman scattering a quantum mechanical transition polarizability tensor is needed, which is discussed in this section, based on Chapter 4 in the book by Long [Lon02a]. The general transition polarizability tensor α_{fi} describes the transition from an initial state i to a final state⁹ f . The components of the tensor are [Lon02a]

$$(\alpha_{NM})_{fi} = \frac{1}{\hbar} \sum_{r \neq i, f} \left\{ \frac{\langle f | p_N | r \rangle \langle r | p_M | i \rangle}{\omega_{ri} - \omega_1 - i\Gamma_r} + \frac{\langle f | p_M | r \rangle \langle r | p_N | i \rangle}{\omega_{rf} + \omega_1 + i\Gamma_r} \right\}, \quad (2.32)$$

where a double sub-scripted frequency ω means a frequency difference, as for example $\omega_{ri} = \omega_r - \omega_i$. Furthermore, p_N and p_M are the N and M components of the electric dipole moment operator and the frequency of the incident electromagnetic wave is resembled by ω_1 , while $2\Gamma_r$ is the full width of state r , with lifetime $\tau_r = 1/2\Gamma_r$. Equation (2.32) does not show any terms of Γ_i and Γ_f for the initial and final state, as the lifetimes of these states are assumed to be infinite, leading to $\Gamma_i = \Gamma_f = 0$. It is important to note, that equation (2.32) is again only an approximation as it is derived with first-order perturbation theory. Furthermore, the summation over the states r is simplified, with excluding the initial and final states i and if , which are mostly zero. For more details see in Long's book [Lon02a].

In the following the frequency denominator $\omega_{ri} - \omega_1 - i\Gamma_r$ from the first term of equation (2.32) is discussed. In order to derive this equation, no restriction was needed for the incident frequency ω_1 or its relation to the absorption frequency ω_{ri} . Additionally, no restriction was defined for state $|r\rangle$, which allows it to be below the initial state, between the initial and the final state or above the final state. Usually, $|r\rangle$ is above both states, which is also assumed in the following discussion. There are two limiting cases for the denominator:

- In the first case, the excitation frequency ω_1 is much smaller than the absorption frequency ω_{ri} , leading to $\omega_1 \ll \omega_{ri}$ for all states r . In this case, the frequency difference $\omega_{ri} - \omega_1$ is approximately ω_{ri} for all states r . Here, the $i\Gamma_r$ term can be neglected, as these terms are small compared to ω_{ri} [Lon02a]. Scattering processes with these excitation frequencies are virtual processes. Here, the virtual state r is not a solution to the Schrödinger equation and does therefore not correspond to a well-defined energy value.

⁹Each state i is described by a time-independent unperturbed wave function ψ_i . In the following the simplified notation of $|i\rangle$ instead of $|\psi_i\rangle$ is used for all states.

- In the second case, the excitation frequency ω_1 is close to one or more particular absorption frequencies ω_{ri} , leading to $\omega_1 \approx \omega_{ri}$, which leads to a denominator of $-i\Gamma_r$ for the particular state r . Terms with these denominators dominate the complete sum over r [Lon02a]. This process is resonant Raman scattering. Here, the Raman scattering intensity for this particular state is increased by a factor of up to 10^6 [Smi19a].

To sum up, resonant Raman scattering highly increases the scattering intensity and is more selective than normal Raman scattering, as the process is sensitive to only one particular state. To obtain resonant Raman scattering an excitation frequency close to or identical to an electronic transition has to be chosen, which can be accomplished with a tunable laser. Furthermore, resonant Raman scattering reveals information on the electronic structure of the sample studied. For in-depth theoretical details Long’s book is recommended [Lon02a], while for more practical details the book by Smith can be a valuable reference [Smi19a].

2.2 Tribology

“Tribology is the science and technology of interacting surfaces in relative motion and of related subjects and practices” [Czi15b]. Tribology deals with the transmission of motion, force, energy and information. Furthermore, mass transfer, as well as material forming and processing are typical fields of tribology. The interdisciplinary science analyzes how friction and wear influence moving interacting surfaces and what the underlying mechanisms are [Czi00].

The effects of tribological processes are observable along various scales. At the macro scale the formation of tribofilms, wear debris and scratches can be observed. Here, the properties of the bulk and coating material govern the tribological behavior. Increasing the level of detail to the microscale, reveals that the contact area of two bodies is significantly smaller than the dimensions of their technical surfaces. Here, microstructural changes in the material affect the tribological process. At even smaller scales, chemical and molecular interactions, as well as atomic interactions govern the tribological behavior. The goal of tribology is to understand the underlying mechanisms and their interactions at all scales in order to reduce the effects of friction and wear.

Friction counteracts the relative motion of interacting bodies. It is characterized by the coefficient of friction

$$\mu = \frac{F_{\text{fric}}}{F_{\text{norm}}}, \quad (2.33)$$

with the friction force F_{fric} and the normal force F_{norm} . The frictional work performed in the system is mostly converted into heat (see also 2.2.3).

In a lubricated tribological system three different states of lubrication are possible, depending on the ratio λ_{fric} of the lubricant film thickness to the average surface roughness of the interacting bodies. The different regimes of the so-called Stribeck curve are:

- the low-ratio regime ($\lambda_{\text{fric}} < 1$), which is called boundary lubrication. Here, the solid surfaces are in direct contact and high values of friction are detected.

- the mid-ratio regime ($1 < \lambda_{\text{fric}} < 3$), which is called mixed lubrication. Here, the coefficient of friction is reduced by the fluid friction of the lubricant and only a few asperities are in direct contact with the opposing surface.
- the high-ratio regime ($3 < \lambda_{\text{fric}}$), which is called hydrodynamic lubrication. Here, the two surfaces are completely separated by a lubricant film and the coefficient of friction is solely ruled by fluid friction.

It is important to note that friction is no material property, but a system property. The coefficient of friction has to be determined experimentally for each tribological system.

Wear is the proceeding loss of material of the surface of a body. It results from relative movement of contacted bodies (tribological stress). Like friction, it is a parameter of the tribological system, rather than a material property and has to be determined experimentally. Wear is mostly influenced by the stress collective and the structure of the tribological system.

The stress collective is formed by the form of movement (for example gliding or rolling movement), the temporal form of movement (continuous, oscillating or intermittent) and the stress variables of the system (load, velocity, temperature and duration of movement).

The structure of the tribological system is given by the elements of the system (the involved bodies, an intermediate material and the ambient medium). Furthermore, the bodies' form and material parameters attribute to the structure of the system, as well as the interactions of the system elements (contact, friction, wear).

Based on these influences, wear can be classified into different types. Among these are sliding wear, rolling wear, impact wear, vibrational wear, erosion and cavitation.

Wear Mechanisms are the mechanisms activated by tribological stress. Next to contact deformation, the main mechanisms are

- Surface disruption, which leads via fatigue and crack formation to material separation (e.g. pitting, delamination, white-etching cracks).
- Abrasion, which is material removal due to scratching (e.g. microploughing).
- Tribochemical reaction, which is a chemical reaction of the interacting bodies and/or ambient medium (e.g. chemisorption, physisorption).
- Adhesion, which is the formation of interfacial adhesive bonds (e.g. fretting, cold welding).

The wear mechanisms might appear on their own or in an intermixed state, which makes the determination of the exact mechanism a non-trivial problem.

2.2.1 Materials and their Mechanical Properties

In order to understand tribology and the mechanics of contacts, it is important to understand which properties are inherent to materials. Therefore, the stress-strain response of a material is explained, which sets the limitations for the follow-up section on linear elastic theory. With the basis of this theory, a theory of contacting bodies is developed in the subsequent section.

The Stress-Strain Diagram depicts the deformation per unit length (normal strain ε) of a body under application of a load per unit surface (normal stress σ) [Bee20]. Depending on the tensile test and on the material the stress-strain diagram may differ. Furthermore, the diagram is influenced by temperature and the speed of loading. Nonetheless, from the stress-strain diagrams two main types of materials can be categorized: ductile and brittle materials.

Ductile materials, such as steel and many alloys used in engineering, are yieldable at room temperature. As an example, a typical stress-strain diagram of a low carbon steel is shown in Figure 2.8. Here, with increasing load ($\propto \sigma$) the length ($\propto \varepsilon$) of a specimen of the material increases linearly with a slow rate until a critical load (yield strength σ_Y of the material) is reached. From this point on, the specimen performs large deformations with rather small additional loads, due to slippage along oblique surfaces. Beyond the maximal value of the applied load (ultimate strength σ_U of the material), the diameter of the specimen decreases (necking phase in Figure 2.8), due to local instabilities. In the necking phase, lower loads are sufficient for an elongation of the specimen. By increasing the strain even further, the material will finally rupture (breaking strength σ_B of the material). For ductile materials, such as low-carbon steel, the ratio of σ_B to σ_Y is in the order of 200.

Contrasting to ductile materials, brittle materials, like cast iron or glass, rupture appears without any drastic changes in the rate of elongation. For such materials, the ultimate strength and the breaking strength are indifferent. Additionally, the strain at breaking is considerably smaller for brittle materials than the strain at breaking for ductile materials. Furthermore, no necking phase is observable in the stress-strain diagram of a brittle material.

Linear Elasticity assumes that solid bodies are linearly deformable by displacements and distortions, which is only true for a selected region of the stress-strain curve (see Figure 2.8). The deformations in this region are related to internal forces inside the body (stresses) and are characterized by local strains [Sla02]. For infinitesimal deformations u along the directions of \mathbb{R}^3 the deformation tensor is [Wit00]

$$\varepsilon = \begin{pmatrix} \varepsilon_x & \gamma_{xy}/2 & \gamma_{xz}/2 \\ \gamma_{yx}/2 & \varepsilon_y & \gamma_{yz}/2 \\ \gamma_{zx}/2 & \gamma_{zy}/2 & \varepsilon_z \end{pmatrix}, \quad (2.34)$$

$$\text{with } \varepsilon_j = \frac{\partial u_j}{\partial j} \quad \text{and} \quad \gamma_{jk} = \gamma_{kj} = \frac{\partial u_j}{\partial k} + \frac{\partial u_k}{\partial j} \quad (j \neq k = x, y, z).$$

Herein, ε_j are the longitudinal strains along the directions of \mathbb{R}^3 and γ_{jk} the shear strains between the j - and k -directions of the \mathbb{R}^3 . For isotropic materials, both strains can be

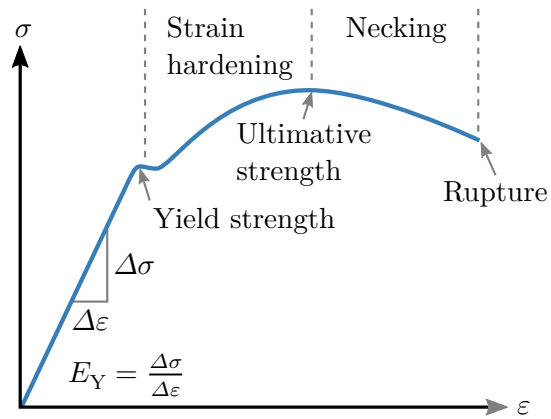


Figure 2.8 Typical stress-strain diagram of a low carbon steel [Bee20]. Adapted with permission from reference [Nic20].

coupled linearly to stresses inside the body¹⁰, namely the normal stresses σ_j and the shear stresses τ_{jk} [Wit00].

$$\sigma_j = \frac{E_Y}{1 + \nu_P} \left[\varepsilon_j + \frac{\nu_P}{1 - 2\nu_P} (\varepsilon_x + \varepsilon_y + \varepsilon_z) \right] \quad (2.35)$$

$$\tau_{jk} = G_S \gamma_{jk} \quad (2.36)$$

The relations (2.35) and (2.36) are called Hooke's law. The coefficient E_Y (G_S) is called Young's modulus (shear modulus) and is a material property. Both moduli are related by the ratio of lateral strain to axial strain (Poisson's ratio ν_P), as an axial extension along direction j is accompanied by a contraction in the other k directions [Sla02]

$$E_Y = 2G_S (1 + \nu_P) \quad \text{with} \quad \nu_P = -\frac{\varepsilon_k}{\varepsilon_j}. \quad (2.37)$$

Contact Problems for different geometries can be solved using the superposition of multiple stress distributions, each being constructed by a normal force acting on a half-space [Wit00]. Each of the stress distributions is rotationally symmetric. The problem for a single distribution was first solved by Boussinesq in 1885 [Hah85].

The two contacting geometries have to fulfill several constraints: They have to be homogeneous, with a linear strain-stress relation and only normal stresses are applicable. Furthermore, it is requested that the contacting area is small in comparison to the body of the geometries, to assure that each contact can be treated as a Boussinesq-problem. For these constraints, it could be shown that the effective elastic modulus E_{eff} of two contacting bodies with elastic moduli E_j and Poisson's ratios ν_j ($j = 1, 2$) is [Pop19; Wit00]¹¹

$$\frac{1}{E_{\text{eff}}} = \frac{1 - \nu_1^2}{E_1} + \frac{1 - \nu_2^2}{E_2}. \quad (2.38)$$

In the following, the dependencies for two contacting balls with radii r_j ($j = 1, 2$) are presented¹². The two balls are exposed to a pressure F_{cont} , which leads to a reduction in the distance d of their centers by [Wit00]

$$\Delta d = \left(\frac{9 F_{\text{cont}}^2}{4 r E^{*2}} \right)^{1/3} \quad \text{with} \quad \frac{1}{r} = \frac{1}{r_1} + \frac{1}{r_2} \quad \text{and} \quad E^* = 2E_{\text{eff}}. \quad (2.39)$$

Here, the area of contact is of circular shape with a radius

$$r_{\text{cont}} = \left(\frac{3 F_{\text{cont}} r}{2 E^*} \right)^{1/3}. \quad (2.40)$$

The maximal stress at the contact, which is often called contact pressure, is

$$\sigma_{\text{max}} = \frac{3 F_{\text{cont}}}{2\pi r_{\text{cont}}^2}. \quad (2.41)$$

¹⁰Here, a constant temperature is assumed. See reference [Wit00] for temperature-dependent equations.

¹¹Note that reference [Wit00] has a factor of two bigger effective elastic modulus than reference [Pop19].

¹²For other contact shapes, see the chapter on technical mechanics by Wittenburg [Wit00] and the book on contact mechanics by Popov [Pop19].

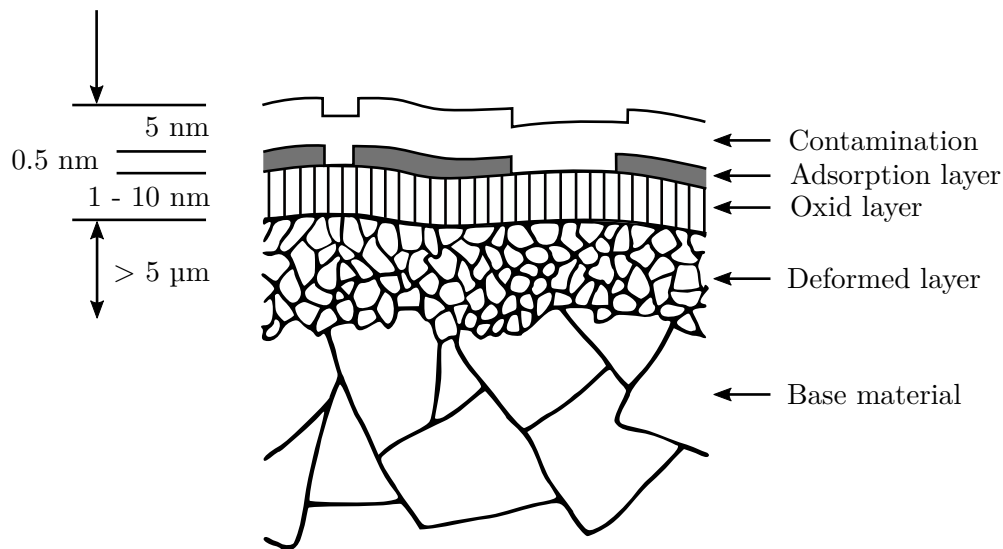


Figure 2.9 Scheme of a technical metallic surface. Translated from reference [Czi15e].

For a contact of a ball with a flat surface, the radius reduces to $r = r_1$, with $r_2 = \infty$. The maximal tensile stress (indicator for the stability of brittle materials) occurs at the circumference of the contact area, while the maximal compressive stress (indicator for the stability of ductile materials) occurs approximately in depth $r_{\text{cont}}/2$ below the center of the contact area. The presented equations are often referred to as the Hertzian theory of an elastic contact. Further details on the theory are presented in the previously mentioned publications and in the book by Johnson [Joh85].

2.2.2 Materials and their Surface Properties

As stated before, wear is influenced by the tribological stress of the bodies in contact. In order to create an understanding of the underlying mechanisms, the surface properties of the moving bodies, their composition, as well as their physical and chemical properties need to be taken into account.

Technical surfaces are the geometric limit of a body. Their properties strongly vary from the material specifications given in data sheets [Czi15e]. For metallic materials, the simplified layer structure of technical surfaces is shown in Figure 2.9. Here, at the surface of the crystalline material, several alterations are observable. At depths of about $5\ \mu\text{m}$ influences of the manufacturing process might change the homogeneity or induce some residual stress. At depths to about 10 nm, effects like oxidation, chemi- and physisorption and contamination change the properties of the base material. These different regions of a material and its surface can be divided into three regions. Firstly, the base material, building the body of the component. Secondly, an inner boundary, which is dependent on the manufacturing process. Thirdly, an outer boundary, which is influenced by the environment and often has a different chemical composition than the base material. For these compositional changes, it is important to determine the chemical composition of the surface in order to gain insight into the tribological mechanisms.

Next to the chemical properties of the surface, the geometry is also of importance. Here,

surface imperfections are detectable as deviations from perfect flatness. These deviations are known as surface roughness, which almost all known surfaces show, regardless of their scale or origin [Sta14b]. The surface roughness can be described with a height probability density function. Assuming a Gaussian height distribution, integration of the density function gives the cumulative probability function of the surface roughness¹³. Furthermore, the surface roughness strongly depends on the process of production. In order to describe the surface roughness, many different parameters are used. Here, only the center line average roughness Ra of the z -direction perpendicular to the sample surface over the sampling length L along the x -direction is used.

$$\text{Ra} = \frac{1}{L} \int_0^L |z(x)| dx \quad (2.42)$$

In general, peaks of the surface asperities are leveled during running-in of newly machined parts, resulting in surface profiles with plateaus and sharp grooves. Here, the height distribution needs to be described by two Gaussian profiles.

2.2.3 Flash Temperatures in Mechanical Contacts

In a tribological contact, mechanical energy is dissipated due to friction, which changes the temperature distribution of the bodies in contact [Czi15e] (see Section 5 in the respective reference). Macroscopically, the energy dissipation is observed by an increase in the mean temperature of the two bodies. Assuming that the complete energy is transformed to heat, a heat density may be defined. Microscopically, the temperature distribution strongly varies with time and space due to the statistically-distributed micro-contacts of the two bodies. These fast variations are called flash temperatures. They are the scope of this section. As an example, infrared measurements in a steel-sapphire system showed that these flash temperatures are spatially in the 10 μm regime and temporally in the 100 μs regime [Czi15e]. The observed temperatures exceed 2000 $^\circ\text{C}$.

To estimate the flash temperature, Blok (1937), Jaeger (1944) and Archard (1958) developed sets of equations to calculate the flash temperatures in various experimental conditions. Blok and Jaeger established equations for flash temperatures in linear and square contacts, whereas Archard developed the theory for circular contacts. The maximum temperature of the contact T_c is the sum of the bulk temperature of the contacting solids T_b and the maximum flash temperature $T_{f,\text{max}}$ [Sta14a].

$$T_c = T_b + T_{f,\text{max}} \quad (2.43)$$

Theoretical estimation of flash temperatures is extremely demanding, due to chemical interface layers, local fluctuations of the friction forces and a lack of knowledge about the exact temperature dependencies of material properties. Therefore, multiple simplifications are made:

- The properties of the contacting bodies are independent of temperature.
- All micro-contacts are accumulated to one contact area, where the frictional energy is dissipated. This area is considered to be the source of heat.

¹³Using statistical methods for surface analysis was introduced by Abbott, which is the reason that the cumulative probability function of surface roughness is sometimes called Abbott-curve [Sta14b; Bod13].

- The coefficient of friction in the contact is constant and known.
- The heat is uniformly distributed in the contact.
- All heat is dissipated among both bodies in contact.
- The temperature in the contact area is the same for both bodies.
- The calculated flash temperature is an estimation of a temperature rise above the mean temperature of the bodies.

These simplifications neglect the presence of a lubricant, which will take some of the heat generated in the contact. Furthermore, the coefficient of friction depends on the generated heat, lubrication and many more parameters, leading to a broad variation, even when they are measured experimentally. Therefore, a flash temperature range needs to be calculated, using the minimum and the maximum of the coefficient of friction. With all these assumptions, the estimation of flash temperatures is not very precise, but rather an indicator of temperatures that might be expected in the contact of interest (see Section 6 in reference [Sta14a] and also Section 5 in reference [Czi15e]).

To estimate the flash temperatures, a measure for heat penetration into the bulk material is needed. As, for the slow-speed regime, there is sufficient time to dissipate the generated heat into the material, while, for the high-speed regime, more heat is generated than dissipated, leading to different equations for the different speed regimes. A measure to differentiate between these speed regimes is the Peclet number¹⁴ L_{Pec}

$$L_{\text{Pec}} = \frac{v r_{\text{cont}}}{2\chi} \quad \text{with} \quad \chi = \frac{k_{\text{h}}}{\rho c_{\text{spec}}}, \quad (2.44)$$

with the velocity of the moving body v , the contact radius r_{cont} (see equation (2.40)) and the thermal diffusivity of the material χ , being constructed from its thermal conductivity k_{h} , its density ρ and its specific heat capacity c_{spec} .

The different speed and flash temperature regimes are defined by the following Peclet number ranges [Sta14a]:

- $L_{\text{Pec}} < 0.1$. The surfaces move slowly with respect to each other, providing sufficient time for heat dissipation. Here, a model with a stationary heat source can be used.
- $0.1 < L_{\text{Pec}} < 5$. The surfaces move faster with respect to each other, providing less time for heat dissipation. This leads to a model assuming a slowly moving heat source.
- $5 < L_{\text{Pec}}$. The surfaces move fast with respect to each other, providing insufficient time for heat dissipation. Here, a fast moving heat source is used for modeling. Due to the fast movement, the heat penetrates the stationary body only to small depths compared to the contact dimensions.

¹⁴Named after the French physicist Jean Claude Eugène Péclet (*1793; †1857).

Circular Contacts – The Theory of Archard In this model a base body (ball) is contacted to an antibody (disc) by a circular contact area, which is constructed from all micro-contacts. This contact moves with the antibody with velocity v . Due to heat dissipation from friction, this leads to a stationary source of heat for the base body, while the antibody is heated by a translational source of heat [Czi15e]. To calculate the maximum flash temperature $T_{f,\max}$ the following two parameters are defined for the two plastically deformed (metal) bodies:

$$N' = \pi \cdot \frac{\mu \sigma_Y}{\rho c_{\text{spec}}}, \quad (2.45)$$

$$L' = \frac{v \rho c_{\text{spec}}}{2 k_h} \left(\frac{F_N}{\pi \sigma_Y} \right)^{1/2}. \quad (2.46)$$

Here, the variables are the coefficient of friction μ , the yield strength σ_Y of the material, with the unit Pa, its density ρ in kg/m^3 , its specific heat capacity c_{spec} in $\text{J}/(\text{kg K})$ and its thermal conductivity k_h in $\text{W}/(\text{m K})$.

For the different Peclet ranges, Archard derived the following equations [Sta14a]:

- $L_{\text{Pec}} < 0.1$ for low velocities. Here, the flash temperature can be estimated using

$$T_{f,\max} = 0.25 N' \cdot L'. \quad (2.47)$$

The heat is distributed evenly among the two bodies.

- $0.1 < L_{\text{Pec}} < 5$ for intermediate velocities. The flash temperature is estimated using

$$T_{f,\max} = 0.25 \beta_{\text{Ar}} N' \cdot L' \quad \text{with} \quad \beta_{\text{Ar}} = \begin{cases} 0.95, & \text{for } L' = 0.1, \\ 0.5, & \text{for } L' = 5. \end{cases} \quad (2.48)$$

Assuming a linear behavior it follows

$$\beta_{\text{Ar}} = -\frac{9}{98} L' + \frac{94}{98}. \quad (2.49)$$

Here, the heat is distributed unevenly, less than half is taken by the base body.

- $5 < L'$ for high velocities. The flash temperature can be estimated using

$$T_{f,\max} = 0.435 \gamma_{\text{Ar}} N' \cdot L'^{1/2} \quad \text{with} \quad \gamma_{\text{Ar}} = \begin{cases} 0.72, & \text{for } L' = 5, \\ 0.92, & \text{for } L' = 100, \\ 1, & \text{for } L' > 100. \end{cases} \quad (2.50)$$

Assuming a linear behavior it follows

$$\gamma_{\text{Ar}} = \frac{1}{475} L' + \frac{337}{475}, \quad (2.51)$$

for γ_{Ar} in the range of $L' = 5$ to 100. Here, the heat is mainly gathered by the antibody.

For an in-depth discussion see the original publication by Archard [Arc59]. For equations of average flash temperatures and different geometries, see also reference [Sta14a].

Exemplary, the flash temperatures in a ball-on-disc tribometer for a steel-steel contact are estimated using the presented theory. The material parameters used are listed in Table 2.3. A normal force of $F_N = 10$ N results in a contact radius of $r_{\text{cont}} = 58$ μm for a flat surface and a ball with radius $r_{\text{ball}} = 3$ mm, leading to a Peclet number of $L_{\text{Pec}} = 1.012$. This shows that equation (2.48) has to be used for the estimation of the flash temperatures. With a velocity of $v = 0.4$ m/s, this leads to a flash temperature of $T_{\text{f,max}} = 11$ $^{\circ}\text{C}$ ($T_{\text{f,max}} = 240$ $^{\circ}\text{C}$) for a coefficient of friction of $\mu = 0.1$ ($\mu = 0.9$) and a low (high) yield strength. With a bulk temperature of the contacting solids of $T_b = 120$ $^{\circ}\text{C}$, these flash temperatures lead to an estimated temperature range of $T_c = 131$ $^{\circ}\text{C}$ to 360 $^{\circ}\text{C}$ in the contact¹⁵.

In order to generate more accurate estimations, it is necessary to use an iterative procedure to calculate the flash temperature, starting with material parameters at room temperature and standard conditions for the first estimation. In subsequent estimations material parameters of the previously determined flash temperature should be used for a more accurate estimation of the real flash temperature. This iteration can be repeated until the needed accuracy is met.

In addition, Ashby et al. developed a computational model to estimate bulk and flash temperatures for common sliding geometries (flat-on-flat, pin-on-disc, ball-on-flat, four-balls). With this model temperature maps can be generated to show how the bulk and flash temperatures vary in dependence of the sliding velocity and the contact pressure. The model can be applied to any couple of sliding materials. Ashby et al. showed the validity of their model by comparing the predictions made with experimental data [Ash90].

2.3 Fundamental Properties of Selected Materials

In this section some of the fundamental properties of the materials investigated throughout this thesis are presented. The section is started with iron oxides and other iron corrosion products, as the investigated technical surfaces are formed by different steels. Subsequent, the properties of different coatings are presented. The coatings are applied to the top of the technical surfaces to adapt their surface properties to the tribological process¹⁶. This tailoring of the surface properties enables to meet the requirements of the operating conditions, like efficiency, reliability and life time of the system [Hol00; Kha17]. The coatings used are

Table 2.3 Material parameters of 100Cr6 used to estimate a flash temperature range [Ova21].

parameter	value	unit
E	210	GPa
ν	0.3	
k_h	42	W/(m K)
c_{spec}	470	J/(kg K)
ρ	7800	kg/m ³
$\sigma_{\text{Y,low}}$	410	MPa
$\sigma_{\text{Y,high}}$	2000	MPa

¹⁵A `python` script performing the presented calculations is attached to this thesis.

¹⁶Detailed descriptions of surface coatings and their tribological behavior are given in the book of Holmberg [Hol09a].

- amorphous carbon (a-C) coatings, which are used for their wear resistance and their lubricating properties [Hol00],
- molybdenum disulfide (MoS₂) coatings, which are mainly used for their lubricating properties [Hol00] and
- tungsten carbide (WC) coatings, which are used for their wear resistance [Woo18].

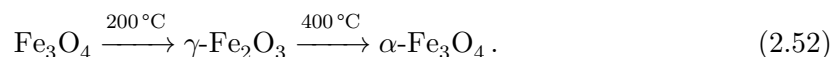
Here, properties like structure, point group, important Raman modes, as well as some mechanical properties are presented. Furthermore, each subsection contains literature for further reading.

2.3.1 Iron Oxides

This section gives a brief introduction to some iron oxides and oxyhydroxides. Resources for further reading are the paper by Faria, the overview chapter by Colomban and the vast collection by Cornell [Far97; Col11; Cor03b]. Iron oxides are widely used as pigments for paints, as well as catalysts in industrial synthesis processes and as raw materials for the iron and steel industry. These and other applications are presented in the overview chapter of iron oxide applications by Cornell [Cor03a]. In general, the metal corrosion products (oxides and oxyhydroxides¹⁷) strongly absorb infrared radiation, but are poor scatterers and high laser powers might lead to sample degradation [Far97].

Hematite (Fe₂O₃) is of corundum structure and belongs to the D_{3d} point group [Far97]. An exemplary Raman spectrum is shown in Figure 2.10. Observed are two A_{1g} modes (220 cm⁻¹ and 495 cm⁻¹) and five E_g modes (250 cm⁻¹, two modes around 290 cm⁻¹ only resolvable at low temperatures, 400 cm⁻¹ and 605 cm⁻¹) [Far97] as well as a strong mode at 1310 cm⁻¹, which can be attributed to either two-magnon scattering [Far97] or two-phonon scattering [Mas90]. The Raman spectrum can be altered by increasing in laser excitation power, which causes a broadening of the Raman lines and slightly shifts them to lower wavenumbers. This process is fully reversible [Far97]. Hematite has a hardness of 8.2 GPa [Chi11], which is harder than air cooled steel (around 300 HV, e.g. 3 GPa) and a little softer than martensitic steel (around 940 HV, e.g. 9 GPa) [Ova21]. Naturally oxidized steel shows a strongly softened hematite with a reduced hardness of 2.7 GPa [Chi11].

Magnetite (Fe₃O₄) is of spinel structure and belongs to the O_h point group [Far97]. An exemplary Raman spectrum is shown in Figure 2.10. There are two T_{2g} modes (190 cm⁻¹ and 540 cm⁻¹), one E_g mode (310 cm⁻¹) and one A_{1g} mode (670 cm⁻¹) [She03a]. Magnetite is very sensitive to laser power: It can easily be transformed into hematite. The transformation is irreversible [Far97]. This transformation process (martitization) is a common natural phenomenon. The martitization is temperature dependent with the following phases [Far97]



¹⁷Other corrosion processes, like carbonatation, phosphatation and sulfatation are not considered here. Some of these corrosion products are presented in the special focus chapter by Colomban [Col11].

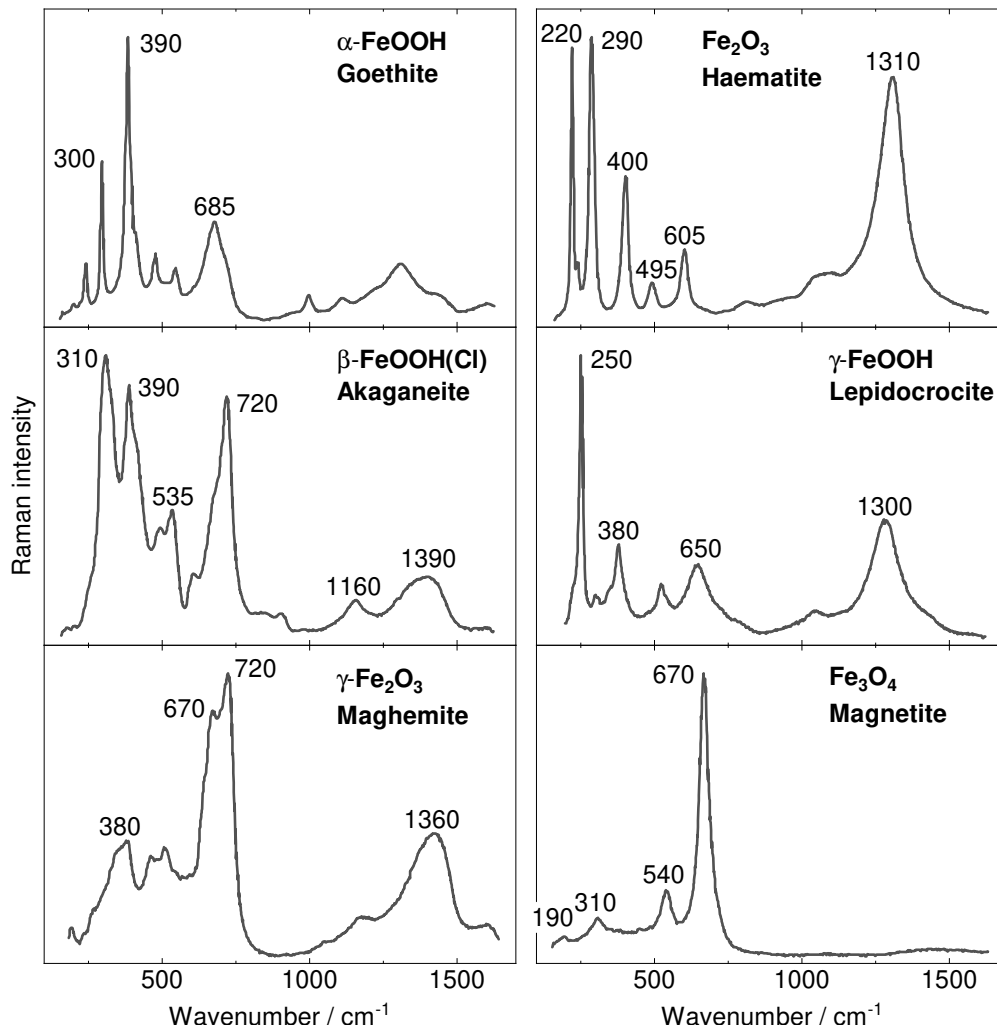


Figure 2.10 Raman spectra of different iron oxides. Image modified from reference [Col11].

Firstly, at temperatures around 200 °C, Magnetite is transformed to maghemite ($\gamma\text{-Fe}_2\text{O}_3$). This is followed by a further phase transformation of maghemite to hematite at around 400 °C. Comparable temperatures are reached by flash temperatures in metal-metal contacts, as stated before (compare Section 2.2.3). Magnetite has a hardness of 6.3 GPa [Chi11], which is a bit softer than hematite. For naturally oxidized magnetite, the hardness is slightly reduced to 5.3 GPa [Chi11].

Other Iron Oxides and Oxyhydroxides and their Raman spectra are shown in Figure 2.10. Maghemite ($\gamma\text{-Fe}_2\text{O}_3$) shows typical Raman features around 380 cm^{-1} , 670 cm^{-1} , 720 cm^{-1} and 1360 cm^{-1} . It is produced in the martitization process of hematite to magnetite. The most common oxyhydroxides are goethite and its polymorphisms (lepidocrocite and akaganeite). They form in the presence of water and oxygen from air [God98]. Their growth is accelerated by halide ions (e.g. Cl^-) and will completely convert a piece of metal to

rust. In deaerated water the conversion does not take place, as shown by intact ancient anchors found on the bottom of the ocean. Goethite (α -FeOOH) shows the most distinctive Raman signatures at 300 cm^{-1} , 390 cm^{-1} and 685 cm^{-1} . The Raman features of lepidocrocite (γ -FeOOH) are most significant at 250 cm^{-1} , 380 cm^{-1} , 650 cm^{-1} and 1300 cm^{-1} and the most characteristic Raman signatures of akaganeite (β -FeOOH(Cl)) are the modes at 310 cm^{-1} , 390 cm^{-1} , 720 cm^{-1} and 1390 cm^{-1} .

2.3.2 Carbon and Related Structures

This section gives an introduction to the wide field of carbon and related amorphous structures. They are often used as protective coatings in various fields and their ease of production has contributed to their spread of usage [Rob02]. Here, the most thesis-relevant information are presented. For an in-depth discussion of the field, the comprehensive review of J. Robertson is recommended [Rob02].

The great variety of the different carbon structures is due to the ability of carbon to exist in the sp^1 , sp^2 or sp^3 hybridization states¹⁸. In sp^3 hybridization (diamond) the four valence electrons are tetrahedrally coordinated, forming strong σ bonds¹⁹. In sp^2 hybridization (graphite) only three electrons are trigonally coordinated forming σ bonds, with the remaining electron forming a π bond perpendicular to the hybrid orbital plane. In sp^1 hybridization two valence electrons form a linear hybrid orbital, with the remaining electrons in p-orbitals, forming π bonds.

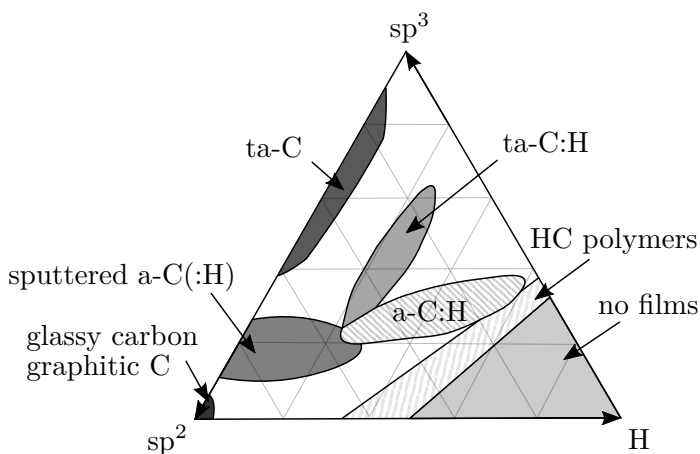


Figure 2.11 Ternary phase diagram of amorphous carbon. Image reproduced from reference [Rob02].

The properties of the different carbon species are derived from the strong directional σ bonds and the relatively weak π bonds [Rob02]. These σ bonds make diamond the material with the largest bulk modulus of any solid, the material with the highest atom density and the largest room temperature thermal conductivity, as well as the material with the smallest coefficient of thermal expansion. The same σ bonds take care that graphite has strong intra-layer bonding, but due to the perpendicular π bonds the layers can

¹⁸Orbital hybridization is the mixing of atomic orbitals into new hybrid orbitals, with new energies and shapes other than the original atomic orbitals. There are many different hybrid orbitals. Some of them are the sp^1 (linear), sp^2 (trigonal planar) and sp^3 (tetrahedral) hybrid orbitals. There are also sd^x and $sp^x d^y$ orbitals. For an introduction to orbitals and atomic bonds in general see reference [Gro12a].

¹⁹The σ and π bonds are formed by the overlap of two atomic orbitals, with the π bonds being usually weaker than the σ bonds due to a smaller degree of overlap in the π bonds than in the σ bonds [Bro14]. In σ bonds the ends of the bonding orbitals are overlapping (end-to-end), with the electron density concentrated between the nuclei of the bonding atoms. Contrasting, in π bonds the lobes of the bonding orbitals overlap another (side-by-side), with the electron density concentrated above and below the plane of the nuclei of the bonding atoms.

easily be separated [Nov04; Cai12]. Amorphous carbon inherits some of the extreme properties of diamond, like hardness and elastic modulus, but the material is rather a disordered film with no grain boundaries, than a crystal with a regular lattice structure.

There are various different species of amorphous carbon (**a-C**), such as hydrogenated amorphous carbon (**a-C:H**), tetrahedral amorphous carbon (**ta-C**) and hydrogenated tetrahedral amorphous carbon (**ta-C:H**), depending on the amount of sp^2 and sp^3 coordinated carbons and the amount of hydrogenation. The different compositions are displayed in a ternary phase diagram developed by Jacob and Möller in Figure 2.11 [Jac93]. Here, the corresponding axes of the compositional amount are indicated by arrows, pointing at 100%. The grid indicates the composition in steps of 20%. In the lower left corner, amorphous carbons like graphite, glassy carbon and evaporated a-C are found. With increasing hydrogen concentration the possibilities for interconnecting carbon networks are reduced. The limits for these networks are given by polyethylene and polyacetylene, defining the lower right corner. Here, instead of films only molecules form. Diamond, fully sp^3 hybridized carbon, forms the top of the triangle. Between these three corners, the prior stated amorphous carbon species are located (see Figure 2.11).

In the following some carbon material parameters like their point group, phonon and Raman active modes, as well as exemplary Raman spectra are given. In Table 2.4 the band gap and hardness of some materials are listed.

Diamond is of a two-atomic base of two carbon atoms and forms a face-centered cubic lattice. The structure of diamond belongs to the O_h point group [Sol70]. The diamond structure directly results from the sp^3 hybridization, with each carbon atom binding equivalently to four neighboring carbon atoms [Gro12c]. An exemplary Raman spectrum of diamond is shown in Figure 2.12. The Raman mode is at 1332 cm^{-1} and of T_{2g} symmetry [Rob02]. The mode was extensively studied. It is sensitive to doping, perfection of the crystal lattice, mechanical stress, temperature and even different origins of natural diamonds can be determined [Zai01]. For many of the named sensitivities, linear and quadratic relations were derived to use diamond as a sensor for the parameter of choice. For deviations from the perfect crystal other Raman modes occur in the spectrum. They are reported in detail in the diamond properties handbook by Zaitsev [Zai01].

Table 2.4 Band gap and hardness of some carbon species [Rob02].

	Gap/eV	Hardness/GPa
Diamond	5.5	100
Graphite	0	
sputtered C	0.5	
a-C:H soft	1.7 - 4	< 10
a-C:H hard	1.1 - 1.7	10 - 20
ta-C:H	2.0 - 2.5	50
ta-C	2.5	80

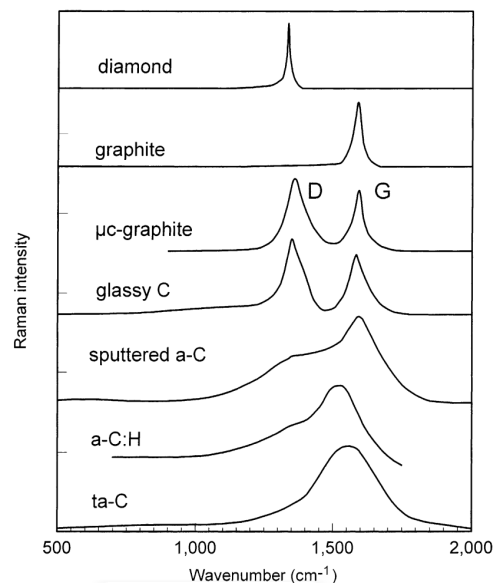


Figure 2.12 Typical Raman spectra of carbon structures. Image taken from reference [Rob02].

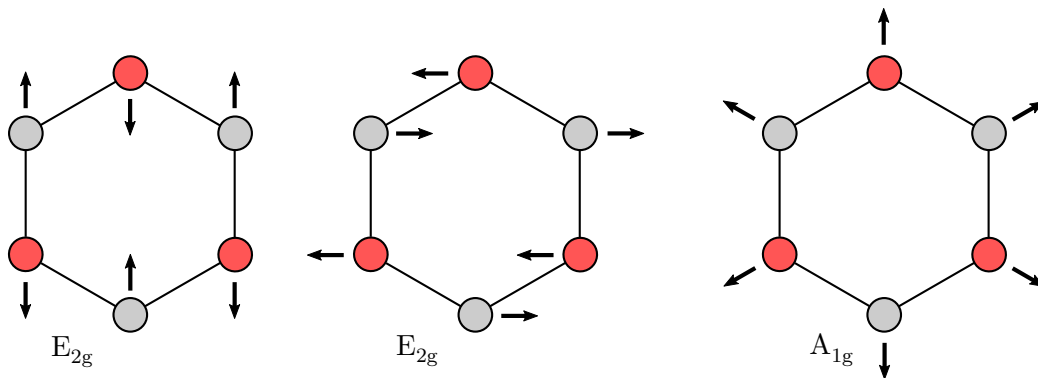


Figure 2.13 Phonon modes of the graphene lattice. Indicated are the E_{2g} modes, with the two sub-lattices vibrating against each other, and the A_{2g} mode, which is a “breathing” mode of the graphene ring. Image modified from reference [Neu18].

Graphite and Graphene are of hexagonal lattice structure. This structure belongs to the D_{6h} point group [Mer17; Koc17]. The structure of both materials results from the sp^2 hybridization, leading to planar σ bonds in the carbon plane and one weak π bond perpendicular to this plane. Graphene is a two-dimensional material. Stacking multiple layers of graphene forms the three-dimensional material graphite. An exemplary Raman spectrum of single crystal graphite is shown in Figure 2.12. The so called G mode (G for graphite) is at 1580 cm^{-1} and of E_{2g} symmetry [Rob02]. If the crystal symmetry is broken, a second Raman mode at around 1350 cm^{-1} arises. This mode is called D mode (D for disorder) and of A_{1g} symmetry²⁰.

Both phonon modes are shown in Figure 2.13. Here, the E_{2g} mode is a degenerate mode of the longitudinal and transversal in-plane optical phonons. The mode corresponds to a vibration of the two sub-lattices of graphene against each other [Neu18]. The A_{2g} mode is a radial oscillation of the hexagonal carbon ring. Due to its movement, the mode is also called the “breathing” mode of the graphene ring. In an infinite and perfect graphene lattice this mode is forbidden and not Raman active. The mode is only observable if disorder is present in the lattice [Fer00].

If there are defects in the graphene lattice, the sp^2 hybridization is altered locally, changing the band structure and phonon dispersion relation, leading to the appearance of additional Raman lines [Neu18]. This makes Raman spectroscopy a powerful tool to detect structural changes in carbon structures. Furthermore, through shifts in the Raman signatures effects like doping and other modifications are detectable. Raman spectroscopy can even determine if graphene is strained, if one or multiple layers of graphene are investigated and whether the material is hydrogenated or oxidized.

Amorphous Carbon is neither diamond nor graphite and has no long-range ordering. Therefore no point group can be assigned. Nonetheless, the Raman spectra of these materials remain dominated by the D and G modes of graphite [Rob02]. Exemplary Raman spectra of various amorphous carbon species are shown in Figure 2.12. Whereas for micro graphite and glassy carbon the D and G modes are clearly separated, for sputtered, hydro-

²⁰A more in-depth discussion on graphene is given in the book of Dieing et al. [Neu18]

generated and tetrahedral amorphous carbon species the Raman signatures are significantly broadened and overlap each other.

Due to the breakdown of periodicity in amorphous carbon structures, the Raman spectra correspond to a weighted vibrational density of states [Rob02]. Therefore, the Raman and infrared spectra should resemble each other. This resemblance is observed for amorphous silicon, but not for amorphous carbon. In amorphous carbon materials the Raman spectra are mainly dominated by scattering by the sp^2 sites, having a 50 to 230 times larger Raman cross-section, than sp^3 sites. But still, the Raman spectrum does not follow the weighted vibrational density of states of the sp^2 sites. The spectrum is rather controlled by the order of the sp^2 sites, than by the sp^2 fraction [Rob02]. While the G mode is a stretching vibration of any pair of sp^2 sites, the D mode is a breathing mode of only those sp^2 sites forming rings. That the Raman spectra of amorphous carbon materials are dominated by the D and G modes of graphite is unusual and therefore of scientific interest. Ferrari and Robertson developed a model to explain this phenomenon of amorphous carbon materials and derive structural information as well as the sp^3 content from the Raman spectra [Fer00; Fer01].

The phenomenological three-stage model is described in the following. Generally, the Raman spectrum of a graphite sheet with small defects (bond-angle disorder, bond-length disorder and hybridization differences) depends on [Fer00]

- the clustering of the sp^2 phase,
- the bond disorder,
- the presence of sp^2 rings and chains and
- the sp^2/sp^3 ratio.

Each of these factors has a different influence on the Raman spectrum, shown schematically in Figure 2.14. With more carbon atoms clustered in six-fold rings, the intensity of the D mode increases. The G mode is altered by bond disorder, which reduces the Raman shift of the mode for an increased disorder. Additionally, the G mode is influenced by chains and clustering, both increase the Raman shift for an increased disorder.

Ferrari and Robertson define an amorphization trajectory, containing three stages

1. graphite to nanocrystalline graphite,
2. nanocrystalline graphite to amorphous carbon and
3. amorphous carbon to tetrahedral amorphous carbon or defected diamond.

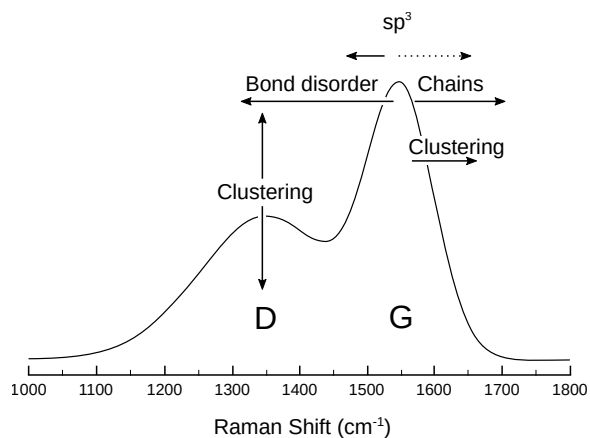


Figure 2.14 Schematic influences of amorphous carbon properties on their Raman spectrum. Image taken from reference [Fer00].

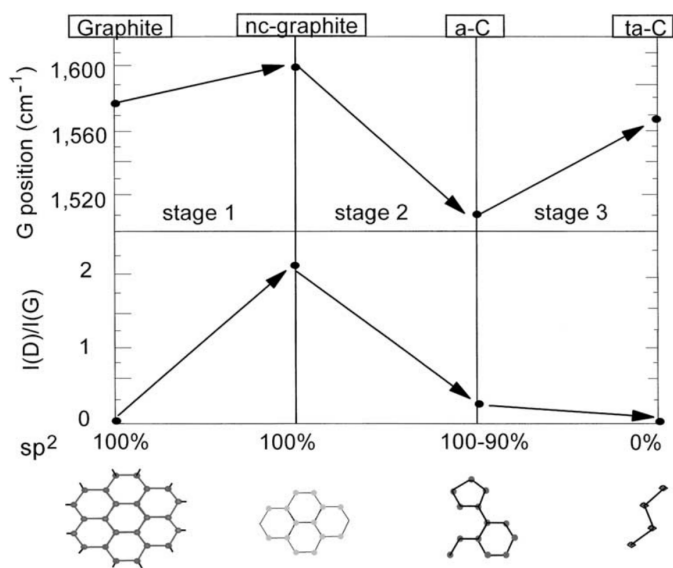


Figure 2.15 Three stage model by Ferrari and Robertson, showing the variations of the G mode and the $I(D)/I(G)$ ratio in dependence of the degree of disorder and the sp^2 content. Image taken from reference [Rob02].

close to zero. Here, defects are introduced into the graphite layer (loss of aromatic bonding and odd-numbered rings) and the stage becomes more and more disordered, with a maximum of approximately 10% sp^3 content. A typical example for this stage is sputtered amorphous carbon.

In stage 3 the G mode shifts from 1510 cm^{-1} to 1570 cm^{-1} and the $I(D)/I(G)$ ratio is very close to zero throughout the whole stage. While the sp^2 sites are gradually transformed from rings to chains, the sp^3 content rises to almost 100%. With increasing sp^3 contents, the G mode becomes more and more symmetric.

It is important to note, that most of the changes in the visible Raman spectra are driven by the evolution of the sp^2 clusters. This model is only an estimation of the sp^3 content. For precise measurements, the actual sp^3 content has to be verified by complementary methods, like Nuclear Magnetic Resonance (**NMR**) or Electron Energy Loss Spectroscopy (**EELS**). In order to get an improved estimation of the sp^3 content Ferrari and Robertson extend their three stage model to multi-wavelength Raman spectroscopy [Fer00] (see also Section 5.1).

2.3.3 Molybdenum Disulfide

Molybdenum disulfide (MoS_2) is widely used as solid lubricant [Chu11a]. It has a layered structure with alternating layers of molybdenum and sulphur atoms. Strong bonds are formed within the sandwich planes, while the different MoS_2 layers are only weakly bonded [Hol09b].

The three-stage model is presented in Figure 2.15 and is described in the following. In stage 1 the G mode shifts from 1580 cm^{-1} to 1600 cm^{-1} and the D mode appears, leading to an increase in the intensity ratio of the two peaks ($I(D)/I(G)$). This is explained by the vibrational density of states and phonon confinement. In this phase, the material is transformed from monocrystalline to polycrystalline, relaxing the $q = 0$ selection rule and allowing additional phonons. Here, the grain size of clusters of aromatic rings is gradually reduced, without forming sp^3 bonds.

In stage 2 the G mode shifts from 1600 cm^{-1} to 1510 cm^{-1} and the $I(D)/I(G)$ ratio decreases

Bulk MoS₂ is, like graphite and graphene, of hexagonal structure and belongs to the D_{6h} point group. There are 18 normal vibration modes, with the translational acoustic A_{2u} and E_{1u} modes, the Raman active A_{1g} (408 cm⁻¹), E_{1g} (286 cm⁻¹) and E_{2g} (33 cm⁻¹ and 383 cm⁻¹) modes, as well as the infrared active A_{2u} and E_{1u} modes [Li12; Zha13a]. Only the A_{1g} and E_{2g} modes can be observed at laser excitation normal to the basal plane. An exemplary Raman spectrum is given in Figure 2.16.

Single layer MoS₂ is of D_{3h} symmetry, with an infrared active A_{2''} mode, an A_{1'} and E'' Raman active mode and an E' mode, which is infrared and Raman active. The Raman active modes are around 384 cm⁻¹ (E') and 403 cm⁻¹ (A_{1'}) [Zha13a].

In *N*-layer MoS₂ there are *N* - 1 rigid-layer vibrations (layer breathing modes) along the *c* axis and *N* - 1 shear modes perpendicular to it. For even *N*, there are zero Raman active layer breathing modes and *N*/2 Raman active shear modes. For odd *N*, there are *N*-1/2 Raman active layer breathing modes and *N* - 1 Raman active shear modes [Zha13a]. These differences for odd and even numbers of MoS₂ layers are also reflected by the exemplary Raman spectra for five (5L) and six (6L) layers. In Figure 2.16 the details around 30 cm⁻¹ differ for the different numbers of layers. The layer breathing and shear modes are very sensitive to *N*: The low frequency Raman modes below 100 cm⁻¹ are shifted with *N*. This effect can be used to determine the number of up to 19 MoS₂ layers [Zha13a; Zha13b], which corresponds to a thickness of approximately 12 nm [Fri66; Li12; Zha13a]. Therefore, several μm thick films show bulk like Raman signals. The hardness of MoS₂ is in the range of 0.08 GPa to 4 GPa [Pet12; Vie12]. This wide range might be explained by the anisotropy of MoS₂, with different crystal orientations being tested in the different experiments.

As stated earlier, the coefficient of friction of any material is a property of the tribological system (see Section 2.2). Numerous investigations on MoS₂ showed that the tribological performance of the coatings depends on the operating and environmental conditions (e.g. contact pressure, sliding speed, temperature, composition and thickness, surrounding atmosphere, humidity, pressure and others) [Chu11a]. Coefficients of friction between 0.02 (properly oriented, clean MoS₂) and 0.3 (impurity contaminated MoS₂ in humid atmosphere) were reported. Under ultra-high vacuum conditions MoS₂ shows superlubricant properties, with coefficients of friction below 0.001 [Hol09b]. In general, the lubricant properties of MoS₂ are retained at temperatures up to 400 °C in air.

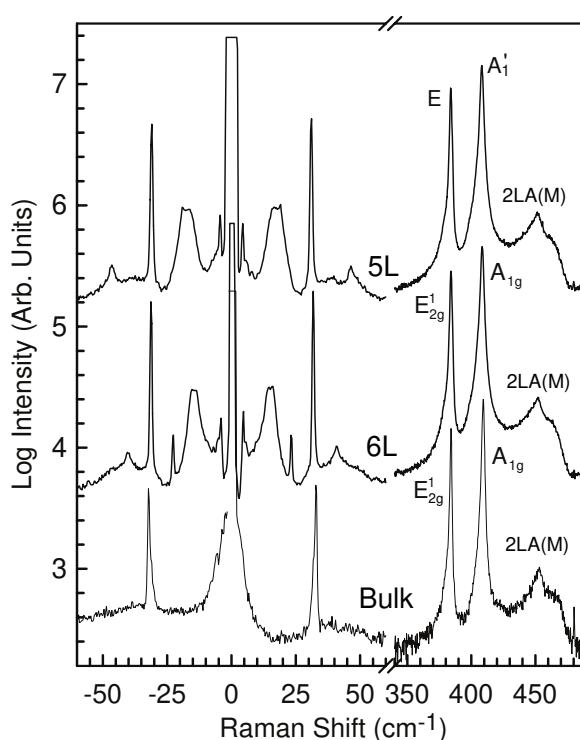


Figure 2.16 Typical Raman spectra of bulk and few layer MoS₂. Image taken from reference [Zha13a].

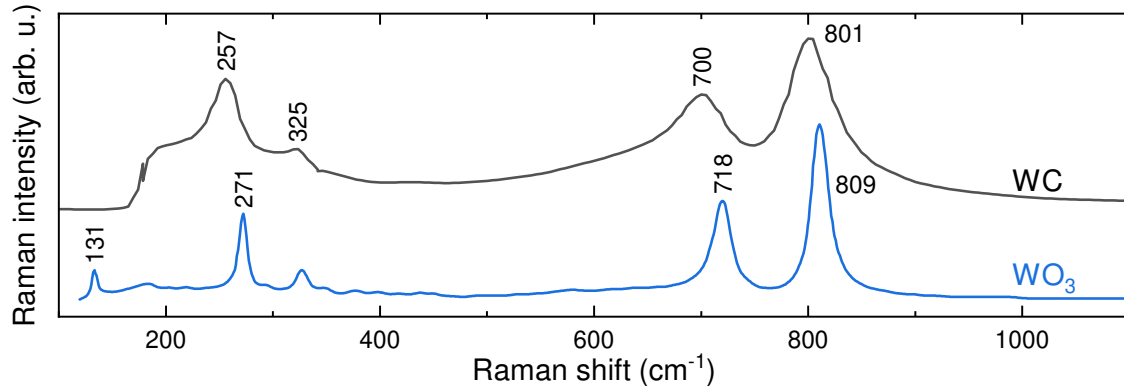


Figure 2.17 Raman modes of WC and WO_3 . Data taken from references [Das13] and [Lu02].

2.3.4 Tungsten Carbides and Oxides

Tungsten carbides are widely used in tool materials, aggressive environments and under high loads. This is due to their high melting point and hardness, which is relatively stable in the temperature range from 300 K to 1300 K [Kur06]. Compared to other carbides, tungsten carbides have an increased elastic modulus as well as a reduced thermal expansion coefficient, which makes them even more favorable to be used for wear-resistant tool materials. There are two main phases of tungsten carbides WC and W_2C . As there is no stable W_2C below 1523 K (see [Kur06]) and all measurements are performed at room temperature, only the WC-phase is discussed.

Tungsten Carbide (WC) is of hexagonal structure and belongs to the D_{3h} point group [Kur06; Fan19]. Other tungsten carbide phases and their point groups are summarized in the paper by Kurlov. A Raman spectrum of powdered WC (grain size 4 μm to 7 μm) is shown in Figure 2.17. The Raman modes are observed at 257 cm^{-1} , 325 cm^{-1} , 700 cm^{-1} and 801 cm^{-1} , with the three lower peaks being assigned to incipient oxidation of WC and the highest mode at 801 cm^{-1} being a stretching mode of WC [Das13; Yan08]. WC has a hardness of 22 GPa [Muk11].

Tungsten Oxide (WO_3) is of perovskite-like structure and belongs to the C_{2h} point group at room temperature [Sal75]. Figure 2.17 shows a Raman spectrum of powdered WO_3 (grain size 1 μm to 5 μm), with major signatures at 809 cm^{-1} (W–O stretching mode) and 718 cm^{-1} (W–O stretching mode). Additional Raman modes are observed at 271 cm^{-1} (W–O bending mode) and 131 cm^{-1} (W–O bending mode) [Lu02]. For hydrated WO_3 the mode at 718 cm^{-1} broadens and shifts to 702 cm^{-1} due to crystal symmetry changes and lattice distortions [Lu02]. Due to the low symmetry of WO_3 , 48 Raman modes can be expected [Sal75], but only 37 (27) modes were observed in a single crystal (powdered sample) [Caz99].

Chapter 3

Experimental Methods and Data Analysis

The three sections of this chapter focus on the experimental methods needed to collect Raman scattering spectra, describe the sample fabrication and characterization processes and show the processing of the recorded Raman data.

The first section presents a basic Raman setup to illustrate the fundamental concepts of experimental Raman scattering. These basic concepts are succeeded by confocal microscopy, which is appended to the basic Raman setup. The section closes with a presentation of the confocal Raman spectrometer used in the experiments of this thesis.

The second section describes the sample fabrication by means of Physical Vapor Deposition (**PVD**). Here, frequently used thin film deposition methods are described. In order to characterize the deposited films, tests for their mechanical (hardness, elastic modulus, coefficient of wear, specific wear rate) and topographical parameters (roughness) as well as tests for their structure (crystallographic orientation, strain) and compositional parameters (chemical composition) are introduced.

The chapter closes with a section describing the post-processing of the recorded Raman data and documenting an analysis software developed in the scope of this thesis. A special focus is drawn on cosmic ray removal and Raman mappings.

3.1 Raman Spectroscopy

3.1.1 Basic Raman Spectroscopy Instrumentation

A setup with basic instrumentation for Raman spectroscopy is shown in Figure 3.1. The light path is divided into two parts, an excitation path and a detection path. The excitation path ranges from the laser source to the sample surface, whereas the detection path ranges from the sample surface to the Charge-Coupled Device (**CCD**) camera. The excitation path starts at a single-frequency Laser¹ (here: 266 nm TopWave, Toptica cleaned by a Semrock LL01-266-25 clean-up filter). The laser light is directed through a Neutral Density (**ND**) filter and is reflected via two mirrors, through a focusing lens (here: 150 mm) to excite the specimen of interest. The ND filter enables a precise adjustment of the laser power to prevent sample degeneration. Using two mirrors allows for full control of the angular and translational displacement of the lens-focused laser spot on the sample². Focusing the laser onto the sample creates high areal intensity densities on the sample surface which are needed to generate intensive Raman signals [McC00a; Smi19c] (compare Section 2.1.3). However,

¹For the verification of the mode structure of a laser, a Fabry-Perot interferometer can be used (see Appendix A.1).

²A good hands-on on laser-beam alignment is given by reference [Opt20].

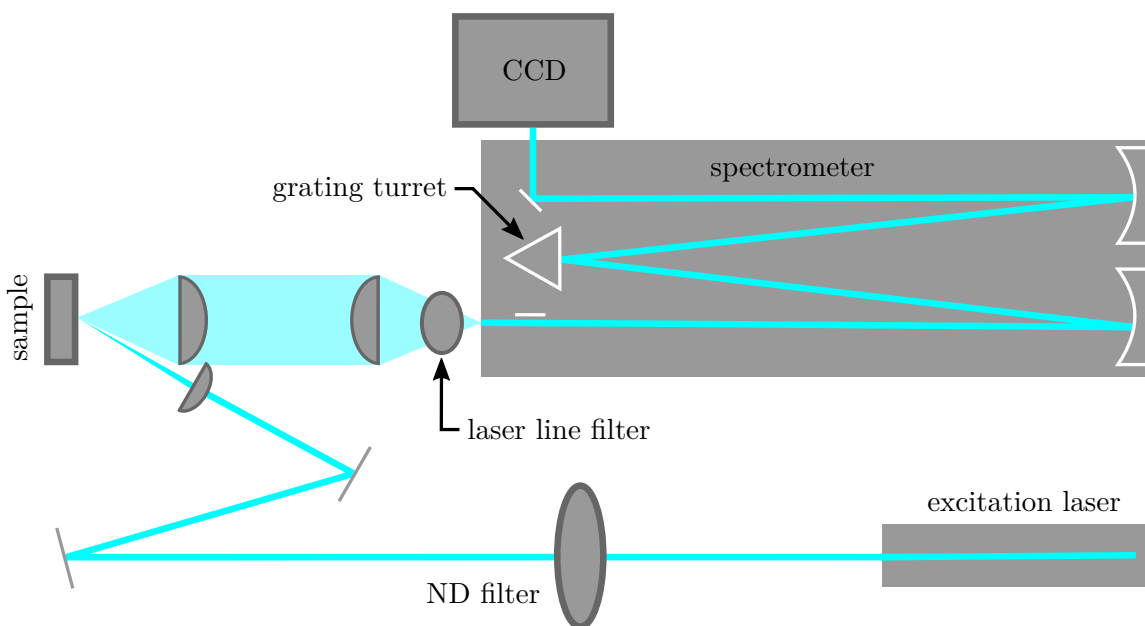


Figure 3.1 Basic Raman setup that allows the laser power to be adjusted with a ND filter. The scattered light is collimated and focused onto a spectrometer entrance slit. To suppress the laser line, the light is filtered with a laser line filter. The filtered light is dispersed by a grating and collected with a CCD camera.

each sample should be carefully checked for degeneration, as high areal laser power densities easily degrade sample surfaces [McC00c; Smi19b].

The light is scattered off the sample surface. The back scattered light is collected and parallelized by the first lens (here: 75 mm, quartz), starting the detection path³. The parallelized light is focused by a second lens with the same focus length onto the entry slit of a spectrometer (here: SpectraPro 2500i, Princeton Instruments). Directly in front of the spectrometer an edge filter (here: 266 nm RazorEdge ultrasteep long-pass edge filter, Semrock) suppresses the laser line to protect the sensitive CCD sensor from laser induced damage. Furthermore, by filtering the scattered light, the Rayleigh line is strongly reduced⁴, setting it to the same scale as the weak Raman signal.

Inside the spectrometer, the light is dispersed by a grating (here: 3600 grooves/mm, 240 nm blaze angle) to be detected by a CCD sensor (here: Pixis, Princeton Instruments). These cameras are used due to their high quantum efficiency, low thermal and low readout noise [Hol10a]. Here, the exposure time strongly depends on the excitation wavelength, the sample's polarizability, and laser power (see Section 2.1.3). The components used for light collection and dispersion (e.g. lenses, detectors and gratings) should as well be optimized for the wavelength region of interest⁵. Taking all these factors into account, the resulting time of exposure ranges from merely seconds to several minutes or even hours.

³A flip mirror might be introduced here, to get an image of the focal points of the excitation and the detection paths on the sample surface.

⁴Typically the reduction is by five to seven orders of magnitude, depending on the wavelength and the filter.

⁵A good overview on Raman instrumentation with examples is given in reference [Hol10a].

3.1.2 Confocal Raman Spectroscopy

With a basic Raman setup developed in the previous section, in this section the more elaborate method of confocal Raman spectroscopy is described. Here, the excitation lens and the first detection lens are merged into a microscope objective. This eliminates the need to match the excitation lens and detection lens foci, as the objective is now used for excitation and detection at the same time (auto-collimation). Furthermore, the back-scattered light is focused onto the entrance slit of the spectrometer, which blocks the scattered light that is not originated from the focal plane of the microscope. Hence, the entrance slit serves as geometric filter (pinhole). Additionally, using a microscope objective allows for a smaller focus spot diameter, and therefore even higher areal intensity densities are reached. The method can be elaborated further by fixing the sample on a two-axis stage, whose axes are moved parallel to the focus-plane of the microscope objective. This allows to add controllable spatial resolution of the sample space.

The basic confocal principle is illustrated in Figure 3.2. A point-like light source is used for exciting the sample. Using a beam splitter the exciting light is directed through an objective onto the sample. Here, a small sample volume is illuminated. The scattered light is collected by the same objective, parallelized and focused again by a second lens on the spectrometer entrance slit⁶. It is important to notice, that only rays that originate from the focal plane of the objective contribute to the detected signal, as their focal points coincide with the spectrometer entrance slit (see Figure 3.2). This focus selection of the signal results in a strongly enhanced image contrast [Hol10b] and a suppressed background signal. Furthermore, this enables transparent samples to be scanned in three dimensions, if the sample is fixed on a two-axis stage and the focus is adjustable.

The discussed confocal principle is used in an optimized setup, which is combined with several add-ons in the Confocal Raman Microscope System CRS+ 750/BX51, S&I (**MonoVista**), shown in Figure 3.3. The system includes different continuous-wave, single-frequency excitation lasers (Zouk 20 355 nm, Cobolt; Samba 100 532 nm, Cobolt; HeNe 632.8 nm, Melles Griot; Rumba 500 1064 nm, Cobolt), which can be selected by its control software. In order to suppress Amplified Spontaneous Emission (**ASE**)⁷ and remove the unwanted emissions from the laser light clean line filters are installed shortly after the lasers (CL-532-ASE for 532 nm and CL-633-ASE for 633 nm, both Ondax). The light paths are controlled by motorized flip mirrors. In addition, retardation wave plates ($\lambda/2$ 355 nm, Thorlabs; $\lambda/2$ 500 nm to 1300 nm, B Halle) in the excitation and detection paths are added, as well as interchangeable laser line filters

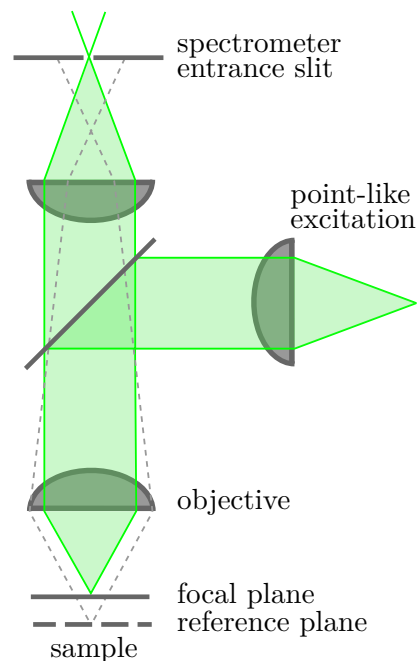


Figure 3.2 Confocal principle using a beam splitter. Image adapted from reference [Hol10b].

⁶The configuration of the point-like illumination and the optically conjugated pinhole is called *confocal*.

⁷Amplified spontaneous emission or superluminescence is spontaneously emitted light that was optically amplified by stimulated emission in the laser medium. ASE commonly occurs in laser diodes.

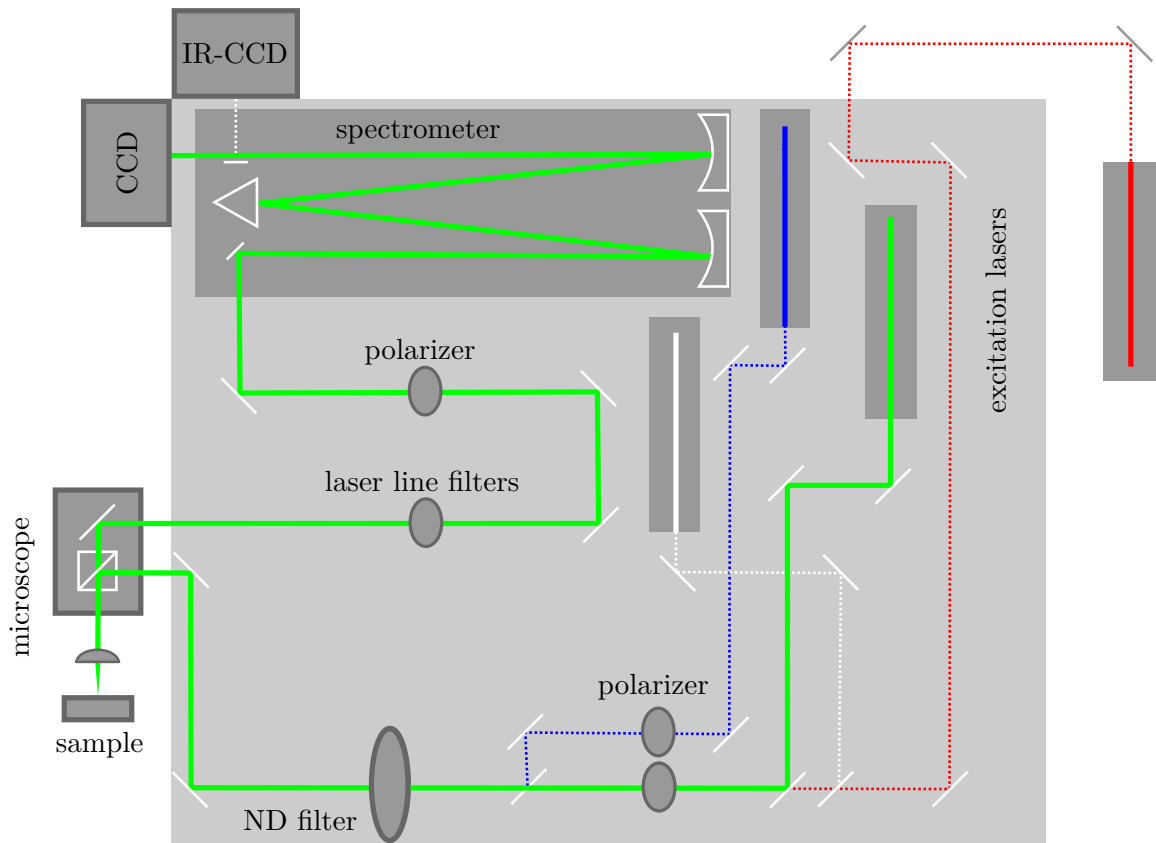


Figure 3.3 Confocal Raman setup of the MonoVista System, showing multiple laser excitation sources and the corresponding paths, namely 355 nm (blue), 532 nm (green), 633 nm (red) and 1064 nm (white). In addition to the basic Raman setup, the polarization of the light may be adjusted.

for each laser. The spectrometer (SpectraPro 2750, Princeton Instruments) is equipped with three gratings (900 grooves/mm H-NIR, 1800 grooves/mm H-VIS, 2400 grooves/mm H-VIS) and connected to two liquid-nitrogen cooled CCD cameras (PyLoN 2KF and PyLoN-IR 1024/1.7, both Princeton Instruments). The sample is mounted onto a two-axis stage (SCAN, Märzhäuser Wetzlar), to which the microscope objective is perpendicular. The focus of the objective is adjustable along this perpendicular axis. A typical spectral resolution is 5 cm^{-1} (see also Appendix A.4), while the minimal spatial resolution is 50 nm.

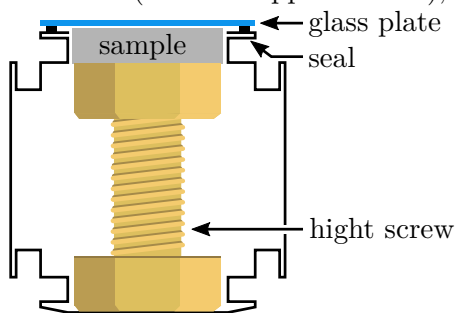


Figure 3.4 Custom vacuum chamber.

The MonoVista comes with a flow cryostat (KONTI Cryostat Type Microscope, CryoVac), which enables measurements of small samples at low temperatures ($T_{\text{min}} \approx 10 \text{ K}$). Furthermore, a custom made vacuum chamber allows for investigation of sensitive samples in vacuum or controlled atmosphere (argon, helium as well as other gases). A scheme of the chamber is shown in Figure 3.4. Here, a suprasil glass plate is loosely placed on a seal and can be removed to insert a sample of maximal 40 mm

in diameter. The sample height can be adjusted using the height screw. The chamber may be evacuated by connecting a vacuum pump to one of its connectors. If a clean seal is used, no further mechanics or pressure is needed to fix the glass plate. It is fixed solely by the suction pressure of the connected vacuum pump⁸. Using the second connector of the chamber, a gas container of choice can be connected to flood the chamber with a custom atmosphere.

3.2 Sample Preparation and Further Characterization

The goal of this section is to give a brief insight into sample production and basic mechanical testing. Here, the basic principle of Physical Vapor Deposition (**PVD**) is explained, while the details on the process parameters are given in the corresponding chapters. Furthermore, methods are presented that are used to determine the topography, the structure and the composition of the specimen.

3.2.1 Sample Preparation by Physical Vapor Deposition

The samples investigated in this thesis are manufactured with Physical Vapor Deposition (**PVD**), which is a vacuum deposition method used for production of thin films and coatings.

During PVD, the sample to be coated (substrate) and the material to be disposed (target) are usually in an evacuated chamber at pressures in the range of 1 mbar to 10^{-6} mbar [Bob13b]. The low pressures are required in order to prevent impurities from ambient air to be embedded in the resulting thin films. The target material is transferred into its gas phase through bombardment with laser pulses (Pulsed Laser Deposition (**PLD**)), electron beams (Electron-Beam Physical Vapor Deposition (**EBPVD**)) or charged ions (cathode sputtering)⁹. For the samples studied collision ionized charged Argon ions are used, which are accelerated towards the negatively charged target and sputter the target material. From this process secondary electrons are triggered, which again ionize Argon atoms to sustain the process. The evaporated target particles move in straight lines of sight from the target and condensate on the substrate's surface. During deposition, in order to generate uniform coatings, the substrate is rotated and translated with respect to the sputtering target [Bob13b]. Furthermore, the process of surface diffusion¹⁰ of the condensing particles plays an important role in the formation of the coating. Details on the deposition process are shown in reference [Hub96] and details of surface diffusion are presented in reference [Ant07]. In order to increase the growth rate and the homogeneity of a deposited coating, a negative charge (bias voltage) can be applied to the substrate [Bob13b].

The low process temperatures in PVD allow plastics and almost all metals, oxides, nitrides and carbides to be deposited. Oxides and nitrides are deposited by adding a reactive gas like oxygen or nitrogen to the vacuum chamber. Typical film thicknesses range from several nm to several μm [Mat10].

⁸For this setup, objectives with a working distance of at least 3 mm have to be used, with the sample being placed close to the bottom of the glass plate. But care has to be taken, to supply sufficient clearance between sample and glass plate, as the suction pressure of the vacuum pump drags the plate around 1 mm closer to the sample surface.

⁹For more details, see reference [Bob13b].

¹⁰Surface diffusion is the movement of particles at solid surfaces.

Multiple variants were developed throughout the years. In the following the relevant PVD variants for the samples studied in the scope of this thesis are presented briefly (see reference [Ohr02d] for details). An unbalanced industrial magnetron sputtering device (CC800/9 Custom, CemeCon AG) is used for the coating deposition.

Direct Current Sputtering uses a Direct Current (DC) applied between target and substrate. The target forms the negative electrode, whereas the substrate forms the positive electrode. This setting provides a continuous stream of positively charged ions (for example argon) directed towards the target, which release particles of the substrate. As a disadvantage of this method only conductive materials can be used, non-conductive materials would get charged and would compensate the DC field.

Radio Frequency Sputtering applies an alternating field between target and substrate. The electrons oscillate between target and substrate and perform more collision ionizations with the argon atoms, reducing the need for secondary electrons emitted through the bombardment. This leads to a high availability of ionized Argon atoms, which allows for a reduction of the Argon pressure at a similar deposition rate. Furthermore, this technique allows for sputtering of isolators, since they are not charged anymore. Here, less electrons arrive at the substrate, therefore, it is only weakly heated. Disadvantages are the expensive generation of radio frequencies and the still low deposition rates.

Magnetron Sputtering adds a magnetic field behind the target. Due the superposition of an electric and a magnetic field the charged particles sense the Lorentz force and their movement is changed from lines to spirals in proximity to the target surface. Like in RF sputtering the ionization collision rate is highly increased. At the same pressure the increased ionization leads to a higher deposition rate compared to bare DC sputtering. Hence, keeping the deposition rate constant allows one to decrease the argon pressure down to 10^{-3} mbar. Magnetron sputtered coatings often outperform coatings produced by other PVD processes [Kel00], which makes it the method of choice for samples investigated in the scope of this thesis.

High Power Magnetron Impulse Sputtering (HiPIMS) is a specialized magnetron sputtering technique, which creates a high percentage of ionized metal atoms [Mün02]. In this technique the cathode power is pulsed in the kHz region, with a pulse duration of several $10 \mu\text{s}$. A generation of metal atoms in the described way reduces the generation of unwanted metal droplets that would imprint defects in the produced coatings [Mün02; Ohr02d]. The pulse frequency, its magnitude and polarity, as well as the pulse width can be varied to tailor the resulting properties of the HiPIMS sputtered coatings.

3.2.2 Characterization of Mechanical Properties

Mechanical properties like hardness, elastic modulus and the coefficient of friction define a surface's suitability for a designed application. Therefore, methods to determine the parameters mentioned are explained in this section.

Hardness and Elastic Modulus are determined using a nanoindenter (here: G200 Agilent). A Berkovich diamond tip¹¹ penetrates the coating using the continuous stiffness method. Additionally, a high frequency oscillatory movement of small amplitude is superimposed on the slow nanoindentation [Siu13]. The indentation is repeated in a matrix of 7×7 points with a distance of $50 \mu\text{m}$. From the resulting indentation curves the hardness and the elastic modulus are calculated with the method from Oliver and Pharr [Oli92]. The mean hardness and elastic modulus over the 49 values is taken as the final result for the requested parameters.

The hardness value is typically measured in the SI unit GPa. It can be converted to the Vickers hardness number (VHN or HV) in kilograms-force per square millimeter by

$$\text{HV} = \frac{g}{1000} \text{HV}_{\text{SI}} = 101,94 \cdot \text{HV}_{\text{SI}}, \quad (3.1)$$

with the standard gravity g .

The Coefficient of Friction is determined using a tribometer (here: ball-on-disc tribometer, CSM-Instruments). The sample, a disc with a diameter of 40 mm, is rotated under a ball with a diameter of 6 mm that is pressed onto the sample's surface with a defined normal force F_{norm} . The coefficient of friction can be calculated from the quotient of the normal force and the resulting force of friction F_{fric} (see equation (2.33)). During the experiment the coefficient of friction is evaluated every second. The coefficients given here are mean values over the complete run or a defined interval of the experiment. In order to conduct tests in controllable atmospheres (here: ambient air, pure argon or pure nitrogen) a cover is built over the setup. The cover is equipped with an inlet, which allows for supplying a continuous gas flow. The gas flow compensates possible leakages.

Specific Wear Rates are wear rates normed by the applied load. Here, the wear volume V_{wear} per sliding distance s is divided by the applied normal force F_{norm} [Czi15d]

$$k = \frac{V_{\text{wear}}}{sF_{\text{norm}}}. \quad (3.2)$$

The specific wear rate is determined using a profilometer (here: Profilometer InfiniteFocus, Alicona). Additionally, focus stacking (see Appendix A.2) is used to generate a 3D model of the sample. From this 3D model the volume V and the length L of a selected region of the wear track can be determined, using the software supplied with the profilometer. From these two parameters the specific volume $V_{\text{spec}} = V/L$ can be calculated, which is used to calculate the total wear volume $V_{\text{wear}} = 2\pi r \cdot V_{\text{spec}}$, where r is the radius of the circular wear track. In order to reduce statistical errors, the specific volume V_{spec} is determined at four different positions for each specimen. The mean value of these volumes is taken to calculate the wear volume. Now, the specific wear rate is calculated, using the measured wear volume, the applied normal force during the tribometer test, and the sliding distance $s = 2\pi r \cdot N$, where N is the number of rotations during testing.

¹¹A three-sided self-similar pyramid, with the same area-to-depth ratio as a Vickers indenter, which is a four-sided diamond pyramid, is commonly used for hardness tests. The Berkovich tip shows the same load-displacement curve as the Vickers indenter [Min04], leading to comparable, but slightly higher hardness values of the Berkovich tip compared to the Vickers tip [Sak09].

3.2.3 Characterization of Topography

The topography of a surface defines its microscopical structure, like surface roughness or surface configuration, which have a strong influence on their physical and chemical properties (see reference [Lüt15b]). To determine the topography of the deposited coatings two high-resolution methods are used. They are explained briefly in the following paragraphs.

Scanning Electron Microscopy (SEM) is an imaging technique that creates images of a surface by scanning a sample with a focused electron beam. The electron beam is generated by an electron gun with a typical energy ranging from a few keV to 50 keV (here: JSM-7001F, JEOL, 20 keV). The beam is focused to ~ 1 nm at the sample surface, where it interacts with the atoms inside the sample [Ohr02b]. This interaction volume ranges from approximately nm to μm , depending on the beam energy, the atomic number of the investigated materials and the density of the sample. This interaction produces several differing signals like secondary electrons, back-scattered electrons, characteristic X-rays and cathodoluminescence or transmitted electrons. The signals from secondary electrons and back-scattered electrons are of interest in this work.

Secondary electrons are produced by inelastic scattering of the incident electrons with the material. Their typical energy is below 50 eV (compare Figure 10-12 in reference [Ohr02b]). Due to this low energy, they originate from the first few nm below the sample surface. Therefore, they are suitable to generate surface images. The signal's brightness depends on the inclination of the sample with respect to the detector: faces perpendicular to the detector appear darker than faces with an inclination [Ohr02b]. Therefore edges develop a high contrast. This sets the experimenter's impression to view the sample from top, whilst being lit up from the direction of the detector.

Back-scattered electrons are elastically scattered electrons with typical energies in the keV range, that are reflected or back-scattered from the sample surface. Due to their high energy, the interaction volume of the back-scattered electrons is bigger than the interaction volume of secondary electrons [Ohr02b]. The comparison of recorded images of the two processes shows a reduced resolution of back-scattered electron images. As heavy materials scatter the electrons more efficiently than light materials, they appear brighter in the resulting image. Due to the differences in secondary and back-scattered electron processes, the secondary electron image can be used to analyze the topography and the back-scattered electron image can be used to get an impression on the distribution of different materials at the sample surface.

SEM is used to create surface images of the samples as well as images of the cryogenically broken sample cross-sections, in order to estimate the thicknesses and deposition rates of the films.

Atomic Force Microscopy (AFM) is a scanning probe microscopy where a sharp tip is used to scan the surface of a sample to generate a high-resolution image (here: Dimension Edge, Bruker). Generally, a spring-like cantilever holds the sharp tip on its far end. The tip is brought into proximity of the sample. The back side of the far end of the cantilever is used as a small mirror for a laser beam, whose reflection indicates and magnifies the cantilever's deflection. The magnified deflection is registered by a detector and is proportional to the sample's structure. Using a laser beam deflection translates the atomic scale interaction

of the sample and cantilever tip to a detectable macro-scale modification of the laser spot position [Voi19]. From these measurements the roughness can be determined by taking the arithmetic mean over a selected region of the sample.

3.2.4 Characterization of Sample Structure and Composition

This section presents methods that analyze the structure and the composition of deposited thin films. Firstly, it is shown how to determine the crystallographic orientation on the sample surface, followed by two methods how to determine the chemical composition of the sample.

X-Ray Diffraction (XRD) arises from monochromatic electromagnetic radiation being scattered by the atoms' electrons. Typical wavelengths of X-rays range from 5 pm to 10 nm. In case of regular arrays of atoms, like crystals, these elastically scattered waves interfere destructively in most directions. In material specific directions they interfere constructively and obey Bragg's law [Ohr02a]

$$2d \sin \theta = n\lambda, \quad \text{with } n \in \mathbb{N}, \quad (3.3)$$

where d is the spacing between diffracting lattice planes, θ is the angle of incidence of the X-ray beam, n is the order of the diffracted beam and λ is the wavelength of the X-rays. Using this technique the crystalline phases, lattice constants, crystal symmetry groups and crystallographic orientations can be determined [Ohr02b]. Here, an XRD diffractometer (Advance D8, Bruker) is used to determine the crystallographic structure of the samples. The diffractometer is equipped with a copper ($\lambda_{\text{Cu-K}\alpha} = 1.5419 \text{ \AA}$) and a chromium ($\lambda_{\text{Cr-K}\alpha} = 2.2911 \text{ \AA}$) radiation source.

$\sin^2\psi$ Measurements are specialized XRD measurements that allow to determine the residual strain ε in the coatings of interest. Here, the angle of incidence of the X-ray beam is set to a small range around a selected reflex of diffraction. Now the sample is rotated around its surface normal axis φ and tilted along its inclination axis ψ , in order to detect variations in the reflex of interest (see also [Gen13]). The residual strain $\varepsilon_{\varphi\psi}$ is described by [Spi09]¹²

$$\begin{aligned} \varepsilon_{\varphi\psi} &= \frac{d_{\varphi\psi} - d_0}{d_0} \\ &= \frac{1}{2}s_2 \sin^2 \psi (\sigma_{11} \cos^2 \phi + \sigma_{22} \sin^2 \phi - \sigma_{33} + \sigma_{12} \sin 2\phi) \\ &\quad + \frac{1}{2}s_2 \sin 2\phi (\sigma_{13} \cos \phi + \sigma_{23} \sin \phi) \\ &\quad + \frac{1}{2}s_2 \sigma_{33} + s_1 (\sigma_{11} + \sigma_{22} + \sigma_{33}), \end{aligned} \quad (3.4)$$

which is the fundamental equation of X-ray stress analysis. Here $d_{\varphi\psi}$ is the lattice spacing under different angles and d_0 the lattice spacing of the stress free lattice. The

¹²A more basic introduction to stress and strain measurements is described in reference [Zol14].

components $\sigma_{j,k}$ are the stress components of the stress tensor and s_1 and $1/2 s_2$ the diffraction elastic constants

$$s_1 = -\frac{\nu_P}{E_Y} \quad \text{and} \quad \frac{1}{2}s_2 = \frac{1 + \nu_P}{E_Y}, \quad (3.5)$$

with ν_P being Poisson's number¹³ and E_Y resembling Young's modulus¹⁴.

Energy Dispersive X-Ray Spectroscopy (EDS) uses characteristic X-rays to determine the chemical composition of a sample. The characteristic X-rays are excited by using either X-rays of high energy or by accelerating electrons onto the sample surface. The exciting energy releases an electron of the inner shell, leaving a hole that is immediately filled by an electron from a higher orbital. The surplus of energy is emitted as characteristic radiation, which is typically detected by a semiconductor detector (here: X-Max 80, Oxford Instruments, coupled to SEM). The energy resolution is ≈ 100 eV. This technique can be used to determine the quantitative composition of a sample [Ohr02b]. The source of excitation defines the resolution of the technique. In case of exciting with X-rays the resolution is in the small μm regime. When exciting with an electron beam of an SEM, the resolution can be improved to the low nm regime [Ram06].

X-Ray Photoelectron Spectroscopy (XPS) uses characteristic electron binding energies emitted from the sample to determine its chemical composition. Here, monochromatic X-rays are utilized to excite inner electrons from the material's atoms. The released electrons are directed through a velocity selector in order to separate them by their kinetic energy. With this selection, the binding energy may be calculated, which is characteristic for each element. For different chemical environments, slight changes in the binding energy are detected. Therefore, the chemical composition of the sample can be analyzed [Ohr02b]. The mean free path of the electrons is in the order of a few nm, making XPS a surface sensitive characterization method. XPS measurements presented in this work are studied at Beamline 11 at the synchrotron radiation facility Dortmund ELekTronenspeicherring-Anlage (**DELTA**).

3.3 Data Processing – The Spectrum Analysis Package

In this section the processing of the recorded data is explained. For simple spectra the proprietary software OriginPro is utilized, whereas for mappings¹⁵ a python software is developed in order to automate data processing. The software package, called **spectrum analysis**, is published and freely available [Mol20].

Independent of the software used several steps have to be performed. At first all data have to be read in properly, in order to perform the analysis. To get an overview of the recorded data all raw data should be plotted and reviewed, whether it shows as expected or any errors occurred during the experiment (like a tilted or unfocused sample, etc.).

¹³Poisson's number is a measure of material expansion perpendicular to its direction of compression.

¹⁴Young's modulus or the elastic modulus is a measure for the stiffness of a solid.

¹⁵Mappings are spatially resolved Raman spectra over an xy region on a sample surface.

In the next step the data have to be reduced to the spectral region of interest for the analysis. Peaks that are not completely recorded shall be removed to ensure a proper background calculation and subtraction.

With the spectral region of interest selected, the remaining parts of the spectra have to be cleaned from cosmic rays. During the accumulation of the spectra, cosmic rays may hit the CCD-detector, causing spike-like signals in a spectrum. These spikes may disturb the fit stability and have to be removed. Furthermore, they do not originate from the sample and are not of interest to further investigations. In order to remove the spikes, wavelet transformation is utilized. Section 3.3.1 is devoted to this topic and explains basic principles.

After this preparation of the spectra the baseline has to be calculated and removed. This has to be done for each spectrum, in order to adapt for non-linear background and to correct shifted peak positions. In the following, the data of a spectrum are normalized by the spectrum's maximum value, as fitting with the `lmfit` package is faster with normalized data.

Subsequently, the starting parameters have to be selected for each single peak in each spectrum. Using `spectrum analysis` for multiple spectra will allow one to choose the peak functions (Lorentzian, Gaussian, Breit-Wigner-Fano or Voigt, see also Section 2.1.4) separately for each peak¹⁶. Following the starting parameter selection, fits of all peaks in all spectra are conducted. The results are saved and plotted.

Again, a careful inspection of the results is necessary to identify unstable fits. Refitting of single spectra might be necessary with slightly different starting parameters to generate a stable fit. If all spectra are significantly described and a mapping is analyzed, the parameters can be plotted as a mapping using the suggested python software (see Section 3.3.2).

3.3.1 Spike Removal

As stated in Section 3.1, CCD sensors are used to record the Raman spectra. A drawback of their high efficiency is their sensitivity to cosmic rays (muons), which increases the possibility of random spikes present in the spectra recorded. Removing these spikes from the spectra is discussed in this section.

Signal analysis broadly uses Fourier analysis to decompose a signal into its frequency content. This is ideal to separate high- from low-frequency signals. Nevertheless, the transformation from the time domain to the frequency domain removes the time information completely, which makes event localization in the time domain impossible. Hence, beginnings and ends of signal features are not detectable, which is however necessary to remove a cosmic ray spike from a spectrum. To overcome the disadvantage of lost time information, wavelet analysis can be taken into consideration instead of Fourier analysis. Here, the procedure presented in reference [Ehr01] is introduced to utilize wavelet transformation for despiking of CCD recorded spectra.

To illustrate the basic idea of wavelets and to show some of their properties the Haar

¹⁶Be aware to always keep the same fit function for the respective peak.

wavelet $H(x)$ (see Figure 3.5) is used in the following. It is defined by [Nic17a]

$$H(x) = \begin{cases} 1, & 0 \leq x < \frac{1}{2}, \\ -1, & \frac{1}{2} \leq x < 1, \\ 0, & \text{otherwise.} \end{cases} \quad (3.6)$$

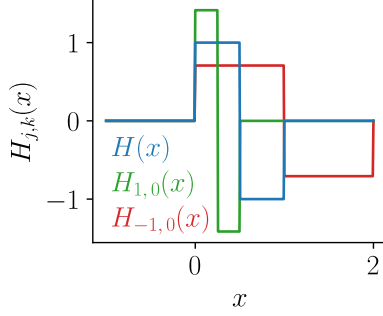


Figure 3.5 Exemplary Haar wavelets for selected $k = 0$ and $j \in \{-1, 0, 1\}$ values.

Note that stretching the wavelet along the y -direction will compress it along the x -direction and vice versa. Two examples of the modified Haar wavelet are shown in Figure 3.5. It can be shown that $H_{j,k}$ is restricted to the interval $[\frac{k}{2^j}, \frac{k+1}{2^j}]$.

The Haar wavelet is orthonormal [Haa10]. This means that the product of any two functions is equal to zero if they are distinct or equal to one if they are equal.

$$\int_{-\infty}^{\infty} H_{j,k} H_{j',k'} = \delta_{j,j'} \delta_{k,k'} = \begin{cases} 1, & j = j' \text{ and } k = k' \\ 0, & \text{otherwise.} \end{cases} \quad (3.8)$$

Additionally, every function $f \in L^2(\mathbb{R})$ has a Haar wavelet series expansion [Haa10]

$$f = \sum_{j=-\infty}^{\infty} \sum_{k=-\infty}^{\infty} w_{j,k} H_{j,k}, \quad \text{with } w_{j,k} = \int_{-\infty}^{\infty} f H_{j,k}, \quad (3.9)$$

where $w_{j,k}$ is the Haar wavelet coefficient. This requests that the integral $\int_{-\infty}^{\infty} f^2$ exists and is finite, meaning that a function in $L^2(\mathbb{R})$ needs to decline rapidly to zero¹⁷.

These ideas are considered to generate the example in Figure 3.6. Here, a model Raman spectrum is presented in the left figure. Two peak-like features are visible: On the one hand, a broad Gaussian feature, representing a typical Raman signal, and, on the other hand, a very narrow feature, representing a cosmic ray. A small linear background is added to the signal. This spectrum is now decomposed by Haar wavelet analysis.

The general Haar wavelet series expansion can be reduced, as the function f is defined in the interval of $[-1, 1]$ and its prior stated restriction has to be valid. Therefore,

$$f = \sum_{j=0}^{\infty} D_j, \quad \text{with } D_j = \sum_{k=-2^j}^{2^j-1} w_{j,k} H_{j,k}, \quad (3.10)$$

¹⁷For more details, see reference [Nic17b].

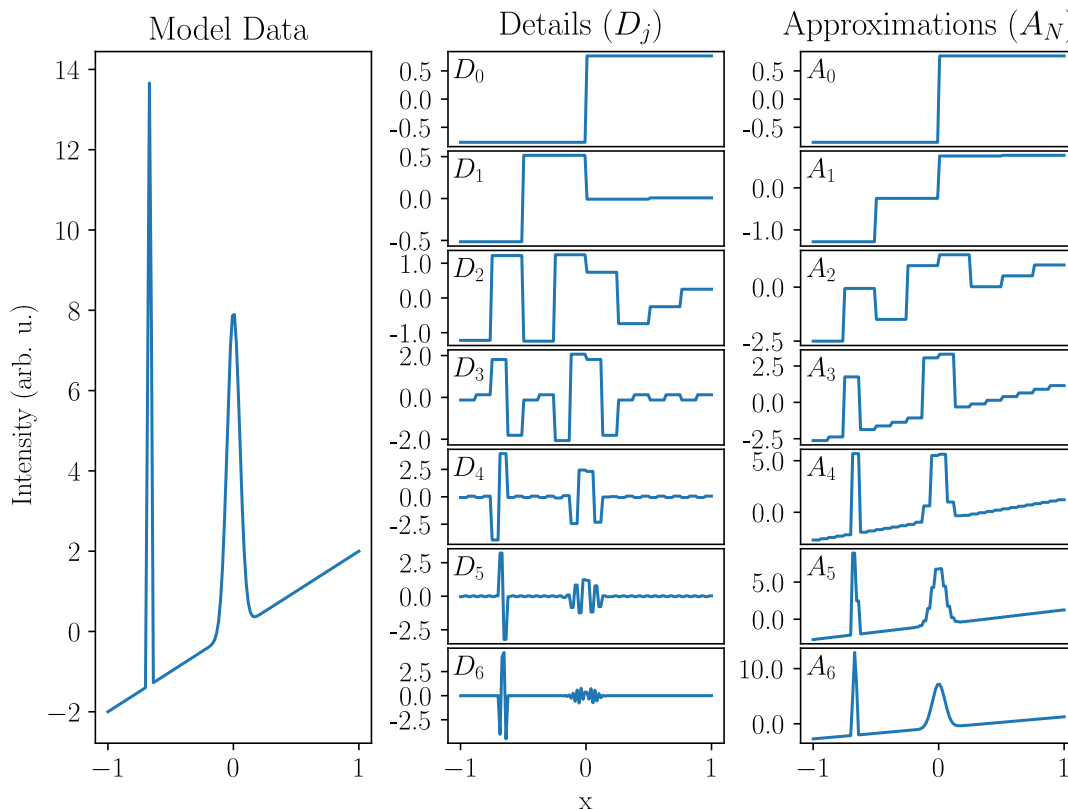


Figure 3.6 Model data with a representative Raman peak and a representative cosmic ray, which is approximated by the Haar wavelet. Details D_j for specific j and approximations A_N for specific N are shown to visualize the Haar wavelet transformation.

where D_j is the sum over all translations of the Haar wavelet at fixed scale j . This parameter describes the details of the function to be approximated. In Figure 3.6 not only the details for specific j are plotted, but also the approximations A_N

$$f = \lim_{N \rightarrow \infty} A_N, \quad \text{with } A_N = \sum_{j=0}^N D_j. \quad (3.11)$$

As the summation to infinity is impractical, a definite N is taken for the approximation.

Careful observation of Figure 3.6 reveals that the two main features of the spectrum behave differently at the details level. However, the intensity of the details of the Raman-like signal decreases with increasing j , the intensity of the details of the muon-like signal stays at the same level. This is in accordance with [Ehr01]¹⁸. This behavior can be utilized to locate spikes in the original spectrum and remove them by linear interpolation, which is done throughout this thesis.

To distinguish the two different signals, a threshold is used. The noise level σ is estimated

¹⁸Note that Ehrentreich et al. use the opposite definition of j , where small j characterize the fine scale.

by the median absolute deviation

$$\sigma = \text{median} \{ \text{abs} [D_N - \text{median}(D_N)] \} / 0.6745, \quad (3.12)$$

assuming Gaussian noise [Rou93]¹⁹. This leads to a soft threshold of

$$\text{thr} = \sigma \cdot \sqrt{2 \log(\#[x_{\min}, x_{\max}])}, \quad (3.13)$$

where $\#[x_{\min}, x_{\max}]$ is the number of elements in the interval to be analyzed. Ehrentreich et al. suggested to use wavelets with a high number of vanishing moments. Therefore, the Sym8 wavelet of the Symlet wavelet base is used here.

3.3.2 Raman Scattering Mappings

In this section, Raman mappings or Raman images are explained. A detailed example procedure to generate Raman mappings is given in Appendix B. As stated earlier, a sequence of Raman spectra is collected: For each spectrum in the sequence, the sample position is varied in the xy plane. In order to connect the spectra with the sample position an image of the sample surface is taken, with additional position markers indicating the positions where a Raman spectrum is collected.

The recorded data are prepared and fitted as described in the beginning of this chapter. Due to combining the fit results with the surface positions two-dimensional maps can be created for each parameter, each error or derived parameter. This enables the experimentalist to link visual information with Raman spectroscopic information.

A drawback of Raman mappings is the time needed for their collection, as already relatively small maps with 15×15 spectra require the measurement of 225 spectra. This demands a very stable system, with a laser fixed in intensity and position for long accumulation times > 10 s per spectrum. Furthermore, for bigger maps the number of the spectra to be fitted rapidly increases. It has always to be kept in mind that these maps only represent small parts of the investigated sample. For a typical experiment, the laser spot is in the range of $1 \mu\text{m}$ to $5 \mu\text{m}$ and a typical step size is $10 \mu\text{m}$. This results in mappings with a scanned surface of $150 \times 150 \mu\text{m}^2$. Faster methods could use lasers focused to a line rather than to a spot or spectral filters directly producing Raman images [Van13b].

3.3.3 Principal Component Analysis

In order to simplify the analysis of the different fitting parameters, this section presents a method to reduce the parameter space and to detect clusters of comparable spectra. The analysis is performed using the `scikit-learn` package [Ped11]. An example script performing the presented analysis is included in the prior discussed `spectrum analysis` package. Additionally, an example analysis is presented in Appendix B.

In the first step of the analysis, the value ranges of the different parameters are scaled to the range between zero and one. This allows for a comparison of the different parameters, removing the predominance of the parameter with the greatest values. Additionally, parameters that are directly correlated are removed, like the FWHM and twice the standard

¹⁹Here, the inverse of the Gaussian scaling factor ($b = 1.4826$) is used to be consistent with the definition in the `statsmodels` package.

deviation of a Lorentzian peak. Furthermore, the intensity ratio I_D/I_G is calculated and included as a new parameter.

Now, the data are prepared for dimension reduction by Principal Component Analysis (**PCA**). The multi-dimensional data of the fitting parameters²⁰ are reduced to a lower-dimensional space, where the variance of each direction is maximized [Sha01]. The new dimensions are the principal components, which are composed by a weighted linear combination of the fitting parameters. Usually, the first few principal components explain the greatest share of the investigated data.

The dimension-reduced data might show subsets of comparable data. Therefore, cluster analysis is utilized to group similar spectra. Here, a clustering algorithm (k-means clustering or spectral clustering) is used. In spectral clustering, each data point is set as a vertex of a graph, with edges weighted by the similarity of the two connected vertices [von07]. From this graph, edges resembling a high difference between the data points are removed. Using this reduced graph, the Laplacian matrix is constructed, whose eigenvectors need to be determined. The eigenvectors are then clustered by k-means clustering. As input parameter only the number of the clusters needs to be set. With k-means clustering the set of data points is clustered into a previously defined number of clusters, with a minimized within-cluster sum-of-squares. Each data point is assigned to one of the clusters.

The detected clusters are colored uniformly in the principal component plot. Additionally for each cluster, a mean spectrum is calculated and plotted to make differences in the spectra visible for the analyst. The mean spectrum of a cluster is calculated from its zero-to-one scaled spectra, to remove the predominance of strong signals from the cluster.

Furthermore, selected parameters composing the principal components are plotted as vectors into the plot²¹. Here, the projection of the length of the vector onto a selected principal component axis demonstrates the impact of the parameter on the selected principal component. The direction of the vector shows along which direction the value of the parameter changes (see also Appendix B).

In order to link the detected clusters with visible features, a mapping of the clusters is generated, as presented in the previous section.

²⁰A typical fitting model used here contains 17 fitting parameters. The model is constructed from one Breit-Wigner-Fano function (7 fitting parameters) and two Lorentzian functions (5 parameters per function).

²¹Plots like this are called biplots.

Chapter 4

Definition of Tribological Material

This chapter addresses the question of "How to define tribological material with respect to Raman scattering?". In order to respond to this question, different surfaces of twin-screw rotors are investigated with multiple techniques, to link optical and mechanical properties.

Twin-screw rotors are widely used in fluid-energy machines to compress and expand gases [Sto05], an example of a female and male rotor pair is shown in Figure 4.1. For the modification of the gas volume, usually oil-injected machines are used, which require a separation of the injected lubricating oil from the processed gas after volumetric modification. This oil separation significantly raises the total cost of ownership of twin-screw machines [Dre14], so there is a possible economical benefit in developing oil-free screw machines. Despite the separation process a small amount of oil always remains in the gas flow [Rin79], which does not satisfy the high demands of semiconductor and coating industries [Dre14]. In return for their disadvantage, oil-injected screw rotors do not need to be synchronized by a timing gear, which is a drawback of dry-running machines. To combine the advantages of dry-running machines (no oil) and oil-injected machines (no timing gear) current research aims at non-synchronized, dry-running screw rotors [Tem07].

These non-lubricated, non-synchronized rotors usually show unacceptable wear due to dry friction between the two rotors. The wear might be reduced using a tungsten carbide coating, as shown in the dissertation by Dämgen [Däm98]. Using these coatings on twin-screw machines short-time operation of several 100 h becomes possible. To increase the lifetime further an increased understanding of the wear mechanisms is required. In addition to tungsten carbide coatings, MoS₂ coatings are promising, due to their dry lubricant properties [Chu11a; Hol09b]. It might help to reduce the friction in the contact area of dry-running, non-synchronized twin-screw machines. Here, an understanding of the wear mechanism is still missing, which is partly developed in the following sections.

The first section of this chapter presents microscopic investigations on uncoated, dry-running twin-screw rotors. Here, a spatial distribution of different iron oxides is detected. This gives a first spectroscopic view on wear, with the identification of some wear-indicators. Subsequent to this section, dry-running tungsten-carbide-coated twin-screw rotors are examined. Here, an oxygen incorporation into the coating of the worn rotors is detected,

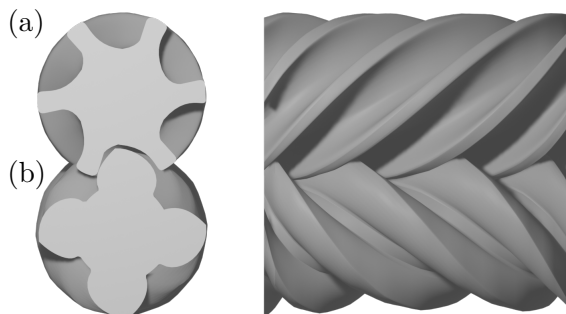


Figure 4.1 Front and side view of (a) a female and (b) a male screw rotor.

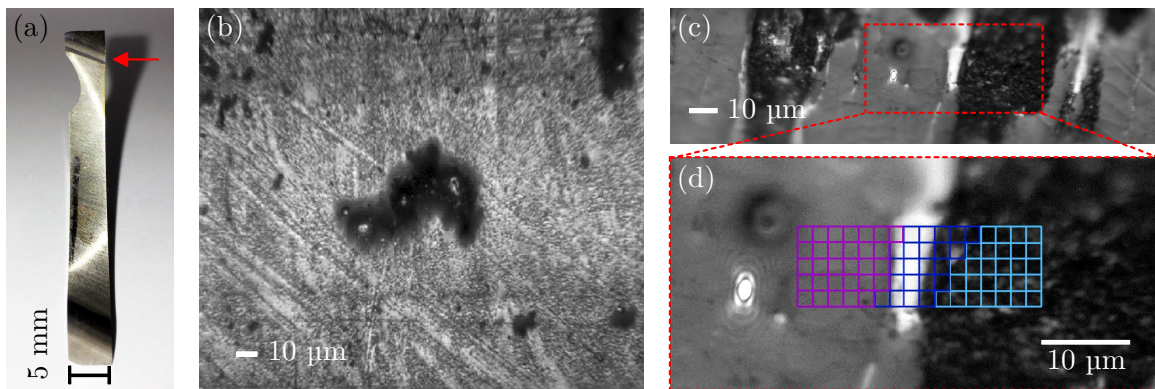


Figure 4.2 (a) Resected part of the female screw rotor. The red arrow indicates the contact line zone on the clipped part. (b) A focus stacked¹ image of a $150\ \mu\text{m} \times 150\ \mu\text{m}$ sized surface region of the screw rotor, composed from multiple optical images. (c) Heavily worn domains at a different position of the contact-zone, magnified in panel (d). Here, the area studied is divided into 80 squares of $2 \times 2\ \mu\text{m}^2$. The bright spot on the left side originates from the laser beam. Reproduced with permission from reference [Mol18].

adding more possible indicators of wear. The last section of this chapter is an investigation on dry-running molybdenum-disulfide-coated samples. This section is focused on the tribofilm formation of the molybdenum-disulfide thin-films in different atmospheres. Here, third-body particles are detected that differ in their chemical behavior compared to the deposited coating or the rest of the wear track.

4.1 Magnetite and Hematite Formation

In this section microscopic wear on uncoated, dry-running screw rotors is investigated. Therefore, the spatial distribution of the iron oxides magnetite (Fe_3O_4) and hematite ($\alpha\text{-Fe}_2\text{O}_3$) in the contact zone of the rotors is analyzed with confocal Raman spectroscopy (see Section 3.1.2). The presented results are published in reference [Mol18].

Experimental Details and Sample Description. A non-synchronized 18CrNiMo7-6 steel (1.6587) rotor pair of a female and a male rotor is operated under liquid-free conditions. Therefore, dry air at a constant inlet pressure of 4 bar and an inlet temperature of $90\ ^\circ\text{C}$ is used. The rotational speed is set to 9500/min, corresponding to a rotor tip speed of 35.7 m/s at the male rotor tip. The rotors are operated for 40 min, leading to 4×10^5 changes of load.

In order to examine the worn surface of the rotor with Raman spectroscopy a part of the female rotor is mechanically resected, see Figure 4.2 (a). In the figure, the horizontal arrow indicates the contact area of the two rotors. A wear trace from the screw rotor operation is visible. A magnified section of a random surface area in the wear trace of $150\ \mu\text{m} \times 150\ \mu\text{m}$ is shown in the monochromatic image of Figure 4.2 (b). As the surface of the wear trace is curved and not planar, multiple images with different focal planes are recorded, using focus stacking to generate an image with an increased depth of field (see Appendix A.2). In this

¹See Appendix A.2 for a brief introduction to focus stacking.

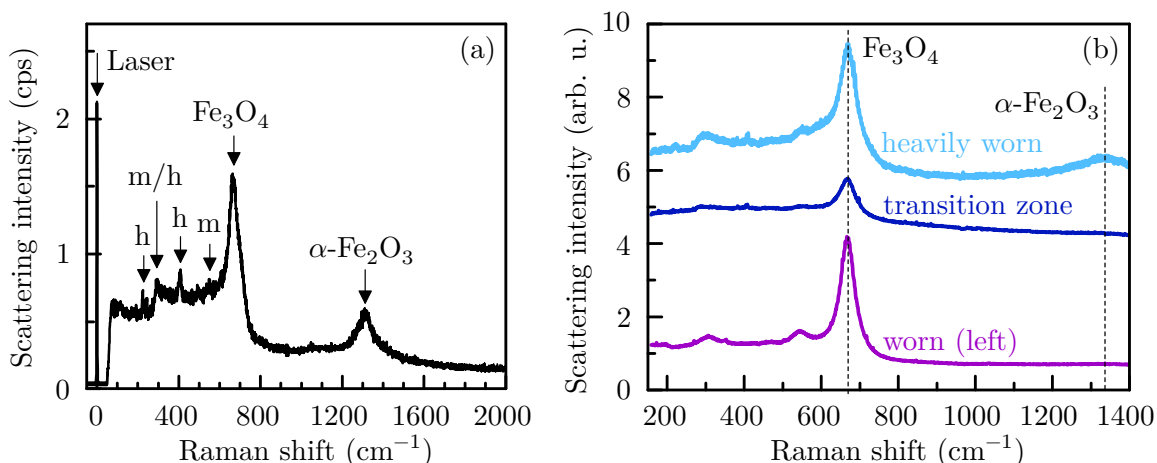


Figure 4.3 (a) Exemplary Raman spectrum at a heavily worn surface position on the female screw rotor, with magnetite (m) and hematite (h) signals marked by arrows, as well as their identifying features. (b) Integrated Raman spectra of the three different spatial domains light blue (heavily worn), dark blue (transition zone) and purple (worn). The colors correspond to the grid pattern shown in Figure 4.2 (d). The spatial distribution of the magnetite line at 668 cm^{-1} and the hematite line at 1310 cm^{-1} are presented in the mappings of Figures 4.4 and 4.5. Reproduced with permission from reference [Mol18].

image shallow strips and several dark domains of different dimension are visible. The dark domains are not detected for surfaces without a wear history. Therefore, one can assume that these domains are formed during the wearing process. The depth of these dark areas is estimated to vary between $5\text{ }\mu\text{m}$ and $20\text{ }\mu\text{m}$.

A second surface area is shown in Figure 4.2 (c). The laser spot and its interference rings are visible at the center of the image. Here, heavily worn domains are visible at the left and the right side of the image. A region of this surface area is investigated with confocal Raman scattering experiments. It is magnified in Figure 4.2 (d). The area investigated is marked with a grid pattern that contains three different domains with different degrees of wear. They are marked in purple (worn surface domain at the left), dark blue (transition zone in the center) and light blue (heavily worn domain in the right). Over all 80 Raman spectra are collected in a xy -matrix of 16×5 with a spacing of $2\text{ }\mu\text{m}$, resulting in a mapped surface area of $320\text{ }\mu\text{m}^2$. The accumulation time for each spectrum is 600 s. The mapping is recorded with confocal Raman spectroscopy (see Section 3.1.2) at room temperature with 532 nm excitation at laser powers well below 1 mW . The sample is carefully checked for degradation, which is not observed for this laser power. The beam is focused with an objective with a $50\times$ magnification onto the screw rotor surface, not exceeding a spot size of $2\text{ }\mu\text{m}$ (see Appendix A.3 for information on spot-size determination).

Assignment of the Raman Lines. An exemplary spectrum of a heavily worn surface position is shown in Figure 4.3 (a). Six Raman lines are observed, with shifts of approximately 230 cm^{-1} , 292 cm^{-1} , 405 cm^{-1} , 544 cm^{-1} , 668 cm^{-1} and 1310 cm^{-1} . The absolute spectral position is detected with an accuracy of $\pm 10\text{ cm}^{-1}$. The analysis focuses on the spatial distribution of the occurrence of the different lines, rather than on their line shifting and

broadening. The lines are assigned to magnetite (544 cm^{-1} and 668 cm^{-1}) and hematite (230 cm^{-1} , 405 cm^{-1} and 1310 cm^{-1}) [Far97; She03a]. The line shift at 292 cm^{-1} cannot be related to definitely stem from an iron-oxide mode, but the spectra in Figure 4.3 (b) suggest that this line is most probably due to a magnetite vibration.

Magnetite. Magnetite has a spinel structure² at room temperature and contains both Fe^{2+} and Fe^{3+} cations [She03a]. The Raman modes are attributed to belong to the T_{2g} mode (544 cm^{-1}) and the A_{1g} mode (668 cm^{-1}) (see also Section 2.1.2 for more details on irreducible representations and Section 2.3.1 for more properties of iron oxides). The T_{2g} mode is an asymmetric stretching of iron and oxygen, whereas the A_{1g} mode is a symmetric stretch of the oxygen atoms along the Fe–O bonds [She03b; Jub10]. It is also possible to assign the selected Raman lines to maghemite ($\gamma\text{-Fe}_2\text{O}_3$), which is the second most stable polymorph of iron oxide and also of the spinel structure [Gra10], but the maghemite lines have a doublet-like structure, being much broader than the lines of magnetite [Far97]. Therefore, as the lines detected here are quite narrow, a presence of maghemite at the worn surface area is ruled out. In the following the A_{1g} mode at about 668 cm^{-1} is taken as an indicator for the presence of magnetite.

Hematite. The hematite Raman lines resemble symmetric stretching of the iron and oxygen atoms (A_{1g} mode at 230 cm^{-1}) and symmetric bending of the iron and oxygen atoms (E_g mode at 405 cm^{-1}), while the line at 1310 cm^{-1} is due to two-magnon scattering [Far97; Mar77] or two-phonon scattering [Mas90] (see also Section 2.3.1). Independent of the origin of the mode, this scattering mode is not a feature of magnetite [Far97] and is used to mark the presence of hematite.

Integrated Spectra of Differently Worn Regions. Figure 4.3 (b) shows the integrated Raman spectra of the three differently worn regions. Therefore, the spectra of each of the different positions are assigned to one of the three regions (compare Figure 4.2 (d)). The average of all spectra of each region is taken as characteristic spectrum for the corresponding region. Comparing the different regions demonstrates that hematite is only present at heavily worn surface positions, whereas magnetite is detected for all surface domains. In the transition zone the intensity of the magnetite lines is substantially weaker than in the worn zones. Taking a more careful look at the T_{2g} line of magnetite reveals a shift in energy from 580 cm^{-1} at heavily worn positions to 572 cm^{-1} in the transition zone and down to 547 cm^{-1} at worn areas. The position of the 300 cm^{-1} line is also wear dependent. It behaves oppositional to the previously described line. It moves from 299 cm^{-1} at heavily worn positions to 307 cm^{-1} at worn positions. The shifting of the T_{2g} line to higher energies might be caused by compressive pressure, which leads to a reduction of the bond length and therefore to an increased interaction strength [She03c]. As signals from hematite are less probable in worn surface locations, it is proposed that the yet unassigned line at about 300 cm^{-1} belongs to magnetite [Mol18].

²Spinel is of the general structure of AB_2X_4 , where A and B are metal cations and X are mostly bivalent oxygen or sulfur anions. The oxidation state of the cations is of value 8.

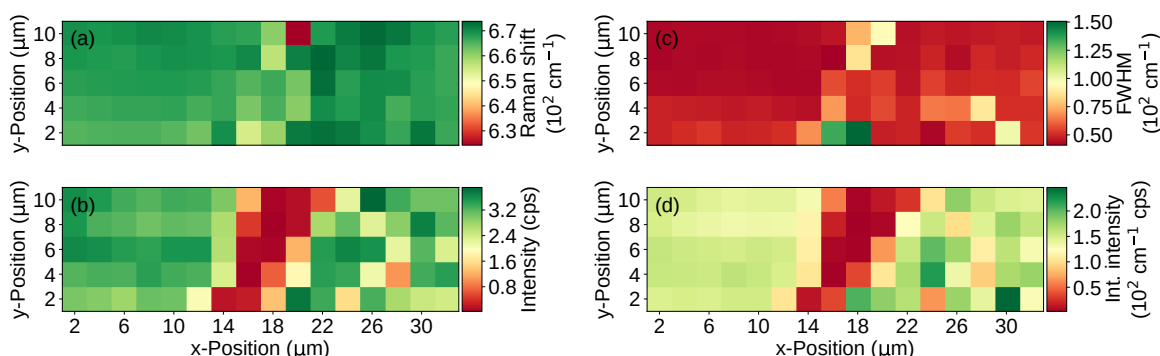


Figure 4.4 Mapping of the magnetite Raman mode at about 668 cm^{-1} across the region marked in Figure 4.2 (d). Here, results of a Lorentzian peak fitting of the magnetite mode are shown, namely (a) the energy shift, (b) the intensity, (c) the full width at half maximum and (d) the integrated intensity. Reproduced with permission from reference [Mol18].

Spatial Distribution of Magnetite and Hematite Signals. In order to get an impression of the distribution of magnetite and hematite among the selected surface region (compare Figure 4.2 (d)) the indicating magnetite (668 cm^{-1}) and hematite lines (1310 cm^{-1}) are used to create spatially resolved mappings. The properties of the magnetite line are shown in Figure 4.4. The Raman line does not considerably exceed shifts from its center position greater than $\pm 10\text{ cm}^{-1}$. Having a look at the intensity high variations are observed. At worn surface positions (left area between $2\text{ }\mu\text{m}$ to $14\text{ }\mu\text{m}$) the Raman intensity is homogeneously distributed. At the transition zone the line almost vanishes and at heavily worn surface locations the intensity fluctuates. Similar behavior can be detected for the the full width at half maximum (FWHM) of the line (see Figure 4.4 (c)) and the integrated intensity (see Figure 4.4 (d)).

The properties of the hematite line are shown in Figure 4.5. It is only detected at heavily worn surface locations, as already stated in the analysis of Figure 4.3. Furthermore each of the line parameters shows strong fluctuations. The line position ranges from 1300 cm^{-1} to 1400 cm^{-1} at some positions. The weak intensities and the large line width indicate a great distribution of different scattering processes and a small amount of hematite across the investigated surface area [Mol18].

The detection of hematite only at heavily-worn surface locations may result due to high temperatures at the female screw rotor during the dry-running operation of the rotors. To transform magnetite to hematite temperatures of $400\text{ }^\circ\text{C}$ are needed [Far97]. Due to the strong variations of the hematite signal parameters it is proposed that such high peak temperatures (flash temperatures³) were present and differed locally. Adding to the temperature input, mechanical deformation and high pressures in the GPa range⁴ may as well cause the formation of $\alpha\text{-Fe}_2\text{O}_3$ [Gil91].

The transition zone has a bright, reflecting character, which hints at a white-etching crack. White-etching cracks are microstructures appearing in polished and etched steel samples. These areas consist of ultra-fine carbide-free areas, that appear white under an

³See Section 2.2.3 for an introduction to the concept of flash temperatures.

⁴Typical Hertzian contact stresses of comparable rotors range from 1 GPa to 3.5 GPa [Utr19].

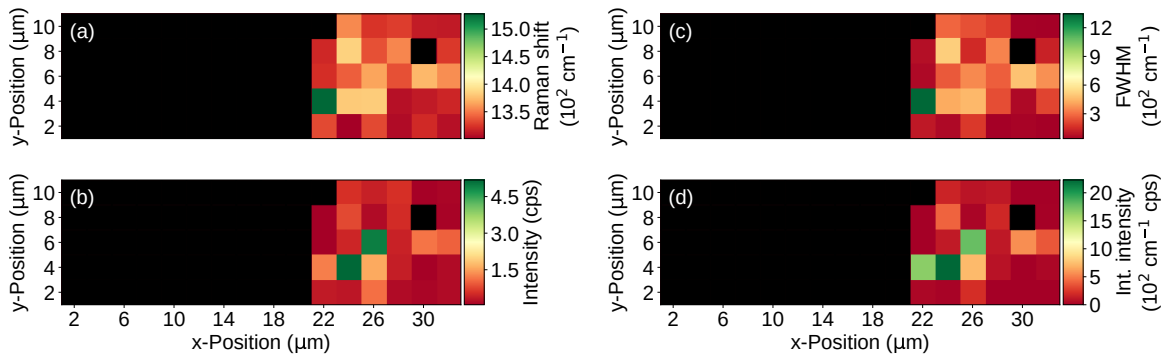


Figure 4.5 Mapping of the scattering mode of hematite at about 1330 cm^{-1} across the region marked in Figure 4.2 (d). Here, results of a Lorentzian peak fitting of the hematite mode are shown, namely (a) the energy shift, (b) the intensity, (c) the full width at half maximum and (d) the integrated intensity. Black colored squares indicate the absence of the mode of interest. Reproduced with permission from reference [Mol18].

optical microscope. More details are described in references [Sta15] and [Eval6]. In this white-etching crack transition zone, the formation of iron oxides seems less probable than in the other regions.

Summary and Conclusion. Summing up, this investigation delivers wear dependent Raman spectroscopic indicators on uncoated screw-rotor surfaces: Magnetite is detected at worn and heavily worn surface locations, whereas hematite is only detected at heavily worn surface locations. Here, a thermally activated transformation of magnetite to hematite is indicated, with temperatures exceeding 400 °C in the liquid-free wear process. Furthermore, strong fluctuations of the hematite Raman line mapped over a sufficient sample space might indicate heavy wear, while surface positions without heavy wear show a homogeneous distribution of the magnetite Raman line. This homogeneous distribution indicates also a homogeneous distribution of the respective bond lengths and strengths. Additionally, the shifting of the T_{2g} mode of magnetite to higher energies for increased wear, indicates a bond-length reduction and in increased interaction strength, which may be caused by compressive pressure.

In conclusion, the analysis of the spatial distribution of the iron oxides magnetite (worn surface locations) and hematite (heavily worn surface locations) on uncoated screw-rotor surfaces delivers a first correlation of Raman scattering signatures with tribological surfaces, supplying an indicator for the degree of wear of the respective surface locations.

4.2 Oxygen Incorporation in Tungsten Carbide

In this section investigations on oxygen incorporation in tungsten carbide/carbide (WC/C) coated screw-rotor surfaces are presented (see Figure 4.6 (a)). The section is based on the publication of Debus et al. [Deb16], with the main findings being replicated in order to generate a deeper spectroscopic understanding of tribological material.

Experimental Details. Here, 16MnCr5 steel (1.7131) rotors are coated with $4\ \mu\text{m}$ of WC/C and run for about 200 h under dry conditions in ambient air (see also [Deb16; Däm98]). Subsequent to the dry-running, multiple surface locations are studied optically, using Raman spectroscopy. The selected locations are excited with 532 nm laser radiation and the scattered light is collected as described in Section 3.1.2. Here a microscope objective with $50\times$ magnification is used. The penetration depth of the laser light into the WC/C coating is estimated to several 10 nm, by using extinction coefficients of 1 to 3 for 600 nm excited WC/C films for calculating the penetration depth as presented in Section 2.1.6 [Aba09]. Additionally, an uncoated reference sample of 90MnCrV8 steel (1.2842) is investigated.

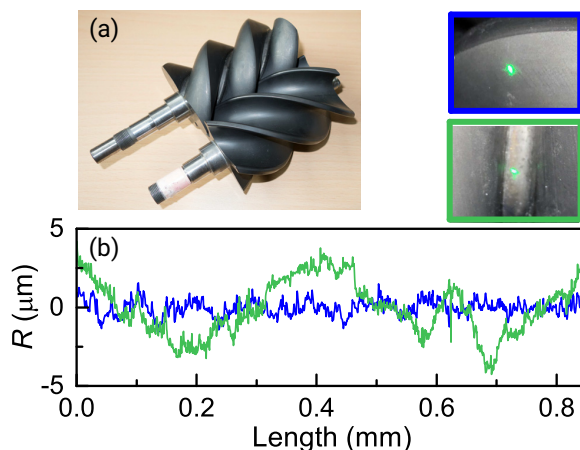


Figure 4.6 (a) Image of the investigated screw-rotor pair. (b) Roughness profiles of the untouched (blue) and worn (green) locations, with images of the corresponding surface locations shown above. Image taken from reference [Deb16].

Surface Roughness of Worn and Unworn Surface Locations. The roughness of an untouched surface location at the male rotor flank and the roughness of a worn surface location at the contact area are compared in Figure 4.6 (b). The roughness R is determined using focus stacking of images collected with a confocal white-light microscope (NanoFocus μsurf) and provided a height variation of $\pm 1.5\ \mu\text{m}$ ($\pm 4\ \mu\text{m}$) for the untouched (worn) surface (see also Appendix A.2). It is observed that the height variation for the worn surface is about twice as large as for the untouched surface.

Raman Spectra of Differently Worn Surface Locations. Raman spectra of the different surface conditions are collected. Exemplary spectra are shown in Figure 4.7. The lines observed are categorized by the frequency of the respective scattering regime. The regimes are low-frequency scattering (ranging from $0\ \text{cm}^{-1}$ to $200\ \text{cm}^{-1}$), mid-frequency scattering (ranging from $200\ \text{cm}^{-1}$ to $400\ \text{cm}^{-1}$) and high-frequency scattering (ranging from $400\ \text{cm}^{-1}$ to $1000\ \text{cm}^{-1}$). The Raman lines at $1360\ \text{cm}^{-1}$ (D-peak) and $1580\ \text{cm}^{-1}$ (G-peak) stem from sp^2 hybridized carbon bonds, where the D-peak arises due to a carbon ring breathing mode, while the G-peak arises due to bond stretching of all pairs of sp^2 carbon atoms [Fer00] (see also Section 2.3.2). As these lines are present due to the graphite content in the tungsten carbide coating, they are not examined any further.

Firstly, the low-frequency scattering regime is discussed. Here several Raman lines are detected, namely lines at 95 cm^{-1} , 130 cm^{-1} , 145 cm^{-1} and 150 cm^{-1} . Except for the 145 cm^{-1} line they are detected at untouched and at worn surface locations. As shown in Figure 4.7 (b), the 145 cm^{-1} mode is detected for heavily worn (black line) conditions only and not for uncoated (red line) conditions. These low-frequency Raman modes are proposed to be lattice modes [Ing05].

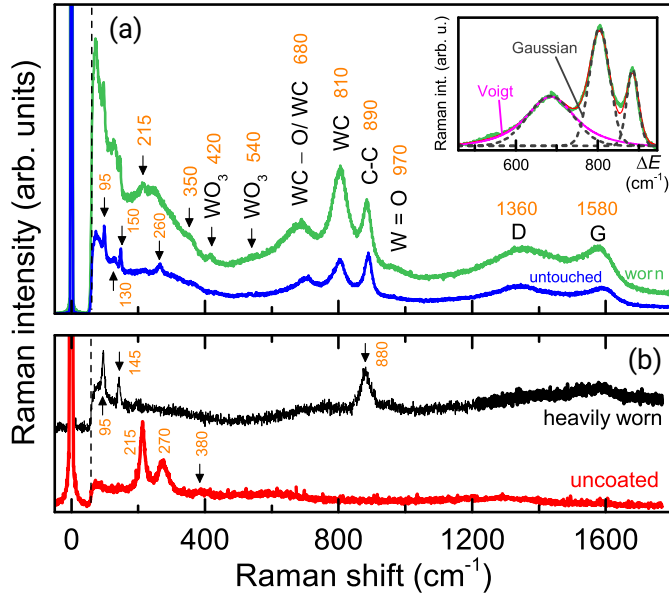


Figure 4.7 (a) Raman spectra of worn (green) and untouched (blue) surface locations, with an inset showing a fitting curve of the WC-O/WC, WC and C-C Raman modes (dashed) and their cumulative fit (red). (b) Raman spectra of an uncoated reference sample (red) and a heavily worn (black) location at the male screw-rotor surface. Image taken from reference [Deb16].

420 cm^{-1} [Ros07] and 540 cm^{-1} [Das16] are assigned to modes of tungsten trioxide⁶. Incipient oxidation influences the WC line at about 680 cm^{-1} [Mra09; Das13], whereas the WC stretching line at 810 cm^{-1} remains uninfluenced by oxygen [Das13]. The Raman line at about 880 cm^{-1} , is attributed to the C-C stretching mode [Soc01]. Detecting this mode only at heavily worn surface locations leads to the assumption of a strong chemisorption of carbon to the metallic substrate [Deb16]. The Raman line at 970 cm^{-1} results from symmetric stretching of terminal W=O bonds [Kuz98]. Comparing the untouched Raman line of 700 cm^{-1} to the shifted worn line at 680 cm^{-1} a line shift and a line broadening of about 30% are observed. Both observations indicate a weakening of the bonding strength, either due to distortions of the bonding, or due to the incorporation of oxygen during the wearing process.

Most remarkable of these findings is the presence of tungsten trioxide Raman modes

Secondly, the mid-frequency scattering regime is discussed. Here Raman modes at 215 cm^{-1} , 260 cm^{-1} and 350 cm^{-1} are detected. The observed modes are also noted at the uncoated reference sample and are therefore assigned to chromium- and/or vanadium-oxygen vibrations, as diffusion of, in particular, Cr atoms to the surface might occur⁵. The absence of the lines at heavily worn surface areas may be explained by a considerable distortion of the bonds, which leads to a strong line broadening or to weak atomic adhesion to the surface [Deb16].

Thirdly, the high-frequency scattering regime is discussed. Here, Raman shifts of 680 cm^{-1} , 810 cm^{-1} and about 880 cm^{-1} are observed for both surface locations. Additionally, at worn surface locations, lines at 420 cm^{-1} , 540 cm^{-1} and 970 cm^{-1} become observable. The lines at

⁵At elevated temperatures of $600\text{ }^{\circ}\text{C}$ and higher Bowen and Brown showed a diffusion of chromium [Bow70; Bra85]. Furthermore, protecting cover layers might form at the surface [Bob13a].

⁶Additional spectroscopic information on WO_3 thin films is published by Diaz-Reyes et al. [Dia08].

at worn surface locations. The incorporated oxygen seems to be an indicator of wear on tungsten carbide coatings. Furthermore, the oxygen-related Raman modes are modeled significantly better by Voigt profiles, whereas the WC and C–C Raman lines show a Gaussian behavior (compare inset in Figure 4.7 (a), see also Section 2.1.4). Here, the 680 cm⁻¹ line shows a Lorentzian portion of about 20 %, hinting at the amorphous character of the tribological material (see Section 2.1.5).

Summary and Conclusion. Summing up, indicators for tribological material on tungsten-carbide coated screw-rotors are detected using Raman scattering signatures. First of all, the worn surfaces show WO₃ and W=O signatures. Furthermore, the tungsten carbide stretching mode is broadened due to oxygen incorporation and shifted to lower frequencies. These findings might be used to characterize the degree of wear in surfaces coated in a similar manner.

4.3 Tribofilm Formation of Sputtered MoS_x Thin Films

In this section the tribofilm formation and the frictional behavior of sputtered MoS_x films⁷ in different atmospheres are investigated. Therefore, the MoS_x coating is deposited on sample discs and ball-on-disc tests are conducted in ambient air, argon and nitrogen atmospheres. Here, the generation of third-body particles is observed and their properties are studied with Raman spectroscopy. It is revealed that these particles differ in their chemical behavior compared to the as-deposited film and the wear track. The results are published in reference [Til19c].

Details on Film Deposition. The MoS_x films are deposited on polished 16MnCr5 steel (1.7131) with an arithmetical mean deviation of Ra = (3.1 ± 0.6) nm using the **HiPIMS** technique, described in Section 3.2.1. The cathode power is set to 3 kW, with a pulse frequency of 1 kHz, a pulse duration of 200 μs, a bias voltage of -100 V and a heating power of 1 kW (see also [Til19c]).

Details on Film Characterization. The as-deposited and the worn MoS_x films are characterized by several methods. Their topography is analyzed by means of **SEM** (see Section 3.2.3) and their crystallographic orientation is studied by **XRD** (λ_{Cr-Kα} = 2.2911 Å, see Section 3.2.4). Additionally to these investigations, the stoichiometric composition (**EDS**), the film thickness (**SEM**), the hardness and the elastic modulus (nanoindenter) of the as-deposited films are determined as well (see Sections 3.2.2 and 3.2.4).

In order to generate a spectroscopic understanding of the wear of MoS_x coatings, Raman scattering is recorded with the setup described in Section 3.1.2. Here, it is important to note that the Raman scattering experiments are conducted under resonant conditions with 633 nm laser excitation (see Section 2.1.7). The radiation is focused with a microscope objective with 20× magnification to a spot diameter of approximately 2 μm. The collected light is diffracted by a 900 grooves/mm holographic grating.

⁷The subscripted *x* indicates that the stoichiometric composition of the sputtered coatings cannot be predicted prior to the deposition process. After the deposition, the composition may be determined using EDS (see Section 3.2.4).

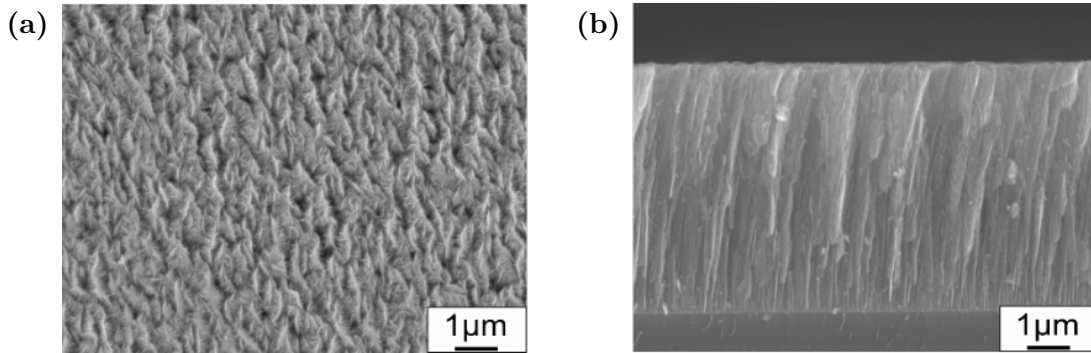


Figure 4.8 (a) Surface (topography) and (b) cross-section (morphology) of a typical as-deposited MoS_x film. Reproduced from reference [Til19c].

The coefficient of friction is determined at room temperature. Here, a tribometer with a 100Cr6 counterpart is used and the number of rotations is set to 5000. The coefficient is measured in ambient air, argon and nitrogen atmosphere (see Section 3.2.2). The gas flow rate is set to 10 bar/s. In each of the three atmospheres the contact (surface) pressure of the ball-on-disc tribometer is varied (1.3 N/mm^2 , 6.4 N/mm^2 , 12.7 N/mm^2) at a constant sliding velocity (40 cm/s). Furthermore, a sliding velocity variation (10 cm/s, 20 cm/s, 40 cm/s) is conducted at a constant surface pressure (6.4 N/mm^2).

The specific wear rate is evaluated with a profilometer (see Section 3.2.2).

The As-Deposited Film. Before spectroscopic methods are applied to the MoS_x films, their structure and stoichiometric composition is determined. The coatings show a columnar cross-section (morphology) and the topography features a granular, needle-like structure (compare Figure 4.8). The samples are composed of 1.65 ± 0.02 sulfur atoms per molybdenum atom. Furthermore, a hardness of $(0.73 \pm 0.06) \text{ GPa}$ and an elastic modulus of $(52.70 \pm 4.20) \text{ GPa}$ are determined.

The initial state of the MoS_x coatings is also determined by XRD (see Figure 4.9 (a)) and Raman spectroscopy (see Figure 4.9 (b)). Figure 4.9 (a) shows a XRD spectrum with typical reflexes of hexagonal MoS₂, namely its (002), (100) and (110) reflexes (marked with circles). The 2θ reflexes in the range from 60° to 80° are attributed to the 16MnCr5 steel substrate. The intensity ratio of the (100) and the (002) reflex indicates a randomized film orientation [Fle87]. It is proposed that the applied bias voltage enhances the formation of the (100) plane. The process may be explained by means of chemical reactivity. The chemical reactivity of the (100) edge plane is higher compared to the inert (002) basal plane [Chi85]. Therefore, the adsorption of the (100) surface is higher, which results in a preferred formation of the (100) plane. As also the (002) reflex is detectable, both planes grow at the same time in a competitive process.

Furthermore, the stoichiometric composition of the films indicates a re-sputtering of the sulfur atoms, leading to a reduced S/Mo ratio compared to MoS₂. This re-sputtering of the sulfur atoms is caused by the applied bias-voltage, which accelerates the evaporated sulfur and molybdenum atoms. Here, the kinetic energy of a sputtered molybdenum atom is higher than the kinetic energy of a sulfur atom, due to the lower atomic mass of sulfur (32 u) compared to molybdenum (96 u). This surplus of kinetic energy of a target-approaching

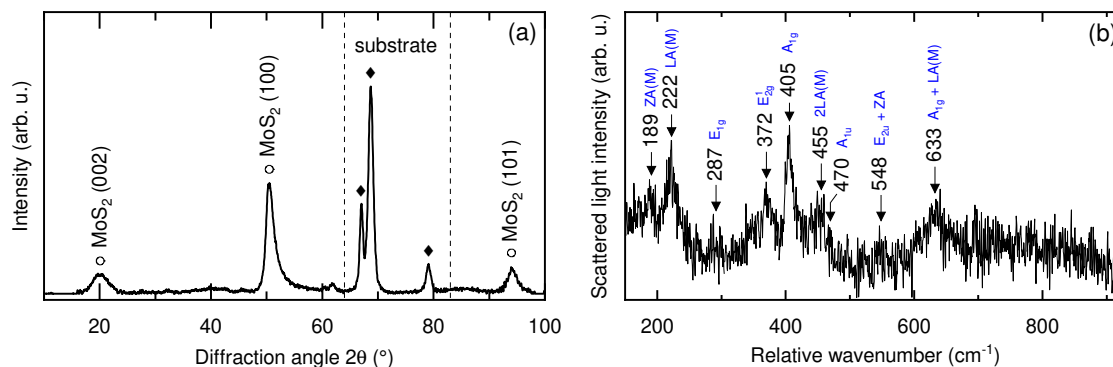


Figure 4.9 (a) Cr-K α excited XRD pattern of the as-deposited MoS_x coating. The dashed lines confine the 2θ region of the substrate. (b) Raman spectrum of an as-deposited MoS_x film. The modes are indicated with arrows and annotated with the corresponding wavenumber and assigned stretching mode. Reproduced from reference [Til19c].

molybdenum atom can unhinge an already condensed atom, favorably sulfur, as less energy is needed to release it from the surface.

A typical Raman spectrum of the as-deposited MoS_x films is shown in Figure 4.9 (b). The laser power is set to 0.18 mW. The spectrum is averaged over 36 spectra with an accumulation time of 300 s for each single spectrum. The spectrum shows several Raman lines (see Table 4.1), which are typical modes of MoS₂ [Kha15; Pla15; Fre99; Sta85]. In the figure the modes are indicated by arrows. They are annotated with their wavenumber ν_N and the irreducible representations of the D_{6h} point group, which MoS₂ belongs to (see Section 2.1.2 for details on point groups and Section 2.3.3 for more properties of MoS₂). All of the detected modes are attributed to MoS₂ and no other material signatures⁸ are detected.

The Coefficient of Friction in Different Atmospheres. In order to get an improved understanding of the MoS_x tribofilm formation, the coatings' coefficients of friction are investigated in different atmospheres. The tests are conducted at different surface pressures and sliding velocities. The results are shown in Figure 4.10. In both test series the coefficients of friction in air are generally higher than the coefficients of friction in argon or nitrogen atmosphere. In detail, at high surface pressures and sliding velocities the coefficients of friction in an argon atmosphere are lower than the coefficients of friction in a nitrogen atmosphere.

The general trend of the frictional values is similar for all three atmospheres. Whereas an increase in surface pressure significantly decreases the coeffi-

Table 4.1 Measured Raman modes ν_N with their assigned phonon modes [Kha15; Pla15; Fre99; Sta85].

ν_N/cm^{-1}	Mode
189	ZA(M)
222	LA(M)
287	E _{1g}
372	E _{2g}
405	A _{1g}
455	2LA(M)
470	A _{1u}
548	E _{2u} + ZA
633	A _{1g} + LA(M)

⁸MoO₃ is a typically expected additional material, as it is easily oxidized from MoS₂.

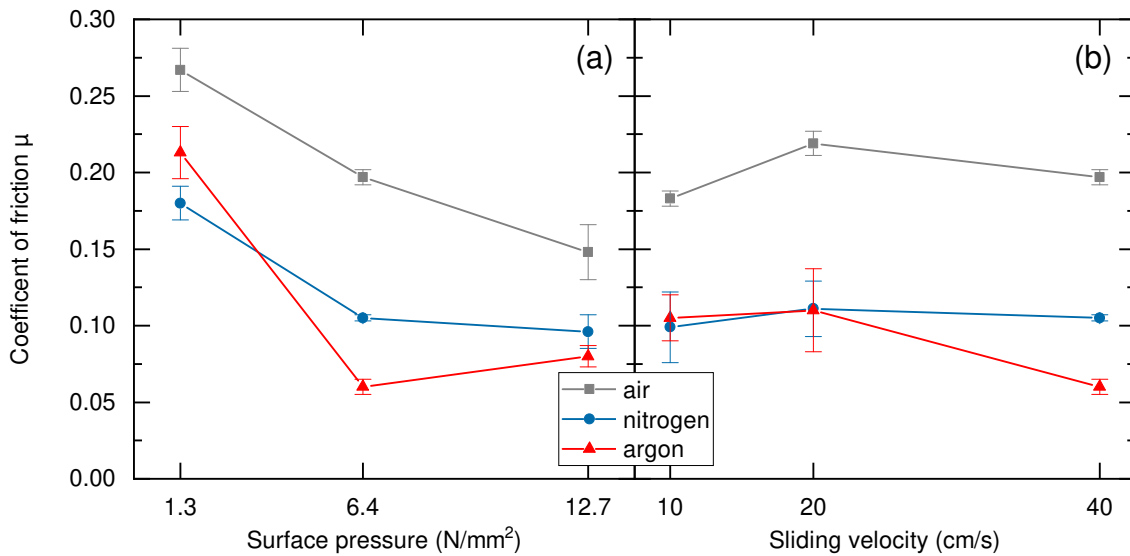


Figure 4.10 Dependence of the coefficient of friction of MoS_x coatings (a) on the surface pressure of the ball onto the disc and (b) on the sliding velocity of the ball on the disc in air, argon and nitrogen. Reproduced from reference [Til19c].

coefficients of friction, a change in sliding velocity has only a weak impact on the coefficients. A possible explanation for the lower coefficient of friction in nitrogen compared to air is developed later by crystallographic orientation measurements.

Summing up, the surrounding atmosphere has a great impact on the frictional behavior of MoS_x coatings. The main difference between ambient air and argon or nitrogen atmospheres is the presence of water vapor in air. This influence of water on MoS_x coatings is discussed in the next paragraph.

The Influence of Water and Temperature on MoS_x Coatings. It was shown that water is favorably adsorbed by the (100) crystallite edges of MoS_2 , leading to increased friction [Zha01]. This adsorption process is enhanced by the columnar structure of the crystallites. Here, the spacing between the crystallites is approximately 100 Å [Vie13], which allows moisture to easily penetrate the coatings [Zha01], resulting in higher friction.

A detailed analysis of the impact of humidity on MoS_x coatings was performed by Matsumoto et al. [Mat99]. They tested three different types of sputtered MoS_2 films in a nitrogen/oxygen atmosphere, where the oxygen content was varied, in pure nitrogen and in air, varying the relative humidity, and in vacuum. At oxygen concentrations exceeding 0.1 % the lifetime decreased with rising oxygen concentration. For humidity, the films tested in air started to degrade at relative humidities exceeding 20 %. For nitrogen-tested films already a few percent of relative humidity caused degradation of the coatings. Matsumoto et al. determined that the humidity was of greater impact on the tribological characteristics than the impact of oxygen. The importance of the surrounding atmosphere was also shown by Colas et al. [Col15].

Apart from the humidity and the surrounding atmosphere, the friction is also influenced by the temperature in the contact area [Czi15e]. The temperature in the contact area is

affected by the sliding velocity and the surface pressure. Here, increasing the test parameters results in a higher temperature in the contact. This rise in temperature causes desorption of the adsorbed water [Col10], which should lead to a decrease in friction at high surface pressures or high sliding velocities. This decrease is observed for high surface pressures (see Figure 4.10 (a)). For high sliding velocities, no or little decrease of friction is observed (see Figure 4.10 (b)).

The increased temperatures may also stimulate an oxidation process [Kha13]. Analyzing the recorded data, the coefficient of friction does not increase with sliding velocity or surface pressure, meaning that the temperatures reached⁹ are too low to start an oxidation process. Therefore no MoO₃ is generated, or at least the oxidation rate of the MoS_x film is not comparable to the rate of removal of the film [Kha13]. This assumption is confirmed using Raman spectroscopy. Figure 4.11 (a) shows Raman spectra recorded at the wear tracks of the worn MoS_x coatings (each spectrum is the average of six spectra with 300 s accumulation time each). The figure shows spectra of coatings tested in air, argon and nitrogen atmosphere at a surface pressure of 1.3 N/mm². The recorded spectra are comparable to the as-deposited MoS_x films (see Figure 4.9 (b)). As here no MoO₃ related Raman signals are detected, the assumption of an inexistent MoO₃ generation is proven. Nevertheless, a generation of MoO₃ is possible. By using high laser powers of 5.7 mW at worn MoS_x locations Raman signals of MoO₃ can be generated, as shown in Figure 4.11 (b). Here, the observed modes at 290 cm⁻¹ and 820 cm⁻¹ can be related to MoO₃ [Seg95]. The spectrum for regular power is the average of six spectra with 300 s accumulation each, while the elevated laser power spectrum is the average of three spectra with 300 s each.

To sum up, atmospheric humidity penetrates the columnar coatings and is adsorbed, leading to higher coefficients of friction. Opposed to the adsorption, desorption of the water molecules takes place at higher surface pressures, leading to a decrease of the coefficient of friction. A generation of MoO₃ is not detected.

As a remark it should be noted that not only water and oxygen define the frictional behavior of the coatings, as the frictional behavior in water-free argon and nitrogen atmospheres shows a comparable behavior (see Figure 4.10).

Oxidation Resistance and Raman Scattering Intensity of Wear Debris. During the Raman measurements it is observed that wear debris accumulated in and around the wear tracks. In order to generate a deeper understanding of the wear processes of MoS_x films, this debris are measured as well and are analyzed in the following. The collected Raman spectra (each spectrum is the average of 36 spectra with an accumulation time of 300 s) of the wear debris at different surface pressures and atmospheres are shown in Figure 4.11 (c). All spectra are from samples with a constant sliding velocity of 40 cm/s.

Remarkable is the enhancement of the overall intensity of MoS_x films tested in air, compared to coatings tested in argon or nitrogen. The underlying mechanism is not yet understood and needs further investigations. Generally, the collected Raman frequencies are in good match with the previously obtained Raman signatures of the as-deposited film (see Table 4.1 and Figure 4.9 (b)) and no molybdenum oxides are detected. At higher wavenum-

⁹Even the flash temperatures present in the wear process do not exceed the temperatures needed for oxidation (see Section 2.2.3 for details on flash temperatures and Section 2.3.3 for details on MoS₂ and its properties).

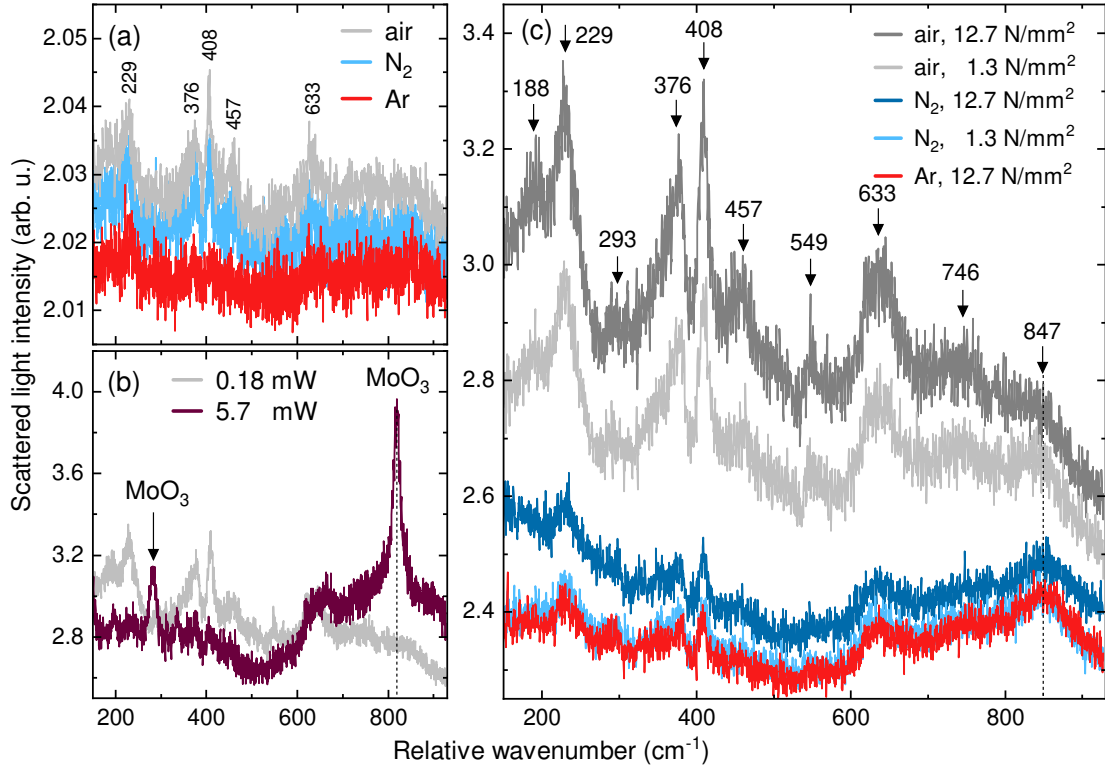


Figure 4.11 (a) Raman spectra of worn MoS_x films in different atmospheres, at a surface pressure of 1.3 N/mm^2 . (b) Raman spectra of worn MoS_x films, excited with two different laser powers. (c) Raman spectra of wear debris of the worn MoS_x films, at a sliding velocity of 40 cm/s . Reproduced from reference [Til19c].

bers, three Raman bands emerge, namely at 630 cm^{-1} , 750 cm^{-1} and 845 cm^{-1} . The first band was already attributed to a $A_{1g} + \text{LA}(M)$ mode [Fre99]. The second band may be attributed to second-order phonon scattering [Che74], while the last band may stem from Mo–N or Mo–C vibrations [Qiu16].

Furthermore, it is observed that the wear debris are more resistant to oxidation than the as-deposited film. All recorded spectra in Figure 4.11 (c) are recorded at high laser powers of 5.7 mW and no MoO_3 is generated, which is in contrast to the previously observed laser-induced MoO_3 generation in the as-deposited films. Therefore, it is assumed, that oxidation does not occur in this wear process.

In order to evaluate this effect, the particle sizes of the wear debris are taken into account. The particle sizes of the wear debris in nitrogen and air could be estimated from optical images taken during the Raman measurements. The debris particles are of several micrometers in size. These particle sizes limit the chemical reactivity and reduce the rate of oxidation, as Sliney and Lavik showed for micrometer sized MoS_2 particles [Sli63; Lav68]. In addition, the particle size might change the light scattering probability and reduce the absorption of light [Yad14; Chi02]. This possible reduction of light absorption may lead to less heat placed into the particles, resulting in seemingly more (oxidation) resistant particles.

Condensed, the oxidation resistance of the wear debris and the enhanced Raman scatter-

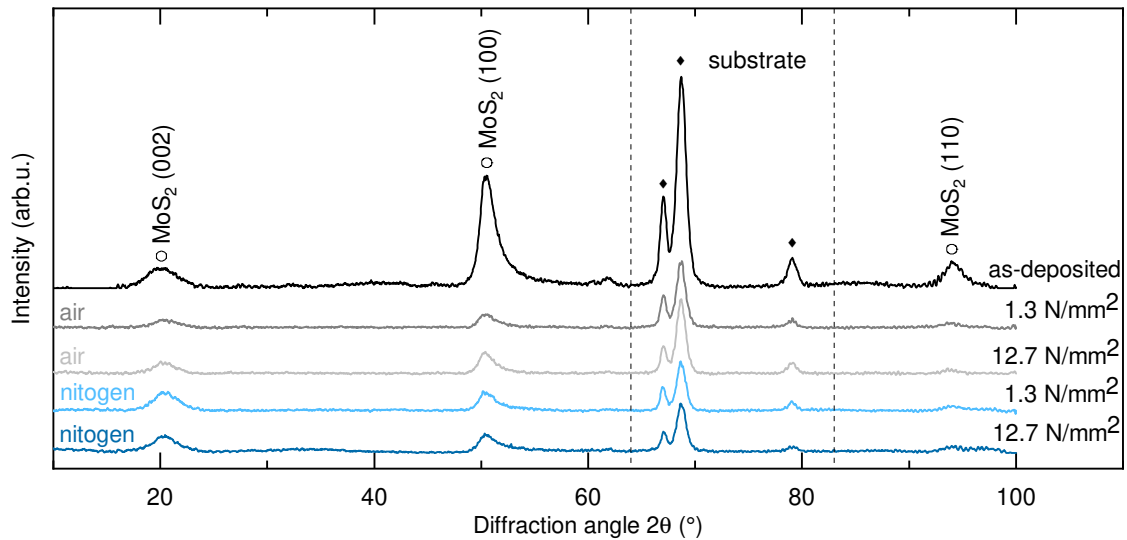


Figure 4.12 Cr- $K\alpha$ excited XRD spectra of as-deposited and worn MoS_x films, in air and nitrogen. The region included inside the dashed lines indicates the 2θ region of the substrate. Reproduced from reference [Til19c].

ing intensity might be two characteristic features of MoS_x tribofilms. Furthermore, both effects explain the absence of laser- or temperature-induced surface oxidation [Til19c].

The Crystallographic Orientation of the Worn Surface. In order to study the crystallographic orientation of the worn surfaces and compare them to the initial state of the surfaces, XRD spectra of the wear tracks of the air and nitrogen worn specimen are recorded. The recorded spectra are shown in Figure 4.12. In the figure the (100), (002) and (110) reflexes of MoS_2 are indicated by circles. First, a decrease of the (100) reflex is detected by comparing the spectra of the worn films with the spectrum of the as-deposited film. This decrease is independent of the atmosphere the tribological testing took place in. Second, the (002) reflex is more distinct after tests conducted in nitrogen than after tests in air. At last, the (110) reflex almost vanishes at the worn surfaces, again independent of the surrounding testing atmosphere. Changes in surface pressure do not significantly modify the reflexes' intensities.

The observed intensity changes indicate a crystallographic reorientation of the MoS_x films. Comparable crystallographic changes were reported by Fleischauer and Zhang et al. [Fle84; Zha04]. Furthermore, the intensity comparison of the (002) reflexes of nitrogen- and air-worn samples provides an explanation for the lower coefficient of friction in nitrogen (as reported before, see Figure 4.10). For the explanation it is important to note that the lubricating properties of MoS_2 are ascribed to the (002) basal orientation [Fle87]. As here, for nitrogen-worn samples, the (002) intensity is higher, the MoS_x crystallites are preferably (002) oriented. Therefore, taking Fleischauer into account, the nitrogen-worn samples show a lower coefficient of friction, compared to air-worn samples.

Summing up, crystallographic reorientation of the worn MoS_x coatings is observed. Here, the comparison of the (002) reflexes of air- and nitrogen-worn coatings indicates a stronger

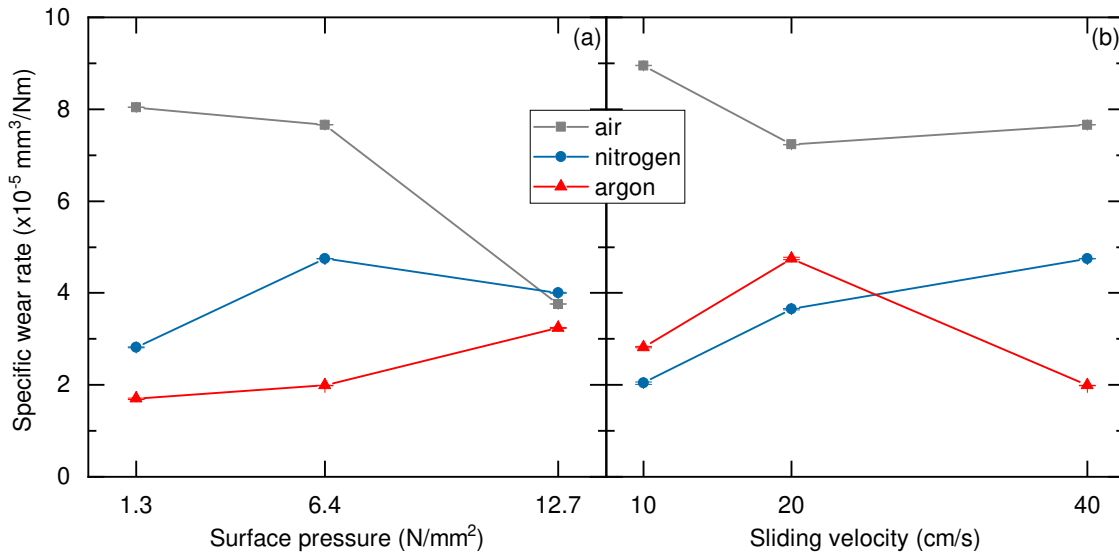


Figure 4.13 Specific wear rate dependence of MoS_x coatings on (a) surface pressure and (b) sliding velocity in air, argon and nitrogen. Reproduced from reference [Til19c].

basal orientation in nitrogen atmosphere. This preferred (002) orientation might explain the lower coefficient of friction in nitrogen compared to air.

The Distribution of Wear Debris. The distribution of wear debris along the wear track has a great impact on the friction of the sliding process, as Singer et al. reported [Sin03]. They state that the two-body sliding processes of friction and wear are instead three-body processes, as small wear particles form in the contact. These particles detach from one of the sliding surfaces and are transferred to the other surface, circulating between the two surfaces. During this circulation the particles agglomerate and become visible as debris particles, which are responsible for the frictional behavior of the two sliding interfaces.

This process is taken into account, investigating the MoS_x coatings, as the coatings show a low hardness and material can easily be detached under shear stress, leading to a high probability to form wear debris. To demonstrate this formation of wear particles, the wear rates are shown in Figure 4.13 (see Section 3.2.2 for details on specific wear rates). The highest removal of material is detected for MoS_x films tested in air, for both surface pressure and sliding velocity. Furthermore, the trends of the wear rates are contrary to each other, comparing air to argon or nitrogen. While the wear rate tends to decrease in air, it increases in argon and nitrogen. Again, similar to the coefficient of friction, the surface pressure has a greater impact on the tribological properties, than the sliding velocity.

The increased debris formation is also visible through the optical microscope of the Raman microscope system. Here, air- and nitrogen-worn MoS_x films contain the highest amounts of wear debris, whereas argon-worn films show smaller debris concentrations. This is also confirmed by SEM images, where additional local EDS spectra are taken of the specimen (images and spectra not shown here). All images show grooves along the sliding direction, with flattened roughness asperities. At low surface pressures of 1.3 N/mm^2 the MoS_x films cover the entire contact area for argon and nitrogen, whereas the film material is completely

removed in air-worn surfaces. Increasing the surface pressure leads to a film removal at local spots in nitrogen environments, exposing some substrate material. For higher surface pressures in argon atmospheres the film stays intact. In air-worn surfaces the higher surface pressures lead to a reduced wear rate, so that the MoS_x film is only partially removed. For all surfaces wear particles agglomerate at the edge of the wear track.

The complete removal of the MoS_x coating in air-worn samples at low surface pressures explains the large coefficients of friction reported before. Nevertheless, the coefficient of friction is lower than it would be for a steel-steel contact. This fact suggests that wear particles lubricate the two interacting surfaces, and some of the MoS_x particles should be transferred to the surface of the counterpart, as described by Singer et al. This transfer of MoS_x from the coated specimen to the testing ball is detected by analyzing the ball's surface with EDS (images not shown here). Furthermore, Singer et al. described that 2/3 of the deposited coating is removed during the run-in phase of the tribological process, leading to a reduction of the thickness of the lubricating layer [Sin96]. This run-in removal of the film leads to the assumption that the upper part of the coating is removed and contributes to the formation of the wear particles. Furthermore, this removal reduces the effective thickness of the lubricant, which should be kept in mind when designing applications with lubricating MoS_x coatings. At higher surface pressures and sliding velocities in air the MoS_x coating is only removed locally, leading to lower wear rates and coefficients of friction.

In contrast to the air-worn specimen, for argon- and nitrogen-worn specimen, well distributed MoS_x films are detected at low surface pressures, leading to low wear rates and low friction. With increasing the surface pressure, the fluidity of the MoS_x film is increased [Men18] as well as the temperature in the contact area. This elevated temperature reduces the energy needed to break bonds, leading to more easily formed wear particles [Col10]. These generated particles form the tribofilm. The enhanced creation of the particles does not necessarily lead to high wear rates, as long as the particles remain in the contact area. As soon as the particles are ejected from the contact area the wear rates increase due to newly formed particles. Here, for nitrogen-worn surfaces, generated wear particles remain temporarily in the contact area, leading to only local exposure of the substrate material. Due to this temporary remain, the wear rate is slightly increased in comparison to argon-worn surfaces, where the particles seem to remain longer in the contact area.

Recapitulated, the detected wear debris plays an important role in the sliding process and lubricates the two sliding interfaces. The longer the particles remain in the contact area, the lower the wear rate and the coefficient of friction.

Summary and Conclusion. In the present section the influence of surface pressure and sliding velocity on the tribofilm formation of MoS_x coatings is studied. A special focus is drawn to the influence of different surrounding atmospheres and the generated third-body particles. It is shown that the surrounding atmosphere has a great impact on the tribological processes. The coefficient of friction and the wear rate in air are higher than in argon or nitrogen environments. These differences are explained by several effects. Firstly, the atmospheric humidity of air penetrates the coatings, is absorbed and therefore leads to higher coefficients of friction. Secondly, a crystallographic reorientation takes place, with preferred (002) basal orientation in nitrogen leading to a lower coefficient of friction than in

air. As a third effect, the formation of the wear particles is identified as important process. It is observed that the trends of the coefficient of friction and the wear rate are similar for all test environments. With an increased surface pressure, more third-body particles are generated that lubricate the interfaces, thus leading to a reduced coefficient of wear and wear rates in air. For argon and nitrogen, the particles are distributed all over the contact area. Here, the wear rates are increased by higher surface pressures, as bond breaking becomes more easy. Furthermore, the debris particles are of several micrometers in size and accumulate in and around the wear tracks on the coated sample as well as on the ball.

Adding to these tribological properties, Raman scattering reveals a different chemical behavior of these particles. The debris particles show an increased oxidation resistance and the overall Raman scattering probability is enlarged. These two phenomena may be characteristic properties of MoS_x tribofilms.

Chapter 5

Microstructural Properties and Interatomic Interactions

This chapter presents several studies on the microstructural properties and interatomic interactions of carbon and MoS_x based coatings revealed by Raman scattering processes. In the first section the influence of the deposition parameters Cathode Power (**CP**), Bias Voltage (**BV**) and Mid-Frequency (**MF**) on the properties of amorphous carbon coatings is presented. Using multi-wavelength Raman scattering, the sp^3 content of the coatings is determined to range from 12 % to 18 %. Here, high values of CP and BV seem to reduce sp^3 formation. The second section is based on the influence of the deposition parameters on the properties of MoS_x coatings. Here, influences on the stoichiometry and the mechanical properties are identified. Furthermore, a reorientation process that reduces friction is detected. The third section of this chapter investigates post-growth annealed MoS_x coatings, which show a more shear resistant behavior for high-temperature annealed coatings. Furthermore, the coefficient of friction of these coatings is linearly dependent of the sulfur/molybdenum ratio.

5.1 Effects of the Deposition Parameters on the Properties of Amorphous Carbon Films

In this section the cause-effect relation of multiple magnetron sputtering parameters on the properties of the amorphous carbon (**a-C**) films is studied. The parameters are varied, using a Central Composite Design utilizing the Design of Experiments¹. Subsequent to film deposition, the chemical bonding state of the coatings is characterized using Raman spectroscopy in the visible (532 nm) and ultraviolet (266 nm) wavelength range (see Section 3.1), revealing sp^3 contents ranging from 12 % to 18 % for most of the coatings. Comparable sp^3 contents are detected with complementary X-ray Photoelectron Spectroscopy (**XPS**) measurements using synchrotron radiation (see Section 3.2.4). For high cathode powers and bias voltages a suppression of the sp^3 formation is observed. Furthermore, nanoindentation tests give access to the hardness and the elastic modulus of the films (see Section 3.2.2). The results are published in reference [Til19a].

Details on Film Deposition. The a-C films are deposited by magnetron sputtering as described in Section 3.2.1. Here, (100) oriented, p-doped Si-wafers are used as substrate

¹The Design of Experiments is a method to plan a set of experiments. It helps to find the minimal set of experiments that need to be conducted in order to describe and explain a variation of information under conditions that are hypothesized to reflect this variation.

material. The wafers are prepared for the deposition process by removing possible surface impurities and oxides, using plasma-etching with ionized argon and krypton gas [Vog11] (for details on the plasma-etching parameters see reference [Til19a]). After the preparation, a CrC inter-layer is deposited on the wafers to improve the adhesion of the carbon layer (for details on the inter-layer deposition process see reference [Til18]). Subsequent to the inter-layer, the final a-C films are deposited on the Si-wafers. The parameters used are shown in Table 5.1. Here, argon is used as process gas at a pressure of 300 mPa. The deposition time of each of the films is set to 270 min.

Design of Experiments. In order to systematically investigate the linear and quadratic cause-effect relation of the sputtering parameters on the properties of the a-C films a rotatable Central Composite Design with three factors is chosen (see Figure 5.1).

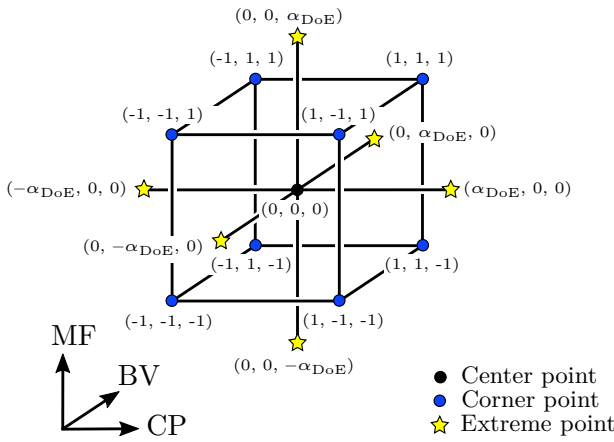


Figure 5.1 Visualization of a three factor Central Composite Design. Redrawn from reference [Til19a].

the corner points (●) are calculated and rounded to whole numbers. Three additional center-runs are added to the design (compare Table 5.1).

The data of the experiments is analyzed using the software JMP Pro 12. Here, the Student's t-test² is utilized to calculate the impact strength of CP, BV and MF and their interactions on the properties of the a-C films. This method is complemented by a p-value³ of 5%, to evaluate for random effects.

Structural and Mechanical Characterization of the Deposited Films. The deposited coatings' structural and mechanical properties are characterized, using SEM (FE-JSEM 7001, Jeol, see Section 3.2.3) to determine their topography. Furthermore, their thicknesses are determined from the cross-sections of the coatings. Additionally, the surface roughness is determined using AFM (Dimension Edge, Bruker, also Section 3.2.3). Here, a silicon

Here, the influences of the Cathode Power (CP) (1500 W to 4000 W), the Bias Voltage (BV) (−100 V to −200 V) and the Mid-Frequency (MF) (20 kHz to 50 kHz) are studied. The supplied parameter range covers the largest possible parameter space of the sputtering device, which provided a stable sputtering process. The spacing between the center point (●) and the extreme values of each parameter, represented by the star points (★), is set to $\alpha_{DoE} = 1.682$ [Gar98]. From this scaling factor

²The Student's t-distribution is a probability distribution for a small number of samples of normally distributed values. It was developed in 1908 by William Sealy Gosset (*1876; †1937) under his pseudonym Student [Stu08]. For large sample numbers the t-distribution tends to a Gaussian distribution. Both distributions differ, as the t-distribution has heavier tails than the normal distribution.

³A p-value indicates if the data analyzed is incompatible to a specified statistical model [Was16]. It is no measure for the correctness of a specified hypothesis. p-values are to be used with care, they are often misinterpreted, which led to the statement by Wasserstein et al. [Was16].

cantilever with a tip radius of 8 nm is used to investigate a region of $100 \times 100 \mu\text{m}^2$, which is used to calculate the arithmetical mean roughness Ra. For the mechanical properties of hardness and elastic modulus a nanoindenter is utilized (G200, Agilent Technology, see also 3.2.2). Here, a Berkovich diamond tip is set to penetrate 10 % of the film thickness. In the applied evaluation procedure, which was suggested by Oliver and Pharr [Oli92], a Poisson ratio of 0.18 is used [Bec06].

Determination of the sp^3 Content of the Deposited Films by Raman Spectroscopy.

In order to determine the sp^3 content, Raman spectroscopy is utilized. Here, non-polarized spectra are recorded at two different laser excitation wavelengths 266 nm (TopWave, Toptica) and 532 nm (Samba, Cobolt). The setup is prepared, as described in Section 3.1.1, with additional laser-specific line filters to remove laser background emission in the excitation path. Here, a 150 mm lens is used to focus the exciting laser light to a spot of approximately 0.3 mm size. The back-scattered light is collected using a 75 mm lens and focused onto the entrance slit of a 500 mm spectrometer (Spectra Pro 2500i, Princeton Instruments) through a second 75 mm lens. In order to suppress the Rayleigh line of the back-scattered light wavelength-specific edge filters are inserted directly in front of the spectrometer (compare Figure 3.1). The filtered light is dispersed with a 3600 grooves/mm grating (blaze angle of 240 nm) at 266 nm excitation, or a 600 grooves/mm grating (blaze angle of 500 nm) at 532 nm excitation. The diffracted light is collected by a Peltier-cooled, UV-enhanced CCD camera (Pixis, Princeton Instruments). Here, the time of accumulation is set to 100 s per Raman spectrum. The laser power at the sample position is varied for the 266 nm excitation (17 mW to 28 mW) and is constant for 532 nm excitation (20 mW). Before and after each measurement the a-C films are carefully checked for laser-induced changes, which are not observed. To enhance the statistical significance, at each coating Raman spectra are collected at three randomly chosen positions.

The collected Raman spectra of the a-C films contain the carbon-related D- and G-peaks, which are used to estimate the sp^3 content (see Section 2.3.2). A procedure to estimate the sp^3 content was suggested by Ferrari and Robertson [Fer01]. Their procedure is adapted for the present analysis and described in the following. A scheme of the evaluation process is presented in Figure 5.2. Subsequent to the measurements, the data is processed, using the

Table 5.1 Overview of the parameters used for the deposition of the a-C films. Additionally the star (★), corner (●) and center (●) points are indicated.

Run	Pattern	CP/ W	BV/ -V	MF/ kHz
1	● (0, 0, 0)	2750	150	35
2	★ (0, $-\alpha$, 0)	2750	100	35
3	● (0, 0, 0)	2750	150	35
4	★ (α , 0, 0)	4000	150	35
5	★ ($-\alpha$, 0, 0)	1500	150	35
6	● (-1, 1, -1)	2007	180	26
7	● (0, 0, 0)	2750	150	35
8	● (1, 1, -1)	3493	180	26
9	● (1, 1, 1)	3493	180	44
10	● (1, -1, 1)	3493	120	44
11	★ (0, 0, $-\alpha$)	2750	150	20
12	● (0, 0, 0)	2750	150	35
13	● (-1, -1, -1)	2006	120	44
14	★ (0, 0, α)	2750	150	50
15	★ (0, α , 0)	2750	200	35
16	● (-1, -1, -1)	2007	120	26
17	● (1, -1, -1)	3493	120	26
18	● (-1, 1, 1)	2007	180	44

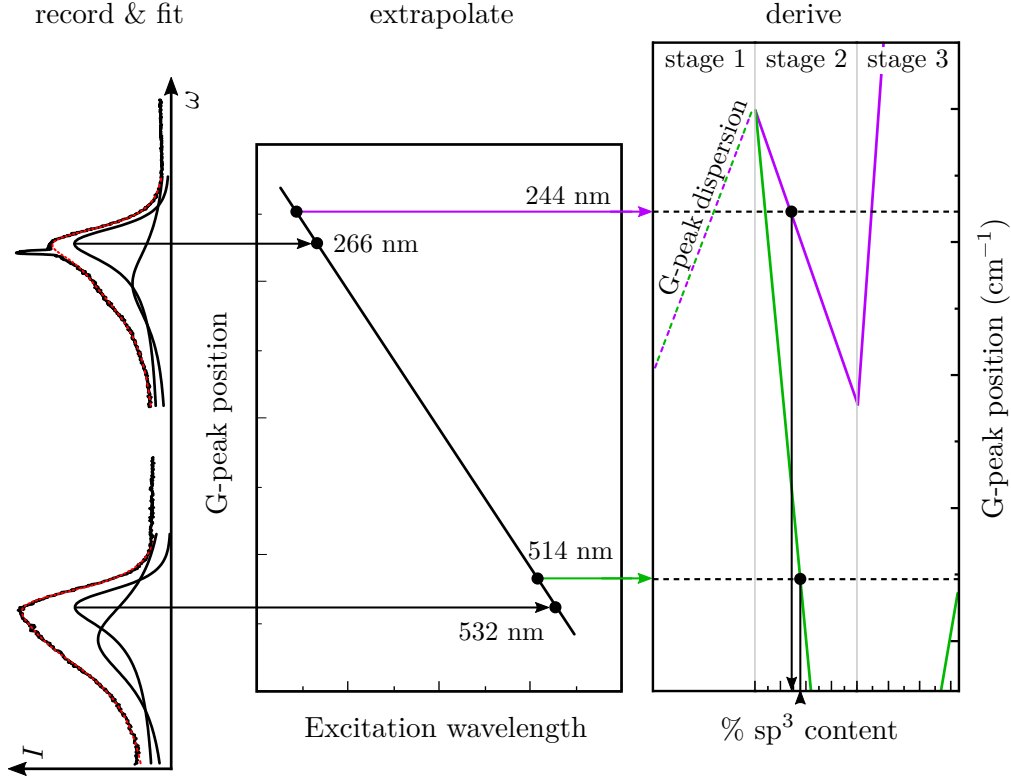


Figure 5.2 Schematically the four steps of determining the sp^3 content of a-C films are shown. In the first step, Raman spectra are recorded at two different excitation wavelengths (here: 266 nm and 532 nm). In the second step, the spectra are fitted in order to determine their D- and G-peak positions. In the third step, the dispersion of the G-peak is calculated by linear extrapolation across the two wavelengths. This dispersion is used to calculate theoretical G-peak positions for excitation-wavelengths of 244 nm and 514 nm, which were used by Ferrari et al. [Fer01]. Finally, in the fourth step, the sp^3 content is derived by inserting the corrected G-peak positions into the three-stage-model suggested by Ferrari. Reproduced with permission from reference [Til19a].

data analysis software OriginPro. Here, the recorded peaks are fitted by a linear combination of a Breit-Wigner-Fano (**BWF**) resonance and a Lorentzian function, as suggested by Ferrari and Robertson [Fer00] (see "record & fit" in Figure 5.2). The fit function is given by

$$I(\omega) = I_0 + I_G \frac{\left(1 + 2 \frac{\omega - \omega_{\text{BWF}}}{q\Gamma_G}\right)^2}{1 + \left(\frac{\omega - \omega_{\text{BWF}}}{\Gamma_G}\right)^2} + \frac{2A_D}{\pi} \frac{\Gamma_D}{4(\omega - \omega_D)^2 + \Gamma_D^2}. \quad (5.1)$$

Here, the intensity I is described by the scattering frequency ω . The intensity is offset by I_0 . The G-peak is described by its intensity I_G , the frequency position of the BWF resonance ω_{BWF} and the Full Width at Half Maximum (**FWHM**) of the G-peak. The resonance's asymmetry factor is given by q^{-1} . The Lorentzian term describes the D-peak. Here, the area under the curve is given by A_D , the peak's position is ω_D and the FWHM is given by Γ_D . The position of the G-peak does not coincide with the position of the BWF resonance,

but it may be derived by

$$\omega_G = \omega_{\text{BWF}} + \frac{\Gamma_G}{2q}. \quad (5.2)$$

The height of the D-peak is given by

$$I_D = \frac{2A_D}{\pi\Gamma_D}. \quad (5.3)$$

Subsequent to the fitting procedure, the sp^3 content is evaluated based on the multi-wavelength amorphization trajectory of Ferrari and Robertson [Fer01]. The trajectory describes the change of the G-peak position with respect to the sp^3 content of amorphous carbon systems. Three different crystallization stages are identified in the trajectory. Linear functions are used to model the behavior in the different stages. Here, the trajectory is shown for 244 nm and 514 nm (see "derive" in Figure 5.2). To account for the deviation of the here used excitation wavelengths (266 nm and 532 nm), corrected G-peak positions are calculated, assuming a linear dispersion of the G-peak position (see "extrapolate" in Figure 5.2). The extrapolated positions are used to derive the sp^3 contents of the amorphous carbon coatings. It is assumed, that the sputtered coatings are part of the last two stages (see "stage 2" and "stage 3" in Figure 5.2).

Determination of the sp^3 Content of the Deposited Films by XPS. Additionally to Raman spectroscopy, the sp^3 content is complementary estimated using X-ray Photoelectron Spectroscopy (XPS) at Beamline 11 at the synchrotron radiation facility Dortmund ELeKTronenspeicherring-Anlage (DELTA) [Wes05]. The measurements are performed in ultra-high vacuum ($\approx 5 \times 10^{-10}$ mbar) at photon energies of 450 eV and 650 eV. Here, survey spectra are collected at both excitation energies under a take-off angle of 0° . High-resolution spectra of the carbon C 1s line are only recorded at a photon energy of 450 eV. In order to fit the XPS spectra the UNIFIT software is used [Hes17]. The background of the spectra, caused by inelastic electron scattering, is estimated using the Shirley method [Van11]. The C 1s line is composed by contributions of sp^2 and sp^3 hybridized carbon atoms. Here, the different components are fitted by Voigt profiles (see 2.1.4), whereas the Lorentzian contribution of the sp^2 component is replaced by the asymmetric Doniach-Sunjić profile (see also 2.1.4) [Chu06]. Other contributions to the low-energy flank of the C 1s peak, like carbon-oxygen signals, are modeled by additional Voigt profiles. For the non-Gaussian contributions of the sp^2 and sp^3 signatures the widths are set to 214 meV [Dia96; Che90; Set90]. In this work, three different fitting procedures of two components in the C 1s peak are discussed.

1. The C 1s signal is fitted varying five parameters: the asymmetry of the sp^2 component, the binding energy shifts and the Gaussian line widths of each component, as suggested by Diaz et al. [Dia96].
2. The C 1s signal is fitted using a fixed binding energy shift of -0.9 eV, as reported by references [Dia96; Hae01].
3. The C 1s signal is fitted with fixed values for asymmetry (0.05 [Che90; Set90]) and binding energy shift (-0.9 eV [Dia96; Hae01]).

Table 5.2 Summary of the mechanical, optical and compositional properties of the a-C films. The determined sp^3_{532} (sp^3_{266}) content has an error of $\pm 0.5\%$ ($\pm 2\%$) due to peak fitting errors.

Run	Deposition rate/ nm/h	Roughness Ra/ nm	I_D/I_G (measured at 532 nm)	I_D/I_G (measured at 266 nm)	sp^3_{532} content (measured at 532 nm)/%	sp^3_{266} content (measured at 266 nm)/%	Hardness/ GPa	Elastic modulus/ GPa
1	169.6 ± 1.7	6.9 ± 1.3	1.26 ± 0.05	0.31 ± 0.03	8.9	12.3	24.2 ± 1.8	213.1 ± 10.7
2	172.9 ± 1.1	6.1 ± 1.2	1.42 ± 0.06	0.35 ± 0.04	11.8	14.4	22.6 ± 1.4	205.4 ± 7.3
3	168.6 ± 0.9	7.0 ± 0.7	1.39 ± 0.03	0.32 ± 0.08	9.3	12.1	23.5 ± 1.3	205.6 ± 5.9
4	110.9 ± 2.1	4.9 ± 0.4	1.06 ± 0.02	0.38 ± 0.03	8.1	4.3	12.9 ± 0.6	158.2 ± 4.4
5	89.6 ± 1.1	5.7 ± 0.9	1.97 ± 0.05	0.25 ± 0.03	11.0	14.0	21.1 ± 1.3	193.5 ± 10.6
6	121.4 ± 1.2	5.9 ± 1.1	1.23 ± 0.09	0.28 ± 0.04	10.8	16.4	23.7 ± 1.3	207.1 ± 5.7
7	169.3 ± 1.5	5.5 ± 0.3	1.24 ± 0.05	0.29 ± 0.03	9.3	17.5	22.3 ± 1.0	197.9 ± 5.0
8	Delaminated		Not measurable				12.7 ± 2.5	158.5 ± 5.2
9	Delaminated		1.72 ± 0.03	0.42 ± 0.03	10.4	7.7	12.9 ± 0.4	168.5 ± 2.7
10	221.9 ± 2.3	6.7 ± 0.4	1.73 ± 0.02	0.36 ± 0.04	11.0	14.7	19.6 ± 1.4	183.7 ± 6.9
11	169.1 ± 1.5	6.6 ± 0.4	1.12 ± 0.04	0.31 ± 0.03	9.4	19.8	22.2 ± 1.8	213.4 ± 8.2
12	168.6 ± 0.9	7.6 ± 2.0	0.73 ± 0.09	0.28 ± 0.03	15.0	14.8	23.9 ± 1.8	223.9 ± 8.3
13	124.3 ± 1.3	5.6 ± 0.7	1.10 ± 0.05	0.25 ± 0.03	9.9	15.9	19.6 ± 1.4	188.3 ± 7.8
14	164.7 ± 0.9	5.8 ± 0.7	1.32 ± 0.05	0.26 ± 0.03	9.8	16.2	24.9 ± 1.1	211.1 ± 7.8
15	Delaminated		Not measurable				12.6 ± 0.7	156.2 ± 5.7
16	122.2 ± 1.2	6.2 ± 0.5	0.90 ± 0.07	0.30 ± 0.04	13.6	15.2	19.0 ± 2.0	183.2 ± 10.1
17	261.5 ± 3.2	6.4 ± 1.1	1.08 ± 0.06	0.42 ± 0.03	10.4	16.5	16.5 ± 1.6	169.5 ± 8.5
18	114.1 ± 0.4	5.4 ± 0.6	1.47 ± 0.03	0.28 ± 0.03	9.5	13.1	22.1 ± 1.0	194.3 ± 4.4

Morphology, Topography and Deposition Rate. In order to determine the morphology (topography) of the deposited a-C films cross-sections (surface regions) are analyzed by SEM (see Section 3.2.3). The films showed a proper architecture, with a CrC inter-layer and the supposed amorphous carbon top layer, whose thickness is additionally determined. All films showed an amorphous morphology with a fully-dense structure. For three films (Runs 8, 9 and 15) delamination is observed, with only the CrC inter-layer preserved. Here, the high BV of -200 V or the combination of high CP (3493 W) and high BV (-180 V) lead to high residual stresses, that result in film delamination.

From the thicknesses of the amorphous carbon films the corresponding deposition rates are evaluated (see Table 5.2). Here, deposition rates of delaminated coatings could not be calculated and, therefore, are omitted from the following data analysis.

Table 5.3 shows the determined effects of the deposition parameters on the deposition rate, the roughness, the sp^3_{266} content, the hardness and the elastic modulus. Here, the t- and p-values are listed. Additionally, the t-value is plotted as unsorted Pareto chart⁴ to visualize the impact of each parameter and their quadratic interactions on the a-C films' properties.

Influences on the Deposition Rate. For the deposition rate, the effects of the interaction between CP and BV, the quadratic CP and BV and the linear BV show statistical significance. Here, all effects show negative t-values, meaning an anti-proportional behavior of the deposition rate on changes of any of the significant parameters. The anti-proportional behavior of the quadratic CP does not meet the expectations, as it was assumed that the quadratic CP would lead to higher deposition rates. However, a

⁴The Pareto chart is a value-sorted diagram to ease the identification of critical factors in a set of parameters.

It is commonly used in quality control and named after the Italian economist Vilfredo Pareto (*1848; †1923) [Wil06]. Pareto and others observed the Pareto principle, which states that 80% of the effects often can be attributed to 20% of the causes. Therefore, this principle is also known as the 80/20 rule.

Table 5.3 Influences of the different deposition parameters and their quadratic interactions on the mechanical and compositional properties of the a-C films. Listed are the t- and p-values, with additionally plotted t-values to visualize each parameter's impact.

Parameter	Deposition rate		Roughness		sp ³ ₂₆₆ content		Hardness		Elastic modulus	
	t-value	p-value	t-value	p-value	t-value	p-value	t-value	p-value	t-value	p-value
CP	0.85	43.6	-0.90	0.4	-2.73	3.4	-5.30	< 0.1	-3.20	1.3
BV	-7.37	< 0.1	-1.53	0.2	-1.81	12.0	-2.95	1.8	-1.66	13.5
MF	-1.46	20.3	-0.70	0.5	-1.18	28.3	1.01	34.2	0.27	79.7
CP ²	-6.42	< 0.1	-2.41	< 0.1	-2.27	6.4	-4.73	< 0.1	-3.76	< 0.1
BV ²	-4.48	< 0.1	-1.62	0.2	-0.75	48.4	-4.31	< 0.1	-3.27	1.1
MF ²	0.40	70.9	-0.86	0.4	2.35	5.7	-0.31	76.4	-0.20	84.9
CP BV	-7.55	< 0.1	-1.35	0.2	-1.53	17.7	-3.36	< 0.1	-1.54	16.1
CP MF	-1.32	24.4	0.52	0.6	-0.14	89.1	0.80	44.9	0.88	40.6
BV MF	0.14	89.1	-0.09	0.9	-0.38	71.6	-0.96	36.5	-0.61	56.0

quadratic decrease of the deposition rate could only be observed at the star CP value of 4000 W. The linear effect of the CP, meaning a proportional increase of the deposition rate, is observed, but shows only little significance. This is attributed to the low sputtering yield of carbon [Ohr02c], leading to a low deposition rate. The linear effect of the BV on the deposition rate is explained by densification mechanisms and re-sputtering of weakly bonded atoms. With a higher BV the kinetic energy of the ions is increased, leading to smaller deposition rates [Gio98]. Here, the BV can only be increased up to a critical value, as residual stresses accumulate in the a-C coatings, leading to delamination (see Run 8, 9 and 15). The MF shows no significant effect on the deposition rate.

Influences on the Surface Roughness. The roughness values Ra of the films are listed in Table 5.2. The roughness ranges from 4.9 nm to 7.6 nm, delaminated coatings are omitted from the statistical analysis. The results of the statistical analysis on the effects of the deposition parameters are listed in Table 5.3. Here, no effect is statistically significant, all effects show only minor impact on the surface roughness of the deposited films. This might be explained by the narrow range of Ra, compared to the large parameter space of CP, BV and MF, leading to no effect with a statistical significance of 95%. Here, SEM micrographs show surface changes with increasing CP, leading to different roughnesses, but a clear effect is not observed.

Chemical Bonding. In order to analyze the sp³ content of the amorphous carbon coatings, multi-wavelength Raman spectroscopy is utilized. A typical Raman spectrum is shown in Figure 5.3. Here, the coating is excited using 266 nm laser light. The recorded spectrum (red line) shows the D- (at the low-frequency flank of the G-peak) and G-peak (at about 1580 cm⁻¹, see also Section 2.3.2). Furthermore, the cumulated fit (dashed line) and the single components (solid lines) are shown. Additionally to the D- and G-peak, remnant laser replica are visible at three positions in the spectrum: The Rayleigh line at approximately 0 cm⁻¹ and two lines at 1552 cm⁻¹ and 2328 cm⁻¹. The assignments are drawn from a comparison of the collected a-C Raman spectra with a reference spectrum of a silicon sample (not shown here).

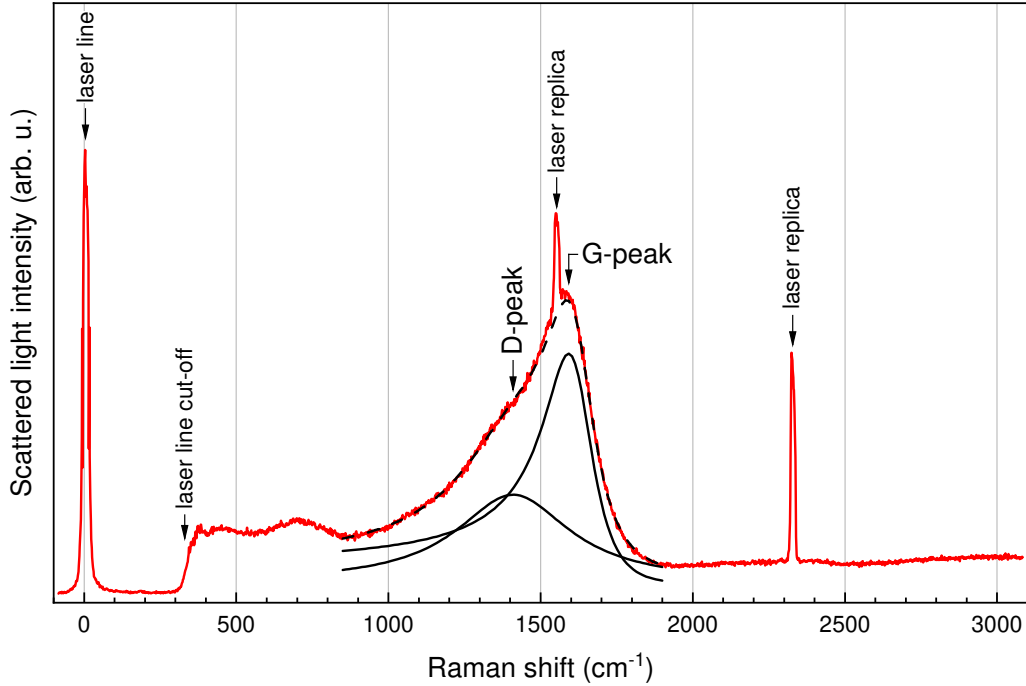


Figure 5.3 Exemplary Raman spectrum of an a-C film under 266 nm laser excitation. Marked by arrows are laser replica as well as the D- and G-peak positions. The respective fits are shown in black solid lines, whereas the sum fit is shown by the dashed line. Reproduced with permission from reference [Til19a].

Table 5.4 Parameter ranges of selected fitting parameters for both excitation wavelengths.

parameter	266 nm exc.		532 nm exc.	
	min	max	min	max
ω_G/cm^{-1}	1577	1595	1537	1566
Γ_G/cm^{-1}	158	221	176	248
ω_D/cm^{-1}	1365	1443	1345	1452
Γ_D/cm^{-1}	332	425	309	497
I_D/I_G	0.25	0.52	0.73	1.97

Figure 5.4 shows the Raman spectra of different a-C films for (a) 532 nm and (b) 266 nm excitation. For 532 nm, the D- and G-peak are of comparable intensity. The fitted peak positions are marked by arrows. For each spectrum, the corresponding run and the determined sp^3 content are marked next to the spectrum. For 266 nm the same a-C films are shown. Selected parameter ranges of the fitted spectra are listed in Table 5.4. Comparing 266 nm excitation and 532 nm excitation, the G-peak is slightly broadened and its position is slightly moved towards lower Raman shifts. The D-peak is strongly broadened, while its position is rather stable. Furthermore, the intensity ratio of the two peaks changes from values ≤ 0.5 to values ≥ 0.7 .

In the recorded spectra around 1000 cm^{-1} no additional Raman signature (the so called T-peak) is detected, which would indicate a significant sp^3 hybridization [Fer01]. This leads to the conclusion that the sp^3 content in the investigated films does not exceed 20% to 30%. Therefore, stage 2 is the stage of interest of the prior presented three-stage model. This is solidified by the fact that the derived sp^3 contents do not strongly differ for the two wavelengths (compare Table 5.2). In case of choosing stage 3 for the sp^3 content determi-

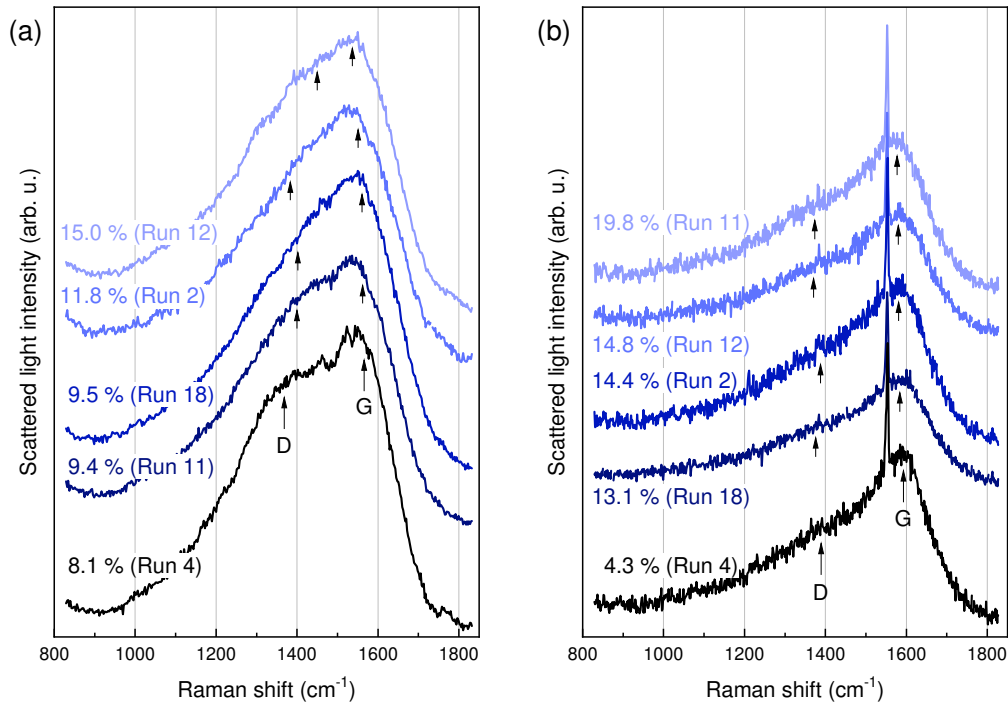


Figure 5.4 Raman spectra of the investigated a-C films excited with (a) 532 nm and (b) 266 nm laser light. Marked by arrows are the D- and G-peak positions. The sp^3 contents are given in percentages with the respective sample ID in brackets. Reproduced with permission from reference [Til19a].

nation the derived contents vary considerably between 30% to 90% for the same sample. Additionally, the intensity ratio I_D/I_G for 532 nm ranges from 0.7 to 2, which supports the selection of stage 2, as this ratio is only characteristic for the first two stages [Fer00]. Stage 1 is not considered, as the films are sputtered a-C and no point of intersection is given for 532 nm excitation. To further support this, several samples (Runs 1, 10 and 18) are additionally inspected with 633 nm laser light. Here, again only a match of the measured G-peak position with the suggested G-peak dispersion is detected in stage 2. The determined sp^3 contents for 633 nm (respectively 14.7%, 12.9% and 16.2%) match the detected ranges for 266 nm (4% to 20%) and 532 nm (8% to 15%) excitation.

In order to estimate the sp^3 content more accurately, the T-peak position could be utilized, which becomes observable for deep UV wavelengths below 244 nm [Fer01; Mer97]. Nevertheless, the D-peak still overlaps the T-peak for sputtered a-C films, even at deep UV wavelengths.

An additional contribution to the sp^3 content might stem from C–H₃ bonds. They are ruled out for the investigated films, as the corresponding Raman bands at approximately 3000 cm^{-1} are not detected (compare Figure 5.3) [Sny82; Soc01]. Hence, the derived sp^3 contents stem solely from a C–C sp^3 hybridization. The calculated values for 266 nm and 532 nm excitation are summarized in Table 5.2. As shown, multiple-wavelength Raman spectroscopy of the amorphous carbon films is essential to determine the specific stage of the three-stage model and to deduce the approximate sp^3 content of the samples.

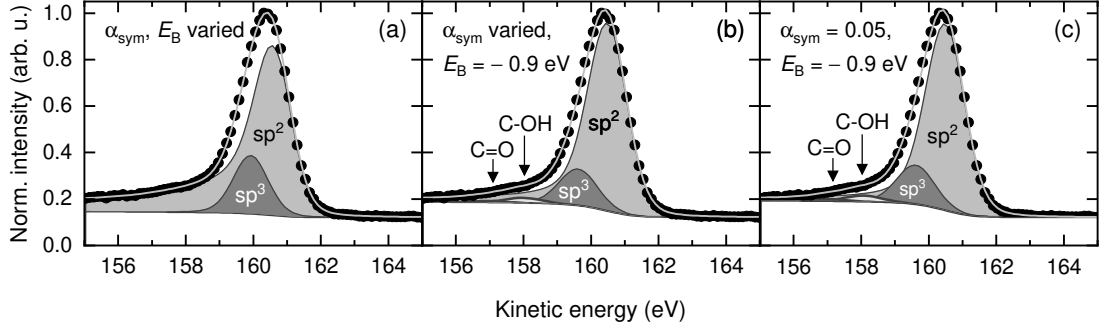


Figure 5.5 Exemplary XPS spectrum of an a-C film (Run 2). The respective fits are shown. Reproduced with permission from reference [Til19a].

XPS Measurements of the Amorphous Carbon Coatings. Additionally to Raman spectroscopy, several coatings (Runs 2, 3, 4, 7, 11, 12 and 18) are representatively analyzed by XPS. The collected spectra and three methods of fitting (see paragraph on the determination of the sp^3 content by XPS) of Run 2 are presented in Figure 5.5. Here, the normalized C 1s peak is shown (data as filled circles), with the beam intensity of the photo-emitted electrons measured as function of their kinetic energy. Additionally to the measured data, the fitted components of the sp^2 and sp^3 hybridized carbon are displayed by filled curves. Arrows mark the small contributions of C–OH and C=O, resulting from surface oxidation of the a-C films in ambient air. The resulting sum curve is superimposed on the data.

Table 5.5 Determined sp^3 contents of selected a-C films using XPS and different methods of fitting. The varied (v) and fixed (f) parameters are indicated.

Run	sp ³ content / %		
	α_{sym} , v E_B , v	α_{sym} , v E_B , f	α_{sym} , f E_B , f
2	16	14	15
3	9	10	18
4	8	5	11
7	8	9	19
11	10	11	18
12	10	11	18
18	11	13	22

For all of the a-C films analyzed with XPS, the sp^3 content is lower than 23 %, independent of the fitting procedure (see Table 5.5). The mean of all sp^3 contents determined amounts to 13 %, which supports the prior determined sp^3 contents with UV and visible Raman spectroscopy. The three different fitting procedures of the XPS spectra yield slightly different ranges for the sp^3 content, each varying by ± 5 %. Allowing the fit to vary the asymmetry α_{sym} and the binding energy shift E_B as suggested in the first fitting procedure by Diaz et al. [Día96], the determined sp^3 content ranges from 8 % to 16 %. For the second procedure, with a fixed binding energy shift of -0.9 eV and a variable asymmetry [Día96; Hae01], the sp^3 content ranges from 5 % to 14 %. For the third fitting procedure, with a constant binding energy shift of -0.9 eV and an asymmetry of 0.05 [Che90; Set90; Día96; Hae01] the sp^3 content ranges from 11 % to 22 %.

The three different fitting procedures used are proposed methods for analyzing carbon related XPS spectra. For all three methods, the determined sp^3 contents are comparable to the sp^3 contents obtained with Raman spectroscopy. Therefore, the effects of the deposition parameters on the sp^3 content are similar to the effects determined with Raman scattering.

However, this data shows that improvements in the determination of the sp^3 content of amorphous carbon films are necessary. Here, Raman scattering spectroscopy with excitation wavelengths below 240 nm or tip-enhanced techniques might be used to increase the carbon-related Raman scattering signals significantly.

Statistical Analysis of the sp^3 Content Determined with Raman Spectroscopy. In order to evaluate the influences of the different deposition parameters, the sp^3 content is analyzed by statistical measures. As the band gap of sp^2 hybridized carbon is approximately 2 eV (620 nm), and the excitation energy of 4.6 eV (266 nm) is well separated from this value and close to the diamond band gap of 5.5 eV (227 nm), the Raman cross-section is mostly defined by sp^3 bonds than by sp^2 states of the carbon network. Therefore, the sp^3 content determined by 266 nm excitation is analyzed statistically [Mer97]. Here, it is even possible to determine the sp^3 content of Run 9, while the sp^3 contents of Run 8 and 15 are not measurable (compare Table 5.2). In Table 5.3 the linear and quadratic effects of the deposition parameters on the sp^3_{266} content are listed. Only the linear influence of CP shows statistical significance. Close to statistical significance are the quadratic effects of MF and CP with p-values of approximately 6 %.

Despite the statistical significance and excluding the quadratic effect of MF, all other effects of the deposition parameters show negative t-values, indicating an anti-proportional behavior of the sp^3_{266} content with increasing parameters. For the linear effect of CP this is in good agreement with Cho et al., who reported an increase of the sp^2 bonding fraction with an increasing power density [Cho90]. Furthermore, the quadratic effect on CP shows a maximum, which was also reported by Dai et al. [Dai16]. A similar behavior is observed for the linear and quadratic effects of the BV on the sp^3 content. Here, the linear BV is anti-proportional on the sp^3 content and the quadratic BV shows a slight maximum. The reduction of the sp^3 content, for high CP and BV values, may be explained by the kinetic energy of the sputtered atoms, which exceeds a critical value, resulting in thermal dissipation, and therefore, in a relaxation of the density and stress [Rob94; Dav93].

Mechanical Properties. Using nanoindentation the hardness and the elastic modulus of the amorphous carbon films are determined (see Table 5.2). In order to evaluate the influences of the deposition parameters on the films' mechanical properties all determined hardness values and elastic modulus values are used in the statistical analysis, even the values of delaminated films. The lowest hardness values of ≈ 12.6 GPa (Runs 8 and 15) correspond to the hardness of the Si substrate [Van07]. Here, the sp^3 content is not determined. For Runs 4 and 9 a hardness of ≈ 12.9 GPa and low sp^3 contents (4.3 % and 7.7 %) are determined, indicating delaminated a-C films. The hardness values are comparable to CrC films sputtered on plasma nitrided AISI H11 steel (X38CrMoV5-1, 1.2343, (13.7 ± 2.0) GPa) [Til18], indicating that the a-C films delaminated, but the CrC inter-layer remained intact.

The statistical analysis shows that the hardness is influenced by the linear and quadratic effects of CP and BV, as well as by their interaction (see Table 5.3). All of the effects show negative t-values, indicating an anti-proportional behavior with respect to an increase of CP or BV. An increase of the hardness of the a-C films is observed up to a critical value, which decreases again by further increasing the CP and BV. A similar trend was reported by Dai

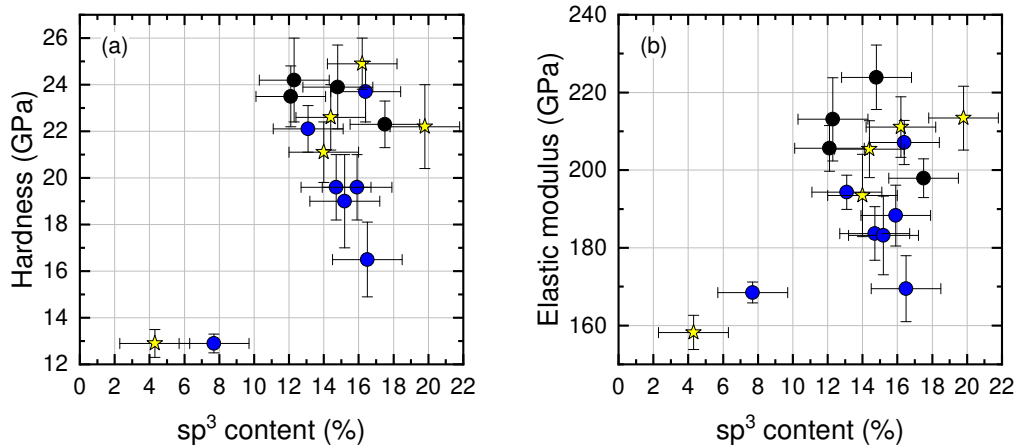


Figure 5.6 Correlation of the sp^3_{266} content with (a) hardness and (b) elastic modulus. Reproduced from reference [Til19a].

et al. [Dai16]. They ascribed the hardness decrease to the decomposition of sp^3 into sp^2 due to thermal dissipation of the high-energy bombarding particles [Til19a]. Furthermore, the MF does not significantly influence the hardness.

For the elastic modulus, significant influence is determined only by the quadratic effects of the CP and BV, as well as the linear effect of the CP (see Table 5.3). Again, these effects show negative t -values, indicating a hardness-comparable behavior. For the elastic modulus a maximum is reached at a critical value, before it decreases with increasing CP and BV. Here, like on the hardness, the MF has no significant influence on the elastic modulus. Therefore, it can be concluded, that the CP and the BV are the two most significant parameters for the mechanical properties of the a-C films. Here, hardness and elastic modulus are influenced in a similar manner by the two parameters. This can be attributed to the fact that the mechanical properties of a-C films are directly related to the sp^3 content [Rob10].

Correlation Between sp^3 Content and Mechanical Properties. Figure 5.6 shows the correlation between the sp^3_{266} content and the mechanical parameters hardness and elastic modulus of the sputtered a-C films. Generally, a high sp^3 content coincides with a high hardness and elastic modulus. However, the highest determined sp^3 content does not correspond with the highest hardness and elastic modulus. Furthermore, the distribution of the points shows a cloud-like distribution, rather than a linear dependency. This might be explained by the small range of the sp^3 values, as well as the narrow range of the values for hardness and elastic modulus, resulting in amorphous carbon films with very similar mechanical properties. In particular, this behavior becomes notable for the center-run coatings (●), which should show identical mechanical parameters, as they are deposited under identical conditions. Nevertheless, they show slightly differing sp^3 contents and mechanical properties.

Amorphous carbon films deposited by magnetron sputtering have comparably low sp^3 contents as films grown by evaporation. In order to get higher sp^3 contents other deposition methods have to be used (see for example reference [Rob02]). In conventional magnetron

sputtering, the kinetic energy of the sputtered carbon atoms is not sufficient to form films with high sp^3 contents [Sch18]. Therefore, the deposited a-C films show sp^3 values below 20 %, despite the strong variations of the deposition parameters. Nevertheless, for the films investigated, an increase of the mechanical parameters hardness and elastic modulus is observed with an increasing sp^3 content. This might be explained by a clustering of the sp^2 sites, as observed by Rybachuk et al. They observed that hydrogenated a-C:H films with increased hardness and elastic modulus were characterized by aromatic sites, arranged in smaller domains with an increased degree of ring distortion and additionally, sp^2 -bonded olefinic⁵ sites with a higher degree of clustering [Ryb06].

Summary and Conclusion. The linear, quadratic and interaction effects of the deposition parameters cathode power, bias voltage and mid-frequency on the structural and mechanical properties of amorphous carbon films are investigated. Here, the deposition rate is mostly influenced by the interaction of CP and BV and by the BV. At very high values for CP and BV the coatings delaminate, due to high intrinsic stresses.

Using multi-wavelength Raman spectroscopy in the UV and visible range, the sp^3 content of the sputtered coatings is determined. The sp^3 values of most of the films range from 12 % to 18 %, excluding two exceptions. The determined sp^3 contents are supported by XPS measurements. Furthermore, high values of CP and BV seem to reduce the probability of sp^3 formation, which is explained by an exceeding of a threshold for the kinetic energy of the bombarding atoms. The statistically significant linear effect of the CP is anti-proportional to sp^3 formation, leading to less sp^3 bonds with higher CP. The quadratic effects of CP and BV, as well as their interaction and the linear BV show anti-proportional behavior as well, despite being statistically insignificant.

For mechanical parameters, again the effects of CP and BV are of greatest influence, while the MF does not change the coatings' properties strongly. Furthermore, an increase of the mechanical parameters hardness and elastic modulus coincides with an increased sp^3 content. Due to the very similar amorphous carbon films, no clear relation between the mechanical parameters and the sp^3 content is derived.

Overall, the Design of Experiment method is successfully utilized to analyze the cause-effect relation of the sputtering parameters and film properties with the help of multi-wavelength Raman scattering. The scattering technique might be used to get a rough estimation of the sp^3 content in amorphous carbon films. Here, the use of multiple excitation wavelengths is required, ideally with at least one wavelength in the 240 nm range.

⁵Olefinic hydrocarbons are all other acyclic or cyclic hydrocarbons with one or more carbon-carbon double bond, which are not of aromatic character [Cha19; Soc01].

Table 5.6 Deposition parameters and structural properties of the HiPIMS deposited MoS_x films. Listed are the sample ID, the heating power P_H , the bias-voltage U_B , the pulse frequency f_p , the pulse duration t_p , the substrate temperature T_S , the coating thickness d_c , the mean roughness Ra, relative atomic contents of molybdenum and sulfur, the S/Mo ratio and the intensity ratio of the (100) and the (002) XRD peaks.

ID	P_H / W	U_B / V	f_p / Hz	t_p / μs	T_S / $^\circ\text{C}$	d_c / μm	Ra/ nm	Mo/ at.%	S/ at.%	S/Mo Ratio	(100)/ (002)
DC	3000	150			312 ± 1	2.70 ± 0.02	79.1 ± 1.5	38.6 ± 0.3	66.4 ± 0.3	1.59 ± 0.02	7.8 ± 0.4
1	3000	150	700	150	311 ± 5	1.75 ± 0.01	18.6 ± 0.7	33.1 ± 0.2	66.9 ± 0.2	2.02 ± 0.02	2.2 ± 0.1
2	500	150	700	150	128 ± 1	1.41 ± 0.01	13.1 ± 1.1	31.0 ± 0.5	68.9 ± 0.5	2.22 ± 0.05	1.2 ± 0.1
3	5500	150	700	150	388 ± 5	2.03 ± 0.02	21.6 ± 2.0	32.4 ± 0.3	67.6 ± 0.3	2.08 ± 0.03	1.4 ± 0.1
4	3000	50	700	150	308 ± 2	2.26 ± 0.01	22.4 ± 3.2	32.2 ± 0.1	67.8 ± 0.1	2.11 ± 0.01	1.6 ± 0.1
5	3000	250	700	150	306 ± 1	1.55 ± 0.02	18.6 ± 3.5	31.5 ± 0.2	68.5 ± 0.2	2.17 ± 0.02	6.7 ± 0.3
6	3000	150	400	150	306 ± 1	1.25 ± 0.01	12.7 ± 0.5	32.0 ± 0.3	68.0 ± 0.3	2.14 ± 0.03	1.9 ± 0.1
7	3000	150	1000	150	308 ± 1	2.48 ± 0.02	29.3 ± 0.6	32.4 ± 0.2	67.6 ± 0.2	2.09 ± 0.02	9.4 ± 0.1
8	3000	150	700	85	306 ± 1	1.47 ± 0.01	16.9 ± 3.3	31.5 ± 0.2	68.5 ± 0.2	2.18 ± 0.02	3.7 ± 0.4
9	3000	150	700	215	305 ± 1	2.10 ± 0.02	80.3 ± 3.7	31.8 ± 0.2	68.2 ± 0.2	2.15 ± 0.02	10.6 ± 0.8

5.2 Structural, Mechanical and Tribological Properties of As-Deposited MoS_x Films

In this section the impact of the High Power Impulse Magnetron Sputtering (**HiPIMS**) deposition parameters on the structural, mechanical and frictional properties of the deposited MoS_x films⁶ is analyzed. It is shown that the stoichiometry of the films is mainly influenced by the bias-voltage and the heating power during the deposition process. The mechanical properties of the films are mostly influenced by pulse frequency and heating power. For low values of these parameters, a shortening of the Mo–S bond length is determined, leading to an enhanced interatomic coupling and to the formation of small crystallites at the film’s surface. Furthermore, a possible friction reducing reorientation process is detected. The findings are published in reference [Kok20].

Details on Film Deposition. The MoS_x films are deposited on polished X38CrMoV5-1 steel (1.2343) substrates with a mean roughness Ra of (4.9 ± 0.5) nm and a hardness of (8.1 ± 4.0) GPa on (100)-oriented silicon wafers, using an unbalanced magnetron sputtering device (see Section 3.2.1). Prior to the deposition process, the surfaces of the substrates are cleaned with a gas-etching mixture of argon and krypton, followed by a booster-etching process using two molybdenum targets in order to improve the adhesion of the MoS_x films. Onto the prepared surfaces, the films are deposited using the HiPIMS method. Here, a MoS_2 target (99.5% purity, 3 kW cathode power) is used at a chamber pressure of 350 mPa. An overview of the sputtering parameters is shown in Table 5.6. The sputtering time is set to 3800 s for all sample IDs.

Details on Film Characterization. The surfaces and cross-sections of the MoS_x films are characterized by SEM (see Section 3.2.3). The composition of the films is determined us-

⁶The subscripted x indicates that the stoichiometric composition of the sputtered coatings cannot be predicted prior to the deposition process. After the deposition, the composition can be determined using EDS (see Section 3.2.4).

Table 5.7 t - and p -values of the statistical analysis on the influence of the pulse duration t_p , the pulse frequency f_p , the substrate temperature T_S and the bias-voltage U_B on mechanical film properties.

Parameter	Roughness		Coating Thickness		Hardness		Coefficient of Friction	
	t-value	p-value	t-value	p-value	t-value	p-value	t-value	p-value
t_p	2.51	0.07	5.68	< 0.01	-0.84	0.45	0.00	1.00
f_p	0.65	0.55	11.00	< 0.01	-3.29	0.03	1.25	0.28
T_S	0.53	0.62	5.85	< 0.01	-2.90	0.04	0.86	0.44
U_B	-0.15	0.89	-6.33	< 0.01	0.60	0.53	-2.51	0.07

ing EDS and XRD (see Section 3.2.4, details on measurement parameters are described in reference [Kok20]). The XRD peaks are fitted using a Lorentzian peak function to determine their intensities and their FWHM. In addition, the arithmetic mean roughness Ra is measured using a confocal white-light microscope (Nanofocus μ surf). Using a confocal Raman spectrometer (see Section 3.1.2), inelastically scattered spectra of the acoustic and optical vibrations of the MoS_x lattice are collected at laser powers below 1 mW and integration times of 100 s. Furthermore, the hardness and elastic modulus are determined using nanoindentation experiments (see Section 3.2.2, Poisson ratio $\nu_P = 0.2$). Using a ball-on-disc tribometer, the coefficient of friction is determined (see Section 3.2.2). Here, MoS_x coated and uncoated 100Cr6 (1.2067) counter bodies are used. The experiments are conducted in ambient air with a relative humidity of 50 % at room temperature. The device is set to 1500 load cycles at a radius of 8 mm, with a velocity of 0.4 m/s. The applied normal force is 5 N.

Structure and Thickness of the MoS_x Films. Most of the films show a dendritic needle-like structure (see Figure 2 in reference [Kok20]). The homogeneity of the coatings becomes more pronounced for short pulse durations, with high bias-voltages and low heating powers (ID8, ID5 and ID2). A statistical analysis of the roughness showed that none of the deposition parameters influences the roughness significantly (see Table 5.7). Nonetheless, an increasing pulse duration seems to increase the surface roughness (compare roughness values for ID8, ID1 and ID9 in Table 5.6). For short pulse durations, a low surface roughness is observed.

In contrast, the deposition parameters affect the coatings' thickness. The thickness of a coating increases with an increase of the pulse frequency, the substrate temperature or the pulse duration (see also the positive t -values in Table 5.7), whereas a stronger bias-voltage leads to a reduction of the coatings' thickness. The highest impact on coating thickness is given by the pulse frequency, the other deposition parameters are of comparable influence, whereas the bias-voltage is the only parameter that reduces the thickness of the coating.⁷

Chemical Composition. As evaluated by EDS and shown in Table 5.6, the S/Mo ratios of the HiPIMS sputtered films are higher than the expected ratio of MoS₂. For the DC sputtered reference sample a lower S/Mo ratio (1.59 ± 0.02) is determined, demonstrating

⁷An additional analysis of the impact of the peak current density on the film-thickness is presented in reference [Kok20], but omitted here.

Table 5.8 t - and p -values of the statistical analysis on the influence of the pulse duration t_p , the pulse frequency f_p , the substrate temperature T_S and the bias-voltage U_B on structural and compositional film properties.

Parameter	(100)/(002) Ratio		(002) Peak Position		S/Mo Ratio		FWHM of (100) Peak					
	t-value	p-value	t-value	p-value	t-value	p-value	t-value	p-value				
t_p	1.55	■	0.20	-0.93		0.40	-0.36		0.74	-1.84	■	0.14
f_p	1.68	■	0.17	2.38	■	0.08	-0.58	■	0.59	-4.72	■	0.01
T_S	0.49		0.65	7.27	■	< 0.01	-1.80	■	0.15	-2.54	■	0.06
U_B	1.15	■	0.32	0.86		0.44	0.70	■	0.52	1.93	■	0.13

that the sputtering method plays a superordinate role for the composition of the films. For an increased substrate temperature among the HiPIMS-sputtered films, the S/Mo ratio seems to be reduced towards 2. This is in accordance with Aubert et al., who reported that an increased substrate temperature from 100 °C to 300 °C leads to a decrease of the S/Mo ratio from 1.90 to 1.71 for DC sputtered thin films [Aub90]. For bipolar pulsed magnetron sputtered MoS_x thin films with even lower S/Mo ratios in the range of 0.8 to 1.5 are reported [Lau00]. Additionally, Bülbül et al. reported that an increasing bias-voltage leads to a reduction of the S/Mo ratio due to re-sputtering of the sulfur atoms and an enhanced ion bombardment [Bül16]. This re-sputtering is attributed to be responsible for the low sulfur content in the DC sputtered sample. Here, the larger duty cycle of the direct-current bias voltage (DC sputtering) compared to the synchronized-pulsed bias voltage (HiPIMS sputtering) leads to a higher selective re-sputtering of the sulfur atoms in the DC sputtered sample.

Diffraction Analysis of the MoS_x Films. Figure 5.7 shows the collected XRD spectra of the as-deposited MoS_x films. Here, the diffraction peaks at around 44° and around 64° stem from the 100Cr6 substrate of the coatings. The other diffraction reflexes are attributed to symmetry planes of MoS₂, namely the (002) plane at around 14°, the (100) plane at around 33°, the (101) plane at around 34° and the (110) plane at around 49° [Gra12; Vai21]. As reported by Aubert et al. [Aub90], MoS_x coatings with concentrations of $x < 1.2$ develop an amorphous crystallization phase. For coatings with concentrations $1.4 \leq x \leq 1.8$ the hexagonal structure is observed and for MoS_x coatings with sulfur concentrations $x > 1.9$ a more crystalline phase with a (110) orientation is observed. Accordingly, the occurrence of multiple crystallographic orientations in the investigated thin films indicates that the films are of polycrystalline structure [Soj17].

Additionally to the polycrystallinity of the films, the diffraction peaks of the MoS_x appear to be broadened. The broadening might be caused by residual strain, leading to crystalline stacking errors, or it is caused by a size narrowing of the surface crystallites [Sha15]. The average crystallite size D_{cryst} can be estimated by the Scherrer equation $D_{\text{cryst}} = K\lambda/\Gamma\sin\theta$, with the Scherrer constant⁸ $K_S = 0.89$, the excitation wavelength λ , the full width at half maximum Γ and the diffraction angle θ [Ing14]. For the (100) peak the crystallite size is estimated to $D_{\text{cryst}} = (9.4 \pm 1.0)$ nm.

⁸Named after Paul Scherrer (*1890; †1969). A detailed review on Scherrer constants or shape factors is presented in reference [Lan78].

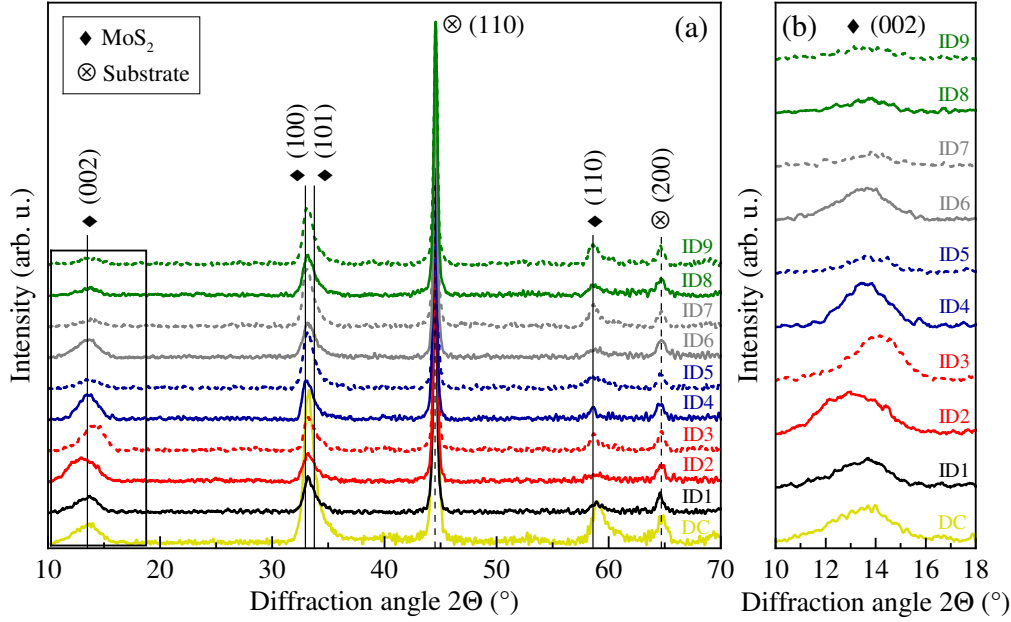


Figure 5.7 (a) XRD spectra of the deposited MoS_x films, substrate peaks and MoS₂ Bragg peaks are indicated. (b) Detail view on the shifting of the (002)-MoS₂ Bragg peak. Reproduced with permission from reference [Kok20].

Furthermore, a considerable decrease of the FWHM in the (100) XRD peak is observed with increasing pulse frequency. This decrease is caused by an increased number of atoms with higher kinetic energy being transferred to the sample surface. Due to the increased mobility of the atoms, more time is needed to dissipate their energy, which is sufficient to position the atoms on surface energy minimized lattice sites (for more details see reference [Lüt15a]), leading to a more crystalline lattice and, respectively, to a reduced FWHM of the XRD peak. The same tendency is observed for increased substrate temperatures. Additionally, the increased mobility of the atoms leads to a reduction of the internal strain in the coatings, resulting in stoichiometry ratios close to 2.

The appearance of the (002) peak in the XRD spectra indicates that there are well-stacked MoS_x layers [Gol13]. The peak's FWHM broadens with increasing bias voltage and shifts with heating power (see also Table 5.8). This shift is attributed to layer-distance changes, which seemingly is reduced for increased temperatures, since the diffraction angle is inversely proportional to the layer distance (see Section 3.2.4).

Raman Scattering Analysis of the MoS_x Films. The deposited coatings are analyzed by means of Raman scattering. The collected spectra are shown in Figure 5.8. Additionally, a typical Raman spectrum of mechanically exfoliated MoS₂ is shown. The figure is separated in (a) a low-frequency and (b) a high-frequency panel. In panel (a) the disorder-induced Raman peaks around 150 cm⁻¹, 180 cm⁻¹ and 230 cm⁻¹ are shown [Mig15], while in panel (b) the optical E_{2g}, A_{1g} and 2LA(M) Raman modes around 376 cm⁻¹, 405 cm⁻¹ and 450 cm⁻¹ are displayed [Pla15].

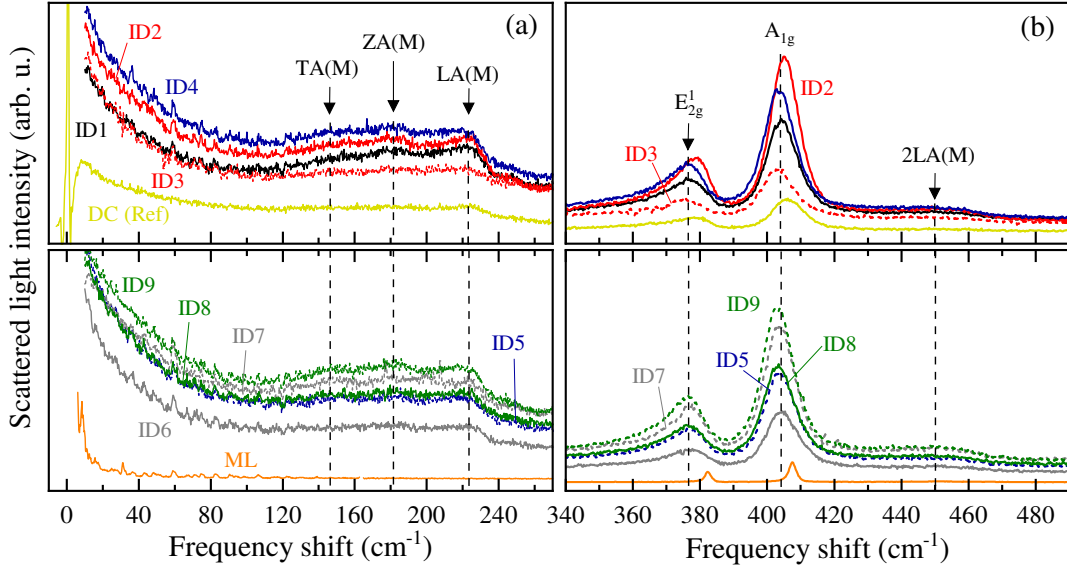


Figure 5.8 Raman spectra of MoS_x films and an exfoliated MoS_2 monolayer (ML). (a) Their acoustic phonon modes and (b) optical phonon modes are shown. Exemplary, the laser line is shown at 0 cm^{-1} for the spectrum of the DC sputtered film. The spectrum of the monolayer is divided by a factor of 100. Image taken with permission from reference [Kok20].

The mean positions of the corresponding Raman lines are indicated by vertical dashed lines. Here, the Raman lines of coating ID2 with $P_{\text{H}} = 500 \text{ W}$ (ID3 with $P_{\text{H}} = 5500 \text{ W}$) are shifted to higher (lower) frequencies. This behavior is inverse to the heating power of the coatings. For a low heating power, the Raman frequencies are increased, while for a high heating power the Raman frequencies are down-shifted. This behavior may be explained by taking into account that the Raman scattering frequency is proportional to the interaction strength and inversely proportional to the bond length and effective mass (see also Section 2.1.5): This proportionality indicates that a reduction of the scattering frequency hints at a decreased coupling strength and an increased bond length. These effects agree with a relaxation of the lattice at elevated temperatures (see reference [Lüt15a]). Concluding, the lattice relaxation in these coatings is reflected by a bond-length adjustment.

The line widths of acoustic and optical phonon modes are broad compared to line widths typically observed [Mol19; Naj12]. This might be due to variations in bond coordination and bond termination, which is originated in the non-uniformity of the S/Mo ratios, and additionally in the variations in bond length and coupling strength, which is originated in the degree of non-single crystallinity. Taking these effects into account, the slightly sharpened acoustic phonon modes of the ID1, ID2 and ID9 coatings might indicate an increased homogeneity of their structure. Here, the lattice might be slightly more uniform and the spatial distribution of the crystallite sizes more homogeneous.

In general, the Raman frequencies of the coatings are uniformly shifted to lower frequencies compared to the MoS_2 monolayer spectrum (see orange line in Figure 5.8). Usually a thickness-dependent change of the spectral distance between the E_{2g} and A_{1g} modes can be observed [Naj12] (see also Section 2.3.3). Here, the uniform frequency decrease might

Table 5.9 Mechanical properties of the HiPIMS deposited MoS_x films. Listed are the sample ID, the hardness, the elastic modulus E , the coefficient of friction for uncoated 100Cr6 counter bodies μ_{100Cr6} and the coefficient of friction for MoS_x coated counter bodies μ_{MoS_x} .

ID	Hardness/ GPa	E / GPa	μ_{100Cr6}	μ_{MoS_x}
DC	0.4 ± 0.1	33.7 ± 3.1	0.05 ± 0.01	0.10 ± 0.03
1	0.7 ± 0.1	50.9 ± 3.4	0.13 ± 0.01	0.14 ± 0.02
2	2.0 ± 0.2	78.8 ± 8.8	0.12 ± 0.02	0.11 ± 0.01
3	0.5 ± 0.1	41.6 ± 3.9	0.15 ± 0.05	0.18 ± 0.08
4	0.4 ± 0.1	28.6 ± 2.6	0.16 ± 0.03	0.14 ± 0.03
5	0.7 ± 0.1	47.4 ± 6.9	0.10 ± 0.02	0.09 ± 0.01
6	2.2 ± 0.1	90.3 ± 8.6	0.10 ± 0.02	0.10 ± 0.02
7	0.3 ± 0.1	31.5 ± 4.2	0.13 ± 0.02	0.13 ± 0.02
8	0.9 ± 0.1	60.1 ± 7.2	0.11 ± 0.02	0.10 ± 0.02
9	0.4 ± 0.1	39.9 ± 2.9	0.11 ± 0.02	0.12 ± 0.03

indicate an adsorption of about 10 % of nitrogen at the surfaces of the coatings [Qia18], but shall not be discussed here in more detail.

Mechanical Properties of the MoS_x Films. The mechanical parameters of the MoS_x coatings are determined as previously described. The results are summarized in Table 5.9, with hardness values ranging from 0.3 GPa to 2.2 GPa and elastic moduli ranging from about 30 GPa to approximately 90 GPa. Comparable values were reported in the literature [Vie13; Zha16].

Figure 5.9 shows the dependence of the hardness on the deposition parameters. Here, a clear dependence on heating power and pulse frequency is observed. The hardness is increased from 0.5 GPa to 2 GPa by lowering the heating power or pulse frequency. The elastic modulus shows a similar behavior. Here, a reduction of the pulse duration increases the elastic modulus.

In the following a model of hardness developed by Gao et al. is briefly presented to explain the behavior of the MoS_x films [Gao10]. In the suggested model, the hardness is proportional to $\exp(-1.2I_{ion})/L^{2.5}$, with the ionicity I_{ion} and the bond length L . Here, the ionicity I_{ion} is proportional to $1 - \exp(-(X_A - X_B)^2/4)$, with the electronegativities X for the materials A and B. From these proportionalities it becomes clear that, for a constant bond length, an increased ion-

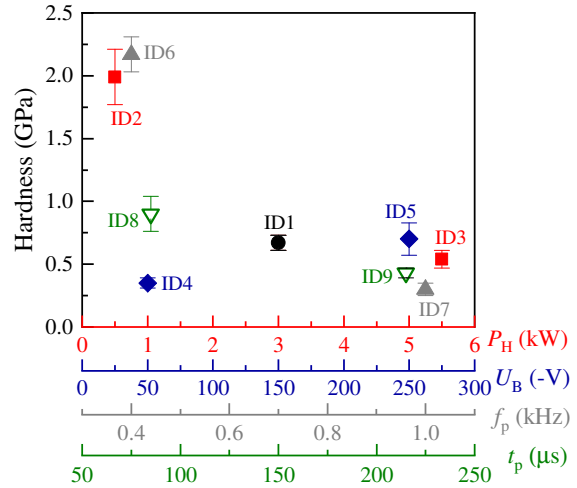


Figure 5.9 Dependence of the hardness of the MoS_x coatings on the deposition parameters. Image taken with permission from reference [Kok20].

icity leads to a reduced hardness. This can be transferred to the MoS_x films: Here, the surplus of sulfur atoms induces a more positive charge on the molybdenum atoms, increasing the ionicity, which leads to low hardness values. This is true for most of the coatings, except ID2 and ID6, which both show an increased hardness. For ID2, the Raman studies show a reduced bond length, which transfers to an increased hardness. For ID6 the XRD analysis reveals the smallest crystallite sizes of all coatings investigated. Here, the hardness might be increased due to the reduced grain size (so called Hall-Petch strengthening, see Chapters 1 and 7 in reference [Zha10]).

Tribological Properties of the MoS_x Films. In ball-on-disc experiments the coefficients of friction are determined, using uncoated and MoS_x coated counter bodies. The coefficients for both material combinations are presented in Table 5.9. Here, no significant difference between the two materials is detected. Overall, the coefficient of friction ranges from 0.09 ± 0.01 to 0.18 ± 0.08 , which corresponds to values reported in the literature [Vie13; Ser17]. A minimum of the coefficient of friction was reported for S/Mo ratios around 1.5 by Aubert et al. [Aub90]. The low coefficients of friction in the films investigated might be ascribed to their basal (002) orientation [Vie12; Mol19].

Investigating on the correlations of the coating properties and the coefficient of friction, it is shown that increases in the (100)/(002) ratio, the (100)-FWHM, the S/Mo ratio and a decrease in hardness are all related to a reduction of the coefficient of friction. While the findings for the FWHM and the S/Mo ratio agree with the literature, the correlation of the (100)/(002) peak is contradictory to literature [Mol19; Zha01]. Didziulis et al. determined that only the initial coefficient of friction depends on the orientation of the deposited films [Did90] and a basal orientation forms during tribological contact. In the present coatings, the low coefficients of friction for initial (100) orientation might hint at an enhancement of the reorientation process forming basal (002) layers in tribological contacts.

Summary and Conclusion. Summing up, several influences of the deposition parameters on the properties of MoS_x coatings are determined. For example, high bias voltage and heating power reduce the structural inhomogeneity, while an increased heating power also shifts the S/Mo ratio towards 2. A weak heating power leads to a shortening of the MoS_x bond lengths and high substrate temperatures reduce the inter-layer spacing along the (002) direction. All coatings show to be non-stoichiometric and polycrystalline. Here, the findings of Raman spectroscopy and XRD complement each other. Furthermore, the smoothness of the films may be adjusted by changing the pulse duration, while the films' hardness depends on the heating power and pulse frequency. The coefficient of friction is not significantly affected by the variation of the deposition parameters, but coating properties might be used as indicators for its value. The coefficient of friction is increased for more homogeneous structures, and reduced for an increased initial (100) orientation, which is reorientated to basal (002) orientation in the tribological contact. This reorientation is also observed in Section 4.3, where a low coefficient of friction is favored by a crystallographic reorientation of the worn MoS_x films to the basal (002) direction. The present reorientation in the tribological contact might be enhanced by the dense (100) HiPIMS films, requiring further investigations.

In conclusion, insights to the microstructural properties of self-lubricating, as-deposited

MoS_x films, their bond-length variation and inter-layer spacing are given. Furthermore, a crystallographic reorientation process favoring reduced coefficients of friction might be enhanced by HiPIMS deposition.

5.3 Raman Characterization of Thermally Annealed MoS_x Films

In this section post-growth-annealed MoS_x thin films⁹ are investigated with Raman spectroscopy in order to determine the structural and tribological properties of the coatings. The investigation determined a temperature dependent reduction of the residual strain. Furthermore, an emerging Raman line at 40 cm⁻¹ is observed for high-temperature annealed coatings, indicating more shear resistant MoS_x films. Additionally, the coefficients of friction of the films are analyzed in ball-on-disc tests, revealing a decrease with lowering the sulfur/molybdenum ratio. The results are published in reference [Mol19].

Details on Film Deposition. The MoS_x films are deposited on polished 16MnCr5 steel (1.7131) with a surface roughness Ra of (3.1 ± 0.6) nm using the HiPIMS technique (see Section 3.2.1). Prior to film deposition the specimen are heated, cleaned and booster etched (for details see reference [Mol19]). Additionally, in order to improve film adhesion, a MoN inter-layer of 1 μm thickness is deposited on the specimen. Onto the prepared samples, multiple series of MoS_x films are deposited. For the first series, the cathode power is set to 3 kW, with a pulse frequency of 400 Hz, a pulse duration of 85 μs, a bias voltage of -150 V and a heating power of 300 W. For the second series, the cathode power is set to 3 kW, with a pulse frequency of 700 Hz, a pulse duration of 215 μs, a bias voltage of -250 V and a heating power of 3 kW (see reference [Mol19]). These processes resulted in a thickness of all deposited MoS_x coatings in the order of several micrometers.

Vacuum Heating. The deposited MoS_x films are annealed at different temperatures T_{an} (300 °C, 400 °C, 500 °C and 600 °C) in a vacuum oven (Torvac), at a pressure of approximately 10⁻⁵ mbar. For each annealing temperature one film of each series is heated up to T_{an} at a rate of 10 K/min with a subsequent dwell time of 2 h. The samples are cooled down in vacuum to room temperature by turning off the heating system of the vacuum oven.

Details on Film Characterization. The different films are characterized with X-Ray Diffraction (XRD) (see also Section 3.2.4). Here, $\lambda_{\text{Cu-K}\alpha} = 1.5419 \text{ \AA}$ is used for survey spectra and $\lambda_{\text{Cr-K}\alpha} = 2.2911 \text{ \AA}$ for detailed spectra. The MoS₂ XRD signals of interest ((100) and (002) reflexes) are fitted using Voigt profiles (see Section 2.1.4 for details on different line profiles).

For spectroscopic analysis, the coatings are investigated at room temperature with confocal Raman scattering (see Section 3.1.2). The specimen are resonantly excited with 633 nm laser excitation (see Section 2.1.7), through a 20× microscope objective with a power of approximately 600 μW. The samples are checked for degradation after each measurement. No degradation is observed. The collected light is dispersed by a grating with 900 grooves/mm.

⁹The subscripted x indicates that the stoichiometric composition of the sputtered coatings cannot be predicted prior to the deposition process. After the deposition, the composition can be determined using EDS (see Section 3.2.4).

Table 5.10 Coating IDs with the corresponding annealing temperatures T_{an} , (100)/(002) intensity ratios I_{12} of the respective XRD MoS₂ peaks, their fitted line widths, $\Omega_{100}^{\text{XRD}}$ and $\Omega_{002}^{\text{XRD}}$, and the EDS-determined S/Mo ratios.

ID	$T_{\text{an}}/^\circ\text{C}$	I_{12}	$\Omega_{100}^{\text{XRD}}/^\circ$	$\Omega_{002}^{\text{XRD}}/^\circ$	S/Mo ratio
1a	–	2.06	2.28 ± 0.05	3.71 ± 0.13	1.61 ± 0.03
1b	300	1.80	2.18 ± 0.06	3.60 ± 0.11	1.63 ± 0.04
1c	400	1.50	2.31 ± 0.05	3.62 ± 0.07	1.70 ± 0.05
1d	500	0.55	1.98 ± 0.05	2.52 ± 0.03	1.80 ± 0.01
1e	600	1.67	2.04 ± 0.20	2.15 ± 0.03	1.66 ± 0.03
2a	–	0.33	0.65 ± 0.03	3.52 ± 0.05	1.25 ± 0.01
2b	300	7.20	0.66 ± 0.02	4.55 ± 0.19	1.24 ± 0.01
2c	400	2.04	0.81 ± 0.04	3.43 ± 0.04	1.28 ± 0.01
2d	500	1.02	0.68 ± 0.02	3.33 ± 0.02	1.30 ± 0.04
2e	600	1.38	0.79 ± 0.06	2.69 ± 0.02	1.19 ± 0.03

Here, a notch filter¹⁰ is used in order to resolve Raman shifts as low as 10 cm^{-1} with respect to the laser line. Only Stokes scattered light is collected and analyzed. The spectra are recorded with an integration time of 300 s and 18 repetitions. In order to compare the different spectra, their intensity is normalized to the maximum of the Raman line observed at 408 cm^{-1} . The nonlinear background of the spectra is modeled by cubic splines and eliminated by subtraction, while the different Raman lines are fitted by Lorentzian functions.

Additionally, tribological tests are performed, to determine the coefficient of friction of the different coatings (see Section 3.2.2). Balls of 100Cr6 steel are slid for 1500 cycles against the films at a velocity of 0.4 m/s and a normal force of 5 N. The topography is pictured using SEM (see Section 3.2.3), whereas the stoichiometry is determined by EDS (see Section 3.2.4).

The Composition of the MoS_x Films. Table 5.10 summarizes the temperature dependent results from XRD and EDS analysis of the deposited coatings.

First, their stoichiometry is analyzed. Here, the S/Mo ratio of the as-deposited coatings is determined to 1.61 ± 0.03 for ID 1a and to 1.25 ± 0.01 for ID 2a. Both ratios are lower than the chemical composition of the MoS₂ sputtering material. The lower stoichiometry of ID 2a may be explained by the difference in heating power of the two coating series (300 W for Series 1, 3000 W for Series 2), which is directly related to the substrate temperature. With increasing substrate temperature the S/Mo ratio decreases [Aub90]. Furthermore, not only the substrate temperature influences the S/Mo ratio, but also the bias voltage. It is reported, that the S/Mo ratio decreases with increasing bias voltage [Bül16], which is the case for the films investigated. Here, the bias voltage is -150 V (-250 V) for Series 1

¹⁰A notch filter is a multilayer rejection filter. By variations of thickness, order and refractive index of the different layers, the optical transmission is tailored to reject a narrow spectral region (e.g. the Rayleigh line), while allowing transmittance for all other frequencies (e.g. Raman scattered light). More details on filters and their properties are described in Chapter 8.2.5 of the book by McCreery [McC00b].

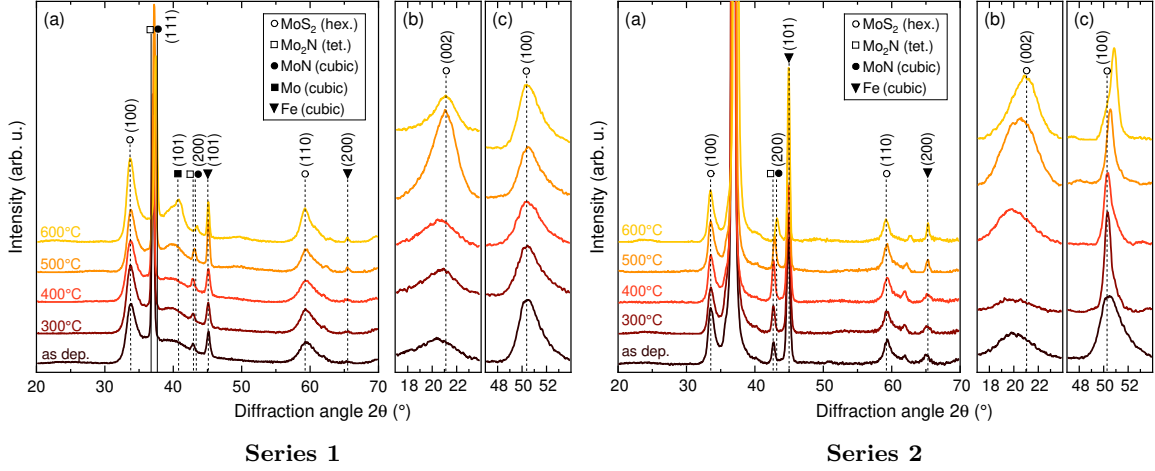


Figure 5.10 (a) Cu-K α excited XRD survey spectra of the MoS_x coatings of Series 1 and Series 2. In (b) and (c) the detailed, Cr-K α excited (002) and (100) MoS₂ reflexes are shown. The spectra are shifted for visual clarity. Figures reproduced from reference [Mol19].

(2). The intensified bias voltage leads to an increased ion bombardment, resulting in an increased re-sputtering of sulfur. Here, sulfur is re-sputtered preferably, as its atomic mass is smaller than the atomic mass of molybdenum, and therefore sulfur atoms are excavated easier from the coated surface. Additionally, for both coatings an increase in the S/Mo ratio is observed for an increase in annealing Temperature T_{an} up to 500 °C. The ratios peak at 1.80 ± 0.01 for ID 1d and 1.30 ± 0.04 for ID 2d. With a further increase in annealing temperature to 600 °C, the S/Mo ratio is reduced for both coatings.

Second, the crystallographic structure of the coatings is analyzed with XRD (see Section 3.2.4). The recorded spectra are shown in Figure 5.10. Here, hexagonal MoS₂ (○), tetragonal Mo₂N (□), cubic MoN (●), cubic Mo (■) and cubic Fe (▼) reflexes are detected. They are marked by the corresponding symbols. For the MoS_x coatings, the typical (100), (002) and (110) MoS₂ reflexes of the hexagonal lattice structure are detected. Taking the annealing temperature into account, the intensity of the (100) reflex behaves rather stable, whereas the intensity of the (002) reflex increases with rising T_{an} . This rise in intensity results in a decrease of the (100)/(002) intensity ratio I_{12} (compare Table 5.10). The intensities of the (002) and (100) reflexes are slightly higher for Series 1 coatings than for Series 2 coatings. Additionally, Series 2 coatings show low S/Mo ratios. Therefore, the (002) basal plane orientation is more pronounced here than in the coatings of Series 1 [Bül16].

Furthermore, the line widths Ω^{XRD} of the reflexes are listed in Table 5.10. The width of an XRD reflex is determined by the size of the nano-crystallites in the coating and by the residual strain in the material [Kho11] (see also Sections 3.2.4 and 5.2). Here, an influence of annealing temperature on $\Omega_{001}^{\text{XRD}}$ and $\Omega_{002}^{\text{XRD}}$ is observed, they decrease with increasing T_{an} . This decrease shows that thermal annealing leads to strain relaxation and recrystallization processes are thermally induced (see reference [Lüt15a]). Furthermore, it was reported that the crystallinity of room temperature sputtered MoS₂ films can be improved by laser-annealing [Sir19].

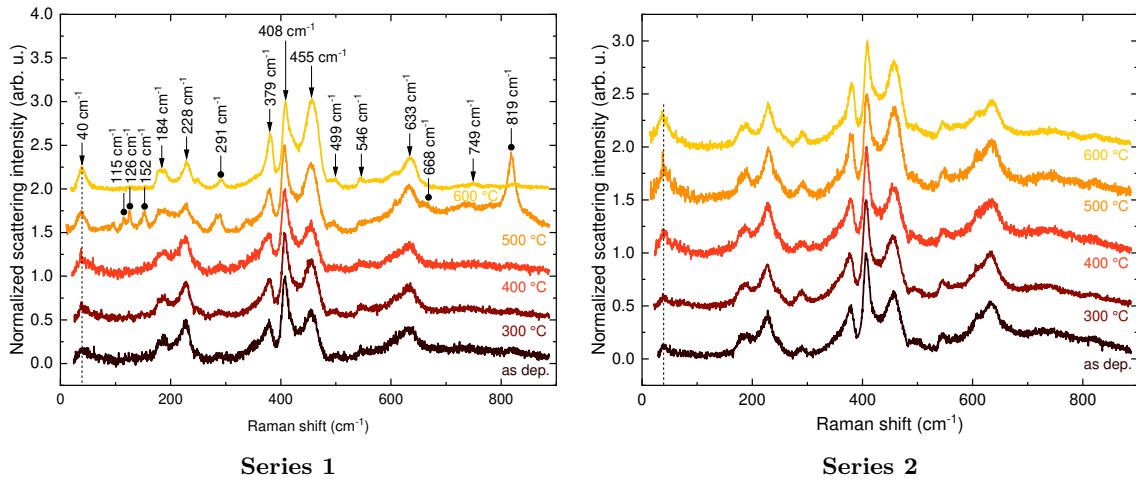


Figure 5.11 Raman spectra of as-deposited and annealed MoS_x coatings of Series 1 and Series 2. The excitation wavelength is set to 633 nm. The most prominent lines are marked, where MoS_2 related lines are marked with arrows and MoO_3 related lines are marked with disc shaped arrows. The spectra are shifted for visual clarity. Figures reproduced from reference [Mol19].

Finally, cubic MoN related signals are detected in the recorded XRD spectra, namely the (200) and the (111) reflexes. The reflexes are located between the tetragonal $\gamma\text{-Mo}_2\text{N}$ and the cubic (101) Fe reflexes [Til19b]. The presence of cubic and tetragonal molybdenum nitride reflexes indicates that the MoN inter-layer is of polycrystalline structure.

Description and Assignment of the Observed Raman Modes. The deposited and annealed MoS_x coatings are studied with resonant Raman scattering. The collected Raman spectra are shown in Figure 5.11. The marked scattering signals are mostly attributed to resonantly excited multilayer or bulk MoS_2 modes [Fre99; Win11; Kha15]. The Lorentzian fitted FWHM of selected Raman modes are shown in Table 5.11. Here, the 379 cm^{-1} and the 408 cm^{-1} mode show a FWHM of approximately 5 cm^{-1} , contrasting to literature, where a FWHM of 2.5 cm^{-1} (4.5 cm^{-1}) is reported for the 379 cm^{-1} (408 cm^{-1}) Raman mode in two layers of MoS_2 [Ber14] and close to 2 cm^{-1} for bulk like MoS_2 . The recorded values of the investigated films exceed the FWHMs reported in the literature, even coatings which are annealed at high temperatures, which showed a reduction of their FWHMs. However, for an increased annealing temperature, the Raman line intensities are increased, which is visible by the improved signal-to-noise ratios in Figure 5.11. Furthermore, at 40 cm^{-1} a high-temperature emerging Raman line is observed for both coatings (see dashed vertical line in Figure 5.11). Additionally, the 291 cm^{-1} line is boosted by higher annealing temperatures. Comparing both coating series shows more pronounced Raman lines for the second series at 291 cm^{-1} and 546 cm^{-1} , as well as a more distinct double-peak structure around 600 cm^{-1} .

Not only typical MoS_2 modes are detected, but also MoO_3 related modes for coating ID 1d, which are marked with disc-shaped arrows in Figure 5.11. The modes appear at 115 cm^{-1} , 668 cm^{-1} and 819 cm^{-1} [Seg95; Mes98]. The modes at 126 cm^{-1} and 152 cm^{-1}

Table 5.11 Fitted FWHM Ω of selected Raman modes for the as-deposited and 600 °C annealed coatings. The tilting of the arrows in the last column indicates changes in the FWHM. Here, neglectable (\rightarrow), small (\searrow) and big (\uparrow , \downarrow) changes are marked, while the up (down) directions represent an increase (a decrease) in the FWHM.

ν_N/cm^{-1}	$\Omega_{1a}/\text{cm}^{-1}$	$\Omega_{1e}/\text{cm}^{-1}$	$\Omega_{2a}/\text{cm}^{-1}$	$\Omega_{2e}/\text{cm}^{-1}$	
228	10.0 ± 0.3	9.5 ± 0.3	12.9 ± 0.3	11.6 ± 0.3	\downarrow
291	16.0 ± 4.7	5.0 ± 0.3	7.0 ± 0.8	5.1 ± 0.4	\downarrow
379	5.9 ± 0.6	5.4 ± 0.2	5.9 ± 0.4	5.8 ± 0.2	\rightarrow
408	5.5 ± 0.3	5.0 ± 0.2	5.7 ± 0.2	5.3 ± 0.2	\searrow
455	11.4 ± 0.4	12.7 ± 0.1	14.3 ± 0.4	15.3 ± 0.2	\uparrow
633	20.1 ± 1.5	11.8 ± 0.4	22.8 ± 1.1	17.8 ± 0.7	\downarrow

may be attributed to Mo–O–Mo deformation modes, shifted by 3 cm^{-1} (5 cm^{-1}) and 6 cm^{-1} (8 cm^{-1}) [Seg95] ([Mes98]).

Summing up, the observed Raman lines are mostly MoS₂ signatures. Raman signatures of MoS_x would result in significantly different spectra, as shown by Deng et al. [Den16]. Taking the penetration depth of 633 nm laser light in MoS₂ into account, approximately at least the top 60 nm of the deposited coatings consist of MoS₂ (see also Section 2.1.6) [Ull18].

Detailed Analysis of Broadening and Signal-to-Noise Ratio. First, the previously described line broadening of the Raman signatures is analyzed. This broadening may be attributed to the non-uniform stoichiometric S/Mo ratio of the coatings. Here, a variation of coordination and termination of bonds might increase the line width of the Raman scattering frequencies. Furthermore, the line broadening might resemble the degree of non-crystallinity of the coatings, as bond length and bond strength strongly influence the position of the Raman signal (see Section 2.1.5).

Next, the signal-to-noise ratio is analyzed. Here, for high-temperature annealed coatings an increase in signal-to-noise ratio and a narrowing of the FWHMs is observed. These two effects indicate an improvement of the homogeneity of the structural and chemical composition of the MoS₂ films [Car83a; Pin83]. It might be stated that the spatial distribution of the crystallite size of the MoS₂ is more homogeneous. However, local strain relaxes due to thermal annealing, and therefore the lattice is arranged more uniformly. This leads to less variations in the bond length and interaction strength of the molybdenum and sulfur bonds. This conclusion agrees with the natural bulk MoS₂ spectra reported by Windom et al. [Win11] and growth induced-strain distortions in technically deposited MoS₂ [Kat17]. To relax the structural and chemical distortions even more, higher annealing temperatures and longer annealing times might be used. Nevertheless, care must be taken, because at temperatures of 900 °C chipping and vaporization of sulfur might occur [Won17].

Detailed Analysis of Selected Raman Modes. In the following the Raman lines at 40 cm^{-1} , 546 cm^{-1} and 291 cm^{-1} are discussed, beginning with the signature at 40 cm^{-1} . The Raman mode at 40 cm^{-1} may be attributed to several different modes. Here, the Layer-Breathing (**LB**) mode, the E_{2g}² shear mode and an electronic Raman scattering process are discussed.

First, the signature may be attributed to the LB mode [Lui19]. Due to inter-layer coupling of MoS₂ layers the LB mode arises. Here, vertical displacement of the MoS₂ layers leads to a restoring van-der-Waals force [Zha13a]. The strength of the restoring force, and therefore the shape of the LB mode, basically depends on the layer-to-layer distance, rather than on lateral lattice distortions. This was observed for twisted and for Bernal-stacked¹¹ bilayers of MoS₂ [Lui15]. Bernal-stacked layers show a higher frequency of the LB mode than twisted bilayers, as the packing is less efficient here, and therefore the inter-layer coupling is weaker. It is crucial to note, that the LB mode only emerges in bilayers with atomically clean surfaces [Lui15]. Following this argumentation, if the Raman signature measured at 40 cm⁻¹ is caused by the LB mode, the mode indicates that Bernal-stacked bilayers of MoS₂ are present at the surface. In other words, pairs of MoS₂ layers are formed within nm sized crystallites at the surface of the coating.

Second, the Raman signature might be attributed to the van-der-Waals-driven E_{2g}² shear mode. The frequency of the mode strongly depends on the number of MoS₂ layers [Zen12]. For MoS₂ bilayers Zeng et al. measured 22 cm⁻¹ and 32 cm⁻¹ for bulk material, whereas they report theoretical values of up to 45 cm⁻¹. To determine whether the shear mode or the LB mode is causing the Raman signature at 40 cm⁻¹ further investigations are needed. Of particular interest is whether the Raman shift can be explained by a layer dependence.

Instead of assigning the Raman signature at 40 cm⁻¹ to a LB mode or to a shear mode, it might as well stem from an electronic Raman scattering process [Zen12]. The electronic scattering process is only observable under quasi-resonant excitation, which is stable with respect to changes in the number of layers. Here, in future experiments the behavior of the Raman line could be studied, by scanning the excitation laser wavelength through the exciton resonance of the MoS₂. If the process stems from an electronic transition, the Raman line should become resonantly enhanced if the laser wavelength matches the exciton resonance.

Furthermore, by tuning the excitation wavelength to shorter wavelengths the penetration depth into the MoS₂ decreases and could help determining the origin of the Raman signature at 40 cm⁻¹ (see Section 2.1.6).

In the following paragraph the Raman line at 546 cm⁻¹ is analyzed in more detail. The line occurs in spectra of both coating series, but is slightly more intense for Series-2 coatings. The mode may be attributed to E_{2u} + ZA symmetry [Pla15]. The E_{2u} is an inactive Raman mode and the ZA mode resembles a one-phonon-forbidden out-of-plane vibration. Observing this dark Raman mode hints at an extrinsic second-order process, where a free exciton scatters inelastically a phonon (electron-phonon interaction) and elastically a defect (electron-impurity interaction) [Pla15; Men85]. The defect could be a stacking fault in growth direction along the *c* axis of the MoS₂. Such defects are typical for layered materials due to low formation energy [He14]. Therefore, the signature measured at 546 cm⁻¹ could be used to indicate stacking faults in the MoS₂ coatings. As this line does not show a temperature dependence, it may be stated that the thermal annealing mostly modifies the strain distribution in the coatings and the layer interactions, instead of the stacking faults.

Lastly, the Raman line at 291 cm⁻¹ is discussed. This mode is observed in all coatings of Series 2 and in high-temperature annealed coatings of Series 1. This signature indicates the

¹¹Bernal stacking is the repetition of two alternating layers (ABABAB). It is named after John Desmond Bernal (*1901; †1971). Three repeating layers are called rhombohedral stacked layers (ABCABC).

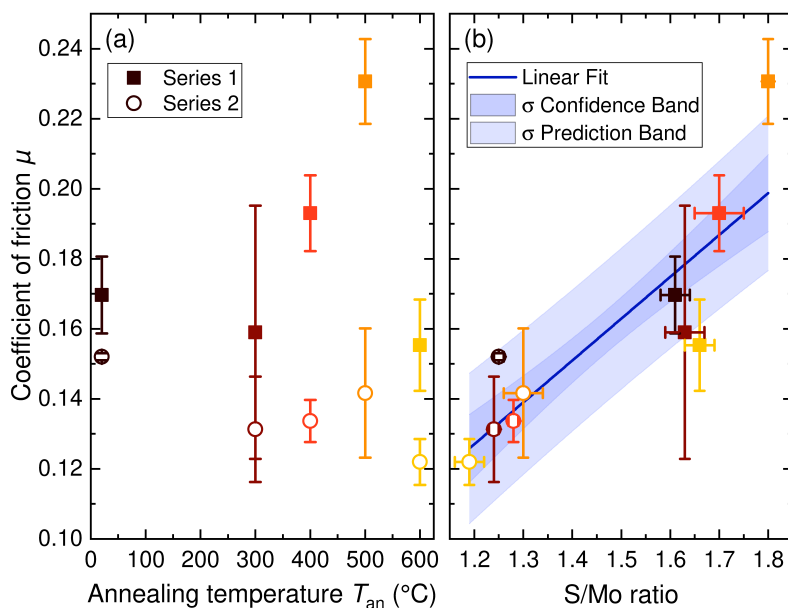


Figure 5.12 (a) Behavior of the coefficient of friction on the annealing temperature for coating Series 1 (■) and Series 2 (○). Error bars are the standard deviation of the mean value. (b) Behavior of the coefficient of friction on the S/Mo ratio. The x -errors are taken from Table 5.10. Reproduced from reference [Mol19].

presence of MoO₃ at the coating surfaces [Die02]. The mode stems from wagging modes of the terminal oxygen atoms [Win11]. The higher absolute scattering intensity of this mode in Series 2 coatings shows that the formation of MoO₃ is slightly more probable in these coatings, than in Series 1 coatings. This is explained by the higher molybdenum content in the coatings (see Table 5.10), supplying more molybdenum atoms for oxidation. Furthermore, the presence of the MoO₃ line at 291 cm⁻¹ shows that MoO₃-related bonds are formed not only in cases of vacuum leakage (compare coating 1d), but also in other processes.

Tribological Behavior. The MoS_x coatings are additionally tested in a ball-on-disc tribometer, to determine their coefficient of friction μ in dependence of their annealing temperature T_{an} . This dependence is shown in Figure 5.12 (a). Here, Series 2 shows a generally lower coefficient of friction than Series 1, independent of the annealing temperature. The coefficient of friction for both series seems to increase with annealing temperature, with a deviation between room temperature and 300 °C. Furthermore, at 600 °C a drop in μ is detected, leading to the lowest measured values. Here, the coefficient of friction for coating 1e amounts to $\mu = 0.16 \pm 0.01$ and the coefficient of friction for coating 2e amounts to $\mu = 0.12 \pm 0.01$.

An additional view on the coefficient of friction is generated by plotting it against the S/Mo ratio, as shown in Figure 5.12 (b). Here, a rise of μ is observed with a rise in the S/Mo ratio. In the figure a linear fit with its σ confidence bands and σ prediction bands are shown. The slope amounts to 0.12 ± 0.03 , whereas the y -axis is intercepted at -0.02 ± 0.04 . While these results differ from the behavior observed by Aubert et al. [Aub90], they suggest

a proportionality of the coefficient of friction and the S/Mo ratio.

The previous Raman scattering analysis showed, that the high-temperature-annealed coatings are structurally more homogeneous, with relaxed strain and layer-to-layer interaction. This interatomic effects attribute to the MoS₂ layer's resistance against structural changes (shear forces) and the coefficient of friction is expected to be larger in these coatings than in low-temperature-annealed coatings. This could explain the observed dependency of μ on T_{an} , even though more data of samples at additional annealing temperatures is required to solidify this argument (e.g. 50 °C steps over the whole range from room temperature to 600 °C).

For coating 1d, high values of friction are observed, which might result from the considerable amount of MoO₃ at the surface, as MoO₃ features a higher coefficient of friction than MoS₂ [Erd00]. However, the surface oxidation in most coatings is of comparable level, leading to a variation free impact of the influence of MoO₃. As shown in Figure 5.12 (b), the S/Mo ratio seems to be of greater influence on the frictional behavior of the coatings. Here, for coatings with low S/Mo ratio, the (002) basal plane is more pronounced (see XRD analysis), forming more oxidation resistant MoS_{*x*} coatings. The surface-parallel basal plane exhibits closed sulfur layers that lead to lower coefficients of friction [Vie12; Vie13].

The strong decrease of μ , for coatings annealed at 600 °C, is of special interest. Here, the coatings show a sudden improvement of their lubricating properties. Additionally, changes in the Raman signatures are observed for the A_{1g} (408 cm⁻¹) and the 2LA mode (455 cm⁻¹), as well as the double-peak signature at about 600 cm⁻¹. These changes might be caused by a preferred formation of the basal oriented (002) MoS₂ layers, which improves their lubrication properties [Win11; Vie12].

Future Experiments. The sliding of two surfaces against each other is usually improved by MoS₂, at least for contact temperatures below the boiling temperature of the sulfur component [Ouy13]. Therefore in future studies, coatings with specific compositions need to be analyzed. Here, the S/Mo ratio as well as the amount of MoO₃ could be controlled by the HiPIMS process parameters. An increased MoO₃ content may be used to improve the wear resistance of the MoS₂ films, as shown by Centers [Cen88].

Furthermore, Raman studies of the worn contact areas of the coated specimen and their counter-part surfaces before and after the ball-on-disc experiments could give further insight into the underlying mechanisms. Additionally, the influence of different ambient atmospheres should be investigated [Don96], as this is still not fully understood.

Summary and Conclusion. Summing up, the MoS_{*x*} coatings investigated are of polycrystalline structure with S/Mo ratios of about 1.7 (Series 1) and 1.2 (Series 2). The S/Mo ratio is influenced by the substrate temperature, the bias-voltage and the annealing temperature. Here, an increasing substrate temperature leads to a decrease of the S/Mo ratio, whereas an increase of the post-growth annealing temperature results in an increase of the S/Mo ratio.

Investigating the thermally annealed MoS_{*x*} coatings with XRD and Raman spectroscopy reveals a relaxation of non-uniform strain, by analyzing the corresponding line widths. In addition, the homogeneity of the film's structural and chemical composition is improved at high temperatures, which is drawn from the overall Raman scattering intensity.

Remarkably, a Raman signature at approximately 40 cm⁻¹ emerges for high temperature annealed coatings. This mode is attributed to an enhanced inter-layer interaction, which depends on the inter-layer distance and the van-der-Waals forces. This signature may stem from a layer-breathing or a shear mode. Observing this Raman line hints at an improved shear resistance of the annealed MoS_x coatings, which is substantiated in the increase of the coefficient of friction. Furthermore, the coefficient of friction is linearly proportional to the S/Mo ratio, where small S/Mo ratios lower the friction, featuring a preferred (002)-basal orientation parallel to the substrate (see also Sections 4.3 and 5.2).

The Raman forbidden mode at 546 cm⁻¹ might be used as an indicator of stacking faults. Due to close-to-resonance excitation (633 nm), and therefore strongly enhanced Raman signals, the observation of this mode is possible. Additionally, weak MoO₃ signatures are detected with Raman scattering spectroscopy.

In conclusion, Raman scattering signatures may be used to estimate the microstructural properties of post-growth annealed MoS_x films. Here, a low frequency Raman mode might be used to estimate the shear resistance of a coating, while a Raman forbidden mode might be used to detect stacking faults in a coating.

Chapter 6

Optical Characterization of Tribological Amorphous Carbon at Steel Surfaces

The formation of carbon-based tribofilms on tribological surfaces is not only observed at catalytically active surfaces as detected by Erdemir et al. [Erd16], but at a wide variety of systems as described by Hoffman et al. [Hof16]. They reported on several carbon films that unintentionally formed at sliding metal-metal interfaces. Depending on the field of research, the carbon films are named differently (friction polymers, diamond-like carbon, varnish, etc.). Nevertheless, all of these carbon films have in common that they form through frictional processes and influence their tribological system. Some of the parameters of the underlying tribological system are the operating temperature, the pressure between the bodies in contact, the duration of the mechanical load, the type of the lubricant, environmental conditions and modification elements within the contacting surfaces (see also reference [Czi15a]).

In the present chapter multiple parameters of the tribofilm formation in steel-steel contacts are investigated by Raman scattering mappings. An overview of the experimental design is shown in Figure 6.1. Here, the varied parameters (atmosphere, pairings, lubricants, number of rotations and temperature), their variation ranges and the conducted experiments (ball-on-disc testing and Raman mapping) are shown. The coefficients of friction are determined with a ball-on-disc tribometer, while Raman spectroscopy is used to generate spatially-resolved Raman images of selected surface regions. Additionally, Principal Component Analysis (**PCA**) is used to handle the complex data set. The analysis of the data reveals two different reaction pathways for the tribofilm formation, with one path favoring carbon film formation, while the second path favors the formation of iron oxides. In the selection of the reaction path oxygen is determined to play a key role.

Sample Preparation. To investigate the formation of amorphous carbon in the tribological contact, 100Cr6 steel (1.2067) specimen with a diameter of 40 mm are polished to a surface roughness with Ra smaller than 3 nm. Multiple stages are performed to test the samples. In Stage I, the initial parameters (load and number of load cycles) are determined. The results are used for the following stages, listed in Table 6.1. The Stages II, III and V investigate on the temperature and runtime dependence of the tribological process in air, while Stage VI investigates on the temperature dependence in argon atmosphere. The influence of the lubricants on the tribological process is addressed in Stages IV, VII, VIII and IX. Here, non-lubricated samples, high-carbon content, low-carbon content and low-water content lubricants are used. Similar experiments are performed in argon and nitrogen atmosphere in Stage X. Additionally, three samples are PVD-coated by a chromium, molybdenum or

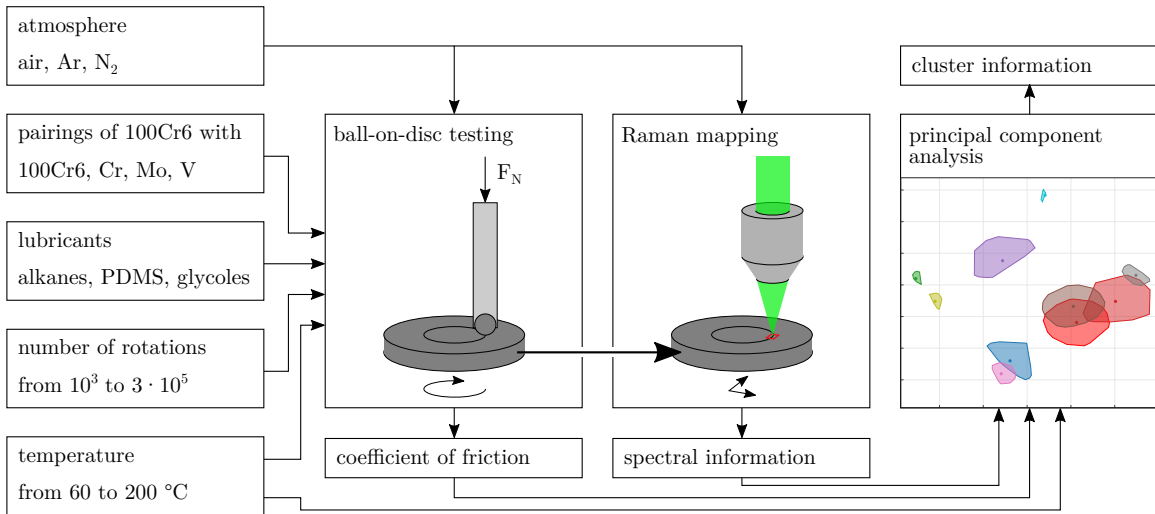


Figure 6.1 Overview of the investigated tribological system, with the input parameter ranges and the overall procedure. For a set of parameters, ball-on-disc tests are performed. From these tests, the specimen, kept in the selected atmosphere, are optically tested. Here, a Raman mapping is collected at a randomly chosen surface area in the wear track (indicated by the red square). Additionally, the circular (wear test) and linear (optical test) movements of the sample are indicated by the subjacent arrows. From these tests, output parameters are generated. The output parameters are the coefficient of friction (wear test) and the spectral information (optical test) of the sample. For final analysis, the temperature and the two output parameters are used in a PCA to get information on the different clusters present in the collected data.

vanadium layer (Stage IX). The specimen are tested in a ball-on-disc tribometer (ball radius $r_{\text{ball}} = 3 \text{ mm}$) with the different parameter combinations listed in Table 6.1. Here, the temperature T , the number of load cycles N_r in the unit of 10^3 revolutions, the atmosphere¹ and the lubricant² are varied. The respective atmosphere is present during the heating and cooling procedure of the tribometer. Subsequent to the tribometer tests, the samples are cleaned with a tissue to remove excessive oil. The non-air prepared samples are stored in argon atmosphere to prevent atmospheric contamination. Their Raman spectroscopic investigations are also performed in an inert atmosphere (see Section 3.1.2).

Details on Lubricants. The lubricants used are listed in Table 6.2. Here, a Poly Alpha Olefin (**PAO**), a Poly DiMethyl Siloxane (**PDMS**), a corn oil and two glycols are used. Their Raman spectra are shown in Figure 6.2. The spectra are comparable to spectra reported in the literature (see reference [Jay03] for PDMS, reference [How01] for corn oil, references [Mac64; Mat72] for ethylene glycol and references [Mac64; Mat87] for diethylene glycol.). For the Optigear Synthetic X320, a Raman spectrum is not found in the literature. Independent of the lubricant, no Raman signatures that indicate amorphous carbon are detected. Here, neither a D- nor a G-peak is observed for the non-tribologically tested lubricant. Due to high fluorescence, the Raman spectrum of the base oil is not measurable.

¹For argon and nitrogen atmospheres a sufficient gas flow is used, while in air no gas flow is applied.

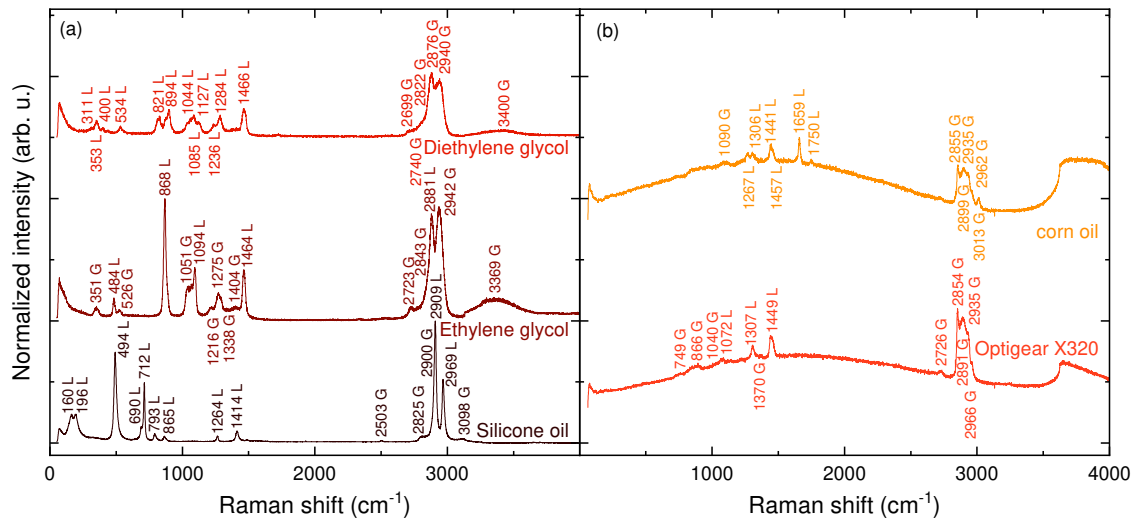
²2 ml of lubricant are used for each ball-on-disc experiment.

Table 6.1 Samples analyzed in the scope of this study. The load is always 10 N. The temperature T , the number of load cycles N_r (in 10^3 revolutions), the atmosphere and the lubricant (base oil (BO), ethylene glycol (EG), diethylene glycol (DEG), additive oil (add), dried oil (dry), silicone oil (SO) and corn oil (CO)) are presented. All samples are measured with approximately 10 mW (*1 mW) laser power using 532 nm laser excitation. The integration time per spectrum t_{spec} is listed as well. Additionally, the relative and absolute numbers of spectra showing amorphous carbon signatures are shown. The general error is ± 2 spectra. Furthermore, the mean coefficients of friction of the first 100 (μ_{start}) and last 100 (μ_{end}) measured coefficients of friction are given. Here, a running in phase of 100 data points and a running out phase of 10 data points is assumed and excluded from the calculations.

Stage	$T / ^\circ\text{C}$	N_r	Atmo.	Lub.	$t_{\text{spec}} / \text{s}$	Comment	a-C / %	μ_{start}	μ_{end}
II	60	300	air	BO	60		2.3 ± 0.9 (5/221)	0.120 ± 0.001	0.105 ± 0.001
II	90	300	air	BO	60		14.9 ± 0.9 (32/225)	0.106 ± 0.004	0.093 ± 0.001
II	120	300	air	BO	60		12.8 ± 1.3 (20/156)	0.109 ± 0.003	0.851 ± 0.039
III	95	300	air	BO	60		27.2 ± 1.2 (46/169)	0.080 ± 0.001	0.145 ± 0.002
III	100	300	air	BO	60		0 ± 0.9 (0/214)	0.096 ± 0.003	0.057 ± 0.002
III	105	300	air	BO	60		14.5 ± 2.9 (10/ 69)	0.114 ± 0.003	0.122 ± 0.004
III	150	1	air	BO	60		2.1 ± 2.1 (2/ 96)	0.109 ± 0.004	0.104 ± 0.004
III	150	10	air	BO	60		34.7 ± 1.3 (52/152)	0.105 ± 0.004	0.095 ± 0.004
III	150	10	air	BO	60	antibody	12.0 ± 8.0 (3/ 25)	0.105 ± 0.004	0.095 ± 0.004
III	150	50	air	BO	60		3.9 ± 1.1 (7/181)	0.104 ± 0.004	0.098 ± 0.000
III	150	50	air	BO	60	antibody	16.0 ± 8.0 (4/ 25)	0.104 ± 0.004	0.098 ± 0.000
III	150	100	air	BO	60		4.8 ± 1.0 (10/210)	0.091 ± 0.004	0.057 ± 0.001
III	150	100	air	BO	60	antibody	8.0 ± 8.0 (2/ 25)	0.091 ± 0.004	0.057 ± 0.001
III	150	100	air	BO	60	antibody	4.0 ± 8.0 (1/ 25)	0.091 ± 0.004	0.057 ± 0.001
III	150	300	air	BO	60		20.4 ± 0.9 (47/230)	0.092 ± 0.004	0.110 ± 0.001
III	150	300	air	BO	60		19.4 ± 1.0 (39/201)	0.092 ± 0.004	0.110 ± 0.001
IV	150	300	air	add	300		35.9 ± 1.3 (55/153)	0.113 ± 0.003	0.117 ± 0.001
IV	150	300	air	add	300		36.7 ± 4.1 (18/ 49)	0.113 ± 0.003	0.117 ± 0.001
IV	150	300	air	no oil	60		0 ± 5.4 (0/ 37)	0.611 ± 0.089	0.112 ± 0.005
V	90	300	air	BO	60	redo III	3.2 ± 0.9 (7/218)	0.121 ± 0.001	0.087 ± 0.000
V	95	300	air	BO	60	redo III	0 ± 1.0 (0/202)	0.093 ± 0.002	0.083 ± 0.002
V	100	300	air	BO	60	redo III	2.4 ± 2.4 (2/ 85)	0.107 ± 0.001	0.081 ± 0.001
VI	90	300	Ar	BO	60		12.9 ± 1.0 (27/209)	0.100 ± 0.003	0.086 ± 0.001
VI	90	300	Ar	BO	15		80.4 ± 0.9 (176/219)	0.100 ± 0.003	0.086 ± 0.001
VI	100	300	Ar	BO	10		74.8 ± 0.9 (163/218)	0.085 ± 0.002	0.341 ± 0.007
VI	120	300	Ar	BO	60		37.1 ± 0.9 (83/224)	0.098 ± 0.004	0.125 ± 0.004
VII	120	300	air	DEG	60		0 ± 2.6 (0/ 77)	0.131 ± 0.033	0.857 ± 0.005
VII	120	300	air	EG	60		0 ± 6.1 (0/ 33)	0.365 ± 0.215	0.880 ± 0.008
VII	120	300	air	SO	60		5.5 ± 1.4 (8/146)	0.262 ± 0.018	0.906 ± 0.046
VII	120	300	air	SO	15	retaken	0.0 ± 1.6 (0/124)	0.262 ± 0.018	0.906 ± 0.046
VIII	90	300	air	CO	60		36.7 ± 1.0 (72/196)	0.102 ± 0.002	0.879 ± 0.015
VIII	100	300	air	CO	60		64.2 ± 1.1 (120/187)	0.071 ± 0.001	0.830 ± 0.008
IX	120	300	air	dry	15		28.8 ± 0.9 (62/215)	0.096 ± 0.005	0.177 ± 0.006
IX*	120	300	air	dry	30		11.9 ± 1.3 (19/159)	0.096 ± 0.005	0.177 ± 0.006
IX	120	300	air	BO	15	Cr layer	25.1 ± 1.0 (51/203)	0.109 ± 0.002	0.316 ± 0.010
IX	120	300	air	BO	15	Mo layer	85.7 ± 1.0 (180/210)	0.120 ± 0.004	0.324 ± 0.007
IX	120	300	air	BO	15	V layer	98.6 ± 0.9 (208/211)	0.095 ± 0.002	0.088 ± 0.004
X	200	300	Ar	no oil	15		12.9 ± 1.7 (15/116)	0.692 ± 0.025	0.662 ± 0.025
X	120	300	Ar	EG	15		97.2 ± 1.1 (173/178)	0.439 ± 0.151	0.924 ± 0.040
X	120	300	N_2	EG	15		96.6 ± 1.7 (115/119)	0.482 ± 0.089	0.908 ± 0.017
X	120	300	N_2	BO	15		99.5 ± 1.0 (207/208)	0.113 ± 0.006	0.303 ± 0.006
X	90	300	N_2	DEG	15		81.5 ± 2.2 (75/ 92)	0.110 ± 0.037	0.972 ± 0.056

Table 6.2 Lubricants used in the tribometer tests. The molecules may be compared for $n = 18$, as $\geq 85\%$ of the fatty acids of corn oil are of this length [OBr09].

Lubricant	Main chem. composition	Comment
Base oil	C_nH_{2n}	Afton Chemical ISO VG (80 % non-hydrated, 20 % hydrated)
Base oil add	C_nH_{2n}	Optigear Synthetic X320, Poly Alpha Olefin (PAO)[Wie13]
Base oil dry	C_nH_{2n}	ISO VG dried with silica gel
Corn oil	$C_3H_5O_3[C_nH_{2n+1}]_3$	mazola germ oil
Silicone oil	$[C_2H_6OSi]_n$	M350 Carl Roth, Poly DiMethyl Siloxane (PDMS)
Ethylene glycol	$C_2H_6O_2$	
Diethylene glycol	$C_4H_{10}O_3$	

**Figure 6.2** Raman spectra of the lubricants used. Wavenumbers and the Lorentzian (L) and Gaussian (G) peak types are indicated.

Experimental Details. The Raman measurements are conducted with the setup described in Section 3.1.2. Throughout the experiments a 532 nm laser focused through a 20 \times objective is used. The corresponding integration times per spectrum t_{spec} are listed in Table 6.1. Additionally, the table contains the number of spectra showing amorphous carbon (**a-C**) signatures versus the number of fitable spectra of a mapping and their relative values. Generally, the measurements are conducted using a 900 grooves/mm grating, except for stages IX and X, where a more efficient grating (600 grooves/mm, 500 nm blaze angle) is used. For samples tested in argon or nitrogen atmospheres, the Raman spectra are recorded in a protective gas chamber (see Section 3.1.2).

At each wear track of a sample a randomly chosen surface region of $150 \times 150 \mu m^2$ is mapped by Raman spectroscopy (see also Section 3.3.2). Figure 6.3 (a) shows a typical wear track of such a surface region. Here, all samples show a several 100 μm wide wear track with grooves, while at some samples pitting is observed (compare Figure 6.5 (a), see also wear mechanisms in Section 2.2). With a step width of 10 μm a total of 225 Raman spectra are collected of each sample. The data is reduced to the Region Of Interest (**ROI**) (compare ROI in Figure 6.3 (b) ranging from approximately 900 cm^{-1} to 1800 cm^{-1}) and

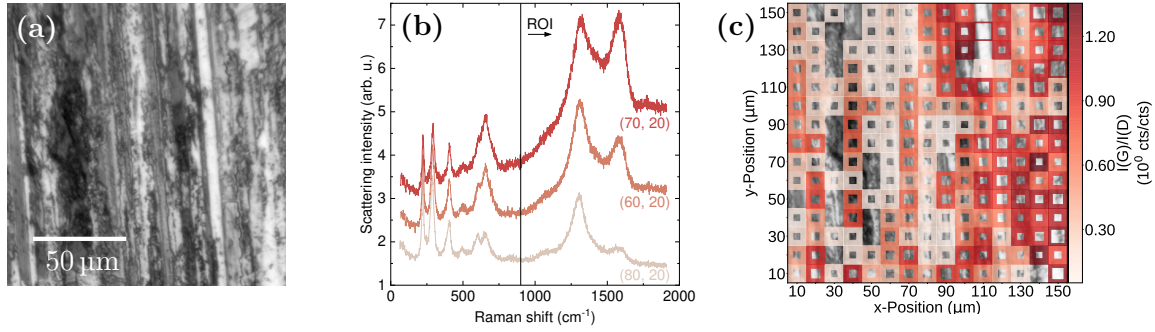


Figure 6.3 The displayed images are exemplarily taken at the chromium coated sample (Stage IX, 120 °C). (a) A worn sample region, (b) Raman spectra from this region and (c) the corresponding Raman mapping for the I_G/I_D ratio are shown.

processed as described in Section 3.3. Details on the procedure using the self-developed python package `spectrum analysis` are given in Appendix B.

Typical Raman Spectra at Random Surface Positions in Wear Tracks. Figure 6.3 (b) shows three typical Raman spectra detected among the different samples and sample positions. The peaks outside of the ROI are fitted using Lorentzian peak shapes, while the peaks in the ROI are fitted using linear combinations of Lorentzian and Breit-Wigner-Fano peak shapes, as suggested by Ferrari and Robertson [Fer00] (see also Section 5.1).

The Raman signatures in the spectral region outside the ROI detected at 222 cm^{-1} (A_{1g}), 287 cm^{-1} (E_g), 405 cm^{-1} (E_g) and 498 cm^{-1} (A_{1g}) stem from hematite [Far97], while the mode around 658 cm^{-1} stems from magnetite [Far97]³. Additionally, a weak mode around 385 cm^{-1} is fitted, but might as well be only an asymmetry of the hematite 405 cm^{-1} mode, as it is not reported in the literature. The mode around 598 cm^{-1} might be a shifted E_g mode of hematite or it stems from a thermal decomposition of wüstite, as reported by Faria et al. [Far97].

Inside the spectral ROI the intensive Raman line at around 1300 cm^{-1} might be assigned to two-magnon scattering of hematite [Mar77; Far97]. The mode is accompanied by a weak mode around 1100 cm^{-1} , which was also detected by Martin and Faria, but was not discussed further. Instead of attributing two-magnon scattering to the 1300 cm^{-1} mode, Massey et al. state that this mode results from two-phonon scattering [Mas90]. They calculate the magnetic Grüneisen parameter, which is well below theoretically expected values for a two-magnon process. Therefore, the attribution of a two-phonon process in hematite for the 1300 cm^{-1} mode is followed (see also Section 4.1). Additionally, Massey et al. suggested that the shoulder-like Raman mode around 1580 cm^{-1} is due to two-magnon scattering, which is followed as well.

The Raman modes observed around 1330 cm^{-1} and 1590 cm^{-1} are the D- and G-peaks of amorphous carbon [Fer00]. They stem from the excitation of the π -states of sp^2 hybridized carbon atoms (see also Section 2.3.2), with the D-mode corresponding to a ring-breathing mode and the G-mode corresponding to a chain-stretching mode. Furthermore, a weak unknown mode around 1770 cm^{-1} is detected. This mode is not reported in the literature.

³See also Section 2.3.1 for more details on the iron oxides and their properties.

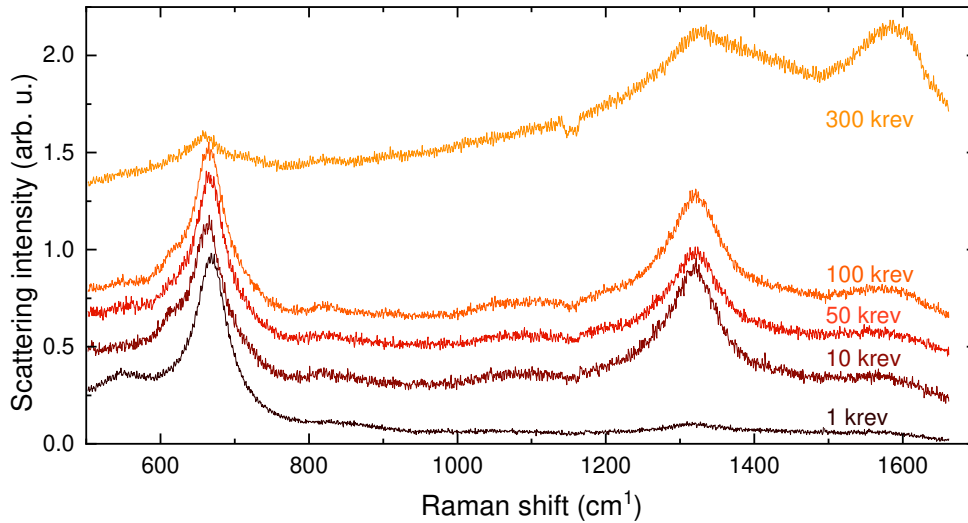


Figure 6.4 Raman spectra in dependence on the number of load cycles in 10^3 revolutions (krev). The dip at about 1150 cm^{-1} is caused by a contaminant particle, which is removed for subsequent measurements.

Only Kawashima et al. observed a Raman band in basal Highly Oriented Pyrolytic Graphite (**HOPG**) in this spectral region, but could not determine the origin of this mode [Kaw95].

Formation of Amorphous Carbon as Function of the Wear Test Parameters. The conditions for the formation of amorphous carbon films are analyzed in this paragraph. Therefore, different samples are tested in a ball-on-disc tribometer at room temperature with different loads (5 N and 10 N) and numbers of rotations (10^3 , 10^4 , 10^5 and 3×10^5). For 5 N load, hardly any wear is visible and no amorphous carbon signatures are detectable with Raman spectroscopy, therefore, these samples are omitted from this study. For 10 N load, at several random surface positions⁴ amorphous carbon signatures are detectable for numbers of rotations exceeding 10^5 cycles. Therefore, 10 N load and 3×10^5 load cycles are taken as experimental ball-on-disc parameters for all of the following samples (compare experimental parameters listed in Table 6.1).

Figure 6.4 shows the mean spectra of the load dependent measurements. Here, for small numbers of load cycles, a significant Raman feature around 660 cm^{-1} is observed, indicating the formation of magnetite. The small Raman peak around 540 cm^{-1} may also be attributed to magnetite [Far97]. With an increasing number of load cycles a second intensive Raman signature around 1300 cm^{-1} is observable, indicating the formation of hematite. Additionally, the Raman mode around 540 cm^{-1} vanishes with an increasing number of load cycles. A further increase of the load cycles up to 10^5 does not change the spectra significantly. Only for spectra exceeding 10^5 load cycles, changes are observed. Here, the hematite and magnetite signatures are damped and two new Raman signatures around 1300 cm^{-1} and 1600 cm^{-1} are observed, indicating the formation of amorphous carbon.

The described findings are also supported by the Raman images recorded of the Stage-

⁴Here, only single spectra are recorded at some randomly chosen spots.

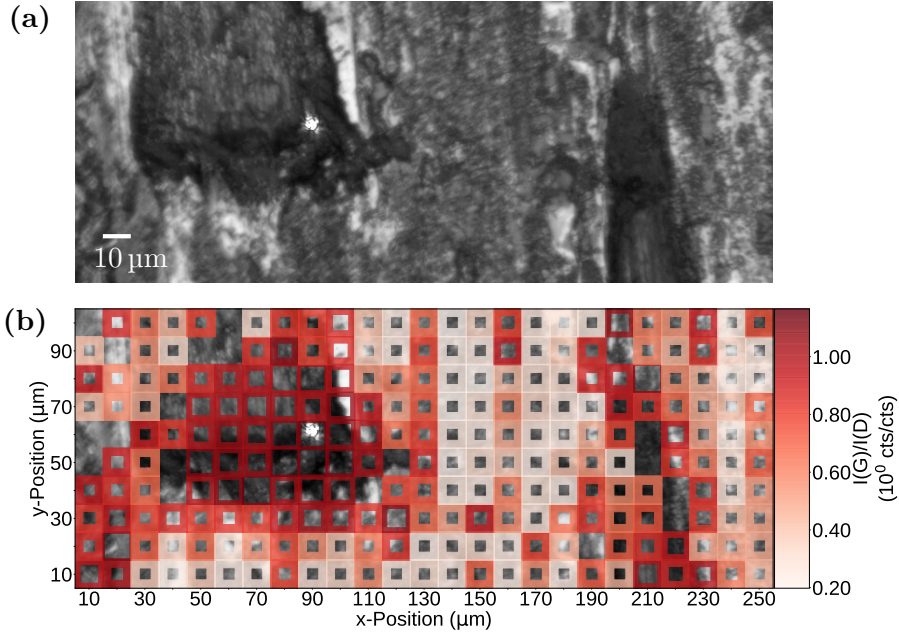


Figure 6.5 The displayed images are taken from Stage III, 150 °C, 300 krev. (a) The worn sample region with pitting areas and (b) the corresponding Raman mapping for the I_G/I_D ratio are shown.

III-samples kept at a temperature of 150 °C. Here, for $N_r = 1$ krev hardly any hematite is detected, while for an increased number of load cycles hematite is detectable. Furthermore, the number of amorphous carbon rich spectra increases with respect to the number of load cycles. Here, the sample with $N_r = 10$ krev with an a-C content of approximately 35 % builds an exception, as the selected surface region includes a pitting area, where most of the amorphous carbon accumulates. This carbon accumulation is also observed for other samples, like Stage III, 150 °C, $N_r = 300$ krev (compare Figure 6.5). The accumulation of amorphous carbon is discussed in greater detail in the following paragraph.

To sum up, the time-dependent formation of the tribofilm is as follows: Firstly, magnetite is formed, which is then further oxidized to hematite. In an additional step, which might be parallel or successive to the hematite formation, amorphous carbon forms in between the contacting surfaces. The amorphous carbon seems to accumulate in pitting areas. Most likely, the amorphous carbon forms from a decomposition of the lubricants used in the ball-on-disc experiments.

Raman Images of the Spectral Fitting Parameters. During the fitting procedure seventeen parameters are used to describe the spectral ROI of each spectrum. In order to simplify the analysis of 225 spectra per sample and numerous samples, for each parameter a Raman image (or Raman mapping) is generated (see also Section 3.3.2 and Appendix B). Exemplary mappings are shown in Figures 6.3 (c) and 6.5 (b). Here, the spatially resolved

I_G/I_D ratio is shown, which allows for simple identification of carbon rich Raman spectra⁵. The value of the parameter is color coded, while the width of each of the marker squares resembles the sum area under the curve of all peaks fitted in the spectrum. Here, for an enlarged region of the background image, a higher sum area under the curve is recorded. This allows for easily estimating the overall intensity of each spectrum with respect to the other spectra in the mapping. At surface positions where no signal is detected, the overlaying marker is omitted. In the background of the mapping the optical image of the sample is plotted. The exemplarily presented data in Figure 6.3 (c) shows that carbon rich regions are favorably in the right half of the investigated wear track region. Despite this tendency, no clear visual features of amorphous carbon accumulation are identified. For other samples, as exemplarily shown in Figure 6.5, pitting areas are identified as regions that favorably accumulate amorphous carbon. But it has to be noted that the amorphous carbon is not solely located in the pitting areas, as the signatures are still recorded outside these areas. Nevertheless, the probability of detecting amorphous carbon signatures in pitting areas is significantly increased, compared to other surface areas. This might indicate that the surfaces in the pitting areas are more tribological active than the surfaces in different regions [Hof16]. Here, tribologically formed amorphous carbon particles might precipitate out of the lubricant solution and accumulate in the pitting areas.

Layer Structure of the Tribofilm. In general, all of the collected spectra can be assigned to one of the following types of spectra: They are either hematite rich (compare sample position (80, 20) in Figure 6.3 (b)), carbon rich (see sample position (70, 20) in Figure 6.3 (b)) or a superposition of both phases (see sample position (60, 20) in Figure 6.3 (b)). In detail, a special focus should be drawn to the intensity of the magnetite line at about 660 cm^{-1} , which rises with the increase of the amorphous carbon signal, while the intensity of the hematite signatures decreases. Here, the penetration depth δ_p of light into the different materials can be accounted. As shown in Section 2.1.6, the wavelength-dependent penetration depth δ_p ranges from $\delta_{p, \text{a-C}} = 50\text{ nm}$ to $\delta_{p, \text{a-C}, 450^\circ\text{C}} = 250\text{ nm}$ for amorphous carbon, to $\delta_{p, \text{Fe}_2\text{O}_3} = 76\text{ nm}$ for hematite and to $\delta_{p, \text{Fe}_3\text{O}_4} = 470\text{ nm}$ for magnetite (see also Table 2.2). So for amorphous carbon and hematite signatures, the light penetrates approximately the first 100 nm of the tribofilm, while for magnetite signatures depths of approximately 500 nm are investigated. This observation and the run time dependence of the Raman signatures allow one to assume that the tribofilm has a layered structure. Seemingly, hematite builds the base of the film, with magnetite layered on top. Lastly, the film is covered with amorphous carbon.

The proposed layer structure is neither clearly disproved nor supported by the results of the laser power variation measurements from Stage IX. At some positions, the amorphous carbon signatures feature a lower intensity in accordance with lower applied excitation powers, while at other positions only iron oxide signatures are detected at low excitation powers instead of amorphous carbon signatures. To clarify this behavior additional investigations with a focus on excitation power are necessary.

⁵Carbon rich spectra show a I_G/I_D ratio close to one (red), while spectra with a small carbon content have ratios smaller than 0.5 (white).

Particle Sizes in the Tribofilm. The line widths of the Raman modes might supply some information on the particles present in the tribofilm [Gou07]. Chernyshova et al. for example showed that the FWHM of several hematite Raman lines changes with their particle size. They observed that the A_{1g} mode at around 230 cm^{-1} changes its width from 5 cm^{-1} to 9 cm^{-1} for particles with sizes 120 nm and 7 nm, respectively. The E_g mode around 410 cm^{-1} behaves similarly, changing its width from 10 cm^{-1} to 12 cm^{-1} for the same particle sizes [Che07]. In the present samples the observed FWHMs of the Raman lines are even broader. They are 16 cm^{-1} for the A_{1g} mode and 24 cm^{-1} for the E_g mode, indicating nano-sized particles⁶. The formation of small particles is also supported by the comparably broad FWHM (100 cm^{-1}) of the magnetite mode around 1300 cm^{-1} , which is usually around 60 cm^{-1} to 70 cm^{-1} for crystalline hematite [Mar20]. Furthermore, the absence of broad features of disorder-related longitudinal-optical phonon modes around 660 cm^{-1} and the tetrahedral defect-related T band around 690 cm^{-1} indicates that the hematite particles are larger than $(42 \pm 9)\text{ nm}$ [Sch17].

The situation for particle sizes of amorphous carbon is a bit different. Here, the coherence length L_a and thus the size of the a-C particles is coupled to the intensity ratio of the D- and G-peak [Mer17]. Depending on the particle size two relations were derived. Firstly, for particles bigger than 2 nm, the I_D/I_G ratio scales with L_a^{-1} (Tuinstra-Koenig relation). Secondly, for particles smaller than 2 nm, the I_D/I_G ratio scales with L_a^2 (Ferrari's relation). For the here observed I_D/I_G ratios ranging from 0.8 to 1.2, amorphous carbon particles with sizes of approximately 6 nm to 4 nm (Tuinstra-Koenig) or 1 nm to 2 nm (Ferrari) are present in the tribofilm [Fer00]. With typical carbon-carbon bond lengths of 0.15 nm [Rie18] the particles measure between 7 and 40 carbon-carbon bond lengths in diameter. Taking the typical line widths of the peaks of approximately 150 cm^{-1} into account, it is assumed that L_a is rather in the 1 nm to 2 nm range than in the 6 nm to 4 nm range (compare Figure 41 in reference [Rob02]).

In a first estimation the tribofilms consist of comparably large iron oxide particles of sizes exceeding 10 nm with small amorphous carbon particles of sizes in the nm range. In order to gain more detailed insight and a better particle size estimation other methods like XRD or AFM need to be utilized.

Configuration of the Amorphous Carbon. Raman spectra recorded at carbon-rich surface positions typically exhibit a G-peak which is more pronounced than the D-peak. The G-peak is sensitive to all sp^2 hybridized carbon bonds, while the D-peak is only sensitive to clusters of aromatic carbon rings [Chh00; Rob02]. Therefore, as both peaks are detected in the present amorphous carbon films (see for example Figures 6.3 or 6.6), carbon chains and aromatic carbon rings compose the amorphous carbon films. Taking the mainly linear structure of the lubricant molecules into account, it may be assumed that a linear configuration of the amorphous carbon is preferred, as linear amorphous carbon is easier to build from linear lubricant molecules, than six-fold aromatic amorphous carbon rings. Nevertheless, aromatic carbon rings are formed as well. As no additional T-peak around 1000 cm^{-1} is observed, a possible sp^3 content in the tribofilms does not exceed 20 % to 30 %, multi-wavelength Raman spectroscopy is needed to improve this estimation (see section 5.1).

⁶The differences in resolution for Chernyshova et al. (1.5 cm^{-1}) and the used setup (5 cm^{-1}) are neglectable (see also Appendix A.4)

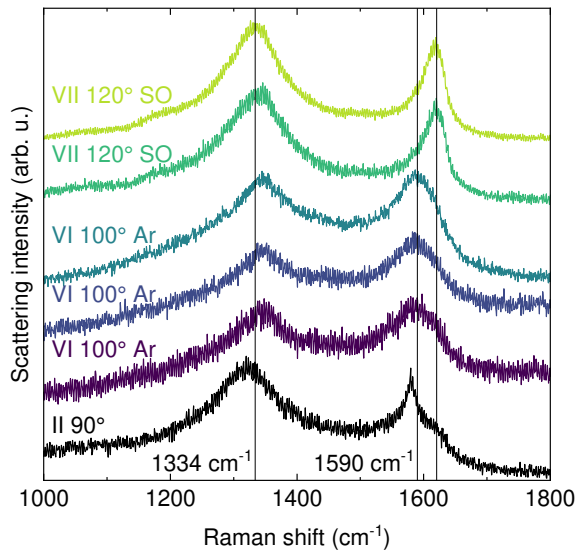


Figure 6.6 Narrowing of the amorphous carbon D (1334 cm^{-1}) and G (1590 cm^{-1}) Raman features at several samples. Additionally, a mode at 1620 cm^{-1} is observed.

They might be induced by flash temperatures (see Section 2.2.3). Using the theory of Archard for circular contacts, the maximum flash temperature⁷ is estimated to range from $11\text{ }^{\circ}\text{C}$ to $240\text{ }^{\circ}\text{C}$. With an additional bulk temperature of $120\text{ }^{\circ}\text{C}$, temperatures of up to $360\text{ }^{\circ}\text{C}$ may be reached for atmospheric conditions, leading to more structured amorphous carbon. The flash temperatures may also be roughly estimated by comparing the present Raman spectra to the spectra collected by Bhargava and Jacobsohn. This comparison leads to flash temperatures of $700\text{ }^{\circ}\text{C}$ or higher.

Summing up, the non-ordered sp^2 -bonded amorphous carbon is mainly formed by linear chains with some distorted six-fold rings, becoming more ordered at elevated temperatures. Most likely flash temperatures ranging from $130\text{ }^{\circ}\text{C}$ to $700\text{ }^{\circ}\text{C}$ are reached in the tribological contact.

Oxygen Presence Controls the Reaction Pathway of the Tribological Material. The comparison of the base oil series and the ethylene glycol series across different atmospheres shows strongly different tribofilms. For ball-on-disc tests in air, no (little) amorphous carbon is formed using ethylene glycol (base oil), whereas a high carbon coverage is detected for comparable tests in argon and nitrogen atmosphere (see Table 6.3). Here, ethylene glycol shows an amorphous carbon coverage of 97% in both atmospheres, while the base oil shows a carbon content of 37% in argon atmosphere and almost 100% in nitrogen atmosphere. Similar trends are detected for other sample combinations, which are also listed in Table 6.3 but do not include all three atmospheres. Additionally, the coefficient of friction significantly increases throughout the testing (compare μ_{start} and μ_{end}). Only for base oil lubrication at temperatures below $100\text{ }^{\circ}\text{C}$, the friction is not significantly increased. For base oil lubrication

Additionally at a few pitting areas, which are of intensive dark color in the visual image, a significant narrowing of the D-peak and especially the G-peak is observed. The spectra of interest are presented in Figure 6.6. Here, FWHMs of about 100 cm^{-1} are detected, compared to typical line widths of 150 cm^{-1} and more. A comparable narrowing of the Raman lines was also observed by Bhargava et al. in thermally annealed amorphous carbon films [Bha96]. They could correlate changes in Raman spectra at temperatures around $600\text{ }^{\circ}\text{C}$ with a release of defects in the amorphous carbon, increasing the short range order without changes in the correlation length L_a . Chhowalla and Jacobsohn observed a similar behavior [Chh00; Jac00]. As the here analyzed samples are not thermally annealed, the changes in the carbon structure have to be induced

⁷The flash temperature calculation is presented in Section 2.2.3, with all material parameters listed in Table 2.3.

Table 6.3 Samples sorted by amorphous carbon formation in dependence on the ambient atmosphere. All samples are exposed to 3×10^5 load cycles. The experimental parameters are described in the caption of Table 6.1.

Stage	T / °C	Lub.	$t_{\text{spec}} / \text{s}$	Atmo.	aC / %	μ_{start}	μ_{end}
II	120	BO	60	air	12.8 ± 1.3	0.109 ± 0.003	0.851 ± 0.039
VI	120	BO	60	Ar	37.1 ± 0.9	0.098 ± 0.004	0.125 ± 0.004
X	120	BO	15	N ₂	99.5 ± 1.0	0.113 ± 0.006	0.303 ± 0.006
VII	120	EG	60	air	0 ± 6.1	0.365 ± 0.215	0.880 ± 0.008
X	120	EG	15	Ar	97.2 ± 1.1	0.439 ± 0.151	0.924 ± 0.040
X	120	EG	15	N ₂	96.6 ± 1.7	0.482 ± 0.089	0.908 ± 0.017
II	90	BO	60	air	14.9 ± 0.9	0.106 ± 0.004	0.093 ± 0.001
VI	90	BO	60	Ar	12.9 ± 1.0	0.100 ± 0.003	0.086 ± 0.001
VI	90	BO	15	Ar	80.4 ± 0.9	0.100 ± 0.003	0.086 ± 0.001
III	100	BO	60	air	0 ± 0.9	0.096 ± 0.003	0.057 ± 0.002
VI	100	BO	10	Ar	74.8 ± 0.9	0.085 ± 0.002	0.341 ± 0.007
VII	120	DEG	60	air	0 ± 2.6	0.131 ± 0.033	0.857 ± 0.005
X	90	DEG	15	N ₂	81.5 ± 2.2	0.110 ± 0.037	0.972 ± 0.056

at 100 °C in air, the coefficient of friction is even reduced. Seemingly, the lubricating film does not remain intact in between the contacted bodies and the amorphous carbon does not improve the lubricating properties of the tribofilm. Through the different behavior of the tribofilm formation under different atmospheres, it is assumed that there are two underlying mechanisms influencing the tribofilm formation:

- The first reaction pathway, under the presence of atmospheric oxygen, is built by the oxidation of magnetite to hematite, with a subsequent or parallel formation of amorphous carbon. Here, the formation of iron oxides seems to be favored over amorphous carbon formation.
- The second reaction pathway, under oxygen-free atmospheres, is built by direct formation of amorphous carbon, without a concurring iron-oxidation process. In absence of the atmospheric oxygen the oxidation of iron is impossible, therefore eliminating the process, leading to a direct formation of amorphous carbon.

The observations of an increased tendency of amorphous carbon formation in oxygen-free atmospheres leads to the assumption that atmospheric oxygen selects the underlying mechanism of the tribofilm formation. Whether the tribo-formed amorphous carbon is beneficial or harmful for the tribological system cannot be evaluated. Here, the coefficient of friction is increased from start to end in most cases, but this tendency might be reasoned in the observed discontinuous behavior of the coefficient of friction throughout the ball-on-disc testing. This discontinuity is commonly observed in friction testing devices and is rooted in

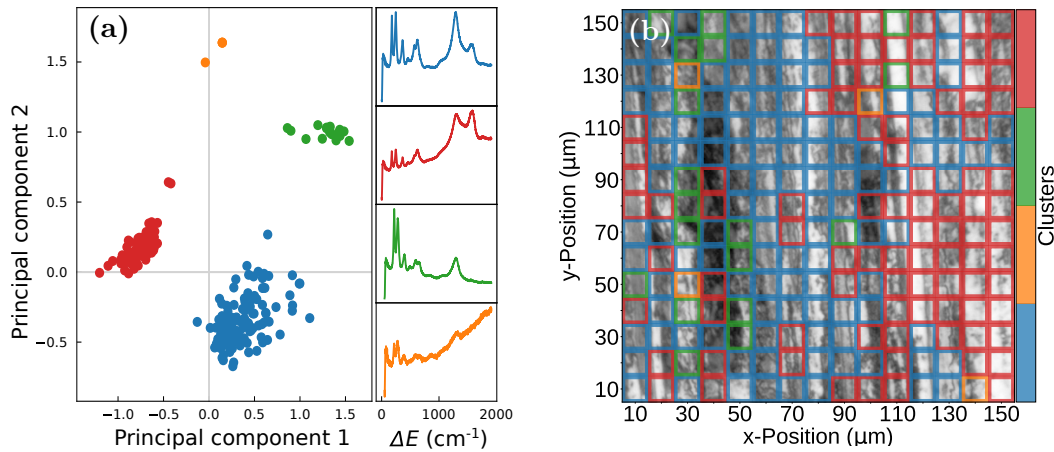


Figure 6.7 The displayed images are exemplarily taken from the chromium coated sample (Stage IX, 120 °C). Here, (a) the principal component analysis with the corresponding mean Raman spectra of the clusters and (b) the related spatially resolved clustered mapping are shown.

vibrations of the testing device or long-term changes of the sliding conditions (see reference [Lud00] for more details). To reduce these discontinuities, the testing conditions could be adapted accordingly, machine vibrations might be reduced or the long-term changes of the sliding conditions need to be reduced.

Principal Component Analysis of a Single Mapping. In order to reduce the parameter space and detect spectral similarities between the spectra of a single mapping, the parameters determined through the fitting procedure are analyzed with a Principal Component Analysis (PCA) (see Section 3.3.3). An exemplary analysis is shown in Figure 6.7. Each data point in the plot represents the projection of the spectral features of one spectrum into the space of the first two principal components. Here, four well separated clusters are detected in principal component space (see Figure 6.7 (a)). Additionally to the projection into the first two principal components, the mean spectra of each cluster are plotted. Here, the main Raman signatures are detected, as described before: The clustering algorithm detects clusters that are mainly hematite (green) and mainly amorphous carbon (red). Furthermore, a third cluster that is a transition between both signatures (blue) is detected. The fourth cluster (orange) shows two exceptions collected throughout the mapping, they do not match any of the three main clusters. Here, utilizing data reduction and clustering algorithms detects the previously described spectral similarities among multiple spectra, which allows for a fast identification of major spectral trends. This method is used to ease the analysis of huge data sets.

Figure 6.7 (b) shows the clusters plotted in a similar manner to the Raman mappings, with the optical image of the investigated sample region displayed in the background. Here, no clear correlation of optical features and cluster features is detected. This is also the case for all other samples. Only for pitting areas and non-fitable surface regions, a correlation of the optical image and the clusters is visible.

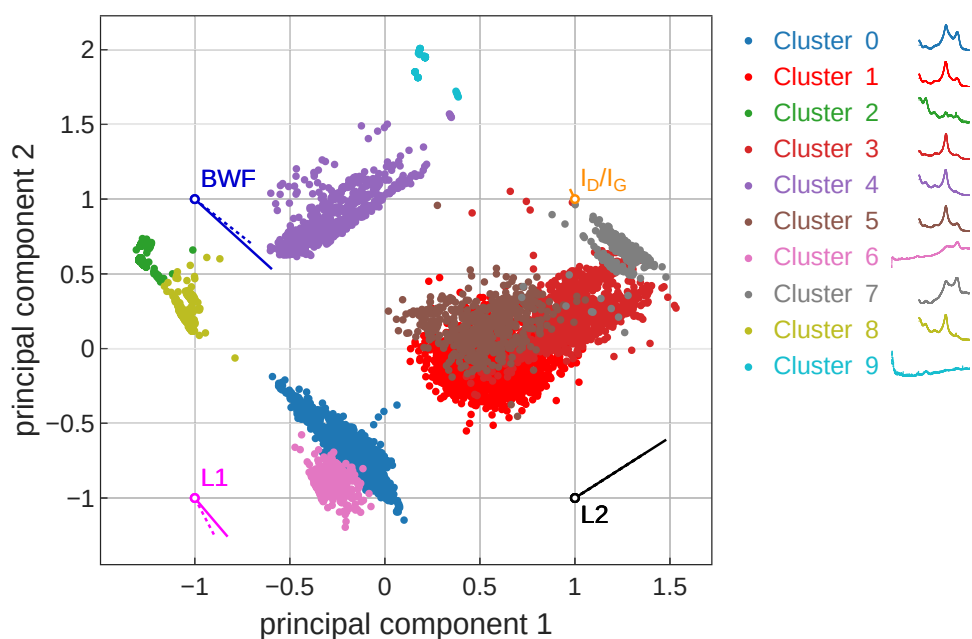


Figure 6.8 Projection of the complete a-C data set onto the first two principal components. The reduced space is divided into ten clusters, with the mean spectra of each cluster shown in the legend. The spectra range from 0 cm^{-1} to 2000 cm^{-1} . Here, Clusters 0, 6 and 7 show amorphous carbon signatures, Clusters 1 and 5 show a transition spectrum with small contents of amorphous carbon and significant contributions of hematite, whereas Clusters 3, 4, and 8 exhibit mainly hematite signatures. The Clusters 2 and 9 do not show significant Raman signatures. Furthermore, for each of the three fitting functions (one Breit-Wigner-Fano and two Lorentzians), the projection of their centers (FWHMs) in the principal component space is displayed by the solid (dotted) line. The influence of the I_D/I_G ratio is indicated as well.

Principal Component Analysis of the Complete Data Set. In a comparable manner like for a single spectrum, the complete data set is analyzed by means of principal component analysis in the following. The parameter space of the data of all investigated samples is even bigger than the parameter space for one single mapping. Here, the spectral data and the tribometer data (temperature and coefficient of friction) are used to detect clusters with similar properties. The clustered data are shown in Figure 6.8 with ten different clusters. Again, four main groups are identified in the figure. The mean spectra of each cluster are shown in the legend of Figure 6.8. Additionally, the projection of the center position (solid line) and the FWHM (dotted line) of each of the three fitting function components to the principal component space are displayed. A data point moves along these axes if the corresponding parameter of the spectrum is changed. The projection of the previously created parameter I_D/I_G is also included in the plot. It does not show a significant influence. Other projections are omitted for clarity. The clustering reveals three clusters with mainly amorphous carbon signatures (Clusters 0, 6 and 7), three clusters with mainly hematite signatures (Clusters 3, 4 and 8) and two clusters that show mainly hematite signatures with small signatures of amorphous carbon (Clusters 1 and 5). The Clusters 2 and 9 do not demonstrate significant Raman signatures.

Table 6.4 Coefficients for the different parameters forming the first few Principal Components (PCs), with their explained variance ratio indicated. The parameters are the applied temperature T during tribo-testing and the measured coefficient of friction μ . The spectra are corrected by a background with offset c_0 and slope c_1 , while the peaks are described by an additional offset c , their area under the peak A , their central position ω , their FWHM Γ , their asymmetry factor q and their variance σ , as well as their height h . Additionally, the influence of each parameter on the corresponding principal component is indicated by the bar graph.

Parameter	PC 1 (35%)	PC 2 (24%)	PC 3 (12%)	PC 4 (8%)	PC 5 (5%)
T	0.000	0.000	0.000	0.000	0.000
μ	0.000	0.000	0.000	0.000	0.000
A_{BWF}	-0.011	-0.133	-0.048	0.022	-0.030
ω_{BWF}	0.406	-0.469	-0.078	0.152	-0.054
Γ_{BWF}	0.295	-0.294	-0.227	0.143	-0.084
q_{BWF}	-0.043	0.065	0.350	0.404	0.136
σ_{BWF}	0.361	-0.317	-0.191	0.156	-0.031
A_{L1}	0.120	-0.042	-0.085	-0.104	0.165
ω_{L1}	0.173	-0.259	0.562	-0.494	-0.162
Γ_{L1}	0.102	-0.247	0.423	-0.194	-0.001
A_{L2}	0.292	0.245	0.081	0.166	-0.042
ω_{L2}	0.480	0.390	0.001	-0.269	0.223
Γ_{L2}	0.368	0.299	0.012	0.069	0.095
h_{L2}	0.323	0.275	0.090	0.066	-0.016
A_{L3}	-0.006	-0.029	0.051	0.053	0.116
ω_{L3}	-0.031	-0.141	0.241	0.257	0.527
Γ_{L3}	-0.026	-0.119	0.203	0.213	0.473
h_{L3}	-0.006	-0.029	0.050	0.051	0.111
$h_{\text{L1/BWF}}$	-0.040	0.104	0.154	-0.142	0.042
c	0.041	0.135	0.362	0.466	-0.552
c_0	-0.007	0.008	0.063	0.094	-0.143
c_1	0.009	0.003	0.032	0.063	-0.034

Influence of Spectral and Tribo-Parameters on Principal Components. The calculated principal components leading to Figure 6.8 are summarized in Table 6.4. Here, the influence of each of the spectral and tribological parameters on the first five principal components is presented. For the present data set, the first five principal components explain about 84% of the observed variance in the data. The first two principal components are dominated by the parameters of the Breit-Wigner-Fano and the second Lorentzian function. Here, the parameters of the second Lorentzian influence both principal components proportionally, while the parameters of the Breit-Wigner-Fano function have an opposed influence on the two principal components. A comparable behavior is observed for the influence of the parameters of the first Lorentzian on the third and fourth principal components. Furthermore, none of the principal components is influenced by temperature or friction. This behavior can be explained with the different resolution of the parameters: While the spectral parameters are determined with one set of parameters per spectrum and 225 spectra per mapping, the tribological parameters are only determined once per sample. For the optical parameters, there is a rather wide variation per mapping, while for the tribological parameters no

Table 6.5 Optical and tribological composition of the clusters, grouped by their spectral features. Here, the mean values are calculated using the `uncertainties` package, weighted with the cluster sizes [Leb]. Non-existing values are excluded from the calculations. The peak parameters are given in cm^{-1} .

Label	Clusters	μ	$T/^\circ\text{C}$	ω_{BWF}	Γ_{BWF}	ω_{L1}	Γ_{L1}	ω_{L2}	Γ_{L2}	ω_{L3}	Γ_{L3}
No signal	2, 9	0.38 ± 0.35	129 ± 24								
Iron oxides	1, 3, 4, 5, 8	0.35 ± 0.15	118 ± 13	1581 ± 7	167 ± 19	1315 ± 4	110 ± 13	1095 ± 14	138 ± 29		
Carbons	0, 6, 7	0.32 ± 0.23	119 ± 18	1590 ± 8	145 ± 28	1334 ± 11	198 ± 48			1768 ± 11	247 ± 68

variation is observable per mapping. This leads to a small correlation between the optical and tribological parameters, which is also detected by the clustering algorithm, leading to vanishing coefficients for the tribological parameters.

Optical and Tribological Composition of the Grouped Clusters. The mean values of the spectrally grouped clusters' optical and tribological composition are presented in Table 6.5 (see Appendix D for the non-grouped data). Here, spectral features with mean values of the center position that are outside of the spectral ROI are omitted. The no-signal cluster group (Clusters 2 and 9) does not show a spectral feature with mean center positions inside the spectral ROI for any of the optical parameters. While the coefficient of friction is comparable to the other two cluster groups, the temperature seems to be slightly increased compared to the two other groups. The iron oxide and transition cluster group (Clusters 1, 3, 4, 5 and 8) shows mean values for three different Raman features, which are identified as the previously described hematite modes. While their peak positions are well-determined with errors around 1 %, the peak widths vary strongly with errors of 10 % to 20 %. The carbon dominated cluster group (Clusters 0, 6 and 7) shows also three Raman modes, of which two are the D- and G-modes of amorphous carbon. The origin of the third mode around 1770 cm^{-1} is unknown. Again, the peak positions are well determined with errors not exceeding 1 %, while the peak widths vary strongly with errors ranging from 20 % to 30 %.

Applying PCA to the complete data set leads to optical mean values that match well with the Raman positions reported in the literature. Although the peak widths show non-neglectable errors, the determined optical mean values can be used to describe the data set and reduce it to its main differences.

Atmospheric and Lubricational Composition of the Grouped Clusters. The mean values of the spectrally grouped clusters' atmospheric and lubricational composition are presented in Table 6.6 (see Appendix D for the non-grouped data), with the number of spectra indicated. In total 8689 spectra are investigated, with 13 % of the spectra showing little to no signal, 48 % showing mainly iron oxide signatures and 39 % showing mainly carbon signatures.

The overall contribution of air is $(79 \pm 2) \%$ for all clustered spectra, whereas the contribution of non-air atmospheres sums up to $(21 \pm 3) \%$. This reproduces the overall distribution of the measured atmospheres. Within its errors, this also fits to the components detected in the clusters with no signal, where the contribution of air is $(75 \pm 2) \%$ and the non-air contribution sums up to $(25 \pm 3) \%$. In the iron oxide dominated clusters the contributions of air $(87 \pm 2) \%$ and non-air atmospheres $(13 \pm 3) \%$ do not fit to the atmospheric distribution. Here, the oxygen-rich atmospheres are significantly over-represented. In the carbon

Table 6.6 Atmospheric and lubricational composition of the clusters, grouped by their spectral features. The number of spectra of each cluster is reported, as well as the cluster's relative atmospheric composition and its relative composition of lubricants used in the cluster. Here, the atmospheres are ambient air (air), argon (Ar) and nitrogen (N₂). The lubricants are base oil (BO), ethylene glycol (EG), additive oil (add), no oil (no), corn oil (CO), silica-gel-dried oil (dry), silicone oil (SO) and diethylene glycol (DEG). Additionally, the total compositions of the clustered and measured spectra are presented (see Table 6.1).

Label	Clusters	Spectra	air	Ar	N ₂	BO	EG	add	no	CO	dry	SO	DEG
No signal	2, 9	1164	75	14	11	43	26	20	5	2	2	1	1
Iron oxides	1, 3, 4, 5, 8	4154	87	13	0	60	5	1	9	4	5	10	5
Carbons	0, 6, 7	3371	71	19	10	70	11	5	1	7	6	1	0
Clustered spectra		8689	79	15	5	61	10	5	5	5	5	5	2
Measured spectra		8689	77	16	8	61	8	5	5	5	5	5	5

dominated clusters the contributions of air (71 ± 2)% and non-air atmospheres (29 ± 3)% are also noticeable. Here, the oxygen-rich atmospheres are significantly under-represented.

The error for the relative compositions is estimated as follows. It is assumed, that one set of carbon signatures from a sample might be assigned inaccurately by the clustering algorithm. Taking the carbon containing spectra from Table 6.1, each of the 42 samples shows on average 50 spectra with amorphous carbon signatures. Taking the cluster analysis instead, each of the 42 samples shows an average of 80 carbon containing spectra (compare Table 6.6). Taking the greater number, the error is estimated to be in the range of $\pm 80/8689 \approx \pm 1\%$. Here, it is assumed that the error does not exceed twice the roughly estimated error. Therefore, an error of 2% is used for all relative values. For combined values, error propagation is used to calculate the combined error.

The observed over- and under-representation of oxygen-rich atmospheres supports the assumption that the presence of air increases the probability of iron oxide formation, while it reduces the probability to form carbon bonds. The assumption of oxygen playing a key role in this tribological process is rooted in the composition of air, which mainly consists of 78% nitrogen, 21% oxygen and $\approx 1\%$ argon, and identical tribo-tests being performed in three different atmospheres (air, nitrogen and argon), where the only difference is the presence of oxygen in the surrounding atmosphere (compare Table 6.3).

Summary and Conclusion. A multi-parametric Raman spectroscopic investigation on the formation of tribofilms on steel-steel surfaces is performed, providing insight into the microstructural properties of the tribological surfaces. In the investigated tribo-material, three main constituents are identified. Here, hematite builds the base of the film, followed by magnetite, which is covered by amorphous carbon. A high amorphous carbon coverage of the surface is correlated with high loads (10 N) and high numbers of load cycles (exceeding 10^5 cycles). The particles forming the tribofilm are nanometer sized, with large iron oxide particles (exceeding 42 nm) and smaller amorphous carbon particles (1 nm to 2 nm).

Furthermore, spatially resolved Raman images showed that pitting areas have a higher

probability for amorphous carbon accumulation than other surface regions. This accumulation might indicate an increased tribological activity of the pitting areas, where amorphous carbon particles might form and precipitate out of the lubricant solution. Additionally, the Raman spectra revealed that flash temperatures of up to 700 °C are reached in the tribo-contact. The amorphous carbons are mainly sp^2 hybridized linear carbon chains, with some distorted six-fold rings. A sp^3 content of up to 30% is possible, but such an evaluation needs further investigation. Hints are detected that the reaction pathway of the tribofilm formation is selected by atmospheric oxygen, showing an increased tendency of amorphous carbon formation for oxygen-free atmospheres.

Additionally to the analysis, the spectral differences in the data are also detected with the chemometrical methods of principal component and cluster analysis. These methods support the key role of oxygen for the tribological process. Neither the mapping of the different spectral parameters, nor the mapping of the clustered spectra showed a clear correlation of the data with the optical image of the sample. Nevertheless, the data reduction and clustering algorithms led to comparable results as the traditional analysis, proving that chemometrical methods might be used to gain a fast insight into huge data sets and help to find analyze-worthy correlations.

In conclusion, combining Raman spectroscopy with chemometrical methods creates a powerful technique that allows one to correlate spectral information with surface properties. In order to correlate the spectral information with tribological data an increased spatial resolution of the tribological data is required.

Chapter 7

Summary and Outlook

In this chapter, the gathered results are summarized and are taken to a broader context. Additionally, an outlook on experimental improvements is given. At first, each chapter is summarized to recover the main findings. Subsequently, the characteristics of tribological surfaces are bundled and main conclusions are drawn. Finally, the chapter closes with an outlook to future experiments and suggests improvements on the Raman scattering technique.

In Chapter 4 three examples of tribological materials are presented, generating an optical impression of wear on tribological surfaces. Firstly, on uncoated screw-rotor surfaces, iron oxides are detected, indicating worn (magnetite) and heavily worn surface regions (hematite and magnetite). Additionally, the mapping of the characteristic Raman lines revealed strong fluctuations of the lines, indicating regions of heavy wear. Here, the occurrence of a specific Raman mode might be used to detect heavily worn uncoated steel surfaces. Secondly, on tungsten-carbide coated screw-rotor surfaces, tungsten oxides are detected, indicating an oxygen incorporation into the tungsten carbide coatings. The oxygen incorporation and the concomitant broadening and shifting of the Raman modes might be exploited to determine the degree of wear in these coatings. Thirdly, the tribofilm formation of MoS_x coatings in different atmospheres is studied. Here, third-body MoS_2 particles are observed. These particles have a different chemical behavior, oxidation resistance and increased Raman scattering probability compared to the as-deposited films. Monitoring the third-body particles could help estimating the degree of wear of the coatings.

In Chapter 5 the influences of deposition parameters and post-growth annealing on the microstructure and interatomic interactions of amorphous carbon films and MoS_x coatings are investigated. In the first section of the chapter, the deposition parameters bias voltage and cathode power are detected to be of greatest influence on amorphous carbon coatings, reducing the probability for the formation of sp^3 hybridized carbon bonds and inducing intrinsic stress into the coatings. In the second section of the chapter, MoS_x coatings are investigated. Here, an increased heating power in the deposition process is identified to shift the S/Mo ratio towards 2, while a reduced heating power shortens the MoS_x bond lengths. Additionally, high substrate temperatures are identified to reduce the inter-layer spacing along the (002) direction of the different MoS_x layers. Furthermore, the coefficient of friction is reduced for coatings with high initial (100) orientation, indicating a reorientation process from initial (100) orientation to basal (002) orientation in the tribological contact. In the third section of the chapter, post-growth annealed polycrystalline MoS_x coatings are

investigated. Here, the relaxation of non-uniform strain is detected, as well as an improvement of the film's structural and chemical composition for high annealing temperatures. Additionally, two Raman modes may be exploited to determine the frictional behavior of the coatings (low frequency Raman mode around 40 cm^{-1}) and to detect stacking faults in the molybdenum disulfide layers (Raman forbidden mode around 550 cm^{-1}).

In Chapter 6 the tribofilm formation in steel-steel contacts is investigated. Here, a layered film is detected, with nano-sized hematite, magnetite and amorphous carbon particles from base to top. Spatially resolved Raman images revealed an accumulation of amorphous carbon in pitting areas. Furthermore, the Raman spectra allowed for an estimation of the flash temperatures present in the tribo-contact, ranging up to $700\text{ }^\circ\text{C}$. The amorphous carbon is mainly linearly coordinated, with some distorted carbon rings. Additionally, two reaction pathways forming the tribofilm are identified, with oxygen playing a key role in the selection of the pathway. Performing principal component analysis on the data set led to comparable results, allowing for fast insights into the complete dataset.

In Conclusion, the correlation of Raman scattering signatures with microstructural properties of tribological surfaces identified several characteristics. The first characteristic for heavily worn surfaces is the presence of oxides, which are observed in different material systems. Here, iron oxides (Chapters 4.1 and 6), tungsten oxides (Chapter 4.2) and molybdenum oxides (Chapters 4.3 and 5.3) are detected. The degree of wear is described by monitoring their spatial distribution, their broadening and shifting or their chemical behavior. A second characteristic of tribological material may be that it is micro- (molybdenum disulfide, see Chapter 4.3) or nano-sized (iron oxides and amorphous carbon, see Chapters 4.1 and 6). The size of the tribo-generated particles might be estimated from the FWHMs of the recorded Raman signatures or simply from visual images. An additional property of tribological surfaces is provided by their tailoring through distinct external parameters. Here, the deposition process (Chapters 5.1 and 5.2), post-processing (Chapter 5.3) and the surrounding atmosphere (Chapters 4.3 and 6) strongly influence the tribological behavior of the respective coatings.

In general, Raman spectroscopy proves to be a useful technique to analyze various tribological surfaces. The careful analysis of the collected spectra allows for a detailed insight into the properties of these surfaces. Adding spatial resolution to the scattering technique, allows one to correlate visual information with spectral information, which enhances the understanding of tribological surfaces and their properties.

Outlook. In order to use spatial Raman spectroscopy to monitor wear in real-time applications, several improvements are required: The method needs to be speed up. This could be performed by changing from a point-wise spectrum collection to a line-wise spectra collection. Using fiber arrays or liquid-crystal tunable filters allow for an even faster collection of the Raman images [Tre01].

Combining Raman spectroscopy and chemometrical methods, like principal component analysis, provides the analysis of huge data sets and one gains a fast insight into the data. Here, mean centering could be used to only detect changes from the overall mean spectrum [Sha01], which simplifies the identification of spectral differences. Also introducing chemical

color imaging or hyperspectral imaging¹ could help to simplify the analysis of the data of interest.

Furthermore, spatially resolved temperature and frictional data would further improve the understanding of the underlying processes. This could be achieved by adding thermometric methods [Shi07; Lun13; Bri12] and also performing micro- and nano-friction experiments [Chu11b]. In order to gain a more detailed insight to the Raman measurements, the anti-Stokes signal could also be collected and Raman thermometric methods² could be introduced to determine the influence of the laser on the sample surfaces. Additionally, the simulation of the Raman spectra with density functional perturbation theory³ could give more in depth insight into the material and the underlying processes at atomic scale.

¹A good introduction to hyperspectral imaging is given by Horiba [Hor21b].

²First experiments were already performed, which are summarized in a report by Rittmann [Rit18].

³A brief introduction to the topic is given by the Bachelor's thesis by Beckmann [Bec19].

Appendix A

Supporting Methods

In this appendix some additional methods used during the preparation of this thesis are presented. Some of these methods were topic of a Bachelor's thesis. The methods presented are

- Fabry-Perot interferometry, which can be used to inspect the mode structure of a laser,
- focus stacking, which can be used to increase the depth of field of an image,
- the knife-edge method, which can be used to determine the spot size of a laser beam,
- an estimation of the spectral resolution of a spectrometer and its line width.

A.1 Fabry-Perot Interferometry

A Fabry-Perot interferometer¹ is an optical resonator with two partially transmitting mirrors [Har03]. Through this configuration, an incident light beam may only be transmitted by the interferometer when wavelength and resonator are in resonance. The interferometer can be used as optical filter, transmitting only a narrow spectral range from a wide spectrum. By introducing tunability to the length of the resonator, through adding piezoelectric transducers, the spectral properties of the transmitted beam can be adjusted. By constantly scanning the length of the resonator (so called free spectral range of the interferometer), a scanning Fabry-Perot interferometer can be used to examine the spectral characteristics of a laser beam.

An experimental setup of a scanning Fabry-Perot interferometer, with a photo-diode, controllers for diode and transducer and an oscilloscope, is described on the website of Thorlabs [Tho21]. For alignment, calibration and more details on Fabry-Perot interferometers it is recommended to read the guide supplied by Thorlabs. In case of a single-mode laser, the observed frequency response is a single Lorentzian detected over the complete free spectral range of the resonator. For lasers that are not single mode, more than one Lorentzian is detected over the scanning range of the interferometer. For nearly single-mode lasers, two or more overlapping Lorentzians are observed.

¹The interferometer is named by its developers the french physicists Charles Fabry (*1867; †1945) and Alfred Perot (*1863; †1925).

A.2 Focus Stacking

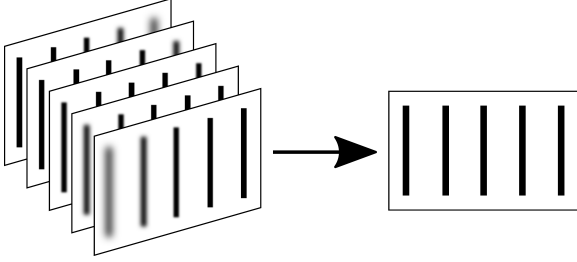


Figure A.1 Scheme of focus stacking. Multiple images with different focal planes are combined to one image with an increased depth of field.

of fields that are physically impossible, and images with non-planar focus regions can be generated. This is helpful in microscopy when large, uneven sample regions are of interest, as high-numerical aperture objectives only supply a small depth of field. To generate a focus stacked image, the `enblend` and `enfuse` tools from the `hugin` software can be used. A detailed tutorial is given in Pat David’s blog [Dav13].

Focus stacking or focal plane merging is a technique to increase the depth of field of an image [Joh17]. Therefore, multiple images with different focus distances are collected (compare Figure A.1). In a following digital processing step, the focused image regions are detected (with edge detection, Fourier analysis or other algorithms) and combined to a new image containing the focused regions of all input images. This technique allows one to generate images with depths

A.3 Knife-Edge Method

Here, a brief introduction to measure the beam waist of a laser spot with the knife-edge method is given. A laser beam is a Gaussian beam² with its intensity in cylindrical coordinates (ϱ, z) given by [Hau16]

$$I(\varrho, z) = I_0 \left(\frac{w_0}{w(z)} \right)^2 \exp \left(-\frac{2\varrho^2}{w^2(z)} \right), \quad \text{with} \quad w(z) = w_0 \sqrt{1 + \left(\frac{(z - z_0)\lambda M^2}{\pi n w_0^2} \right)^2}. \quad (\text{A.1})$$

Here, $w(z)$ is the z -dependent beam width (beam waist) of the laser beam, with the beam waist w_0 at $z = z_0$, the refractive index n of the medium, the wavelength λ of the laser beam and the beam quality factor M^2 , which is 1 for an ideal Gaussian beam, but slightly bigger for a real beam³.

The beam width can be measured, with the knife-edge method. Here, a sharp edge is used to scan across the laser beam profile (compare Figure A.2 (a)) and an intensity signal (fluorescence, Raman, etc.) from a sample is measured with respect to sample displacement (compare Figure A.2 (b)).

With a signal originated solely from the sample surface, the displacement-dependent

²Details on lasers, Gaussian beams and their properties are given in the book by Siegman, Chapters 16 and 17 [Sie86].

³Typically values ranging from 1 to 1.1 are reached for He–Ne lasers and values ranging from 1.1 to 1.7 are reached for ion-gas lasers [Hau16]. For the solid state lasers used in this thesis lasers with beam qualities $M^2 < 1.1$ are used.

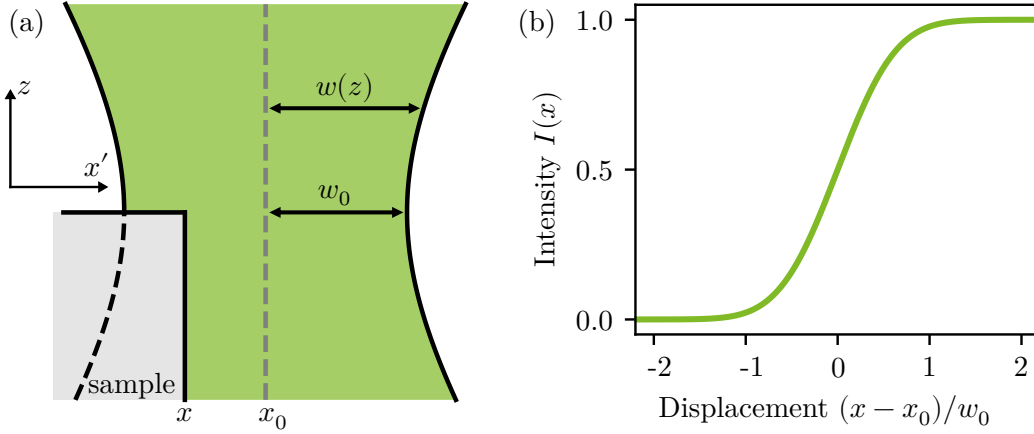


Figure A.2 Schemes of the Knife-Edge Method, where (a) a sample is moved into a Gaussian beam profile and (b) the signal intensity is recorded with respect to the sample displacement.

Table A.1 Numerical aperture (NA) and working distance (WD) of objectives used in this thesis. Additionally, the measured beam waists for 532 nm excitation in dependence of objective and material are given. Here, the Raman lines of diamond (1336 cm^{-1}) and silicon (519 cm^{-1}) were investigated to determine the corresponding beam waists $w_{0,\text{Dia}}$ and $w_{0,\text{Si}}$.

Objective	NA	WD/mm	$w_{0,\text{Dia}}/\mu\text{m}$	$w_{0,\text{Si}}/\mu\text{m}$
Olympus PLN4x	0.1	18.5	6.4 ± 0.2	
Olympus UPLFLN20x	0.5	2.1	2.27 ± 0.03	1.1 ± 0.3
Olympus LMPLFLN50x	0.5	10.6	1.21 ± 0.03	

intensity $I(x)$ at position $z = Z$ is given by [Hau16]

$$I(x) = \frac{I_0}{2} \left(1 + \operatorname{erf} \left(\frac{\sqrt{2}(x - x_0)}{w(Z)} \right) \right), \quad (\text{A.2})$$

with the center of the beam x_0 , the maximum intensity I_0 , the error function erf and the beam waist $w(Z)$ in the plane of measurements. By performing the described measurement of the intensity of a Raman line of choice and fitting the parameters of $I(x)$ the beam waist can be determined. The spot size is defined as the beam diameter in the focal plane, leading to a spot size of $2w_0$. Some beam waists were determined during the Bachelor's thesis of Grisard [Gri18]. An overview of the results is given in Table A.1.

Table A.2 Typical resolutions and spectral ranges $\Delta\omega$ for the combination of a PyLoN-2K CCD combined with a SP-2750 spectrometer for different gratings and central wavelengths λ_c in first-order diffraction. The values are calculated using the grating dispersion calculator supplied by Princeton Instruments [Ins21].

Grating/ grooves/mm	λ_c / nm	Slit width/ μm	$\Delta\omega$ / cm^{-1}	Resolution/ cm^{-1}
600	563	100	54 – 1919	6.7
600	563	25	54 – 1919	2.4
900	552	100	31 – 1288	4.5
900	552	25	31 – 1288	1.6

A.4 Spectrometer Resolution and Line Width

The measured $\text{FWHM}_{\text{measured}}$ of a recorded spectral line can be approximated by the generalized bandpass equation [Ler06]⁴

$$\text{FWHM}_{\text{measured}} = \sqrt{\text{FWHM}_{\text{natural}}^2 + \text{FWHM}_{\text{slit}}^2 + \text{FWHM}_{\text{resolution}}^2} \quad (\text{A.3})$$

with the natural $\text{FWHM}_{\text{natural}}$ of the emitting source, the bandpass $\text{FWHM}_{\text{slit}}$ determined by the spectrometer slit width and the limiting resolution of the instrument $\text{FWHM}_{\text{resolution}}$. Usually, the limiting resolution of the instrument is not reached, making the spectrometer's slit the dominating influence on the measured FWHM (compare Table A.2). For typically measured FWHMs ranging from 10 cm^{-1} to 20 cm^{-1} , a resolution of 5 cm^{-1} ($100 \mu\text{m}$ slit width) instead of 1.5 cm^{-1} ($25 \mu\text{m}$ slit width) does only lead to an underestimation of the natural FWHM of approximately 1 cm^{-1} . As integration times are significantly reduced by using a wider slit, the small losses in resolution are tolerated and for most of the measurements a slit width of $100 \mu\text{m}$ is used.

⁴These and other properties of spectrometers are also described in the optics tutorial by Horiba [Hor21a]

Appendix B

Spectrum Analysis

The `spectrum_analysis` package is a python package, written in the scope of this thesis to analyze Raman mapping data. The software is published on github and free to use [Mol20]. Example files are supplied with the package. The installation procedure is described in the `README` of the package. In case of installation errors, several python packages might need installation. In the following some details on the usage of the software are explained.

B.1 How to Generate Mappings

The principal steps of how to generate a mapping of recorded data is described in Section 3.3. Here details using the `spectrum_analysis` package are presented.

To generate a mapping, all spectra of the mapping of interest have to be fitted. This can be performed using the `map_tester.py` from the `examples` folder of the `spectrum_analysis` package. To get started with a non-example mapping, two lines of the file have to be modified. The `peaks` list is used to define which peak functions should be used by the software. Here, the peak functions `breit_wigner`, `lorentzian`, `gaussian` and `voigt` are implemented. The built-in functions of the `lmfit` package are addable [New20]. Therefore, the `ChoosePeakType` function in `spectrum.py` and the `StartingParameters` function in `starting_params.py` have to be modified accordingly.

Next to choosing the demanded peak profiles, the data folder (`foldername`) needs to be defined. The data folder contains the data files of the mapping. The files have to be `txt` files and should contain only two columns of data¹.

Subsequent to these settings, the software is started via the command line. Running `python map_tester.py` starts the fitting procedure. At first a window opens that asks the user to select a region of interest (compare Figure B.1). The left mouse button is used to select the lower and upper region of interest. Once the region is selected, it is marked in green. The window is closed² using `CTRL + W`.

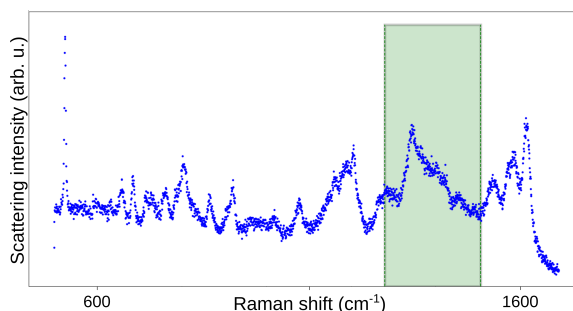


Figure B.1 Raw Raman spectrum, with a region of interest selected and marked in green.

¹The file format can be changed by using the `datatype` keyword and set it accordingly (`csv`, `dat`, etc.).

²The window can also be closed by clicking on the `x` of the window, but using `CTRL + W` speeds up the procedure.

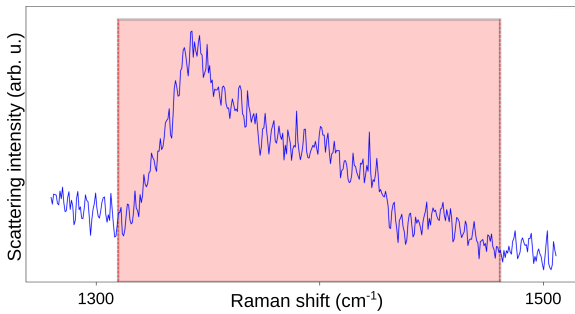


Figure B.2 The excluded region from the background fitting is marked in red.

peak is selected by using the left mouse button. In case of error, deselection of the last peak is possible by using the right mouse button. Each time all peaks of a selected type are selected in a spectrum, the window needs to be closed to proceed³. This is now repeated until all peaks in all spectra are selected.

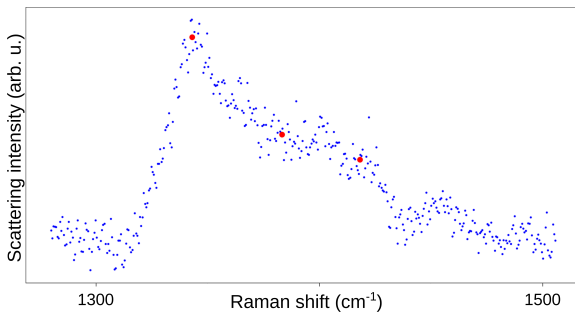


Figure B.3 The red dots mark the selected peaks for fitting the spectrum.

(`fitlines` folder) all fit parameters (`fitparameter` folder) and all the plots of the fitted spectra (`plot` folder) are stored. Here the user can check whether the fit routine worked as expected. All analyzed spectra should be checked carefully to check for fitting mistakes. The spectra that should be fitted again should be noted. Common fitting errors are huge 3σ bands on the resulting fit, which might arise from bad starting parameters.

If several spectra should be fitted again, the software has to be run a second time (`python map_tester.py`). This time `spectrum analysis` asks the user whether to fit all spectra again (`y`) or to refit only several spectra (`n`). The submission needs to be confirmed using the return key. In case of adding peaks to the fit or changing the fitting routine, the generated subfolder structure needs to be deleted. In case of refitting several spectra, `spectrum analysis` asks the user which spectra should be fit again. Therefore, all possible spectra are printed to the command line. The spectra of interest need to be entered and confirmed solely (using the return key). For a faster workflow, only the tailing numbers need to be entered in the command line window. `spectrum analysis` tells the user whether the entered spectrum is added, or if it is misspelled and the entered spectrum does not exist.

A new window will open, showing the selected region, asking the user to select a region that should be excluded from the fitting of the background signal. Again, the left mouse button is used to select the lower and upper limits of the region that should be excluded. The excluded region is drawn in red (compare Figure B.2). As before, the window needs to be closed to proceed.

Now, for each spectrum and peak type in the data folder a window will open and ask the user to select the designated peaks. A

Once the selection procedure is finished, the fitting procedure will start. Now `spectrum analysis` will iterate through all spectra and use the selections as starting model for fitting the peaks of interest. This might take some time, but the command line will communicate the current status.

After fitting, the results are saved and plotted as well. Therefore, several subfolders are generated in the data folder. In the `raw` folder the raw spectra are plotted. In the `results` folder the fitted baselines (`baselines` folder), the lines of the sum-fits

³Using CTRL + W really fastens up the whole process

Once all spectra are entered, the selection process is terminated typing `x` to the command line and confirming using the return key. Now the selected spectra are fitted again.

Once the user is satisfied with the fitting results, mappings of the different parameters can be generated. Therefore, the `map_plot_tester.py` program from the `examples` folder of `spectrum analysis` can be used. The file has to be modified accordingly to the data of interest. Single or multiple mappings can be plotted, as shown in the example. It is important that the dimensions (`dims`) fit to the dimensions of the recorded mapping. Otherwise, the program will collapse. The `stepsize` should correspond to the step size of the mapping, as these values are used to define the x - and y -axes. The `background` is a visual collected from the sample surface and has to be in the same folder like the data files. Prior to plotting the mappings, the image of the sample surface needs to be cropped to the size of the sample region investigated with the mapping. The image is used as background image, to visually link Raman results with the visual image (see Figure B.4). In case no background image is recorded, this option can be deactivated by setting `bg_plot` to `False`.

Additionally, for each parameter histograms are plotted. The number of bins can be adjusted using `bins`.

If multiple mappings are recorded and all of them should be plotted on the same scale, the `scaled` value can be set to `True`. With this option additional plots with a shared scale are generated.

In order to plot all raw spectra, the `plotrawspectra` value has to be set to `True`.

Furthermore, `spectrum analysis` allows one to plot modified parameter values. Parameters can be added (`add`), subtracted (`sub`), divided (`div`) and multiplied (`mult`) at the users need. Once set up accordingly, the script has to be started by running `python map_plot_tester.py`. Depending on the size of the mappings, the execution might take some time. The results are saved to the `results/plot` folder.

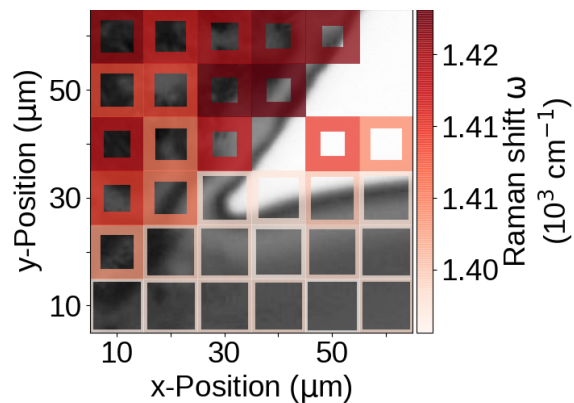


Figure B.4 Finished mapping of a test sample with three different regions.

B.2 How to Interpret Mappings

The generated mappings like the one shown in Figure B.4 are spatially resolved mappings of a single parameter from the fitted Raman data. At each position of the sample, one Raman spectrum is recorded and fitted. In order to reduce the data, only the fitting parameters are plotted in mappings. Here, x and y correspond to the two dimensions of the sample. The value of the selected parameter is color coded (here: Raman shift ω). The width of the markers corresponds to the sum area under the curve of all peaks fitted in the spectrum: For an increased region of the background image, a higher sum area under the curve is recorded. This way the intensity of a single spectrum can easily be estimated with respect to the other spectra of the mapping. At surface positions where no signal is detectable, the overlaying marker is omitted.

B.3 Exemplary Principal Component Analysis

To perform a Principal Component Analysis (PCA) the `pca_analysis.py` or the `jupyter notebook` from the `examples` folder of `spectrum analysis` can be used⁴. Here, again a dictionary is used to describe the properties of the mappings. The `mapfolderList`, `dims`, `stepsize`, `background` and `markersize` have to be set accordingly to the settings defined in the `map_plot_tester.py`. Additionally, the number of clusters `n_clusters` and multiple variables can be set to modify the analysis as requested by the experimenter. The variables are explained in the following.

`components` defines the number of principal components used for the PCA.

`component_x` defines which component is plotted on the x -axis.

`component_y` defines which component is plotted on the y -axis.

`show_hover_plot` needs to be set to `True` if an interactive plot should be displayed. By using the mouse and hovering over the plot's data points, the corresponding fit spectra are displayed, as well as their fit parameters. This option might be helpful to analyze a cluster in detail.

`display_parameter_values` is `True` by default. By setting this value to `False` the fit parameters are not displayed anymore at hovering.

`print_PCA_results` is `False` by default. By setting it to `True` the explained variance ratios for the set number of `components` are printed to the command line.

`print_PC_components` is `False` by default. By setting this parameter to `True` the linear combinations of the principal components are printed to the command line.

`plot_parameter_directions` adds the projections of the fit parameters to the principal component space. A so called biplot is created.

`plot_only_dirs` helps to plot only selected directions in a biplot. As fit models with ten or more fitting parameters create confusing plots, only selected fit parameters may be plotted by this dictionary. By default the `fwhm`, the `center` and the `height` of each fitting parameter are plotted. For each parameter type the `linestyle` is defined separately.

`clustering` defines the clustering algorithm used. The package `scikit-learn` supplies many different methods, but only the `SpectralClustering` is properly implemented in the example analysis.

`numberOfSamples` defines the minimal number of samples in a cluster generated by the `OPTICS` clustering algorithm.

`brim` Defines an additional white space around the plotted data. Usually this parameter does not need a modification.

⁴Here, only the `pca_analysis.py` is explained, as the documentation of the `jupyter notebook` is included in the notebook.

`imagesize` allows to change the size of the image displayed at hovering.

`imageshift` shifts the image displayed at hovering. Has to be modified if the `imagesize` is changed.

`plot_clustered_fitlines` is set to `False` by default, so that the raw data of the spectra is taken for the summation of the mean spectrum of a cluster. By setting this parameter to `True`, the fit lines of the corresponding spectra are taken for the calculation of the mean spectrum of the clusters. **Caution** This setting works only if all the fit lines are created in the same fitting process.

`plot_histogramm_parameters` is set to `True` by default. Set this parameter to `False` if the histogrammed parameters should be omitted in the cluster plots.

`histogram_parameters` allows to plot histograms of selected fit parameters into the plot of the mean spectrum of the corresponding cluster. If no histograms are needed, the list can be set to an empty list `histogramm_parameters = []`.

`bins` sets the number of bins for the histogrammed parameters in the mean spectrum plots of the different clusters.

With all the parameters set to the needs of the experimenter the PCA can be performed. The results are saved in the `plot` folder of the analyzed mapping. Additionally, a `SpectralClustering` folder is created in the directory of the `pca_analyis.py`. Here, the same images are stored, as well as images of the different clusters.

The PCA of a test sample is shown in Figure B.6. In the left plot the first two principal components are plotted along the x - and y -axis. Each data point corresponds to one of the collected spectra. The scatter plot shows a clustering of the spectra. Here, 4 clusters are displayed. The mean spectrum of each cluster is shown in the right part of the graph. Here, the intensity (counts) versus wavenumber are plotted. The colors of the lines coincide with the colors of the clusters in the PC scatter plot. Additionally, the histograms of the FWHM and the center position of selected peaks are plotted. Each cluster plot contains the number of the cluster (CN) and the number of spectra building the cluster (NS).

The clustered data are also plotted as a mapping. The resulting mapping is shown in Figure B.5. Here, the colors of the clusters correspond to the colors shown in Figure B.6. Plotting the clustered data as presented, allows to link visible information, collected by an optical camera, with spectral information, collected with a CCD camera. Here for example, the green, red and orange clusters correspond to the different surface regions of the sample. The small blue cluster is a transition

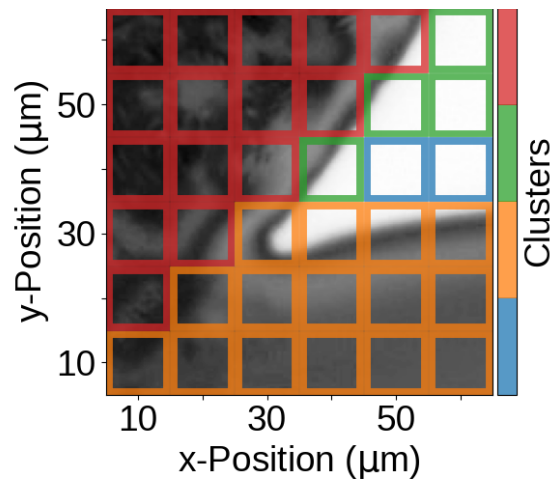


Figure B.5 Clustered mapping of the test sample with different regions.

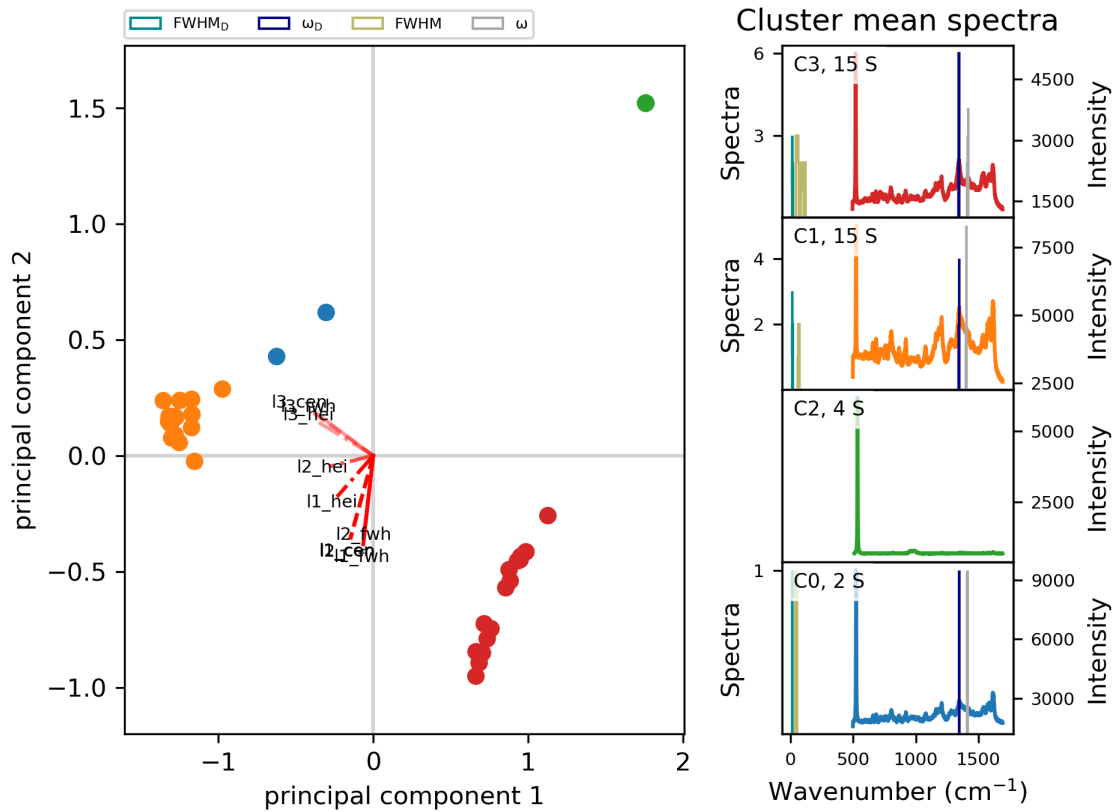


Figure B.6 Principal component analysis of a test sample with four different clusters. In the left panel the projections of the fitting parameters onto the first two principal components are displayed. Furthermore, the directions of the **height** (**hei**), **center** (**cen**) and **fwhm** (**fwh**) of the three Lorentzian peaks used for fitting are displayed. The right panel shows the mean spectra of each of the clusters, the number of spectra contained in the cluster and the FWHM and center position of selected modes.

region of the orange to the green cluster, with spectral features of both clusters (compare Figure B.6).

Appendix C

Character Tables

Character tables for symmetry groups of the materials used throughout this thesis [Cot90a].

Table C.1 Character table of the C_{2h} point group (here WO_3 [Sal75]).

C_{2h}	E	C_2	i	σ_h		
A_g	1	1	1	1	R_z	x^2, y^2, z^2, xy
B_g	1	-1	1	-1	R_x, R_y	xz, yz
A_u	1	1	-1	-1	z	
B_u	1	-1	-1	1	x, y	

Table C.2 Character table of the D_{3d} point group (here Fe_2O_3 [Far97]).

D_{3d}	E	$2C_3$	$3C_2$	i	$2S_6$	$3\sigma_d$	
A_{1g}	1	1	1	1	1	1	$x^2 + y^2, z^2$
A_{2g}	1	1	-1	1	1	-1	R_z
E_g	2	-1	0	2	-1	0	(R_x, R_y) $(x^2 - y^2, xy), (xz, yz)$
A_{1u}	1	1	1	-1	-1	-1	
A_{2u}	1	1	-1	-1	-1	1	z
E_u	2	-1	0	-2	1	0	(x, y)

Table C.3 Character table of the D_{3h} point group (here WC [Fan19]).

D_{3h}	E	$2C_3$	$3C_2$	σ_h	$2S_3$	$3\sigma_v$	
A'_1	1	1	1	1	1	1	$x^2 + y^2, z^2$
A'_2	1	1	-1	1	1	-1	R_z
E'	2	-1	0	2	-1	0	(x, y) $(x^2 - y^2, xy)$
A''_1	1	1	1	-1	-1	-1	
A''_2	1	1	-1	-1	-1	1	z
E''	2	-1	0	-2	1	0	(R_x, R_y) (xz, yz)

Appendix C Character Tables

Table C.4 Character table of the D_{6h} point group (here graphite [Mer17] and MoS_2 [Zha13a]).

D_{6h}	E	$2C_6$	$3C_3$	C_2	$3C'_2$	$3C''_2$	i	$2S_3$	$2S_6$	σ_h	$3\sigma_d$	$3\sigma_v$	
A_{1g}	1	1	1	1	1	1	1	1	1	1	1	1	$x^2 + y^2, z^2$
A_{2g}	1	1	1	1	-1	-1	1	1	1	1	-1	-1	R_z
B_{1g}	1	-1	1	-1	1	-1	1	-1	1	-1	1	-1	
B_{2g}	1	-1	1	-1	-1	1	1	-1	1	-1	-1	1	
E_{1g}	2	1	-1	-2	0	0	2	1	-1	-2	0	0	(R_x, R_y)
E_{2g}	2	-1	-1	2	0	0	2	-1	-1	2	0	0	(xz, yz) (x^2-y^2, xy)
A_{1u}	1	1	1	1	1	1	-1	-1	-1	-1	-1	-1	
A_{2u}	1	1	1	1	-1	-1	-1	-1	-1	-1	1	1	z
B_{1u}	1	-1	1	-1	1	-1	-1	1	-1	1	-1	1	
B_{2u}	1	-1	1	-1	-1	1	-1	1	-1	1	1	-1	
E_{1u}	2	1	-1	-2	0	0	-2	-1	1	2	0	0	(x, y)
E_{2u}	2	-1	-1	2	0	0	-2	1	1	-2	0	0	

Table C.5 Character table of the O_h point group (here diamond [Sol70] and Fe_3O_4 [Far97]).

O_h	E	$8C_3$	$6C_2$	$6C_4$	$3C_2$	i	$6S_4$	$8S_6$	$3\sigma_h$	$6\sigma_d$	
A_{1g}	1	1	1	1	1	1	1	1	1	1	$x^2 + y^2 + z^2$
A_{2g}	1	1	-1	-1	1	1	-1	1	1	-1	
E_g	2	-1	0	0	2	2	0	-1	2	0	$(2z^2-x^2-y^2, x^2-y^2)$
T_{1g}	3	0	-1	1	-1	3	1	0	-1	-1	(R_x, R_y, R_z)
T_{2g}	3	0	1	-1	-1	3	-1	0	-1	1	(xz, yz, xy)
A_{1u}	1	1	1	1	1	-1	-1	-1	-1	-1	
A_{2u}	1	1	-1	-1	1	-1	1	-1	-1	1	
E_u	2	-1	0	0	2	-2	0	1	-2	0	
T_{1u}	3	0	-1	1	-1	-3	-1	0	1	1	(x, y, z)
T_{2u}	3	0	1	-1	-1	-3	1	0	1	-1	

Appendix D

Amorphous Carbon Layers – Supplementary

Table D.1 Optical and tribological mean parameters of the detected clusters. Here, the mean values of friction μ , temperature T , central position ω_i and FWHM Γ_i for each peak function are presented with their corresponding errors. The central positions and FWHMs are given in cm^{-1} .



















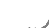

Cluster	μ	$T/^\circ\text{C}$	ω_{BWF}	Γ_{BWF}	ω_{L1}	Γ_{L1}	ω_{L2}	Γ_{L2}	ω_{L3}	Γ_{L3}
2 	0.36 ± 0.38	130 ± 26								
9 	0.58 ± 0.37	118 ± 7								
8 	0.35 ± 0.34	123 ± 23			1311 ± 17	96 ± 29				
4 	0.63 ± 0.34	127 ± 29			1310 ± 12	99 ± 17	1073 ± 91	110 ± 71		
1 	0.43 ± 0.35	124 ± 29	1587 ± 11	155 ± 36	1315 ± 8	127 ± 34	1083 ± 18	89 ± 48		
3 	0.19 ± 0.26	108 ± 22	1566 ± 14	191 ± 21	1319 ± 4	96 ± 14	1125 ± 41	254 ± 54		
5 	0.09 ± 0.02	101 ± 33	1589 ± 8	160 ± 25	1317 ± 5	116 ± 23	1094 ± 19	104 ± 56		
7 	0.37 ± 0.34	110 ± 16	1577 ± 7	137 ± 23	1336 ± 16	214 ± 52				
0 	0.32 ± 0.32	121 ± 25	1590 ± 12	145 ± 39	1331 ± 16	183 ± 67				
6 	0.29 ± 0.24	118 ± 8	1603 ± 6	154 ± 42	1341 ± 10	249 ± 32			1768 ± 11	247 ± 68

Table D.2 Atmospheric and lubricational composition of the detected clusters. Reported are the number of spectra and the cluster's relative atmospheric and lubricational composition, with ambient air (air), argon (Ar) and nitrogen (N_2) atmospheres. The used lubricants are base oil (BO), ethylene glycol (EG), additive oil (add), no oil (no), corn oil (CO), dried oil (dry), silicone oil (SO) and diethylene glycol (DEG). All values are given in %. The error of the compositions is estimated to $\pm 2\%$.

Cluster	Spectra	air	Ar	N_2	BO	EG	add	no	CO	dry	SO	DEG
2 	1073	75	15	10	43	24	22	5	2	2	1	1
9 	91	75	7	19	48	52						
8 	492	96	3	1	42	6	5	20	4	12	10	2
4 	739	89	11		24	20		20	3	0	16	17
1 	1399	78	22		52	2	2	9	9	9	13	3
3 	936	95	5		83	0	1	0	1	4	7	3
5 	588	87	13		100							
7 	510	38	36	26	74	24		1			1	
0 	2332	77	18	5	64	9	7	1	10	9	1	
6 	529	78	8	14	90	10						

List of Acronyms

a-C	amorphous carbon	31
a-C:H	hydrogenated amorphous carbon	31
AFM	Atomic Force Microscopy	44
ASE	Amplified Spontaneous Emission	39
BV	Bias Voltage	71
BWF	Breit-Wigner-Fano	13
CCD	Charge-Coupled Device	37
CP	Cathode Power	71
DC	Direct Current	42
DELTA	Dortmunder ELEkTronenspeicherring-Anlage	46, 75
DS	Doniach-Sunjic	13
EBPVD	Electron-Beam Physical Vapor Deposition	41
EDS	Energy Dispersive X-ray Spectroscopy	46
EELS	Electron Energy Loss Spectroscopy	34
FWHM	Full Width at Half Maximum	13
G	Gaussian	13
HiPIMS	High Power Impulse Magnetron Sputtering	42
HOPG	Highly Oriented Pyrolytic Graphite	106
L	Lorentzian	13
LB	Layer-Breathing	95
MF	Mid-Frequency	71
MonoVista	Confocal Raman Microscope System CRS+ 750/BX51, S&I	39
ND	Neutral Density	37
NMR	Nuclear Magnetic Resonance	34
PAO	Poly Alpha Olefin	102
PC	Principal Component	114

List of Acronyms

PCA	Principal Component Analysis	51, 112, 130
PDMS	Poly DiMethyl Siloxane	102
PLD	Pulsed Laser Deposition	41
PVD	Physical Vapor Deposition	41
ROI	Region Of Interest	104
SEM	Scanning Electron Microscopy	44
ta-C	tetrahedral amorphous carbon	31
ta-C:H	hydrogenated tetrahedral amorphous carbon	31
V	Voigt	13
XPS	X-ray Photoelectron Spectroscopy	46
XRD	X-Ray Diffraction	45

List of Symbols

A	area under the curve	13
a	lattice constant	8
α	polarizability	5
α_{at}	attenuation coefficient	17
A_N	Haar wavelet approximation up to order N of a function	49
$A(\mathbf{q})$	amplitude of a lattice displacement	8
b	distribution-dependent scaling factor	50
β_{hyp}	hyperpolarizability	5
χ	thermal diffusivity	25
C	coupling constant in the crystal lattice	8
c_{spec}	specific heat capacity	25, 26
d	distance	22, 45
D_{cryst}	average crystallite size	86
δ	Dirac delta function	48
δ_{p}	penetration depth	17
D_j	sum over all translations of the Haar wavelet at fixed scale	49
E	electrical field	5
E_0	amplitude of the electrical field	6, 17
ε	residual strain	21, 45
η	atom position in a crystal lattice	8
E_Y	Young's modulus	22
f	function in $L^2(\mathbb{R})$	48
F_{cont}	contact pressure	22
F_{fric}	friction force	19, 43
F_{norm}	normal force	19, 43
f_{p}	pulse frequency	84
Γ	Full Width at Half Maximum (FWHM)	13
γ_{hyp}	2 nd hyperpolarizability	5
G_{S}	shear modulus	22
$H(x)$	Haar wavelet	48

List of Symbols

$H_{j,k}$	modified Haar wavelet	48
HV	Vickers hardness	43
I	intensity	74
I_{12}	(100)/(002) intensity ratio	93
I_{ion}	ionicity	89
j	integer number	48
k	integer number	48
κ	force constant	16
\underline{k}	komplex wave vector	17
\underline{k}_h	thermal conductivity	25, 26
K_S	Scherrer constant	86
L	length	43, 89
$L^2(\mathbb{R})$	function space	48
λ	wavelength	45
λ_{fric}	ratio of the lubricant film thickness to the average surface roughness	19, 20
L_{Pec}	Peclet number	25
m	mass	8
M	integer number	8
m_{red}	reduced mass	12, 16
μ	coefficient of friction	19, 26
\mathbb{N}	set of natural numbers	45
n	order of diffraction	45
\underline{n}	complex index of refraction	17
N	integer number	8, 49
ν_0	oscillation frequency of an incident electrical field	6
ν_P	Poisson's ratio	22
Ω	line width	92
ω	frequency position	8, 13
P	power	84
p	electrical dipole moment	5
ϕ	phase angle	6
φ	rotation around surface normal axis	45
ψ	rotation around inclination axis	45
Q	normal coordinate of a molecule	6
q	asymmetry factor	13, 14

\mathbf{q}	wave vector	8
\mathbf{R}	lattice site of an atom	8
r	radius	22, 43
R_a	mean deviation of the profile	24
ρ	density	25, 26
ϱ	radial distance in cylindrical coordinates	124
\mathbb{R}^n	vector space	8
s	sliding distance	43
s_1	diffraction elastic constant	46
$1/2 s_2$	diffraction elastic constant	46
σ	standard deviation	13, 49
$\sigma_{j,k}$	components of the stress tensor	46
σ_Y	yield strength	26
t	time	6
T_{an}	annealing temperature of a vacuum oven	91
τ_t	lifetime	13
θ	incident angle of a beam	45
T_{min}	minimal temperature of the flow cryostat	40
U	voltage	84
u	displacement of an atom in a lattice	8, 21
V	volume	43
V_{spec}	specific volume	43
V_{wear}	wear volume	43
$w_{j,k}$	Haar wavelet coefficient	48
$w(z)$	beam waist of a Gaussian beam	124
X	electronegativity	89
x	axis of the coordinate system	48
y	axis of the coordinate system	48
\mathbb{Z}	set of integer numbers	48
z	axis of the coordinate system	17
ζ	atom position in a crystal lattice	8

List of Constants

N_A	$6.022\,140\,76 \times 10^{23} \text{ mol}^{-1}$	Avogadro constant
k_B	$1.380\,649 \times 10^{-23} \text{ J K}^{-1}$	Boltzman constant
g	$9.806\,65 \text{ m s}^{-2}$	standard gravity
$\lambda_{\text{Cr-K}\alpha}$	2.2911 \AA	radiation wavelength of chromium
$\lambda_{\text{Cu-K}\alpha}$	1.5419 \AA	radiation wavelength of copper
h	$6.626\,070\,15 \times 10^{-34} \text{ J s}$	Planck constant

List of Figures

2.1	Molecular normal modes indicating Raman and infrared activity.	7
2.2	Exemplary dispersion relation.	9
2.3	Exemplary Lorentzian distributions.	13
2.4	Exemplary Doniach-Sunjic distributions.	14
2.5	Exemplary Gaussian distributions.	14
2.6	Exemplary Voigt distributions.	15
2.7	Exemplary Breit-Wigner-Fano distributions.	15
2.8	Stress-strain diagram.	21
2.9	Scheme of a technical metallic surface.	23
2.10	Raman spectra of different iron oxides.	29
2.11	Ternary phase diagram of amorphous carbon.	30
2.12	Typical Raman spectra of carbon structures.	31
2.13	Phonon modes of graphene.	32
2.14	Influences of amorphous carbon properties on their Raman spectrum.	33
2.15	Three stage model for carbon materials by Ferrari and Robertson.	34
2.16	Typical Raman spectra of MoS ₂	35
2.17	Raman modes of WC and WO ₃	36
3.1	Basic Raman setup.	38
3.2	Confocal principle.	39
3.3	Confocal Raman setup with multiple excitation sources.	40
3.4	Custom vacuum chamber for the MonoVista.	40
3.5	Exemplary Haar wavelets.	48
3.6	Model data approximated by the Haar wavelet.	49
4.1	Front and side view of a female and a male screw rotor.	53
4.2	Overview of domains and studied area on a female screw rotor.	54
4.3	Hematite and Magnetite Raman signals.	55
4.4	Magnetite mapping of the A _{1g} mode.	57
4.5	Hematite mapping to the 1330 cm ⁻¹ mode.	58
4.6	Twin-screw rotor pair and roughness profiles.	59
4.7	Raman spectra of differently worn twin-screw rotors.	60
4.8	Surface and cross-section of a typical MoS _x film.	62
4.9	XRD pattern and Raman spectrum of an as-deposited MoS _x coating.	63
4.10	Coefficient of friction versus surface pressure and sliding velocity.	64
4.11	Raman spectra of worn MoS _x films and wear debris.	66
4.12	XRD spectra of (worn) MoS _x films in different atmospheres.	67
4.13	Specific wear rates of MoS _x coatings in different atmospheres.	68
5.1	Three factor Central Composite Design.	72

5.2	Four-step schema of determining the sp^3 content of a-C coatings.	74
5.3	Exemplary Raman spectrum of an a-C film under 266 nm laser excitation. .	78
5.4	Raman spectra of a-C films under 532 nm and 266 nm laser excitation. . . .	79
5.5	Exemplary XPS spectrum of an a-C film.	80
5.6	Correlation of the sp^3_{266} content with hardness and elastic modulus.	82
5.7	XRD spectra and details of HiPIMS and DC deposited MoS_x thin films. . .	87
5.8	Raman spectra of MoS_x films and an exfoliated MoS_2 monolayer.	88
5.9	Dependence of the hardness of MoS_x coatings on deposition parameters. . .	89
5.10	XRD spectra of MoS_x coatings.	93
5.11	633 nm-excited Raman spectra of MoS_x coatings.	94
5.12	Coefficient of friction versus annealing temperature and S/Mo ratio.	97
6.1	Schematic overview of the investigated amorphous carbon tribosystem. . . .	102
6.2	Raman spectra of the used lubricants.	104
6.3	Exemplary Raman spectra and Raman mapping.	105
6.4	Raman spectra in dependence on the number of load cycles.	106
6.5	Exemplary Raman mapping showing pitting areas in the wear track.	107
6.6	Narrowing of the amorphous carbon D and G Raman features.	110
6.7	Exemplary clustering and principal component analysis.	112
6.8	PCA of the complete a-C data set.	113
A.1	Scheme of focus stacking.	124
A.2	Schemes of the Knife-Edge Method.	125
B.1	Exemplary Raman spectrum, with a region of interest selected.	127
B.2	Region excluded from background fitting.	128
B.3	Peaks selected for fitting.	128
B.4	Exemplary Raman mapping of a test sample with three different regions. .	129
B.5	Clustered mapping of a test sample with different regions.	131
B.6	Principal component analysis of a test sample with four different clusters. .	132

List of Tables

2.1	Character table of the D_{3d} point group.	11
2.2	Penetration depths for different materials and wavelengths.	17
2.3	Material parameters used for flash temperature estimation.	27
2.4	Band gap and hardness of some carbon species.	31
4.1	MoS_2 Raman modes.	63
5.1	Parameters used for a-C film deposition.	73
5.2	Mechanical, optical and compositional properties of a-C films.	76
5.3	Influences of deposition parameters on the properties of a-C films.	77
5.4	Fitting parameter ranges for 266 nm and 532 nm excitation.	78
5.5	XPS-determined sp^3 contents of selected a-C films.	80
5.6	Deposition parameters and properties of HiPIMS deposited MoS_x films.	84
5.7	Influences of selected deposition parameters on mechanical film properties.	85
5.8	Influences of selected deposition parameters on structural and compositional film properties.	86
5.9	Mechanical properties of HiPIMS deposited MoS_x films.	89
5.10	X-ray-determined properties of MoS_x coatings.	92
5.11	FHWM of selected Raman modes of MoS_x coatings.	95
6.1	Overview of wear-induced amorphous carbon film samples.	103
6.2	Lubricants used for wear-induced amorphous carbon films.	104
6.3	Atmosphere-dependent amorphous carbon formation.	111
6.4	Coefficients forming the principal components of the a-C PCA.	114
6.5	Optical and tribological composition of spectrally grouped clusters.	115
6.6	Atmospheric and lubricational composition of the spectrally grouped clusters.	116
A.1	Properties and beam waists of several objectives.	125
A.2	Typical resolutions and spectral ranges of the MonoVista setup.	126
C.1	Character table of the C_{2h} point group.	133
C.2	Character table of the D_{3d} point group.	133
C.3	Character table of the D_{3h} point group.	133
C.4	Character table of the D_{6h} point group.	134
C.5	Character table of the O_h point group.	134
D.1	Optical and tribological composition of detected clusters.	135
D.2	Atmospheric and lubricational composition of detected clusters.	135

List of Publications

- [Fre19] L. FRENTZEL-BEYME, M. KLOSS, R. PALLACH, S. SALAMON, H. MOLDENHAUER, J. LANDERS, H. WENDE, J. DEBUS, and S. HENKE. “Porous Purple Glass – a Cobalt Imidazolate Glass with Accessible Porosity from a Meltable Cobalt Imidazolate Framework.” In: *Journal of Materials Chemistry A* **7.3** (2019), pp. 985–990. DOI: 10.1039/C8TA08016J.
- [Jen19] S. JENDRZEJ, L. GONDECKI, J. DEBUS, H. MOLDENHAUER, P. TENBERGE, S. BARCIKOWSKI, and B. GÖKCE. “Tribological Properties of Laser-Generated Hard Ceramic Particles in a Gear Drive Contact.” In: *Applied Surface Science* **467-468** (2019). ©, pp. 811–818. DOI: 10.1016/j.apsusc.2018.10.060.
- [Kok20] D. KOKALJ, J. DEBUS, D. STANGIER, H. MOLDENHAUER, A. NIKOLOV, A. WITTIG, A. BRÜMMER, and W. TILLMANN. “Controlling the Structural, Mechanical and Frictional Properties of MoS_x Coatings by High-Power Impulse Magnetron Sputtering.” In: *Coatings* **10.755** (2020). ©. DOI: 10.3390/coatings10080755.
- [Kud20] D. KUDLACIK, K. V. KAVOKIN, C. LÜDERS, K. BARTHELMI, J. J. SCHINDLER, H. MOLDENHAUER, P. WALDKIRCH, V. F. SAPEGA, D. R. YAKOVLEV, A. WAAG, M. BAYER, and J. DEBUS. “Asymmetric Spin Transitions of Nonthermalized Mn²⁺ Ions in (Zn,Mn)Se-Based Quantum Wells.” In: *Physical Review B* **101.15** (2020), p. 155432. DOI: 10.1103/PhysRevB.101.155432.
- [Mol18] H. MOLDENHAUER, M. BAYER, J. DEBUS, A. NIKOLOV, and A. BRÜMMER. “Raman Scattering Study of Micrometer-Sized Spots of Magnetite and Hematite Formed at 18CrNiMo7-6 Screw Rotor Surfaces due to Liquid-Free, Unsynchro-nized Operation.” In: *IOP Conference Series: Materials Science and Engineering* **425** (2018). ©, p. 012016. DOI: 10.1088/1757-899x/425/1/012016.
- [Mol19] H. MOLDENHAUER, A. WITTIG, D. KOKALJ, D. STANGIER, A. BRÜMMER, W. TILLMANN, and J. DEBUS. “Resonant Raman Scattering Characterization of Thermally Annealed HiPIMS Deposited MoS_x Coatings.” In: *Surface and Coatings Technology* **337** (2019). ©, p. 124891. DOI: 10.1016/j.surfcoat.2019.124891.
- [Mol20] H. MOLDENHAUER, C. RITTMAN, and S. GRISARD. *Spectrum Analysis*. 2020. URL: https://github.com/hmoldenhauer/spectrum_analysis.
- [Til19a] W. TILLMANN, N. F. L. DIAS, D. STANGIER, W. MAUS-FRIEDRICH, R. GUSTUS, C. A. THOMANN, H. MOLDENHAUER, and J. DEBUS. “Improved Adhesion of a-C and a-C:H Films with a CrC Interlayer on 16MnCr5 by HiPIMS-Pretreatment.” In: *Surface and Coatings Technology* **375** (2019). ©, pp. 877–887. DOI: 10.1016/j.surfcoat.2019.07.076.

- [Til19b] W. TILLMANN, N. F. L. DIAS, D. STANGIER, M. BAYER, H. MOLDENHAUER, J. DEBUS, M. SCHMITZ, U. BERGES, and C. WESTPHAL. “Interaction Effects of Cathode Power, Bias Voltage, and Mid-Frequency on the Structural and Mechanical Properties of Sputtered Amorphous Carbon Films.” In: *Applied Surface Science* **487** (2019). © ⓘ Ⓢ ⊖, pp. 857–867. DOI: 10.1016/j.apsusc.2019.05.131.
- [Til19d] W. TILLMANN, A. WITTIG, D. STANGIER, C. A. THOMANN, H. MOLDENHAUER, J. DEBUS, D. AURICH, and A. BRÜMMER. “Investigation of the Tribofilm Formation of HiPIMS Sputtered MoS_x Thin Films in Different Environments by Raman Scattering.” In: *Lubricants* **7.11** (2019). © ⓘ. DOI: 10.3390/lubricants7110100.
- [Til20a] W. TILLMANN, H. ULITZKA, N. F. L. DIAS, D. STANGIER, C. A. THOMANN, H. MOLDENHAUER, and J. DEBUS. “Effects of Acetylene Flow Rate and Bias Voltage on the Structural and Tribo-Mechanical Properties of Sputtered a-C:H Films.” In: *Thin Solid Films* **693** (2020). © ⓘ Ⓢ ⊖, p. 137691. DOI: 10.1016/j.tsf.2019.137691.
- [Til20b] W. TILLMANN, N. F. LOPES DIAS, D. STANGIER, A. NIENHAUS, C. A. THOMANN, A. WITTRÖCK, H. MOLDENHAUER, and J. DEBUS. “Effect of the Bias Voltage on the Structural and Tribo-Mechanical Properties of Ag-Containing Amorphous Carbon Films.” In: *Diamond and Related Materials* **105** (2020), p. 107803. DOI: 10.1016/j.diamond.2020.107803.
- [Til20c] W. TILLMANN, A. WITTIG, H. MOLDENHAUER, C.-A. THOMANN, J. DEBUS, D. AURICH, and A. BRUEMMER. “Nitrogen Doping of MoS_x Thin Films Sputtered by Reactive High Power Impulse Magnetron Sputtering.” In: *Thin Solid Films* **713** (2020), p. 138267. DOI: 10.1016/j.tsf.2020.138267.
- [Til20d] W. TILLMANN, A. WITTIG, D. STANGIER, H. MOLDENHAUER, C.-A. THOMANN, J. DEBUS, D. AURICH, and A. BRUEMMER. “Influence of the Bias-Voltage, the Argon Pressure and the Heating Power on the Structure and the Tribological Properties of HiPIMS Sputtered MoS_x Films.” In: *Surface and Coatings Technology* **385** (2020), p. 125358. DOI: 10.1016/j.surfcoat.2020.125358.
- [Til21] W. TILLMANN, A. WITTIG, D. STANGIER, H. MOLDENHAUER, C.-A. THOMANN, J. DEBUS, D. AURICH, and A. BRUEMMER. “Temperature-Dependent Tribological Behavior of MoS_x Thin Films Synthesized by HiPIMS.” In: *Tribology International* **153** (2021), p. 106655. DOI: 10.1016/j.triboint.2020.106655.
- [Utr19] M. UTRI, D. AURICH, A. BRÜMMER, A. WITTIG, W. TILLMANN, H. MOLDENHAUER, and J. DEBUS. “Theoretical Investigation of the Rotor Contact Stress in Non-Synchronized, Dry Running Twin-Screw Machines.” In: *Prozesstechnik und Komponenten* (2019), pp. 84–93. URL: <https://bc-v3.pressmatrix.com/de/profiles/ee23a4677553/editions/49f5e58353bad86c052b/pages/page/45>.

Bibliography

- [Aba09] M. D. ABAD, J. C. SÁNCHEZ-LÓPEZ, N. CUSNIR, and R. SANJINES. “WC/a-C Nanocomposite Thin Films: Optical and Electrical Properties.” In: *Journal of Applied Physics* **105.3** (2009), p. 033510. DOI: 10.1063/1.3060717.
- [Ant07] G. ANT CZAK and G. EHRLICH. “Jump Processes in Surface Diffusion.” In: *Surface Science Reports* **62.2** (2007), pp. 39–61. DOI: 10.1016/j.surfrep.2006.12.001.
- [Ara77] E. T. ARAKAWA, M. W. WILLIAMS, and T. INAGAKI. “Optical Properties of Arc-Evaporated Carbon Films between 0.6 and 3.8 eV.” In: *Journal of Applied Physics* **48.7** (1977), pp. 3176–3177. DOI: 10.1063/1.324057.
- [Arc59] J. F. ARCHARD. “The Temperature of Rubbing Surfaces.” In: *Wear* **2.6** (1959), pp. 438–455. DOI: 10.1016/0043-1648(59)90159-0.
- [Ash90] M. F. ASHBY, J. ABULAWI, and H. S. KONG. *On Surface Temperatures at Dry Sliding Surfaces*. Cambridge: University of Cambridge, Department of Engineering, 1990.
- [Aub90] A. AUBERT, J. P. NABOT, J. ERNOULT, and P. RENAUX. “Preparation and Properties of MoS_x Films Grown by D.C. Magnetron Sputtering.” In: *Surface and Coatings Technology* **41.1** (1990), pp. 127–134. DOI: 10.1016/0257-8972(90)90136-Z.
- [Bec06] S. BEC, A. TONCK, and J. FONTAINE. “Nanoindentation and Nanofriction on DLC Films.” In: *Philosophical Magazine* **86.33 - 35** (2006), pp. 5465–5476. DOI: 10.1080/14786430600596845.
- [Bec19] C. BECKMANN. “Simulation der RAMAN-Spektren von Silizium-Nanopartikeln.” Bachelor Thesis. University of Dortmund, 2019.
- [Bee20] F. P. BEER, E. R. JOHNSTON, J. T. DEWOLF, and D. F. MAZUREK. “Stress and Strain - Axial Loading.” In: *Mechanics of Materials*. 8th ed. McGraw-Hill Education, 2020. Chap. 2, pp. 57–148.
- [Ber14] A. BERA and A. K. SOOD. “Insights into Vibrational and Electronic Properties of MoS₂ Using Raman, Photoluminescence, and Transport Studies.” In: *MoS₂*. Springer International Publishing, 2014. Chap. 7, pp. 155–216. DOI: 10.1007/978-3-319-02850-7_7.
- [Bha96] S. BHARGAVA, H. D. BIST, A. V. NARLIKAR, et al. “Effect of Substrate Temperature and Heat Treatment on the Microstructure of Diamondlike Carbon Films.” In: *Journal of Applied Physics* **79.4** (1996), pp. 1917–1925. DOI: 10.1063/1.361081.
- [Bob13a] K. BOBZIN. “Korrosion.” In: *Oberflächentechnik für den Maschinenbau*. WILEY-VCH, 2013. Chap. 3, pp. 65–130.

- [Bob13b] K. BOBZIN. “Physical Vapor Deposition.” In: *Oberflächentechnik für den Maschinenbau*. WILEY-VCH, 2013. Chap. 7, pp. 207–234.
- [Bod13] H. BODSCHWINNA and J. SEEWIG. “Surface Statistics and Probability Density Function.” In: *Encyclopedia of Tribology*. Springer, 2013, pp. 3464–3471.
- [Bop85] H. BOPPART, J. VAN STRAATEN, and I. F. SILVERA. “Raman Spectra of Diamond at High Pressures.” In: *Physical Review B* **32.2** (1985), pp. 1423–1425. DOI: 10.1103/PhysRevB.32.1423.
- [Bow70] A. W. BOWEN and G. M. LEAK. “Solute Diffusion in α - and γ -Iron.” In: *Metallurgical Transactions* **1.9** (1970), pp. 1695–1700. DOI: 10.1007/BF02642019.
- [Bra85] R. BRAUN and M. FELLER-KNIEPMEIER. “Diffusion of Chromium in α -Iron.” In: *physica status solidi (a)* **90.2** (1985), pp. 553–561. DOI: 10.1002/pssa.2210900219.
- [Bri12] C. D. S. BRITES, P. P. LIMA, N. J. O. SILVA, et al. “Thermometry at the Nanoscale.” In: *Nanoscale* **4.16** (2012), pp. 4799–4829. DOI: 10.1039/C2NR30663H.
- [Bro14] B. BROWN and T. POON. “Covalent Bonding and Shapes of Molecules.” In: *Introduction to Organic Chemistry*. 5th ed. John Wiley & Sons, 2014. Chap. 1, pp. 1–40.
- [Bül16] F. BÜLBÜL and İ. EFEOĞLU. “Synergistic Effect of Bias and Target Currents for Magnetron Sputtered MoS₂-Ti Composite Films.” In: *Materials Testing* **58.5** (2016), pp. 471–474. DOI: 10.3139/120.110870.
- [Cai12] M. CAI, D. THORPE, D. H. ADAMSON, and H. C. SCHNIEPP. “Methods of Graphite Exfoliation.” In: *Journal of Materials Chemistry* **22.48** (2012), p. 24992. DOI: 10.1039/c2jm34517j.
- [Car00] M. CARDONA and G. GÜNTHERODT. “Introduction.” In: *Light Scattering in Solids VII*. Springer-Verlag, 2000. Chap. 1, pp. 1–23.
- [Car83a] M. CARDONA. “Introduction.” In: *Light Scattering in Solids I*. 2nd ed. Springer-Verlag, 1983. Chap. 1, pp. 1–22.
- [Car83b] M. CARDONA, ed. *Light Scattering in Solids I. Introductory Concepts*. 2nd ed. Berlin: Springer-Verlag, 1983. ISBN: 0-387-11913-2.
- [Car91] M. CARDONA and G. GÜNTHERODT. “Introduction.” In: *Light Scattering in Solids VI*. Springer-Verlag, 1991. Chap. 1, pp. 1–16.
- [Caz99] E. CAZZANELLI, C. VINEGONI, G. MARIOTTO, A. KUZMIN, and J. PURANS. “Raman Study of the Phase Transitions Sequence in Pure WO₃ at High Temperature and in H_xWO₃ with Variable Hydrogen Content.” In: *Solid State Ionics* **123.1** (1999), pp. 67–74. DOI: 10.1016/S0167-2738(99)00101-0.
- [Cen88] P. W. CENTERS. “Tribological Performance of MoS₂ Compacts Containing MoO₃, Sb₂O₃ or MoO₃ and Sb₂O₃.” In: *Wear* **122.1** (1988), pp. 97–102. DOI: 10.1016/0043-1648(88)90009-9.
- [Cha19] S. J. CHALK. *Compendium of Chemical Terminology*. Ed. by A. D. MCNAUGHT and A. WILKINSON. IUPAC. 2019. DOI: 10.1351/goldbook.

- [Che07] I. V. CHERNYSHOVA, M. F. HOCELLA JR, and A. S. MADDEN. “Size-Dependent Structural Transformations of Hematite Nanoparticles. 1. Phase Transition.” In: *Physical Chemistry Chemical Physics* **9.14** (2007), p. 1736. DOI: 10.1039/b618790k.
- [Che74] J. CHEN and C. WANG. “Second Order Raman Spectrum of MoS₂.” In: *Solid State Communications* **14.9** (1974), pp. 857–860. DOI: 10.1016/0038-1098(74)90150-1.
- [Che90] C. T. CHEN and F. SETTE. “High Resolution Soft X-Ray Spectroscopies with the Dragon Beamline.” In: *Physica Scripta* **T31** (1990), pp. 119–126. DOI: 10.1088/0031-8949/1990/t31/016.
- [Chh00] M. CHHOWALLA, A. C. FERRARI, J. ROBERTSON, and G. a. J. AMARATUNGA. “Evolution of sp² Bonding with Deposition Temperature in Tetrahedral Amorphous Carbon Studied by Raman Spectroscopy.” In: *Applied Physics Letters* **76.11** (2000), pp. 1419–1421. DOI: 10.1063/1.126050.
- [Chi02] V. CHIKAN and D. F. KELLEY. “Size-Dependent Spectroscopy of MoS₂ Nanoclusters.” In: *The Journal of Physical Chemistry B* **106.15** (2002), pp. 3794–3804. DOI: 10.1021/jp011898x.
- [Chi11] D. CHICOT, J. MENDOZA, A. ZAOUI, et al. “Mechanical Properties of Magnetite (Fe₃O₄), Hematite (α -Fe₂O₃) and Goethite (α -FeO·OH) by Instrumented Indentation and Molecular Dynamics Analysis.” In: *Materials Chemistry and Physics* **129.3** (2011), pp. 862–870. DOI: 10.1016/j.matchemphys.2011.05.056.
- [Chi85] R. R. CHIANELLI, A. F. RUPPERT, S. K. BEHAL, et al. “The Reactivity of MoS₂ Single Crystal Edge Planes.” In: *Journal of Catalysis* **92.1** (1985), pp. 56–63. DOI: 10.1016/0021-9517(85)90236-2.
- [Cho90] N.-H. CHO, K. M. KRISHNAN, D. K. VEIRS, et al. “Chemical Structure and Physical Properties of Diamond-Like Amorphous Carbon Films Prepared by Magnetron Sputtering.” In: *Journal of Materials Research* **5.11** (1990), pp. 2543–2554. DOI: 10.1557/JMR.1990.2543.
- [Chu06] P. K. CHU and L. LI. “Characterization of Amorphous and Nanocrystalline Carbon Films.” In: *Materials Chemistry and Physics* **96.2** (2006), pp. 253–277. DOI: 10.1016/j.matchemphys.2005.07.048.
- [Chu11a] Y. W. CHUNG. “Environmental Effects in Tribology.” In: *Micro- and Nanoscale Phenomena in Tribology*. CRC Press, 2011. Chap. 7, pp. 153–187.
- [Chu11b] Y. W. CHUNG. *Micro- and Nanoscale Phenomena in Tribology*. Boca Raton: CRC Press, 2011.
- [Cia13] P. CIAIS and C. SABINE. “Carbon and Other Biogeochemical Cycles.” In: *Climate Change 2013: The Physical Science Basis*. Cambridge University Press, 2013. Chap. 6, pp. 465–570.
- [Col10] R. S. COLBERT and W. G. SAWYER. “Thermal Dependence of the Wear of Molybdenum Disulphide Coatings.” In: *Wear* **269.11** (2010), pp. 719–723. DOI: 10.1016/j.wear.2010.07.008.

- [Col11] P. COLOMBAN. “Potential and Drawbacks of Raman (Micro)Spectrometry for the Understanding of Iron and Steel Corrosion.” In: *New Trends and Developments in Automotive System Engineering*. Ed. by M. CHIABERGE. InTech, 2011. DOI: 10.5772/13436.
- [Col15] G. COLAS, A. SAULOT, E. REGIS, and Y. BERTHIER. “Investigation of Crystalline and Amorphous MoS₂ Based Coatings: Towards Developing New Coatings for Space Applications.” In: *Wear* **330-331** (2015), pp. 448–460. DOI: 10.1016/j.wear.2015.01.011.
- [Com20] B. O. COMMUNITY. *Blender - a 3D Modelling and Rendering Package*. Blender Foundation. 2020. URL: <http://www.blender.org>.
- [Cor03a] R. M. CORNELL and U. SCHWERTMANN. “Applications.” In: *The Iron Oxides*. WILEY, 2003. Chap. 19, pp. 509–526. DOI: 10.5772/13436.
- [Cor03b] R. M. CORNELL and U. SCHWERTMANN. *The Iron Oxides. Structure, Properties, Reactions, Occurrences and Uses*. 2nd ed. Weinheim: WILEY, 2003. DOI: 10.1002/3527602097.
- [Cot90a] F. A. COTTON. *Chemical Applications of Group Theory*. 3rd ed. Wiley, 1990.
- [Cot90b] F. A. COTTON. “Representations of Groups.” In: *Chemical Applications of Group Theory*. 3rd ed. Wiley, 1990. Chap. 4, pp. 68–99.
- [Czi00] H. CZICHOS. “Materialschädigung und Materialschutz.” In: *Die Grundlagen der Ingenieurwissenschaften*. 31st ed. Springer-Verlag, 2000. Chap. D10, pp. D64–D73.
- [Czi15a] H. CZICHOS. “Tribologische Systeme.” In: *Tribologie-Handbuch*. 4th ed. Springer Vieweg, 2015. Chap. 2, pp. 13–28.
- [Czi15b] H. CZICHOS and K.-H. HABIG. “Technik und Tribologie.” In: *Tribologie-Handbuch*. 4th ed. Springer Vieweg, 2015. Chap. 1, pp. 3–12.
- [Czi15c] H. CZICHOS and K.-H. HABIG. *Tribologie-Handbuch*. 4th ed. Wiesbaden: Springer Vieweg, 2015.
- [Czi15d] H. CZICHOS and K.-H. HABIG. “Verschleiß.” In: *Tribologie-Handbuch*. 4th ed. Springer Vieweg, 2015. Chap. 5, pp. 127–180.
- [Czi15e] H. CZICHOS and E. SANTNER. “Tribologische Beanspruchung.” In: *Tribologie-Handbuch*. 4th ed. Springer Vieweg, 2015. Chap. 3, pp. 29–92.
- [Dai16] H. DAI, C. ZHAN, and J. DU. “Studies on the Influence of Sputtering Power on Amorphous Carbon Films Deposited by Pulsed Unbalanced Magnetron Sputtering.” In: *Optik* **127.5** (2016), pp. 2512–2515. DOI: 10.1016/j.ijleo.2015.11.154.
- [Däm98] U. DÄMGEN. “Beanspruchung von verschleißbeständigen Werkstoffverbunden in Schraubenkompressoren.” Dissertation. University of Dortmund, 1998.
- [Das13] T. DASH and B. B. NAYAK. “Preparation of WC–W₂C Composites by Arc Plasma Melting and Their Characterisations.” In: *Ceramics International* **39.3** (2013), pp. 3279–3292. DOI: 10.1016/j.ceramint.2012.10.016.

- [Das16] T. DASH and B. B. NAYAK. “Preparation of Multi-Phase Composite of Tungsten Carbide, Tungsten Boride and Carbon by Arc Plasma Melting: Characterization of Melt-Cast Product.” In: *Ceramics International* **42.1** (2016), pp. 445–459. DOI: 10.1016/j.ceramint.2015.08.129.
- [Dav13] P. DAVID. *Focus Stacking Macro Photos (Enfuse)*. 2013. URL: <https://patdavid.net/2013/01/focus-stacking-macro-photos-enfuse.html>.
- [Dav93] C. A. DAVIS. “A Simple Model for the Formation of Compressive Stress in Thin Films by Ion Bombardment.” In: *Thin Solid Films* **226.1** (1993), pp. 30–34. DOI: 10.1016/0040-6090(93)90201-Y.
- [Deb16] J. DEBUS, J. J. SCHINDLER, P. WALDKIRCH, et al. “Indication of Worn WC/C Surface Locations of a Dry-Running Twin-Screw Rotor by the Oxygen Incorporation in Tungsten-Related Raman Modes.” In: *Applied Physics Letters* **109.17** (2016). DOI: 10.1063/1.4966145.
- [Dem11] W. DEMTROEDER. “Linienbreiten und Profile von Spektrallinien.” In: *Laserspektroskopie 1*. 6th ed. Springer, 2011. Chap. 3, pp. 43–68.
- [Den16] Y. DENG, L. R. L. TING, P. H. L. NEO, et al. “Operando Raman Spectroscopy of Amorphous Molybdenum Sulfide (MoS_x) during the Electrochemical Hydrogen Evolution Reaction: Identification of Sulfur Atoms as Catalytically Active Sites for H^+ Reduction.” In: *ACS Catalysis* **6.11** (2016), pp. 7790–7798. DOI: 10.1021/acscatal.6b01848.
- [Dia08] J. DIAZ-REYES, V. DORANTES-GARCIA, A. PEREZ-BENITEZ, and J. A. BALDERAS-LOPEZ. “Obtaining of Films of Tungsten Trioxide (WO_3) by Resistive Heating of a Tungsten Filament.” In: *Superficies y Vacio* **21** (2008), pp. 12–17. URL: http://www.scielo.org.mx/scielo.php?script=sci_arttext&pid=S1665-35212008000200003&nrm=iso.
- [Did90] S. V. DIDZIULIS, P. D. FLEISCHAUER, B. L. SORIANO, and M. N. GARDOS. “Chemical and Tribological Studies of MoS_2 Films on SiC Substrates.” In: *Surface and Coatings Technology* **43-44** (1990), pp. 652–662. DOI: 10.1016/0257-8972(90)90009-2.
- [Die02] M. DIETERLE and G. MESTL. “Raman Spectroscopy of Molybdenum Oxides Part II. Resonance Raman Spectroscopic Characterization of the Molybdenum Oxides Mo_4O_{11} and MoO_2 .” In: *Phys. Chem. Chem. Phys.* **4** (2002), pp. 822–826. DOI: 10.1039/B107046K.
- [Die18a] T. DIEING, O. HOLLRICHTER, and J. TOPORSKI. *Confocal Raman Microscopy*. 2nd ed. Berlin: Springer-Verlag, 2018.
- [Die18b] B. DIETZEK, D. CIALLA, M. SCHMITT, and J. POPP. “Introduction to the Fundamentals of Raman Spectroscopy.” In: *Confocal Raman Microscopy*. 2nd ed. Springer-Verlag, 2018. Chap. 3, pp. 47–68.
- [Día96] J. DÍAZ, G. PAOLICELLI, S. FERRER, and F. COMIN. “Separation of the sp^3 and sp^2 Components in the C1s Photoemission Spectra of Amorphous Carbon Films.” In: *Phys. Rev. B* **54** (1996), pp. 8064–8069. DOI: 10.1103/PhysRevB.54.8064.

- [Don70] S. DONIACH and M. SUNJIC. “Many-Electron Singularity in X-Ray Photoemission and X-Ray Line Spectra from Metals.” In: *Journal of Physics C: Solid State Physics* **3.2** (1970), pp. 285–291. DOI: 10.1088/0022-3719/3/2/010.
- [Don96] C. DONNET, J. MARTIN, T. L. MOGNE, and M. BELIN. “Super-Low Friction of MoS₂ Coatings in Various Environments.” In: *Tribology International* **29.2** (1996), pp. 123–128. DOI: 10.1016/0301-679X(95)00094-K.
- [Dre14] T. DREIFERT and R. MÜLLER. “Screw Vacuum Pumps.” In: *VDI-Berichte* **2228** (2014), pp. 29–42. URL: <http://www.ft.mb.tu-dortmund.de/Publikationen/ICSM/2014/T.%20dreifert,%20R.%20M%C3%BCller%202014%20-%20Screw%20vacuum%20pumps.pdf>.
- [Dre82] M. S. DRESSELHAUS and G. DRESSELHAUS. “Light Scattering in Graphite Intercalation Compounds.” In: *Light Scattering in Solids III*. Springer-Verlag, 1982. Chap. 2, pp. 3–58.
- [Ehr01] F. EHRENTREICH and L. SÜMMCHEN. “Spike Removal and Denoising of Raman Spectra by Wavelet Transform Methods.” In: *Analytical Chemistry* **73.17** (2001), pp. 4364–4373. DOI: 10.1021/ac0013756.
- [Erd00] A. ERDEMIR. “Solid Lubricants and Self-Lubricating Films.” In: *Modern Tribology Handbook*. CRC Press, 2000. Chap. 22, pp. 787–826.
- [Erd16] A. ERDEMIR, G. RAMIREZ, O. L. ERYILMAZ, et al. “Carbon-Based Tribofilms from Lubricating Oils.” In: *Nature* **536** (2016), pp. 67–71. DOI: 10.1038/nature18948.
- [Erm20] G. A. ERMOLAEV, Y. V. STEBUNOV, A. A. VYSHNEVYY, et al. “Broadband Optical Properties of Monolayer and Bulk MoS₂.” In: *npj 2D Materials and Applications* **4.1** (2020), pp. 2397–7132. DOI: 10.1038/s41699-020-0155-x.
- [Eva16] M.-H. EVANS. “An Updated Review: White Etching Cracks (WECs) and Axial Cracks in Wind Turbine Gearbox Bearings.” In: *Materials Science and Technology* **32.11** (2016), pp. 1133–1169. DOI: 10.1080/02670836.2015.1133022.
- [Fal00] L. FALKOVSKY and J. CAMASSEL. “Disorder Effect on Optical Phonons.” In: *Physica B: Condensed Matter* **284 - 288** (2000), pp. 1145–1146. DOI: 10.1016/S0921-4526(99)02547-8.
- [Fan19] H. FANG, A. ROLDAN, C. TIAN, et al. “Structural Tuning and Catalysis of Tungsten Carbides for the Regioselective Cleavage of C-O Bonds.” In: *Journal of Catalysis* **369** (2019), pp. 283–295. DOI: 10.1016/j.jcat.2018.11.020.
- [Far97] D. L. A. de FARIA, S. V. SILVA, and M. T. de OLIVEIRA. “Raman Microspectroscopy of Some Iron Oxides and Oxyhydroxides.” In: *Journal of Raman Spectroscopy* **28.11** (1997), pp. 873–878. DOI: 10.1002/(SICI)1097-4555(199711)28:11<873::AID-JRS177>3.0.CO;2-B.
- [Fer00] A. C. FERRARI and J. ROBERTSON. “Interpretation of Raman Spectra of Disordered and Amorphous Carbon.” In: *Physical Review B* **61** (2000), pp. 14095–14107. DOI: 10.1103/PhysRevB.61.14095.

- [Fer01] A. C. FERRARI and J. ROBERTSON. “Resonant Raman Spectroscopy of Disordered, Amorphous, and Diamondlike Carbon.” In: *Physical Review B* **64** (2001), p. 075414. DOI: 10.1103/PhysRevB.64.075414.
- [Fle84] P. D. FLEISCHAUER. “Effects of Crystallite Orientation on Environmental Stability and Lubrication Properties of Sputtered MoS₂ Thin Films.” In: *ASLE Transactions* **27.1** (1984), pp. 82–88. DOI: 10.1080/05698198408981548.
- [Fle87] P. D. FLEISCHAUER. “Fundamental Aspects of the Electronic Structure, Materials Properties and Lubrication Performance of Sputtered MoS₂ Films.” In: *Thin Solid Films* **154.1** (1987), pp. 309–322. DOI: 10.1016/0040-6090(87)90375-0.
- [Fox01] M. FOX. “Introduction.” In: *Optical Properties of Solids*. Oxford University Press, 2001. Chap. 1, pp. 1–24.
- [Fre99] G. L. FREY, R. TENNE, M. J. MATTHEWS, M. S. DRESSELHAUS, and G. DRESSELHAUS. “Raman and Resonance Raman Investigation of MoS₂ Nanoparticles.” In: *Phys. Rev. B* **60.4** (1999), pp. 2883–2892. DOI: 10.1103/PhysRevB.60.2883.
- [Fri66] R. F. FRINDT. “Single Crystals of MoS₂ Several Molecular Layers Thick.” In: *Journal of Applied Physics* **37.4** (1966), pp. 1928–1929. DOI: 10.1063/1.1708627.
- [Gao10] F. M. GAO and L. H. GAO. “Microscopic Models of Hardness.” In: *Journal of Superhard Materials* **32.3** (2010), pp. 148–166. DOI: 10.3103/S1063457610030020.
- [Gar98] W. P. GARDINER and G. GETTINBY. “Response Surface Methods.” In: *Experimental Design Techniques in Statistical Practice*. Horwood Publishing, 1998. Chap. 11, pp. 322–354.
- [Gen13] C. GENZEL, I. A. DENKS, and M. KLAUS. “Residual Stress Analysis by X-Ray Diffraction Methods.” In: *Modern Diffraction Methods*. John Wiley & Sons, 2013. Chap. 5, pp. 127–154.
- [Gil91] B. GILLOT, H. NOUAIM, F. MATHIEU, and A. ROUSSET. “Effect of a Pretreatment Under High Pressure on the Oxidation Mechanism of Magnetite to γ -Fe₂O₃ and on the Transformation γ -Fe₂O₃ to α -Fe₂O₃.” In: *Materials Chemistry and Physics* **28.4** (1991), pp. 389–397. DOI: 10.1016/0254-0584(91)90074-5.
- [Gio98] M. GIOTI and S. LOGOTHETIDIS. “The Effect of Substrate Bias in Amorphous Carbon Films Prepared by Magnetron Sputtering and Monitored by in-situ Spectroscopic Ellipsometry.” In: *Diamond and Related Materials* **7.2** (1998), pp. 444–448. DOI: 10.1016/S0925-9635(97)00297-5.
- [God98] D. GODFREY. “Iron Oxides and Rust (Hydrated Iron Oxides) in Tribology.” In: *Tribology & Lubrication Technology* **55.2** (1998), p. 33.
- [Gol13] A. S. GOLOVESHKIN, I. S. BUSHMARINOV, N. D. LENENKO, et al. “Structural Properties and Phase Transition of Exfoliated-Restacked Molybdenum Disulfide.” In: *The Journal of Physical Chemistry C* **117.16** (2013), pp. 8509–8515. DOI: 10.1021/jp400087c.

- [Gou07] G. GOUADEC and P. COLOMBAN. “Raman Spectroscopy of Nanomaterials: How Spectra Relate to Disorder, Particle Size and Mechanical Properties.” In: *Progress in Crystal Growth and Characterization of Materials* **53.1** (2007), pp. 1–56. DOI: 10.1016/j.pcrysgrow.2007.01.001.
- [Gra10] R. GRAU-CRESPO, A. Y. AL-BAITAI, I. SAADOUNE, and N. H. D. LEEUW. “Vacancy Ordering and Electronic Structure of γ -Fe₂O₃ (Maghemite): a Theoretical Investigation.” In: *Journal of Physics: Condensed Matter* **22.25** (2010), p. 255401. DOI: 10.1088/0953-8984/22/25/255401.
- [Gra12] S. GRAŽULIS, A. DAŠKEVIČ, A. MERKYS, et al. “Crystallography Open Database (COD): An Open-Access Collection of Crystal Structures and Platform for World-Wide Collaboration.” In: *Nucleic Acids Research* **40.D1** (2012), pp. D420–D427. DOI: 10.1093/nar/gkr900.
- [Gri18] S. GRISARD. “Anwendung der Knife-Edge-Methode in der konfokalen Raman-Mikroskopie.” Bachelor Thesis. University of Dortmund, 2018.
- [Gro12a] R. GROSS and A. MARX. “Bindungskräfte in Festkörpern.” In: *Festkörperphysik*. Oldenbourg Wissenschaftsverlag, 2012. Chap. 3, pp. 101–151.
- [Gro12b] R. GROSS and A. MARX. “Dynamik des Kristallgitters.” In: *Festkörperphysik*. Oldenbourg Wissenschaftsverlag, 2012. Chap. 5, pp. 177–223.
- [Gro12c] R. GROSS and A. MARX. “Kristallstruktur.” In: *Festkörperphysik*. Oldenbourg Wissenschaftsverlag, 2012. Chap. 1, pp. 1–56.
- [Haa10] A. HAAR. “Zur Theorie der orthogonalen Funktionensysteme.” In: *Mathematische Annalen* **69.3** (1910), pp. 331–371. DOI: 10.1007/BF01456326.
- [Hae01] R. HAERLE, E. RIEDO, A. PASQUARELLO, and A. BALDERESCHI. “sp²/sp³ Hybridization Ratio in Amorphous Carbon from C1s Core-Level Shifts: X-Ray Photoelectron Spectroscopy and First-Principles Calculation.” In: *Phys. Rev. B* **64** (2001), p. 045101. DOI: 10.1103/PhysRevB.65.045101.
- [Hah85] H. G. HAHN. “Räumliche Elastizitätsprobleme.” In: *Elastizitätstheorie*. Springer, 1985. Chap. 9, pp. 272–306.
- [Har03] P. HARIHARAN. “Interference Spectroscopy.” In: *Optical Interferometry*. 2nd ed. Academic Press, 2003. Chap. 10, pp. 157–172.
- [Hau16] P. HAUER, J. GRAND, A. DJOROVIC, G. R. WILLMOTT, and E. C. LE RU. “Spot Size Engineering in Microscope-Based Laser Spectroscopy.” In: *The Journal of Physical Chemistry C* **120.37** (2016), pp. 21104–21113. DOI: 10.1021/acs.jpcc.6b04574.
- [He14] J. HE, K. HUMMER, and C. FRANCHINI. “Stacking Effects on the Electronic and Optical Properties of Bilayer Transition Metal Dichalcogenides MoS₂, MoSe₂, WS₂, and WSe₂.” In: *Phys. Rev. B* **89** (2014), p. 075409. DOI: 10.1103/PhysRevB.89.075409.
- [Hec17] E. HECHT. “The Propagation of Light.” In: *Optics*. Pearson, 2017. Chap. 4, pp. 96–158.

- [Hes17] R. HESSE. *Spectrum Processing, Analysis and Presentation Software for XPS, XAS and AES: version 2017*. Unifit Scientific Software GmbH. 2017. URL: <https://www.unifit-software.de/PDF/Manual-unifit2017.pdf>.
- [Hof16] E. E. HOFFMAN and L. D. MARKS. “Graphitic Carbon Films Across Systems.” In: *Tribology Letters* **63.32** (2016). DOI: 10.1007/s11249-016-0720-9.
- [Hol00] K. HOLMBERG, H. RONKAINEN, and A. MATTHEWS. “Tribology of Thin Coatings.” In: *Ceramics International* **26.7** (2000), pp. 787–795. DOI: 10.1016/S0272-8842(00)00015-8.
- [Hol09a] K. HOLMBERG and A. MATTHEWS. *Coatings Tribology. Properties, Mechanisms, Techniques and Applications in Surface Engineering*. 2nd ed. Amsterdam: Elsevier, 2009.
- [Hol09b] K. HOLMBERG and A. MATTHEWS. “Lamellar Coatings.” In: *Coatings Tribology: Properties, Mechanisms, Techniques and Applications In Surface Engineering*. 2nd ed. Elsevier, 2009. Chap. 4.3, pp. 211–225.
- [Hol10a] O. HOLLRICHTER. “Raman Instrumentation for Confocal Raman Microscopy.” In: *Confocal Raman Microscopy*. Springer-Verlag, 2010. Chap. 3, pp. 43–60.
- [Hol10b] O. HOLLRICHTER and W. IBACH. “High-Resolution Optical and Confocal Microscopy.” In: *Confocal Raman Microscopy*. Springer-Verlag, 2010. Chap. 1, pp. 1–20.
- [Hol17] K. HOLMBERG and A. ERDEMIR. “Influence of Tribology on Global Energy Consumption, Costs and Emissions.” In: *Friction* **5.3** (2017), pp. 263–284. DOI: 10.1007/s40544-017-0183-5.
- [Hor21a] HORIBA SCIENTIFIC. *Optics Tutorial*. 2021. URL: <https://www.horiba.com/uk/scientific/products/optics-tutorial/>.
- [Hor21b] HORIBA SCIENTIFIC. *Raman Hyperspectral Imaging*. 2021. URL: https://static.horiba.com/fileadmin/Horiba/Application/Health_Care/Pharmaceuticals_and_Medicine_Manufacturing/Pharmaceuticals/RA-WhPap_Raman_Hyperspectral_Imaging_Essential_Tool_Pharmaceutical_Field.pdf.
- [How01] N. K. HOWELL, H. HERMAN, and E. C. Y. LI-CHAN. “Elucidation of Protein-Lipid Interactions in a Lysozyme-Corn Oil System by Fourier Transform Raman Spectroscopy.” In: *Journal of Agricultural and Food Chemistry* **49.3** (2001), pp. 1529–1533. DOI: 10.1021/jf001115p.
- [Hub96] G. HUBLER and J. SPRAGUE. “Energetic Particles in PVD Technology: Particle-Surface Interaction Processes and Energy-Particle Relationships in Thin Film Deposition.” In: *Surface and Coatings Technology* **81.1** (1996), pp. 29–35. DOI: 10.1016/0257-8972(95)02617-7.
- [Ida00] T. IDA, M. ANDO, and H. TORAYA. “Extended Pseudo-Voigt Function for Approximating the Voigt Profile.” In: *Journal of Applied Crystallography* **33.6** (2000), pp. 1311–1316. DOI: 10.1107/S0021889800010219.

- [Ing05] B. INGHAM, S. V. CHONG, and J. L. TALLON. “Layered Tungsten Oxide-Based Organic–Inorganic Hybrid Materials: An Infrared and Raman Study.” In: *Journal of Physical Chemistry B* **109** (2005), pp. 4936–4940. DOI: 10.1021/jp0450661.
- [Ing14] B. INGHAM and M. F. TONEY. “Defects.” In: *Metallic Films for Electronic, Optical and Magnetic Applications*. Woodhead Publishing, 2014. Chap. 1.5, pp. 21–28.
- [Ins21] T. P. INSTRUMENTS. *Grating Dispersion Calculator*. 2021. URL: <https://www.princetoninstruments.com/learn/calculators/grating-dispersion>.
- [Jac00] L. JACOBSON, R. PRIOLI, F. FREIRE, et al. “Comparative Study of Anneal-Induced Modifications of Amorphous Carbon Films Deposited by Dc Magnetron Sputtering at Different Argon Plasma Pressures.” In: *Diamond and Related Materials* **9.3-6** (2000), pp. 680–684. DOI: 10.1016/S0925-9635(99)00341-6.
- [Jac93] W. JACOB and W. MÖLLER. “On the Structure of Thin Hydrocarbon Films.” In: *Applied Physics Letters* **63.13** (1993), pp. 1771–1773. DOI: 10.1063/1.110683.
- [Jay03] L. JAYES, A. P. HARD, C. SÉNÉ, S. F. PARKER, and U. A. JAYASOORIYA. “Vibrational Spectroscopic Analysis of Silicones: A Fourier Transform-Raman and Inelastic Neutron Scattering Investigation.” In: *Analytical Chemistry* **75.4** (2003), pp. 742–746. DOI: 10.1021/ac026012f.
- [Joh17] C. S. JOHNSON. “How to Get Very High Magnification.” In: *Science for the Curious Photographer*. 2nd ed. Taylor & Francis, 2017. Chap. 12, pp. 91–108.
- [Joh85] K. L. JOHNSON. “Normal Contact of Elastic Solids: Hertz Theory.” In: *Contact Mechanics*. Cambridge University Press, 1985. Chap. 4, pp. 84–106.
- [Jub10] A. M. JUBB and H. C. ALLEN. “Vibrational Spectroscopic Characterization of Hematite, Maghemite, and Magnetite Thin Films Produced by Vapor Deposition.” In: *ACS Applied Materials & Interfaces* **2.10** (2010), pp. 2804–2812. DOI: 10.1021/am1004943.
- [Kat17] S. KATARIA, S. WAGNER, T. CUSATI, et al. “Growth-Induced Strain in Chemical Vapor Deposited Monolayer MoS₂: Experimental and Theoretical Investigation.” In: *Advanced Materials Interfaces* **4.17** (2017), p. 1700031. DOI: 10.1002/admi.201700031.
- [Kaw95] Y. KAWASHIMA and G. KATAGIRI. “Fundamentals, Overtones, and Combinations in the Raman Spectrum of Graphite.” In: *Physical Review B* **52.14** (1995), pp. 10053–10059. DOI: 10.1103/PhysRevB.52.10053.
- [Kee96] G. KEELER. “Phonon Dispersion Curves and the Density of States.” In: *Solid State Physics Simulations*. John Wiley & Sons, 1996. Chap. 2, pp. 23–55.
- [Kel00] P. J. KELLY and R. D. ARNELL. “Magnetron Sputtering: A Review of Recent Developments and Applications.” In: *Vacuum* **56** (2000), pp. 159–172. DOI: 10.1016/S0042-207X(99)00189-X.

- [Kha13] H. S. KHARE and D. L. BURRIS. “The Effects of Environmental Water and Oxygen on the Temperature-Dependent Friction of Sputtered Molybdenum Disulfide.” In: *Tribology Letters* **52** (2013), pp. 485–493. DOI: 10.1007/s11249-013-0233-8.
- [Kha15] D. N. KHAEMBA, A. NEVILLE, and A. MORINA. “A Methodology for Raman Characterisation of MoDTC Tribofilms and its Application in Investigating the Influence of Surface Chemistry on Friction Performance of MoDTC Lubricants.” In: *Tribology Letters* **59.3** (2015), p. 38. DOI: 10.1007/s11249-015-0566-6.
- [Kha17] M. KHADEM, O. V. PENKOV, H.-K. YANG, and D.-E. KIM. “Tribology of Multi-layer Coatings for Wear Reduction: A Review.” In: *Friction* **5.3** (2017), pp. 248–262. DOI: 10.1007/s40544-017-0181-7.
- [Kho11] A. KHORSAND ZAK, W. H. ABD. MAJID, M. E. ABRISHAMI, and R. YOUSEFI. “X-Ray Analysis of ZnO Nanoparticles by Williamson–Hall and Size–Strain Plot Methods.” In: *Solid State Sciences* **13.1** (2011), pp. 251–256. DOI: 10.1016/j.solidstatedsciences.2010.11.024.
- [Koc17] D. KOCHAN, S. IRMER, and J. FABIAN. “Model Spin-Orbit Coupling Hamiltonians for Graphene Systems.” In: *Physical Review B* **95.16** (2017), p. 165415. DOI: 10.1103/PhysRevB.95.165415.
- [Kok20] D. KOKALJ, J. DEBUS, D. STANGIER, et al. “Controlling the Structural, Mechanical and Frictional Properties of MoS_x Coatings by High-Power Impulse Magnetron Sputtering.” In: *Coatings* **10.755** (2020). © ⓘ. DOI: 10.3390/coatings10080755.
- [Kum14] R. KUMAR, G. SAHU, S. K. SAXENA, H. M. RAI, and P. R. SAGDEO. “Qualitative Evolution of Asymmetric Raman Line-Shape for NanoStructures.” In: *Silicon* **6.2** (2014), pp. 117–121. DOI: 10.1007/s12633-013-9176-9.
- [Kur06] A. S. KURLOV and A. I. GUSEV. “Tungsten Carbides and W-C Phase Diagram.” In: *Inorganic Materials* **42.2** (2006), pp. 121–127. DOI: 10.1134/S0020168506020051.
- [Kuz98] A. KUZMIN, J. PURANS, E. CAZZANELLI, C. VINEGONI, and G. MARIOTTO. “X-Ray Diffraction, Extended X-Ray Absorption Fine Structure and Raman Spectroscopy Studies of WO₃ Powders and (1 – x)WO_{3–y} · x ReO₂ Mixtures.” In: *Journal of Applied Physics* **84.10** (1998), pp. 5515–5524. DOI: 10.1063/1.368596.
- [Laj13] L. LAJAUNIE, F. BOUCHER, R. DESSAPT, and P. MOREAU. “Strong Anisotropic Influence of Local-Field Effects on the Dielectric Response of α -MoO₃.” In: *Phys. Rev. B* **88.11** (2013), p. 115141. DOI: 10.1103/PhysRevB.88.115141.
- [Lam86] L. LAMPORT. *LaTeX: A Document Preparation System*. Reading, Massachusetts: Addison-Wesley, 1986. URL: <https://www.latex-project.org/help/documentation/>.
- [Lan78] J. I. LANGFORD and A. J. C. WILSON. “Scherrer After Sixty Years: A Survey and Some New Results in the Determination of Crystallite Size.” In: *Journal of Applied Crystallography* **11.2** (1978), pp. 102–113. DOI: 10.1107/S0021889878012844.

- [Lau00] W. LAUWERENS, J. WANG, J. NAVRATIL, et al. “Humidity Resistant MoS_x Films Prepared by Pulsed Magnetron Sputtering.” In: *Surface and Coatings Technology* **131.1** (2000), pp. 216–221. DOI: 10.1016/S0257-8972(00)00796-9.
- [Lav68] M. T. LAVIK, T. M. MEDVED, and G. D. MOORE. “Oxidation Characteristics of MoS₂ and Other Solid Lubricants.” In: *ASLE Transactions* **1.1** (1968), pp. 44–55. DOI: 10.1080/05698196808972207.
- [Leb] E. O. LEBIGOT. *Uncertainties: A Python Package for Calculations with Uncertainties*. URL: <http://pythonhosted.org/uncertainties/>.
- [Ler06] J. M. LERNER. “Imaging Spectrometer Fundamentals for Researchers in the Biosciences —A Tutorial.” In: *Cytometry Part A* **69A.8** (2006), pp. 712–734. DOI: 10.1002/cyto.a.20242.
- [Lew01] I. R. LEWIS and H. G. M. EDWARDS, eds. *Handbook of Raman Spectroscopy. From the Research Laboratory to the Process Line*. New York: Marcel Dekker, 2001.
- [Li12] H. LI, Q. ZHANG, C. C. R. YAP, et al. “From Bulk to Monolayer MoS₂: Evolution of Raman Scattering.” In: *Advanced Functional Materials* **22.7** (2012), pp. 1385–1390. DOI: 10.1002/adfm.201102111.
- [Lon02a] D. A. LONG. “Quantum Mechanical Theory of Rayleigh and Raman Scattering.” In: *The Raman Effect*. John Wiley & Sons, 2002. Chap. 4, pp. 49–84.
- [Lon02b] D. A. LONG. “Vibrational Raman Scattering.” In: *The Raman Effect*. John Wiley & Sons, 2002. Chap. 5, pp. 85–152.
- [Lu02] Z. LU, S. M. KANAN, and C. P. TRIPP. “Synthesis of High Surface Area Monoclinic WO₃ Particles Using Organic Ligands and Emulsion Based Methods.” In: *Journal of Materials Chemistry* **12.4** (2002), pp. 983–989. DOI: 10.1039/B107993J.
- [Lud00] K. C. LUDEMA. “Measuring Friction.” In: *Modern Tribology Handbook*. CRC Press, 2000. Chap. 5.8, pp. 220–227.
- [Lui15] C. H. LUI, Z. YE, C. JI, et al. “Observation of Interlayer Phonon Modes in van der Waals Heterostructures.” In: *Phys. Rev. B* **91** (2015), p. 165403. DOI: 10.1103/PhysRevB.91.165403.
- [Lui19] C. H. LUI. “Raman Spectroscopy of van der Waals Heterostructures.” In: *Raman Spectroscopy of Two-Dimensional Materials*. 1st ed. Springer, 2019. Chap. 4, pp. 81–98.
- [Lun13] N. LUNDT, S. T. KELLY, T. RÖDEL, et al. “High Spatial Resolution Raman Thermometry Analysis of TiO₂ Microparticles.” In: *Review of Scientific Instruments* **84.10** (2013), p. 104906. DOI: 10.1063/1.4824355.
- [Lüt15a] H. LÜTH. “Morphology and Structure of Surfaces, Interfaces and Thin Films.” In: *Solid Surfaces, Interfaces and Thin Films*. 6th ed. Springer-Verlag, 2015. Chap. 3, pp. 65–128.
- [Lüt15b] H. LÜTH. *Solid Surfaces, Interfaces and Thin Films*. 6th ed. Berlin: Springer-Verlag, 2015.

- [Mac64] K. MACHIDA and T. MIYAZAWA. “Infrared and Raman Spectra of Polyethyleneglycol Dimethylethers in the Liquid State.” In: *Spectrochimica Acta* **20.12** (1964), pp. 1865–1873. DOI: 10.1016/0371-1951(64)80191-0.
- [Mar20] C. P. MARSHALL, W. J. B. DUFRESNE, and C. J. RUFLEDT. “Polarized Raman Spectra of Hematite and Assignment of External Modes.” In: *Journal of Raman Spectroscopy* **51.9** (2020), pp. 1522–1529. DOI: 10.1002/jrs.5824.
- [Mar77] T. MARTIN, R. MERLIN, D. HUFFMAN, and M. CARDONA. “Resonant Two Magnon Raman Scattering in α -Fe₂O₃.” In: *Solid State Communications* **22.9** (1977), pp. 565–567. DOI: 10.1016/0038-1098(77)90137-5.
- [Mas90] M. J. MASSEY, U. BAIER, R. MERLIN, and W. H. WEBER. “Effects of Pressure and Isotopic Substitution on the Raman Spectrum of α -Fe₂O₃: Identification of Two-Magnon Scattering.” In: *Phys. Rev. B* **41.11** (1990), pp. 7822–7827. DOI: 10.1103/PhysRevB.41.7822.
- [Mat10] D. M. MATTOX. “Introduction.” In: *Handbook of Physical Vapor Deposition (PVD) Processing*. 2nd ed. Elsevier, 2010. Chap. 1, pp. 1–24.
- [Mat72] H. MATSUURA, M. HIRAISHI, and T. MIYAZAWA. “Raman Spectra and Energy Difference Between Rotational Isomers of Ethylene Glycol.” In: *Spectrochimica Acta Part A: Molecular Spectroscopy* **28.12** (1972), pp. 2299–2304. DOI: 10.1016/0584-8539(72)80209-5.
- [Mat87] H. MATUOURA, K. FUKUHARA, and H. TAMAOKI. “Raman Spectra of Perdeuterated Ethylene Glycol Dimethyl Ether and Diethylene Glycol Dimethyl Ether and the Molecular Force Field of Oxyethylene Compounds.” In: *Journal of Molecular Structure* **156.3** (1987), pp. 293–301. DOI: 10.1016/0022-2860(87)87032-1.
- [Mat99] K. MATSUMOTO and M. SUZUKI. “Tribological Performance of Sputtered MoS₂ Films in Various Environment - Influence of Oxygen Concentration, Water Vapor and Gas Species.” In: *8th European Space Mechanisms and Tribology Symposium*. **438**. ESA Special Publication. 1999, pp. 43–48. URL: <https://ui.adsabs.harvard.edu/abs/1999ESASP.438...43M>.
- [Mau19a] R. C. MAURYA and J. MIR. “Molecular Symmetry and Group Theory to Vibrational Spectroscopy.” In: *Molecular Symmetry and Group Theory*. De Gruyter, 2019. Chap. 3, pp. 143–376.
- [Mau19b] R. C. MAURYA and J. MIR. “Symmetry Elements and Symmetry Operations: Molecular Symmetry.” In: *Molecular Symmetry and Group Theory*. De Gruyter, 2019. Chap. 1, pp. 1–28.
- [McC00a] R. L. MCCREERY. “Magnitude of Raman Scattering.” In: *Raman Spectroscopy for Chemical Analysis*. John Wiley & Sons, 2000. Chap. 2, pp. 15–34.
- [McC00b] R. L. MCCREERY. *Raman Spectroscopy for Chemical Analysis*. New York: John Wiley & Sons, 2000.
- [McC00c] R. L. MCCREERY. “Sampling Modes in Raman Spectroscopy.” In: *Raman Spectroscopy for Chemical Analysis*. John Wiley & Sons, 2000. Chap. 6, pp. 95–126.

- [Men18] F. MENG, C. YANG, and H. HAN. “Study on Tribological Performances of MoS₂ Coating at High Temperature.” In: *Proceedings of the Institution of Mechanical Engineers, Part J: Journal of Engineering Tribology* **232.8** (2018), pp. 964–973. DOI: 10.1177/1350650117735272.
- [Men20] Y. MENG, J. XU, Z. JIN, B. PRAKASH, and Y. HU. “A Review of Recent Advances in Tribology.” In: *Friction* **8.2** (2020), pp. 221–300. DOI: 10.1007/s40544-020-0367-2.
- [Men85] J. MENÉNDEZ and M. CARDONA. “Interference Effects: A Key to Understanding Forbidden Raman Scattering by LO Phonons in GaAs.” In: *Phys. Rev. B* **31** (1985), pp. 3696–3704. DOI: 10.1103/PhysRevB.31.3696.
- [Mer17] A. MERLEN, J. G. BUIJNSTERS, and C. PARDANAUD. “A Guide to and Review of the Use of Multiwavelength Raman Spectroscopy for Characterizing Defective Aromatic Carbon Solids: From Graphene to Amorphous Carbons.” In: *Coatings* **7.10** (2017), p. 153. DOI: 10.3390/coatings7100153.
- [Mer97] I. V. MERKULOV, J. S. LANNIN, C. H. MUNRO, et al. “UV Studies of Tetrahedral Bonding in Diamondlike Amorphous Carbon.” In: *Phys. Rev. Lett.* **78.25** (1997), pp. 4869–4872. DOI: 10.1103/PhysRevLett.78.4869.
- [Mes98] G. MESTL and T. K. K. SRINIVASAN. “Raman Spectroscopy of Monolayer-Type Catalysts: Supported Molybdenum Oxides.” In: *Catalysis Reviews* **40.4** (1998), pp. 451–570. DOI: 10.1080/01614949808007114.
- [Mig15] S. MIGNUZZI, A. J. POLLARD, N. BONINI, et al. “Effect of Disorder on Raman Scattering of Single-Layer MoS₂.” In: *Physical Review B* **91.19** (2015), p. 195411. DOI: 10.1103/PhysRevB.91.195411.
- [Min04] L. MIN, C. WEI-MIN, L. NAI-GANG, and W. LING-DONG. “A Numerical Study of Indentation Using Indenters of Different Geometry.” In: *Journal of Materials Research* **19.1** (2004), pp. 73–78. DOI: 10.1557/jmr.2004.19.1.73.
- [Mit69] S. S. MITRA. “Infrared and Raman Spectra Due to Lattice Vibrations.” In: *Optical Properties of Solids*. Springer, 1969. Chap. 14, pp. 333–452.
- [Mol18] H. MOLDENHAUER, M. BAYER, J. DEBUS, A. NIKOLOV, and A. BRÜMMER. “Raman Scattering Study of Micrometer-Sized Spots of Magnetite and Hematite Formed at 18CrNiMo7-6 Screw Rotor Surfaces due to Liquid-Free, Unsynchronized Operation.” In: *IOP Conference Series: Materials Science and Engineering* **425** (2018). ©, p. 012016. DOI: 10.1088/1757-899x/425/1/012016.
- [Mol19] H. MOLDENHAUER, A. WITTIG, D. KOKALJ, et al. “Resonant Raman Scattering Characterization of Thermally Annealed HiPIMS Deposited MoS_x Coatings.” In: *Surface and Coatings Technology* **337** (2019). ©, p. 124891. DOI: 10.1016/j.surfcoat.2019.124891.
- [Mol20] H. MOLDENHAUER, C. RITTMAN, and S. GRISARD. *Spectrum Analysis*. 2020. URL: https://github.com/hmoldenhauer/spectrum_analysis.

- [Mra09] S. E. MRABET, M. D. ABAD, C. LÓPEZ-CARTES, D. MARTÍNEZ-MARTÍNEZ, and J. C. SÁNCHEZ-LÓPEZ. “Thermal Evolution of WC/C Nanostructured Coatings by Raman and In Situ XRD Analysis.” In: *Plasma Processes and Polymers* **6.S1** (2009), S444–S449. DOI: 10.1002/ppap.200931004.
- [Muk11] A. MUKHOPADHYAY and B. BASU. “Recent Developments on WC-Based Bulk Composites.” In: *Journal of Materials Science* **46.3** (2011), pp. 571–589. DOI: 10.1007/s10853-010-5046-7.
- [Mün02] W.-D. MÜNZ, A. P. EHIASARIAN, and P. HOVSEPIAR. “Kombiniertes Beschichtungs-Verfahren, magnetfeldunterstützte Hochleistungs-Impuls-Kathodenzerstäubung und unbalanziertes Magnetron.” European Patent **1260603 A2**. 2002. URL: <https://data.epo.org/publication-server/document?PN=EP1260603%20EP%201260603&iDocId=2071375&iPosition=0&iFormat=0>.
- [Naj12] S. NAJMAEI, Z. LIU, P. M. AJAYAN, and J. LOU. “Thermal Effects on the Characteristic Raman Spectrum of Molybdenum Disulfide (MoS₂) of Varying Thicknesses.” In: *Applied Physics Letters* **100.1** (2012), p. 013106. DOI: 10.1063/1.3673907.
- [Neu18] C. NEUMANN and C. STAMPFER. “Characterization of Graphene by Confocal Raman Spectroscopy.” In: *Confocal Raman Microscopy*. 2nd ed. Springer-Verlag, 2018. Chap. 8, pp. 177–194.
- [New20] M. NEWVILLE, R. OTTEN, A. NELSON, et al. *LMFIT Non-Linear Least-Squares Minimization and Curve-Fitting for Python*. 2020. URL: <https://doi.org/10.5281/zenodo.598352>.
- [Nia16] J. NIAN, Y. SI, and Z. GUO. “Advances in Atomic-Scale Tribological Mechanisms of Solid Interfaces.” In: *Tribology International* **94** (2016), pp. 1–13. DOI: 10.1016/j.triboint.2015.08.013.
- [Nic17a] P. NICKOLAS. “An Overview.” In: *Wavelets: A Student Guide*. Cambridge University Press, 2017. Chap. 1, pp. 1–30.
- [Nic17b] P. NICKOLAS. *Wavelets: A Student Guide*. Cambridge: Cambridge University Press, 2017.
- [Nic20] NICOGUARO. *Stress-Strain Diagram for a Ductile Material*. © ⓘ. 2020. URL: https://en.wikipedia.org/wiki/File:Stress_strain_ductile.svg.
- [Nik17] D. L. NIKA and A. A. BALANDIN. “Phonons and Thermal Transport in Graphene and Graphene-Based Materials.” In: *IOP Publishing* **80.3** (2017), p. 036502. DOI: 10.1088/1361-6633/80/3/036502.
- [Nov04] K. S. NOVOSELOV. “Electric Field Effect in Atomically Thin Carbon Films.” In: *Science* **306.5696** (2004), pp. 666–669. DOI: 10.1126/science.1102896.
- [OBr09] R. D. O’BRIEN. “Characterization of Thin Films and Surfaces.” In: *Fats and Oils*. 3rd ed. CRC Press, 2009. Chap. 1, pp. 1–72.
- [Ohr02a] M. OHRING. “A Review of Materials Science.” In: *Materials Science of Thin Films*. 2nd ed. Academic Press, 2002. Chap. 1, pp. 1–56.
- [Ohr02b] M. OHRING. “Characterization of Thin Films and Surfaces.” In: *Materials Science of Thin Films*. 2nd ed. Academic Press, 2002. Chap. 10, pp. 559–640.

- [Ohr02c] M. OHRING. “Discharges, Plasmas, and Ion-Surface Interactions.” In: *Materials Science of Thin Films*. 2nd ed. Academic Press, 2002. Chap. 4, pp. 145–202.
- [Ohr02d] M. OHRING. “Plasma and Ion Beam Processing of Thin Films.” In: *Materials Science of Thin Films*. 2nd ed. Academic Press, 2002. Chap. 5, pp. 203–276.
- [Oli77] J. OLIVERO and R. LONGBOTHUM. “Empirical Fits to the Voigt Line Width: A Brief Review.” In: *Journal of Quantitative Spectroscopy and Radiative Transfer* **17.2** (1977), pp. 233–236. DOI: 10.1016/0022-4073(77)90161-3.
- [Oli92] W. OLIVER and G. M. PHARR. “An Improved Technique for Determining Hardness and Elastic Modulus Using Load and Displacement Sensing Indentation Experiments.” In: *Journal of Materials Research* **7.6** (1992), pp. 1564–1583. DOI: 10.1557/JMR.1992.1564.
- [Opt20] E. OPTICS. *Simplifying Laser Alignment*. 2020. URL: <https://www.edmundoptics.com/knowledge-center/application-notes/lasers/simplifying-laser-alignment/>.
- [Ouy13] J. H. OUYANG and X. S. LIANG. “High-Temperature Solid Lubricating Materials.” In: *Encyclopedia of Tribology*. Springer, 2013, pp. 1671–1681.
- [Ova21] OVAKO. *100Cr6*. 2021. URL: <https://steelnavigator.ovako.com/steel-grades/100cr6/>.
- [Pag91] J. B. PAGE. “Many-Body Approach to the Theory of Resonance Raman Scattering by Vibronic Systems.” In: *Light Scattering in Solids VI*. Springer-Verlag, 1991. Chap. 2, pp. 17–72.
- [Par14] J. Y. PARK and M. SALMERON. “Fundamental Aspects of Energy Dissipation in Friction.” In: *Chemical Reviews* **114.1** (2014), pp. 677–711. DOI: 10.1021/cr200431y.
- [Ped11] F. PEDREGOSA, G. VAROQUAUX, A. GRAMFORT, et al. “Scikit-Learn: Machine Learning in Python.” In: *Journal of Machine Learning Research* **12** (2011). <https://scikit-learn.org>, pp. 2825–2830. URL: <https://jmlr.csail.mit.edu/papers/v12/pedregosa11a.html>.
- [Pet12] M. I. PETRESCU. “Theoretical Hardness Calculated from Crystallo-Chemical Data for MoS₂ and WS₂ Crystals and Nanostructures.” In: *Acta Crystallographica Section B Structural Science* **68.5** (2012), pp. 501–510. DOI: 10.1107/S0108768112033149.
- [Pin83] A. PINCZUK and E. BURSTEIN. “Fundamentals of Inelastic Light Scattering in Semiconductors and Insulators.” In: *Light Scattering in Solids I*. 2nd ed. Springer-Verlag, 1983. Chap. 2, pp. 23–78.
- [Pla15] M. PLACIDI, M. DIMITRIEVSKA, V. IZQUIERDO-ROCA, et al. “Multiwavelength Excitation Raman Scattering Analysis of Bulk and Two-Dimensional MoS₂: Vibrational Properties of Atomically Thin MoS₂ Layers.” In: *2D Materials* **2.3** (2015), p. 035006. DOI: 10.1088/2053-1583/2/3/035006.
- [Pla34] G. PLACZEK. “Rayleigh-Streuung und Raman-Effekt.” In: *Handbuch der Radiologie*. 2nd ed. Vol. 6. Akademische Verlagsanstalt, 1934. Chap. 3, pp. 205–374.

- [Pol20] M. N. POLYANSKIY. *Refractive Index Database*. 2020. URL: <https://refractiveindex.info>.
- [Pop19] V. L. POPOV, M. HESS, and E. WILLERT. “Normal Contact Without Adhesion.” In: *Handbook of Contact Mechanics*. Springer, 2019. Chap. 2, pp. 5–66.
- [Qia18] Q. QIAN, Z. ZHANG, and K. J. CHEN. “In Situ Resonant Raman Spectroscopy to Monitor the Surface Functionalization of MoS₂ and WSe₂ for High-k Integration: A First-Principles Study.” In: *Langmuir* **34.8** (2018), pp. 2882–2889. DOI: 10.1021/acs.langmuir.7b03840.
- [Qiu16] J. QIU, Z. YANG, Q. LI, et al. “Formation of N-doped Molybdenum Carbide Confined in Hierarchical and Hollow Carbon Nitride Microspheres with Enhanced Sodium Storage Properties.” In: *J. Mater. Chem. A* **4** (2016), pp. 13296–13306. DOI: 10.1039/C6TA05025E.
- [Que85] M. R. QUERRY. *Optical Constants*. 1985. URL: <https://apps.dtic.mil/docs/citations/ADA158623>.
- [Ram06] D. RAMMLMAIR, M. WILKE, K. RICKERS, et al. “Geology, Mining, Metallurgy.” In: *Handbook of Practical X-Ray Fluorescence Analysis*. Springer, 2006. Chap. 7.6, pp. 640–686.
- [Ram28a] C. V. RAMAN and K. S. KRISHNAN. “A New Type of Secondary Radiation.” In: *Nature* **121** (1928), pp. 501–502. DOI: 10.1038/121501c0.
- [Ram28b] C. V. RAMAN and K. S. KRISHNAN. “The Optical Analogue of the Compton Effect.” In: *Nature* **121** (1928), p. 711. DOI: 10.1038/121711a0.
- [Rie18] E. RIEDEL and H.-J. MEYER. *Allgemeine und Anorganische Chemie*. 12th ed. Berlin: de Gruyter, 2018.
- [Rin79] L. RINDER. “Einführung.” In: *Schraubenverdichter*. Springer-Verlag, 1979. Chap. 1, pp. 1–18.
- [Rit18] C. RITTMANN. *Measuring the Local Temperature at the Laser Spot with the Raman Microscopy Device MonoVista*. 2018.
- [Rob02] J. ROBERTSON. “Diamond-Like Amorphous Carbon.” In: *Materials Science and Engineering: R: Reports* **37.4** (2002), pp. 129–281. DOI: 10.1016/S0927-796X(02)00005-0.
- [Rob10] J. ROBERTSON. “Diamond-Like Carbon for Applications.” In: *Industrial Plasma Technology*. WILEY-VCH Verlag, 2010. Chap. 23, pp. 277–299.
- [Rob94] J. ROBERTSON. “The Deposition Mechanism of Diamond-Like a-C and a-C:H.” In: *Diamond and Related Materials* **3.4** (1994), pp. 361–368. DOI: 10.1016/0925-9635(94)90186-4.
- [Ros07] E. I. ROSS-MEDGAARDEN and I. E. WACHS. “Structural Determination of Bulk and Surface Tungsten Oxides with UV–Vis Diffuse Reflectance Spectroscopy and Raman Spectroscopy.” In: *Journal of Physical Chemistry C* **111.41** (2007), pp. 15089–15099. DOI: 10.1021/jp074219c.
- [Rou93] P. J. ROUSSEEUW and C. CROUX. “Alternatives to the Median Absolute Deviation.” In: *Journal of the American Statistical Association* **88.424** (1993), pp. 1273–1283. DOI: 10.1080/01621459.1993.10476408.

- [Ryb06] M. RYBACHUK and J. M. BELL. “The Observation of sp^2 Fraction Disorder Using Dual Wavelength Raman Spectroscopy in a-C:H Films Fabricated Using an Open Inductively Coupled Plasma Reactor.” In: *Diamond and Related Materials* **15.4** (2006), pp. 977–981. DOI: 10.1016/j.diamond.2005.12.001.
- [Sak09] N. SAKHAROVA, J. FERNANDES, J. ANTUNES, and M. OLIVEIRA. “Comparison Between Berkovich, Vickers and Conical Indentation Tests: A Three-Dimensional Numerical Simulation Study.” In: *International Journal of Solids and Structures* **46.5** (2009), pp. 1095–1104. DOI: 10.1016/j.ijsolstr.2008.10.032.
- [Sal75] E. SALJE. “Lattice Dynamics of WO_3 .” In: *Acta Crystallographica Section A* **31.3** (1975), pp. 360–363. DOI: 10.1107/S0567739475000757.
- [San14] E. SANI and A. DELL’ORO. “Optical Constants of Ethylene Glycol Over an Extremely Wide Spectral Range.” In: *Optical Materials* **37** (2014), pp. 36–41. DOI: 10.1016/j.optmat.2014.04.035.
- [Sch12] J. SCHIMEL. *Writing Science. How to Write Papers That Get Cited and Proposals That Get Funded*. New York: Oxford University Press, 2012.
- [Sch17] S. P. SCHWAMINGER, R. SURYA, S. FILSER, et al. “Formation of Iron Oxide Nanoparticles for the Photooxidation of Water: Alteration of Finite Size Effects from Ferrihydrite to Hematite.” In: *Scientific Reports* **7.1** (2017), p. 12609. DOI: 10.1038/s41598-017-12791-9.
- [Sch18] B. SCHULTRICH. “Activated Sputter Deposition of ta-C Films.” In: *Tetrahedrally Bonded Amorphous Carbon Films I*. Springer-Verlag, 2018. Chap. 17, pp. 679–720.
- [Sch91] A. SCHOENFLIES. *Krystallsysteme und Krystallstruktur*. ark:/13960/t3rv11r4n. Leipzig, 1891.
- [Seg95] L. SEGUIN, M. FIGLARZ, R. CAVAGNAT, and J.-C. LASSÈGUES. “Infrared and Raman Spectra of MoO_3 Molybdenum Trioxides and $MoO_3 \cdot x H_2O$ Molybdenum Trioxide Hydrates.” In: *Spectrochimica Acta Part A: Molecular and Biomolecular Spectroscopy* **51.8** (1995), pp. 1323–1344. DOI: 10.1016/0584-8539(94)00247-9.
- [Ser17] E. SERPINI, A. ROTA, A. BALLESTRAZZI, et al. “The Role of Humidity and Oxygen on MoS_2 Thin Films Deposited by RF PVD Magnetron Sputtering.” In: *Surface and Coatings Technology* **319** (2017), pp. 345–352. DOI: 10.1016/j.surfcoat.2017.04.006.
- [Set10] W. SETYAWAN and S. CURTAROLO. “High-Throughput Electronic Band Structure Calculations: Challenges and Tools.” In: *Computational Materials Science* **49.2** (2010), pp. 299–312. DOI: 10.1016/j.commatsci.2010.05.010.
- [Set90] F. SETTE, G. K. WERTHEIM, Y. MA, et al. “Lifetime and Screening of the C1s Photoemission in Graphite.” In: *Phys. Rev. B* **41** (1990), pp. 9766–9770. DOI: 10.1103/PhysRevB.41.9766.
- [Sha01] J. M. SHAVER. “Chemometrics for Raman Spectroscopy.” In: *Handbook of Raman Spectroscopy*. Marcel Dekker, 2001. Chap. 7, pp. 288–319.

- [Sha15] P. M. SHAFI and A. C. BOSE. “Impact of Crystalline Defects and Size on X-Ray Line Broadening: A Phenomenological Approach for Tetragonal SnO₂ Nanocrystals.” In: *AIP Advances* **5.5** (2015), p. 057137. DOI: 10.1063/1.4921452.
- [She03a] O. N. SHEBANOVA and P. LAZOR. “Raman Spectroscopic Study of Magnetite (FeFe₂O₄): A New Assignment for the Vibrational Spectrum.” In: *Journal of Solid State Chemistry* **174.2** (2003), pp. 424–430. DOI: 10.1016/S0022-4596(03)00294-9.
- [She03b] O. N. SHEBANOVA and P. LAZOR. “Raman Study of Magnetite (Fe₃O₄): Laser-Induced Thermal Effects and Oxidation.” In: *Journal of Raman Spectroscopy* **34.11** (2003), pp. 845–852. DOI: 10.1002/jrs.1056.
- [She03c] O. N. SHEBANOVA and P. LAZOR. “Vibrational Modeling of the Thermodynamic Properties of Magnetite (Fe₃O₄) at High Pressure from Raman Spectroscopic Study.” In: *Journal of Chemical Physics* **119.12** (2003), pp. 6100–6110. DOI: 10.1063/1.1602072.
- [She84] H. SHEN and F. H. POLLAK. “Raman Study of Polish-Induced Surface Strain in $\langle 100 \rangle$ GaAs and InP.” In: *Applied Physics Letters* **45.6** (1984), pp. 692–694. DOI: 10.1063/1.95359.
- [Shi07] Y. SHIMIZU, J. ISHII, and T. BABA. “Reflectance Thermometry for Microscale Metal Thin Films.” In: *Japanese Journal of Applied Physics* **46.5R** (2007), p. 3117. DOI: 10.1143/JJAP.46.3117.
- [Sie86] A. E. SIEGMAN. *Lasers*. Sausalito, California: University Science Books, 1986.
- [Sin03] I. L. SINGER, S. D. DVORAK, K. J. WAHL, and T. W. SCHARF. “Role of Third Bodies in Friction and Wear of Protective Coatings.” In: *Journal of Vacuum Science & Technology A* **21.5** (2003), S232–S240. DOI: 10.1116/1.1599869.
- [Sin96] I. SINGER, S. FAYEULLE, and P. EHNI. “Wear Behavior of Triode-Sputtered MoS₂ Coatings in Dry Sliding Contact with Steel and Ceramics.” In: *Wear* **195.1** (1996), pp. 7–20. DOI: 10.1016/0043-1648(95)06661-6.
- [Sir19] B. SIROTA, N. GLAVIN, and A. A. VOEVODIN. “Room Temperature Magnetron Sputtering and Laser Annealing of Ultrathin MoS₂ for Flexible Transistors.” In: *Vacuum* **160** (2019), pp. 133–138. DOI: 10.1016/j.vacuum.2018.10.077.
- [Siu13] K. W. SIU and A. H. W. NGAN. “The Continuous Stiffness Measurement Technique in Nanoindentation Intrinsically Modifies the Strength of the Sample.” In: *Philosophical Magazine* **93.5** (2013), pp. 449–467. DOI: 10.1080/14786435.2012.722234.
- [Sla02] W. S. SLAUGHTER. “Activated Sputter Deposition of ta-C Films.” In: *The Linearized Theory of Elasticity*. Springer, 2002. Chap. 1, pp. 1–22.
- [Sli63] H. E. SLINEY. “Decomposition Kinetics of Some Solid Lubricants Determined by Elevated-Temperature X-Ray Diffraction Techniques.” In: *Proceedings of the USAF Aerospace Fluids and Lubricants Conference*. Southwest Research Institute, 1963, pp. 350–367. URL: <https://babel.hathitrust.org/cgi/pt?id=coo.31924004053363&view=1up&seq=1>.

- [Smi19a] E. SMITH and G. DENT. “Resonance Raman Scattering.” In: *Modern Raman Spectroscopy*. 2nd ed. John Wiley & Sons, 2019. Chap. 4, pp. 100–117.
- [Smi19b] E. SMITH and G. DENT. “The Raman Experiment - Raman Instrumentation, Sample Presentation, Data Handling and Practical Aspects of Interpretation.” In: *Modern Raman Spectroscopy*. 2nd ed. John Wiley & Sons, 2019. Chap. 2, pp. 21–76.
- [Smi19c] E. SMITH and G. DENT. “The Theory of Raman Spectroscopy.” In: *Modern Raman Spectroscopy*. 2nd ed. John Wiley & Sons, 2019. Chap. 3, pp. 77–99.
- [Smi84] F. W. SMITH. “Optical Constants of a Hydrogenated Amorphous Carbon Film.” In: *Journal of Applied Physics* **55.3** (1984), pp. 764–771. DOI: 10.1063/1.333135.
- [Sny82] R. G. SNYDER, H. L. STRAUSS, and C. A. ELLIGER. “Carbon-Hydrogen Stretching Modes and the Structure of n-Alkyl Chains. 1. Long, Disordered Chains.” In: *The Journal of Physical Chemistry* **86.26** (1982), pp. 5145–5150. DOI: 10.1021/j100223a018.
- [Soc01] G. SOCRATES. *Infrared and Raman Characteristic Group Frequencies. Tables and Charts*. 3rd ed. Chichester: John Wiley & Sons Ltd., 2001.
- [Soj17] M. SOJKOVÁ, Š. CHROMIK, A. ROŠOVÁ, et al. “MoS₂ Thin Films Prepared by Sulfurization.” In: *Nanoengineering: Fabrication, Properties, Optics, and Devices XIV*. **10354**. 2017, pp. 218–224. DOI: 10.1117/12.2273846.
- [Sol07] J. SOLYNOM. “Dynamics of Crystal Lattices.” In: *Fundamentals of the Physics of Solids*. Springer, 2007. Chap. 11, pp. 331–386.
- [Sol70] S. A. SOLIN and A. K. RAMDAS. “Raman Spectrum of Diamond.” In: *Physical Review B* **1.4** (1970), pp. 1687–1698. DOI: 10.1103/PhysRevB.1.1687.
- [Spi09] L. SPIESS, G. TEICHERT, R. SCHWARZER, H. BEHNKEN, and C. GENZEL. “Röntgenographische Spannungsanalyse.” In: *Moderne Röntgenbeugung*. 2nd ed. Vieweg+Teubner, 2009. Chap. 10, pp. 305–382.
- [Sta14a] G. W. STACHOWIAK and A. W. BATCHELOR. “Elastohydrodynamic Lubrication.” In: *Engineering Tribology*. 4th ed. Butterworth-Heinemann, 2014. Chap. 7, pp. 293–370.
- [Sta14b] G. W. STACHOWIAK and A. W. BATCHELOR. “Fundamentals of Contact between Solids.” In: *Engineering Tribology*. 4th ed. Butterworth-Heinemann, 2014. Chap. 10, pp. 475–524.
- [Sta14c] G. W. STACHOWIAK and A. W. BATCHELOR. “Introduction.” In: *Engineering Tribology*. 4th ed. Butterworth-Heinemann, 2014. Chap. 1, pp. 1–10.
- [Sta15] K. STADLER, J. LAI, and R. H. VEGTER. “A Review: The Dilemma With Premature White Etching Crack (WEC) Bearing Failures.” In: *Bearing Steel Technologies: 10th Volume, Advances in Steel Technologies for Rolling Bearings*. ASTM International, 2015, pp. 487–508. DOI: 10.1520/STP158020140046.

- [Sta85] A. STACY and D. HODUL. “Raman Spectra of IVB and VIB Transition Metal Disulfides Using Laser Energies Near the Absorption Edges.” In: *Journal of Physics and Chemistry of Solids* **46.4** (1985), pp. 405–409. DOI: 10.1016/0022-3697(85)90103-9.
- [Sto05] N. STOSIC, I. SMITH, and A. KOVACEVIC. In: *Screw Compressors*. Springer, 2005. Chap. 1, pp. 1–18.
- [Sto52] G. G. STOKES. “XXX. On the Change of Refrangibility of Light.” In: *Philosophical Transactions of the Royal Society of London* **142** (1852), pp. 463–562. DOI: 10.1098/rstl.1852.0022.
- [Str71] H. J. W. STRUTT. “XV. On the Light from the Sky, its Polarization and Colour.” In: *The London, Edinburgh, and Dublin Philosophical Magazine and Journal of Science* **41.271** (1871), pp. 107–120. DOI: 10.1080/14786447108640452.
- [Stu08] STUDENT. “The Probable Error of a Mean.” In: *Biometrika* **6.1** (1908), p. 1. DOI: 10.2307/2331554.
- [Tem07] J. TEMMING. “Stationärer und instationärer Betrieb eines unsynchronisierten Schraubenladers.” Dissertation. University of Dortmund, 2007.
- [Tho21] THORLABS. *Scanning Fabry-Perot Interferometers*. Thorlabs. 2021. URL: https://www.thorlabs.de/newgrouppage9.cfm?objectgroup_id=859.
- [Til18] W. TILLMANN, N. F. L. DIAS, and D. STANGIER. “Tribo-Mechanical Properties of CrC/a-C Thin Films Sequentially Deposited by HiPIMS and mfMS.” In: *Surface and Coatings Technology* **335** (2018), pp. 173–180. DOI: 10.1016/j.surfcoat.2017.12.035.
- [Til19a] W. TILLMANN, N. F. L. DIAS, D. STANGIER, et al. “Interaction Effects of Cathode Power, Bias Voltage, and Mid-Frequency on the Structural and Mechanical Properties of Sputtered Amorphous Carbon Films.” In: *Applied Surface Science* **487** (2019). © ⓘ ⊕ ⊖, pp. 857–867. DOI: 10.1016/j.apsusc.2019.05.131.
- [Til19b] W. TILLMANN, D. KOKALJ, and D. STANGIER. “Influence of the Deposition Parameters on the Texture and Mechanical Properties of Magnetron Sputtered Cubic MoN_x Thin Films.” In: *Materialia* **5** (2019), p. 100186. DOI: 10.1016/j.mtla.2018.100186.
- [Til19c] W. TILLMANN, A. WITTIG, D. STANGIER, et al. “Investigation of the Tribofilm Formation of HiPIMS Sputtered MoS_x Thin Films in Different Environments by Raman Scattering.” In: *Lubricants* **7.11** (2019). © ⓘ. DOI: 10.3390/lubricants7110100.
- [Tre01] P. J. TREADO and M. P. NELSON. “Raman Imaging.” In: *Handbook of Raman Spectroscopy*. Marcel Dekker, 2001. Chap. 5, pp. 204–263.
- [Ull18] M. S. ULLAH, A. H. bin YOUSUF, A. D. ES-SAKHI, and M. H. CHOWDHURY. “Analysis of Optical and Electronic Properties of MoS₂ for Optoelectronics and FET Applications.” In: *AIP Conference Proceedings* **1957.1** (2018), p. 020001. DOI: 10.1063/1.5034320.
- [Urb10] M. URBAKH and E. MEYER. “The Renaissance of Friction.” In: *Nature Materials* **9.1** (2010), pp. 8–10. DOI: 10.1038/nmat2599.

- [Utr19] M. UTRI, D. AURICH, A. BRÜMMER, et al. “Theoretical Investigation of the Rotor Contact Stress in Non-Synchronized, Dry Running Twin-Screw Machines.” In: *Prozesstechnik und Komponenten* (2019), pp. 84–93. URL: <https://bc-v3.pressmatrix.com/de/profiles/ee23a4677553/editions/49f5e58353bad86c052b/pages/page/45>.
- [Vai21] A. VAITKUS, A. MERKYS, and S. GRAŽULIS. “Validation of the Crystallography Open Database Using the Crystallographic Information Framework.” In: *Journal of Applied Crystallography* **54.2** (2021), pp. 661–672. DOI: 10.1107/S1600576720016532.
- [Van07] L. VANDEPERRE, F. GIULIANI, S. LLOYD, and W. CLEGG. “The Hardness of Silicon and Germanium.” In: *Acta Materialia* **55.18** (2007), pp. 6307–6315. DOI: 10.1016/j.actamat.2007.07.036.
- [Van11] P. VAN DER HEIDE. “Data Collection and Quantification.” In: *X-Ray Photoelectron Spectroscopy*. John Wiley & Sons, 2011. Chap. 4, pp. 61–100.
- [Van13a] P. VANDENABEELE. *Practical Raman Spectroscopy. An Introduction*. Chichester: John Wiley & Sons, 2013.
- [Van13b] P. VANDENABEELE. “Raman Spectroscopy in Daily Lab-Life.” In: *Practical Raman Spectroscopy*. John Wiley & Sons, 2013. Chap. 5, pp. 101–148.
- [Van13c] P. VANDENABEELE. “Theoretical Aspects.” In: *Practical Raman Spectroscopy*. John Wiley & Sons, 2013. Chap. 1, pp. 1–38.
- [Vie12] B. VIERNEUSEL, S. TREMMEL, and S. WARTZACK. “Effects of Deposition Parameters on Hardness and Lubrication Properties of Thin MoS₂ Films.” In: *Materialwissenschaft und Werkstofftechnik* **43.12** (2012), pp. 1029–1035. DOI: 10.1002/mawe.201200942.
- [Vie13] B. VIERNEUSEL, T. SCHNEIDER, S. TREMMEL, S. WARTZACK, and T. GRADT. “Humidity Resistant MoS₂ Coatings Deposited by Unbalanced Magnetron Sputtering.” In: *Surface and Coatings Technology* **235** (2013), pp. 97–107. DOI: 10.1016/j.surfcoat.2013.07.019.
- [Vog11] E. VOGLI, W. TILLMANN, U. SELVADURAI-LASSL, G. FISCHER, and J. HERPER. “Influence of Ti/TiAlN-Multilayer Designs on their Residual Stresses and Mechanical Properties.” In: *Applied Surface Science* **257.20** (2011), pp. 8550–8557. DOI: 10.1016/j.apsusc.2011.05.013.
- [Voi19] B. VOIGTLAENDER. “Introduction.” In: *Atomic Force Microscopy*. 2nd ed. Springer, 2019. Chap. 1, pp. 1–14.
- [von07] U. VON LUXBURG. “A Tutorial on Spectral Clustering.” In: *Statistics and Computing* **17.4** (2007), pp. 395–416. DOI: 10.1007/s11222-007-9033-z.
- [Wan13] Q. J. WANG. *Encyclopedia of Tribology*. New York: Springer, 2013. DOI: 10.1007/978-0-387-92897-5.
- [Was16] R. L. WASSERSTEIN and N. A. LAZAR. “The ASA Statement on P-Values: Context, Process, and Purpose.” In: *The American Statistician* **70.2** (2016), pp. 129–133. DOI: 10.1080/00031305.2016.1154108.

- [Web00] W. H. WEBER, R. MERLIN, A. ZUNGER, et al., eds. *Raman Scattering in Materials Science*. **42**. Berlin, Heidelberg, 2000. DOI: 10.1007/978-3-662-04221-2.
- [Wes05] C. WESTPHAL, U. BERGES, S. DREINER, et al. “The Plane-Grating Monochromator Beamline at the U55 Undulator for Surface and Interface Studies at DELTA.” In: *Journal of Electron Spectroscopy and Related Phenomena* **144 - 147** (2005), pp. 1117–1123. DOI: 10.1016/j.eispec.2005.01.287.
- [Wie13] B. R. WIESENT. “Miniaturisiertes Infrarot-Spektrometer zur Online-Ölzustandsüberwachung in Offshore-Windkraftgetrieben.” Dissertation. Technische Universität München, 2013.
- [Wil06] L. WILKINSON. “Revising the Pareto Chart.” In: *The American Statistician* **60.4** (2006), pp. 332–334. DOI: 10.1198/000313006X152243.
- [Win11] B. C. WINDOM, W. G. SAWYER, and D. W. HAHN. “A Raman Spectroscopic Study of MoS₂ and MoO₃: Applications to Tribological Systems.” In: *Tribology Letters* **42.3** (2011), pp. 301–310. DOI: 10.1007/s11249-011-9774-x.
- [Wit00] J. WITTENBURG, J. ZIEREP, and K. BÜHLER. “Technische Mechanik.” In: *Die Grundlagen der Ingenieurwissenschaften*. 31st ed. Springer-Verlag, 2000. Chap. E5, E61–E119.
- [Won17] W. WONG, S. NG, H. WONG, et al. “Effect of Post-Annealing on Sputtered MoS₂ Films.” In: *Solid-State Electronics* **138** (2017), pp. 62–65. DOI: 10.1016/j.sse.2017.07.009.
- [Woo18] R. J. K. WOOD, S. HERD, and M. R. THAKARE. “A Critical Review of the Tribocorrosion of Cemented and Thermal Sprayed Tungsten Carbide.” In: *Tribology International* **119** (2018), pp. 491–509. DOI: 10.1016/j.triboint.2017.10.006.
- [Woo67] L. A. WOODWARD. “General Introduction.” In: *Raman Spectroscopy*. 1st ed. Plenum Press, 1967. Chap. 1, pp. 1–43.
- [Yad14] L. YADGAROV, C. L. CHOI, A. SEDOVA, et al. “Dependence of the Absorption and Optical Surface Plasmon Scattering of MoS₂ Nanoparticles on Aspect Ratio, Size, and Media.” In: *ACS Nano* **8.4** (2014), pp. 3575–3583. DOI: 10.1021/nn5000354.
- [Yak93] R. YAKIMOVA, T. PASKOVA, I. IVANOV, K. GERMANOVA, and M. PEEV. “Raman Scattering Study of Crystal Perfection of MOVPE-Grown GaAs.” In: *Semiconductor Science and Technology* **8.2** (1993), pp. 179–184. DOI: 10.1088/0268-1242/8/2/006.
- [Yan08] B. Q. YANG, X. P. WANG, H. X. ZHANG, Z. B. WANG, and P. X. FENG. “Effect of Substrate Temperature Variation on Nanostructured WC Films Prepared Using HFCVD Technique.” In: *Materials Letters* **62.10** (2008), pp. 1547–1550. DOI: 10.1016/j.matlet.2007.09.020.
- [Yog16] P. YOGI, S. K. SAXENA, S. MISHRA, et al. “Interplay Between Phonon Confinement and Fano Effect on Raman Line Shape for Semiconductor Nanostructures: Analytical Study.” In: *Solid State Communications* **230** (2016), pp. 25–29. DOI: 10.1016/j.ssc.2016.01.013.

- [Zai01] A. M. ZAITSEV. “Scattering.” In: *Optical Properties of Diamond*. Springer, 2001. Chap. 4, pp. 69–124.
- [Zen12] H. ZENG, B. ZHU, K. LIU, et al. “Low-Frequency Raman Modes and Electronic Excitations in Atomically Thin MoS₂ Films.” In: *Phys. Rev. B* **86** (2012), p. 241301. DOI: 10.1103/PhysRevB.86.241301.
- [Zha01] X. ZHANG, R. G. VITCHEV, W. LAUWERENS, et al. “Effect of Crystallographic Orientation on Fretting Wear Behaviour of MoS_x Coatings in Dry and Humid Air.” In: *Thin Solid Films* **396.1** (2001), pp. 69–77. DOI: 10.1016/S0040-6090(01)01141-5.
- [Zha04] X. ZHANG, W. LAUWERENS, J. HE, and J.-P. CELIS. “Reorientation of Randomly Oriented MoS_x Coatings During Fretting Wear Tests.” In: *Tribology Letters* **17** (2004), pp. 607–612. DOI: 10.1023/B:TRIL.0000044510.19983.0d.
- [Zha10] S. ZHANG. *Nanostructured Thin Films and Coatings. Mechanical Properties*. Boca Raton: CRC Press, 2010.
- [Zha13a] X. ZHANG, W. P. HAN, J. B. WU, et al. “Raman Spectroscopy of Shear and Layer Breathing Modes in Multilayer MoS₂.” In: *Phys. Rev. B* **87** (2013), p. 115413. DOI: 10.1103/PhysRevB.87.115413.
- [Zha13b] Y. ZHAO, X. LUO, H. LI, et al. “Interlayer Breathing and Shear Modes in Few-Trilayer MoS₂ and WSe₂.” In: *Nano Letters* **13.3** (2013), pp. 1007–1015. DOI: 10.1021/nl304169w.
- [Zha16] X. ZHANG, L. QIAO, L. CHAI, et al. “Structural, Mechanical and Tribological Properties of Mo–S–N Solid Lubricant Films.” In: *Surface and Coatings Technology* **296** (2016), pp. 185–191. DOI: 10.1016/j.surfcoat.2016.04.040.
- [Zol14] E. ZOLOTAYABKO. “Applications to Materials Science: Residual Strain/Stress Measurements.” In: *Basic Concepts of X-Ray Diffraction*. John Wiley & Sons, 2014. Chap. 16, pp. 189–192.

Acknowledgments

In the end, I would like to thank all the people I met during my studies, that supported, helped and encouraged me to finish this thesis. At first I would like to thank Prof. Dr. Manfred Bayer for the opportunity to work at his chair and the possibility to work with cutting edge equipment, supplying various measurement techniques. I also thank Dr. Jörg Debus for supervising me, sharing his knowledge and giving valuable advice.

Many thanks goes to Lars Wieschollek, Thomas Stöhr, Michaela Wäscher, Nina Colette and Katharina Sparka for excellent technical assistance and administrative support. I have to thank my office colleagues Janina Schindler, Dr. Janina Rautert and Eiko Evers for fruitful discussions, emotional support and various assistance. The measurements in the lab became even more exciting with the helpful suggestions of Carl Arne Thomann and multiple Bachelor students diversified the daily routine. Thank you! With in-depth conversations during long measurements Dr. Felix Godejohann shortened the time felt in the lab significantly.

I very much appreciated the collaboration with the PVD group of the LWT at TU Dortmund. Here, a great deal of thanks goes to Dominic Stangier, Nelson Filipe Lopes Dias and Alexandra Wittig for an extremely productive and comfortable cooperation. Of our chair I notably thank Dr. Felix Spitzer, Dr. Julian Heckötter, Erik Kirstein, Lars Klompmaker, Laura Krauß-Kodytek and Jan Mundry for unreserved helpfulness and support, uncounted motivating conversations and creative ideas. I thank all members of EII and associated colleagues for supplying a working-worth environment and the legendary board game nights. I am very thankful to Jörg Debus, Carl Arne Thomann, Julian Heckötter, Lars Klompmaker, Dr. Robert Temminghoff and Marie Schmitz for proofreading and commenting on my thesis, helping me to significantly improve it. I am grateful that I became part in the alumni association of the faculty (PeP). This brought me unforgettable memories, honest friends and taught me valuable lessons.

My special thanks goes to my girlfriend Marie, who supported me in all situations of my PhD, despite her own demands of writing her thesis. Moreover, I deeply thank all my friends and family for providing tremendous backup in all circumstances, invariably motivating me. Last but not least, I want to thank my parents Silke and Reinhard, for unconditional love and support, as well as their upbringing, making me the person I am today.